UNIVERSITY OF CALIFORNIA

Los Angeles

# The eukaryotic histones H2A and H3:

# From chromatin compaction to copper homeostasis

A dissertation submitted in partial satisfaction of the

requirements for the degree of Doctor of Philosophy

in Molecular Biology

by

Oscar A. Campos

2018

ABSTRACT OF THE DISSERTATION

The eukaryotic histones H2A and H3:

From chromatin compaction to copper homeostasis

by

Oscar A. Campos

Doctor of Philosophy in Molecular Biology

University of California, Los Angeles, 2018

Professor Siavash K. Kurdistani, Chair

In eukaryotes, genome size varies disproportionately relative to nuclear size such that larger genomes are generally more compact than smaller genomes. We found that the histone H2A N-terminal domain (NTD) and the histone H2B C-terminal domain have co-evolved with genome size, and that the co-evolving residues contribute to the differential chromatin compaction in organisms as diverse as the budding yeast and humans. Interestingly, histones appear to predate eukaryotes and evolved from archaeal histone-like proteins. The structural simplicity of the ancestral histones raises doubts as to whether they participated in the types of chromatin regulatory functions histones perform today. We therefore asked whether histones performed a different function in the early eukaryotes. In the nucleosome structure, the interface region of the two histone H3 proteins forms a potential transition metal coordination site. Interestingly, the appearance of eukaryotes roughly coincided with the accumulation of oxygen, which led to the

oxidation of essential transition metals like copper, and challenged cells to maintain metal homeostasis. Could histones, through a copper coordination site at the H3-H3' interface, have provided a mechanism for maintaining the reduced Cu(I) ions to support copper-dependent processes? We show that in the budding yeast, genetic perturbation of the putative metal coordination site indeed disrupts mitochondrial respiration and superoxide dismutase function in a manner recoverable by provision of excess copper, but not other metals. These phenotypes are not explained by a deficiency in cellular copper accumulation, nor by gene expression perturbation, but are recapitulated by disruption of cellular redox state. Together, these findings suggest that histones maintain Cu(I) levels. Indeed, the histone H3-H4 tetramer assembled *in vitro* from recombinant histones exhibits copper reductase activity, catalyzing the conversion of Cu(II) to Cu(I). This unprecedented enzymatic function is altered by mutation of histidine and cysteine residues in the putative metal coordination region. We propose that eukaryotic chromatin is an oxidoreductase enzyme, which provides biousable copper for cellular processes. As the emergence of eukaryotes coincided with increased oxidation and therefore decreased biousability of essential metals, the enzymatic function of histones could have facilitated eukaryogenesis.

The dissertation of Oscar A. Campos is approved.

Albert J. Courey

Reid C. Johnson

Siavash K. Kurdistani, Committee Chair

University of California, Los Angeles

2018

TABLE OF CONTENTS

FIGURES

TABLES

ACKNOWLEDGEMENTS

CHAPTERS AND PUBLICATIONS

The work presented in this dissertation was performed in collaboration with several members of the Kurdistani lab. I cannot thank them enough for the opportunity to work alongside them. Chapter 2 is a reproduction of a paper we published in 2014 in the journal eLife in which I was a middle author. This was work led by three co-first authors, Ben Macadangdang, Amit Oberai, and Tanya Spektor. The full reference is as follows:

Macadangdang, B.R., Oberai, A., Spektor, T., Campos, O.A., Sheng, F., Carey, M.F., Vogelauer, M., and Kurdistani, S.K. (2014). Evolution of histone 2A for chromatin compaction in eukaryotes. Elife 3: e02792. DOI: 10.7554/eLife.02792.

Ben led the way in developing the molecular biology approaches for analysis of chromatin compaction in cells. Amit was critical for devising the strategy for bioinformatics analysis of histone sequences across eukaryotes. Tanya was instrumental in developing the *in vitro* chromatin compaction assays. All three were also crucial in developing the experimental strategies and together with our PI, Siavash Kurdistani, directed the projected. I had the opportunity to examine the functional consequences of chromatin compaction in the yeast, some of which was used in the publication, and I also contributed to the manuscript writing and editing. Thanks to all of the other contributing authors listed above, and other members of the Kurdistani lab that contributed in other ways.

Chapter 3 is largely based on further efforts by Ben Macadangdang to unravel the contributions of histones to chromatin compaction. I similarly contributed to examining the effects

of the histones on yeast cell biology and have helped along the way with RNA-seq data analysis, and writing and editing the document up to this point. Chapter 3 is intended to become an additional publication that is still in progress. In addition to the main contribution by Ben and Siavash, thanks to Amit Oberai, Maria Vogelauer, and Beena Biju for other intellectual and experimental contributions to the work presented in this chapter.

Chapter 4 is a reproduction of a manuscript that will soon be submitted for publication. It represents the bulk of my work in the PhD and is the culmination of a collaboration between myself, Narsis Attar and Maria Vogelauer. The three of us will share co-first authorship. The author line is as follows as of April 2018:

**The Histone H3-H4 Tetramer is a Copper Reductase Enzyme**

Narsis Attar[1,2,3], Oscar A. Campos[1,2,3], Maria Vogelauer[1,2], Yong Xue[2], Stefan Schmollinger[4], Linda Yen[5], Nathan V. Mallipeddi[2], Sichen Yang[2], Shannon Zikovich[2], Jade Dardine[2], Michael F. Carey[2,3], Sabeeha S. Merchant[4], and Siavash K. Kurdistani[2,3,6,7]

[1]Co-first author, listed alphabetically

[2]Department of Biological Chemistry, [3]Molecular Biology Institute, [4]Institute for Genomics and Proteomics, Department of Chemistry and Biochemistry, [5]Department of Molecular, Cell, and Developmental Biology, and [6]Eli and Edythe Broad Center of Regenerative Medicine and Stem Cell Research, David Geffen School of Medicine, University of California Los Angeles, Los Angeles, CA 90095, USA

[7]Lead Contact

Narsis, Maria, Siavash, and I have contributed intellectually in all aspects of the project, from devising the experimental strategies and data analysis to discussing research direction and writing the manuscript. More specifically, Narsis and I have experimentally examined the regulation of copper homeostasis in cells and Maria and Siavash developed the *in vitro* histone copper reductase assays. We have had additional assistance from Yong Xue who contributed significantly to discussions and overall direction of the project. I want to give huge thanks to Linda Yen and Stefan Schmollinger for their crucial technical expertise in developing our *in vitro* histone preparations and metal quantification by ICP-MS, respectively, as well as Mike Carey and Sabeeha Merchant. Nathan Mallipeddi and Sichen Yang also contributed to important yeast biology experiments and came on to the project at a crucial time for us. Thanks also to Shannon Zikovich and Jade Dardine, who provided some of the very first experimental results in yeast that drove us to pursue this project. Last but not least, Chen Cheng has recently provided important assistance in preparing *in vitro* histone copper reductase experiments.

Chapter 5 is an extension of the work presented in Chapter 4 involving further analysis of the role of histone-based copper reduction in cell biology. It is based on a close collaboration with Narsis Attar, with whom I will share co-first authorship in a planned publication reporting this work. Siavash has also directed the project as PI. The project is ongoing and I must specifically acknowledge Nathan Mallipeddi, who has been helping significantly with advancing the project with his experimental contributions. Maria Vogelauer has also significantly contributed intellectually to this project.

PEOPLE

In high school and college, I often read in textbooks about the major discoveries that have shaped the scientific paradigms. I heard about the strokes of genius that often lead to elegant and simple experiments that have uncovered the fundamental nature of the universe. But I don't remember ever hearing about how difficult it was to get to those points. I didn't hear about the countless hours of work and of lost sleep that ultimately were required to achieve groundbreaking discovery. I have to thank my PhD advisor Siavash for leading by example in this regard. His tenacity, conviction, and courage to explore the paradigm-shifting questions in the face of constant doubts and experimental failures are nothing short of incredible. It has taught me a lot about what it takes to push the limits of understanding and to be truly innovative, and I hope I can take with me those lessons as I continue to forge my own approach to science. I want to similarly acknowledge Maria Vogelauer for continuing to work away on our project beyond the end of hope. Like Siavash, her love of science and discovery kept us going, and even after years of experimental failures, her excitement for the idea never let up. It is truly unfair that the final experiment that led us to breakthrough is deceptively simple, at least on paper, as it betrays the amount of effort required to get there. Thanks Maria for showing me that in the face of struggle, sometimes you just have to remember how cool it is to be on the brink of discovery.

By far the most influential person in my PhD has been my labmate and friend Narsis Attar, and I don't think "thanks" can ever be enough to describe how much gratitude I have for her. We started our doctoral degrees at about the same time and over the years had a partnership in science that I hope will always continue in some capacity in the future as we each build our careers. In addition to the direct contributions she had on the project, like Siavash and Maria, she has exemplified the optimism and dedication it takes to make the big discoveries. And on a more

personal level, she has been a close friend, a confidante, an intellectual partner, and an utterly inspiring role model.

Ben Macadangdang is another individual who has shaped my development as a scientist and person over the course of these last few years. I came in to the lab with very little experience in molecular biology, and with patience and support, he took the time to show me the ropes. But more importantly, he set a standard for what a graduate student and scientist should look like. His skills in diverse aspects of our work, from the computational analysis to the experimental biology was, and continues to be, impressive. And lastly, as a lab mentor who became a close friend, he has had a lasting impact on me. I also need to thank Chen Cheng, my very first mentor in the lab who has also become a good friend over the years. Some of the first scientific discussions I had in the lab were with her, and she is one of the primary reasons I wanted to join the lab in the first place.

I would like to thank many of the other members of the Kurdistani lab that have come and gone over the years, some of whom I've had the opportunity to known and learn from. Yong Xue in particular influenced me greatly, with his intelligence and efficiency in lab. He easily did twice as much work as I did in the same amount of time. Thanks Yong for the inspiration. I want to thank Nathan Mallipeddi for being such a hard-working and confident undergraduate student that I've had the opportunity to mentor.

Thanks to my committee members, Guillaume Chanfreau, Al Courey, Alison Frand, and Reid Johnson for their support and advice throughout the years. Every single meeting with them has been longer than scheduled or expected simply because the discussions were so engaging. I want to thank them for their time, inquisitiveness and interest in the project and my progress.

Last but not least, thanks to my family and closest of friends. I try to avoid cliché when I can, but there's just no other way to describe graduate school than to talk about how long and grueling the process can be at times. And how emotionally taxing it can be. Family and friends have always been there along the way to support me when I had trouble believing in myself, and when I couldn't see how things would work out. I am lucky to have a family that supports my career ambitions so unconditionally as they have done.

FUNDING

I have been personally funded by the Philip Whitcome Pre-doctoral Fellowship program from 2013-2016, and by the UCLA Graduate Division Dissertation Year Fellowship from 2016-2017.

# VITA

## EDUCATION

B.Sc. Specialization in Kinesiology, Minor in Medical Sciences, University of Western Ontario, London, Canada, 2008

M.Sc. Kinesiology, University of Western Ontario, London, Canada, 2011

## PUBLICATIONS

Murias, J.M., Campos, O.A., Hall, K.E., McDonald, M.W., Melling, C.W., and Noble, E.G. (2013). Vessel-specific rate of vasorelaxation is slower in diabetic rats. Diab Vasc Dis Res. 10, 179-186.

Murias, J.M., Dey, A., Campos, O.A., Estaki, M., Hall, K.E., Melling, C.W., and Noble, E.G. (2013). High-intensity endurance training results in faster vessel-specific rate of vasorelaxation in type 1 diabetic rats. PLoS One 8, e59678.

Hall, K.E., McDonald, M.W., Grisé, K.N., Campos, O.A., Noble, E.G., and Melling, C.W.J. (2013). The role of resistance and aerobic exercise training on insulin sensitivity measures in STZ-induced Type 1 diabetic rodents. Metabolism 62, 1485-1494.

Macadangdang, B.R., Oberai, A., Spektor, T., Campos, O.A., Sheng, F., Carey, M.F., Vogelauer, M., and Kurdistani, S.K. (2014). Evolution of histone 2A for chromatin compaction in eukaryotes. Elife e02792.

Xue, Y., Schmollinger, S., Attar. N., Campos, O.A., Vogelauer, M., Carey, M.F., Merchant, S.S., and Kurdistani, S.K. (2017). Endoplasmic reticulum-mitochondria junction is required for iron homeostasis. J Biol Chem 292, 13197-13204.

## PRESENTATIONS

*ORAL PRESENTATIONS*

Effects of moderate intensity exercise training on the aortic eNOS-Hsp90 interaction and insulin mediated vasorelaxation response in rats. *Experimental Biology annual conference, Washington, D.C., Apr 2011*

Physiological implications of altered chromatin compaction in *S. cerevisiae. UCLA Biological Chemistry department retreat, Malibu, CA, May 2013*

Co-evolution of histones with genome size for chromatin compaction. *Cold Spring Harbor Laboratory: Epigenetics and Chromatin meeting, Cold Spring Harbor, NY, Sep 2014*

Functional link between Chromatin Compaction, Vacuoles, And Copper homeostasis. *UCLA Biological Chemistry department Floor meeting, Los Angeles, CA, Jan 2015*

Distorted DNA structure in cancer: Lessons from yeast. *UCLA Grad Slam competition, Los Angeles, CA, Apr 2015*

An extraordinary function of histones in copper metabolism. *UCLA Biological Chemistry department Floor meeting, Los Angeles, CA, Mar 2017*

The nucleosome is a copper reductase enzyme. *UCLA Gene Regulation Intramural meeting, Los Angeles, CA, Oct 2017*

The Nucleosomal Cupric Reductase Mediates Cellular Copper Utilization. *UCLA Biological Chemistry department Floor meeting, Los Angeles, CA, Mar 2018*

*POSTER PRESENTATIONS*

Effect of reinforcement protocol on body temperature and musculoskeletal Hsp70 expression following short-term, moderately intense run training in rodents. *Canadian Society for Exercise Physiology annual conference, Vancouver, Canada, Nov 2009*

Long term low-intensity treadmill exercise in rodents leads to decreased insulin-mediated vasorelaxation *in vitro*. *Canadian Society for Exercise Physiology annual conference, Toronto, Canada, Nov 2010*

Phenotypic effects of H2A-mediated chromatin compaction. *UCLA Molecular Biology Institute annual retreat, Los Angeles, CA, Jan 2014*

Functional interaction between chromatin compaction and vacuoles. *UCLA Molecular Biology Institute annual retreat, Los Angeles, CA, Apr 2015 & 2016 (2 meetings)*

Functional interaction between histones, metals, and vacuoles. *Tokyo Tech's Academy of Computational Life Sciences annual summer school, Oxford, UK, Sep 2015*

Co-evolution of histones H2A and H2B for chromatin compaction. *Gordon Research Conference: Chromatin structure & function, Les Diablerets, CH, May 2016*

The nucleosome is a copper reductase. *Gordon Research Conference: Cell biology of metals, Mount Snow, VT, Jul 2017*

# Chapter 1

## Histones, chromatin, and copper cell biology

## 1.1 Summary

The defining feature of eukaryotes for which they are named is the cell nucleus, within which the nucleoprotein structures of the chromosomes are stored, read, replicated, and otherwise regulated. Genomes and chromosomes vary in size in different species but all are much larger, if stretched out, than the relatively tiny nuclei into which they must be packaged. The challenging task of packaging chromatin into nuclei has been a topic of study for many decades and a host of proteins and other factors that contribute to chromatin compaction have been identified and characterized. Arguably the most important of these are the small positively charged histone proteins, thousands to millions of copies of which bind throughout the genome in the fundamental repeating unit of chromatin, the nucleosome. This DNA-protein structure is the basis on which whole genomes are condensed and Chapters 2 and 3 of this dissertation reveal the role of a previously unappreciated region of the nucleosome participating in chromatin structure regulation. Beyond the level of the nucleosome, it is now recognized that large domains of chromatin compact in nuclei following a hierarchy of structural and architectural principles. Exciting advances have uncovered not only some of the factors that mediate the higher-order chromatin structures, but also that higher-order organization has regulatory roles other than mere packaging of chromosomes.

Eukaryotes have other defining features including an endomembrane system and endosymbiotic organelles like mitochondria and chloroplasts. Certain metabolic processes, cell signaling cascades, and the development of multicellularity are also unique. These characteristics required eukaryotes to not only evolve new molecular factors to enable these functions, but also repurpose some existing genes and networks already existing in our ancestors. One of the general motivating ideas behind the work presented in this dissertation is how some of this cellular physiology, like the various metabolic pathways, is integrated with the functioning of chromatin

and its associated nuclear processes. Chapters 4 and 5 in particular report on an unexpected connection between the nucleosome and the regulation of copper and iron homeostasis, which not only establishes new links in the eukaryotic cellular network, but could also be a connection that was important for the emergence of eukaryotes in the first place.

This introduction has two parts. Part I presents a general overview of the organization of eukaryotic chromatin, with an emphasis on the structure of the nucleosome and the role of the histones. The latter section of this part considers the idea that nucleosomes may have unrecognized cellular functions beyond control of chromatin packaging. Part II presents an overview of eukaryotic copper utilization and regulation mechanisms, from the metalloproteins to chaperones and transporters to the transcription factors, with an emphasis on the mechanisms of the budding yeast *Saccharomyces cerevisiae*. The goal of this introduction is to highlight some of the principles and features of these fundamental eukaryotic processes and to raise important questions that have been unanswered in the respective fields.

## PART I – HISTONES AT THE CORE OF CHROMATIN STRUCTURE

### 1.2 Chromatin structure on a global scale

The contents of the eukaryotic nucleus, although suspected to be biochemically distinct from the rest of the cell since the 18$^{th}$ century, have only relatively recently begun to be understood at a molecular level owing to the advancement of a number of technologies. The majority of nuclear content is chromatin, a term coined in the 1880's by Walther Flemming to describe the darkly-colored material from the nucleus of cells undergoing mitosis (Prakash, 2017). Chromatin is biochemically distinct than most other parts of the cell due in part to the massive scale of the nucleoprotein polymers (i.e. chromosomes) of which it is composed. The task of packaging such

large polymers is made more difficult by the necessity of cells to be able to replicate the genome once per cell cycle and to perform various other processes, like transcription, that require physical access to very specific regions of chromosomes. Decades of research have advanced our understanding of how cells accomplish these remarkable feats and several important principles have emerged. The three dimensional structure of genomes in nuclei can be highly variable and dynamic (Heun et al., 2001; Marshall et al., 1997), differing between different cell types or developmental states (Gaspar-Maia et al., 2011) or even between different cells within a population of the same cell type (Bickmore, 2013; Zimmer and Fabre, 2011). Despite this variability, chromatin compaction is not random and various constraining forces provide a degree of organization. The "organization" of genomes generally follows a hierarchy, not unlike the folding of proteins, where small lower-order structures fold in on themselves to form larger higher-order structures. Nucleosomes are at the base of such a hierarchy, which extends to the level of chromosome territories, a concept describing the spatial segregation of entire chromosomes within interphase nuclei.

### *1.2.1 Chromosome territories and topologically-associating domains*

The need for organization of chromosomes as they fold in the confines of the nucleus would be expected given the fact that certain sets of genomic sequences must have close spatial proximity with each other for the purpose of co-regulated function. The classic example of this is the protein-mediated physical contact between enhancer and promoter elements that occurs during gene transcription activation (Kagey et al., 2010; Weintraub et al., 2017). Beyond simply ensuring that coregulatory genomic elements are close in the linear DNA sequence, organisms have evolved mechanisms to organize the folding of chromatin in such a way as to facilitate spatial juxtaposition of such sequences (Dixon et al., 2016; Dixon et al., 2012; Symmons et al., 2014). Significant

strides in our understanding of chromatin compaction and organization at the largest of scales has been made possible by advances in two orthogonal technological approaches. Imaging techniques, from the electron microscope (Derenzini et al., 2014) to the latest developments of super-resolution fluorescence microscopy (Boettiger et al., 2016) have allowed increasingly detailed examination of the localizations of genomic elements and the path of the linear chromosome in three-dimensional space. Secondly, powerful molecular biology techniques, based on the chromosome conformation capture approach (Dekker et al., 2002; Dixon et al., 2012; Lieberman-Aiden et al., 2009), allow isolation from intact cells genomic regions that are in close physical proximity, indicating interaction. Applying this technique to all regions of the genome coupled with high-throughput sequencing to identify interacting pairs of genomic regions has allowed extensive mapping of interaction frequencies (Dixon et al., 2015; Dixon et al., 2012; Eser et al., 2017; Sexton et al., 2012).

This conformation capture approach has identified several defining patterns in chromatin organization. Chromosomes in animal interphase nuclei are in their least dense state, but individual chromosomes are not so extended and intercrossed with each other such that each of them occupies space throughout the entire nucleus. Instead, chromosomes segregate within sub-nuclear 3D volumes, which have been termed chromosome territories (Bickmore, 2013; Cremer and Cremer, 2010; Schardin et al., 1985). This is evident in the contact frequencies from chromosome capture experiments where regions of any given chromosome infrequently interact with regions of other chromosomes, reflecting the spatial separation (Lieberman-Aiden et al., 2009). This pattern strikingly repeats at the smaller intra-chromosomal scale as well. Large regions within chromosomes—on the scale of hundreds of kilo- to mega-base pairs—are more likely to interact with themselves than with other regions. These regions of enhanced internal interactions, termed

topologically-associating domains (TADs), are thought to be due to sections of chromosomes folding in on themselves in even smaller sub-nuclear volumes separate from similar adjacent regions (Dixon et al., 2016). This tendency for regions to preferentially self-associate continues to some extent at even smaller scales, with some evidence of sub-TADs present within the larger TADs (Rao et al., 2014).

Identification of these chromatin organizational patterns, as well as others, has raised the following lines of inquiry: 1) what are the underlying biochemical and biophysical forces and constraints, and what are the proteins, RNAs, or other molecules that produced the hierarchical organization of chromatin? And, 2) is chromatin structure, including both organization and compaction, in and of itself required for the proper functioning of DNA-based processes or others? Interestingly, the presence of a TAD-like organization is not universal across eukaryotes as the budding and fission yeast genomes do not appear to contain them. Their chromatin structure follows different organizational principles (Duan et al., 2010), some of it based on the tethering of centromeres in a cluster at the nuclear envelope (see below). It is important to note that yeast certainly contain nucleosomes and other fundamental chromatin structural proteins like condensins and cohesins, suggesting that the mere presence of these proteins is not sufficient to induce TAD-like organization. Of course, could the evolution of these fundamental chromatin proteins across eukaryotes (Macadangdang et al., 2014) (see Chapters 2 and 3) account for changes in chromatin organization? In addition to the evolution of histones, other structural proteins like CCCTC binding factor (CTCF) are unique to higher eukaryotes, which thereby helps to determine the differential large scale chromatin organization across the eukaryotic domain (Dixon et al., 2012; Ghirlando and Felsenfeld, 2016).

Alternatively, the budding yeast especially does not contain the complex genomic element interaction network (e.g. enhancer-promoter looping) characteristic of higher eukaryotes. Could it be that the TAD-like chromatin organization only coevolved with the complexity of gene regulatory networks? And if that is the case, is the TAD-like organization required to regulate enhancer-promoter interactions (Dekker and Mirny, 2016) or is it instead a consequence of the bending and clustering of genomic regions due to interactions between many transcription factors and their target genomic elements (Barbieri et al., 2012; Brackley et al., 2016)? Can promoter-enhancer interactions occur in the absence of TADs? Lastly, could the physical properties of the massive chromatin polymers, such as the degree of compaction which is less in yeast compared to higher eukaryotes (Macadangdang et al., 2014; Olmo, 1983) (see Chapters 2 and 3), be important determinants for TAD-like organization (Dekker and Mirny, 2016)? These questions remain intriguing and motivating in the field and while many are difficult to address, combining data gathered from microscopy and chromosome capture techniques with physical simulations and models has led to significant progress in our understanding.

### 1.3 Interactions of chromatin with the nuclear envelope

Unlike prokaryotes, the genomes of eukaryotes are enclosed in the double membrane system of the nuclear envelope which is an extension of the endoplasmic reticulum. The nuclear envelope is not simply a passive physical barrier limiting the extension of chromatin, although such a barrier could in theory control chromatin density as a smaller nucleus would necessarily decrease the available space any given genomic locus could diffuse in (Marshall et al., 1997; Zimmer and Fabre, 2011). Instead, the nuclear envelope also participates in organizing chromatin with varying mechanisms existing in different organisms. In the budding yeast, chromosome centromeres are physically tethered to the nuclear membrane in a single cluster at one end of the

nucleus, and this is accomplished by various proteins that bind to centromeric chromatin (Duan et al., 2010; Guacci et al., 1997; Jin et al., 2000; Zimmer and Fabre, 2011). Additionally, telomeres also attach to the nuclear envelope in clusters mediated by a complex of proteins involving the telomeric Ku complex (Grunstein and Gasser, 2013; Laroche et al., 1998; Zimmer and Fabre, 2011), telomeric repeat binding protein Rap1 (Hecht et al., 1995), a protein that spans the nuclear envelope and thereby potentially links chromatin structure to the cytoskeleton (Antoniacci et al., 2007), proteins involved in heterochromatin formation (Hediger et al., 2002; Palladino et al., 1993), and others. It is interesting that in these cases, particularly with telomeres in yeast, these regions are maintained in a transcriptionally repressed and condensed heterochromatin state (Grunstein and Gasser, 2013). This theme of anchoring transcriptionally inactive chromatin to the nuclear envelope is maintained in higher eukaryotes also, although utilizing different mechanisms. In human cells, the inner side of the nuclear envelope is coated by the intermediate filament network called the nuclear lamina (Hutchison, 2002), and in addition to providing structural integrity to the nucleus (Sullivan et al., 1999), also serves as an anchoring point for chromatin (Guelen et al., 2008; Towbin et al., 2012; van Steensel and Belmont, 2017). Lamina-associated chromatin in humans is enriched for transcriptionally-repressed heterochromatin, including centromeres and telomeres.

One of the main features of the nuclear envelope is the presence of nuclear pore complexes (NPCs), hundreds to thousands of which line the double nuclear membrane in all eukaryotes (Dultz and Ellenberg, 2010). They are the main mechanism for regulated transport of macromolecule complexes in and out of the nucleus, but interestingly, also have roles in interacting with the underlying chromatin structure in the budding yeast. Certain components of the NPCs physically interact with gene transcription machinery, including RNA polymerases. In contrast to the

heterochromatin-based nuclear envelope interactions, chromatin interactions with the NPC can occur when genes are actively transcribed and this interaction mediates the spatial relocalization of genes to the nuclear pores (Ishii et al., 2002; Light et al., 2010). Such an organizational mechanism might be optimal as the nascent mRNAs would emerge from the RNA polymerase II very close to the site of their export.

While the mechanisms are different, the fact that chromatin attaches to the nuclear envelope in various eukaryotes, and particularly in higher eukaryotes, that the lamina provides structural integrity to the nucleus, raises the interesting question about whether physical forces can be transmitted from the cytoplasmic cytoskeleton to chromatin and/or vice versa (Haase et al., 2016). Similarly, attachment of chromatin to the nuclear envelope suggests that structural changes in one might affect the other. This idea has not been well-studied and other than the recognized correlation between nuclear size and cell size (Edens et al., 2013; Neumann and Nurse, 2007), but not DNA content, it is not known whether the nuclear envelope can control chromatin compaction or vice versa. Work that our group recently published (Macadangdang et al., 2014) and that is reported in Chapters 2 and 3 of this dissertation provides some clues to such a connection.

## 1.4 Histone-based mechanism for regulating chromatin structure

### *1.4.1 From TADs to nucleosomes*

The technological advances in both microscopy and chromosome capture have greatly enhanced our understanding of chromatin structure on the scale tens of thousands to millions of base pairs-worth of chromatin. However, these techniques are not yet powerful enough to probe structure at the scale of nucleosomes and multi-nucleosome chromatin fibers and other structures. At this lowest scale, other technologies are much better suited and include approaches based on chromatin immunoprecipitation (ChIP), micrococcal nuclease digestion (MNase), and

transposase-mediated integration (ATAC), among others, all of which are coupled to high-throughput sequencing (Buenrostro et al., 2013; Schones et al., 2008; Wal and Pugh, 2012). These complementary approaches have produced highly-detailed maps of the positions of all nucleosomes, many histone modifications, and many other DNA-binding proteins in various organisms and cell types. These maps, however, are all based on the linear genome sequence and therefore do not contain spatial information. Thus, one of difficulties in the field has been in bridging the gap between the large and small scales of chromatin structure (Risca and Greenleaf, 2015). How does the vast array of nucleosomes and network of nucleosome interactions contribute to forming the large scale domains of chromosomes? Are the TADs emergent properties of the way nucleosomes are arranged or is chromatin structure at different hierarchical levels organized independently? Given the central position of the histones as the basis of chromatin structure, it would be expected that properties of the histones themselves would play at least partial, and possibly significant, roles in shaping the large scale organization. Furthermore, the dynamic nature of histones within organisms and across eukaryotes would be expected to contribute to different chromatin organizational patterns in different contexts. These and related questions will surely drive the field in years to come.

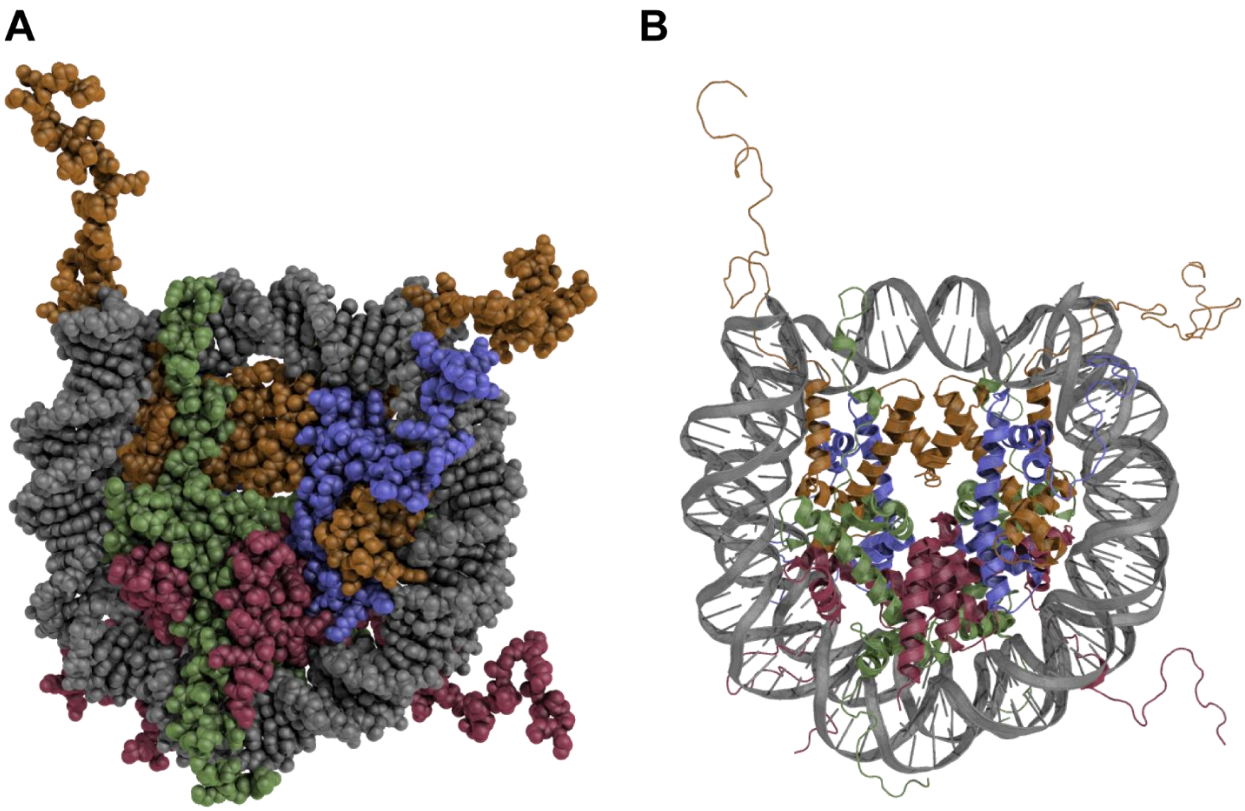


**Figure 1-1: The nucleosome. (A and B)** Space-filling and ribbon representations, respectively, of the nucleosome of *Xenopus laevis* as viewed down the DNA superhelical axis. The histones and DNA are color-coded based on the molecules. The two histone H3s are in brown, H4s in blue, H2As in green, H2Bs in red, and the 146 bp of DNA is in grey. Representations generated using the 1KX5 structure (Davey et al., 2002).

### *1.4.2 The canonical nucleosome*

The fundamental layer of chromatin structure is based on histone proteins, which in nearly all eukaryotes, form the nucleosome. The canonical structure of the nucleosome has been known for a few decades (Richmond et al., 1984) and consists of an octamer of histone proteins, two copies each of histones H2A, H2B, H3, and H4. This octamer is wrapped by 146 bp of DNA in a left handed superhelix of 1.67 turns (Davey et al., 2002; Luger et al., 1997; Tachiwana et al., 2010; White et al., 2001) (Figure 1-1). Comparison of nucleosome structures from different organisms, and even of nucleosomes containing histone variants, reveals a highly conserved structural

organization of the nucleosome despite the sequence differences between species. Even the four core histones, although significantly divergent at the protein sequence level, are all based on the same structural motif, the histone fold (Figure 1-2). The histone folds mediate the formation of the highly stable obligate heterodimers of histones H3 with H4, and H2A with H2B (Arents and Moudrianakis, 1995).

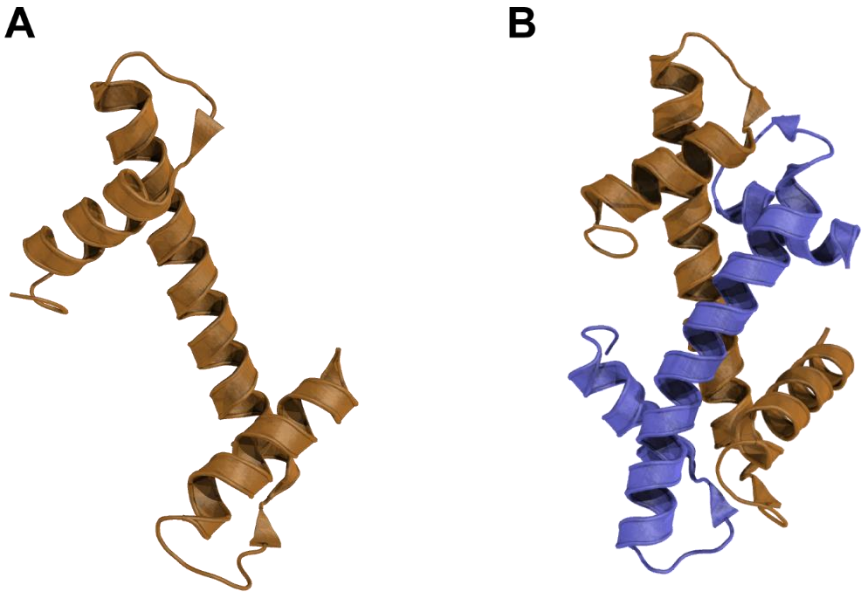


**Figure 1-2: The histone fold domain. (A)** The three alpha helices of the histone fold at the C-terminus of histone H3. The histone fold structural motif is common to all four histones and together form the core of the nucleosome. **(B)** Two histone fold domains from two different histones (H3 and H4 pictured here) mediate dimerization via "handshake motif" (Arents and Moudrianakis, 1995). Color-coding is the same as in Figure 1-1. Representations generated using the 1KX5 structure (Davey et al., 2002).

The nucleosome can be divided into a series of substructures, which exist at least transiently in cells (Burgess and Zhang, 2013; Vlijm et al., 2015). The H3-H4 dimer (Figure 1-3A) subsequently forms a dimer of dimers to make the H3-H4 tetramer (Figure 1-3B). Dimerization occurs between the two H3 proteins. Histone H4 does not mediate the dimerization although it does mediate a similar structural interaction with histone H2B to form the full octamer. The H3-H4 tetramer can bind DNA on its own, forming what is known as the tetrasome (Sauer et

al., 2017), but which only wraps 60 bp of DNA. In the full nucleosome structure, the dimerization of H3-H4 dimers also occurs at the midpoint of the path of DNA as it wraps around the histone octamer. This central point is termed the nucleosome dyad as a reference (Luger et al., 1997). The H2A-H2B dimer, however, does not form a tetramer. To complete the octamer within the nucleosome, two histone H2A-H2B dimers interact on either of the flat faces of the nucleosome (Figure 1-3C and 1-3D).

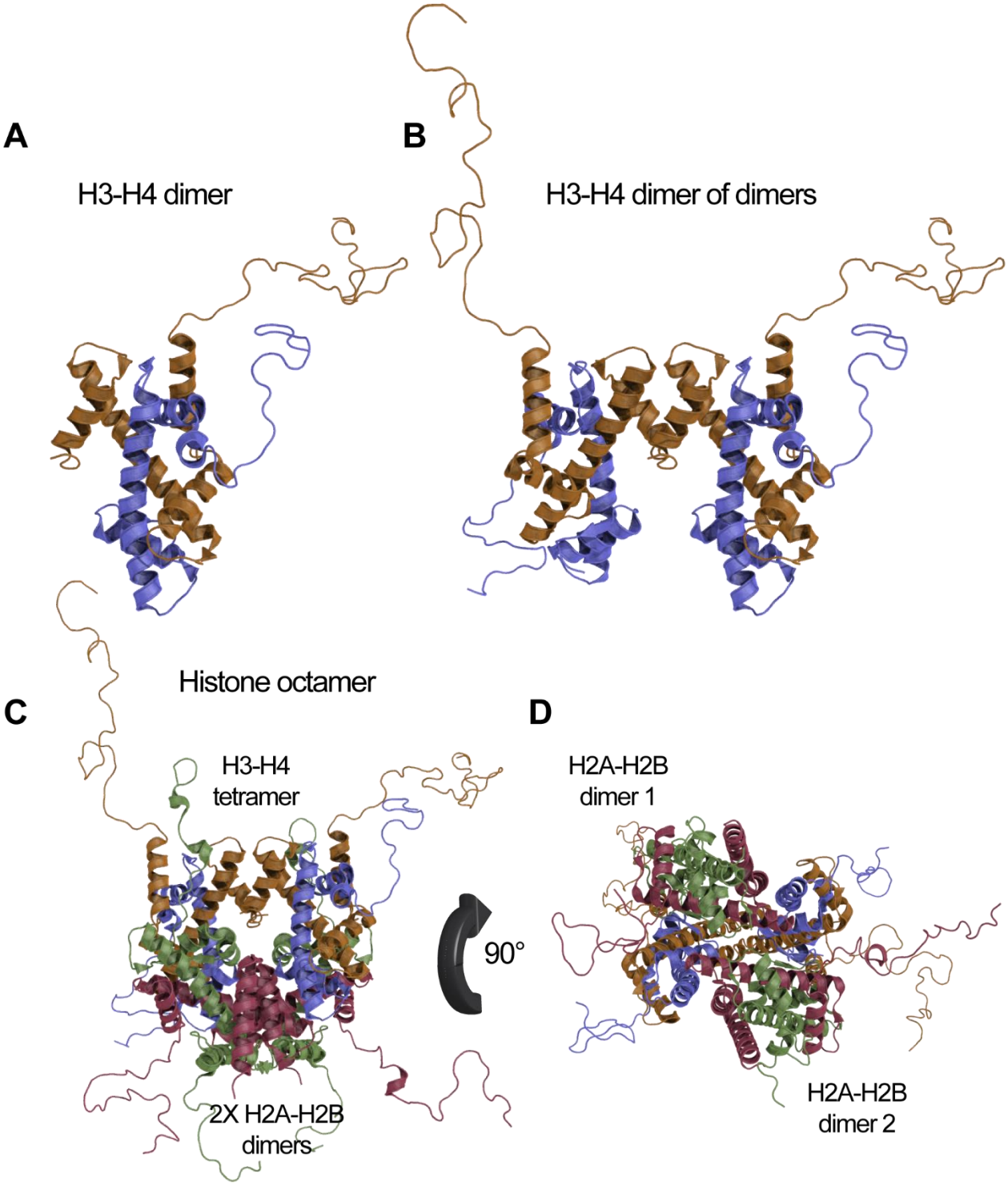
A
H3-H4 dimer
B
H3-H4 dimer of dimers
Histone octamer
C
H3-H4
tetramer
90°
2X H2A-H2B
dimers
D
H2A-H2B
dimer 1
H2A-H2B
dimer 2

**Figure 1-3: Substructures of the nucleosome. (A)** The H3-H4 heterodimer, which does not stably exist in cells. **(B)** The H3-H4 tetramer formed by dimerization between the H3 proteins. **(C)** The histone octamer is completed by the addition of two H2A-H2B dimers on the side of the tetramer away from the H3-H3' dimerization region. **(D)** The octamer from (C) rotated 90° into the plane of the page. This view more easily reveals the positioning of the two H2A-H2B dimers, which do not form a dimerization interface like the H3-H4 dimers. Color-coding is the same as in Figure 1-1. Representations generated using the 1KX5 structure (Davey et al., 2002).

The superhelical wrapping of DNA around the histone octamer is stabilized by a series of interactions between positively-charged lysines and arginines with the DNA phosphates. Notably, as the DNA makes its fourteen helical turns around the nucleosome, fourteen highly conserved arginines insert into the minor groove of DNA, thereby facilitating its positioning and bending (Cutter and Hayes, 2015; Wang et al., 2010).

### *1.4.3 Variability of nucleosome structure*

An important principle to note about the structure of the nucleosome is its relative flexibility and dynamic nature as it can acquire a variety of conformations that are somewhat different than those solved by X-ray crystallography (Choy and Lee, 2012). There are many examples of dynamic behavior. For example, nucleosomal DNA can transiently unwrap and rebind around the octamer core, particularly at the DNA entry/exit sites of the nucleosome. This mobility, sometimes termed DNA breathing (Culkin et al., 2017; Eslami-Mossallam et al., 2016; Li et al., 2005), occurs at timescales and probabilities that are physiologically relevant (Cutter and Hayes, 2015; Ngo et al., 2015) and is a determinant of the ability of other DNA binding proteins to access the DNA normally occluded by the nucleosome (Anderson and Widom, 2000).

Second, nucleosomes are not identical across the genome due not only to the large number of post-translational modifications but also to the presence of histone variant isoforms. Variant histones H3 and H2A exist in most eukaryotes and their expression and incorporation in nucleosomes in the place of the canonical histones are often restricted to certain genomic regions

and sometimes in specific cell types in multi-cellular eukaryotes (Buschbeck and Hake, 2017). One of the most highly conserved histone variants is the centromeric histone H3 variant, CenH3, which forms specially structured nucleosomes at the centromeres of all eukaryotes and facilitates kinetochore assembly (Meluh et al., 1998; Mendiburo et al., 2011). The second highly conserved histone variant is the H2A variant H2A.Z. Nucleosomes containing H2A.Z instead of H2A also alter their structural properties (Jin et al., 2009; Rudnizky et al., 2016), often destabilizing them. H2A.Z tends to be incorporated in nucleosomes at gene promoters (Zhang et al., 2005) and plays roles in regulating transcription (Draker et al., 2012; Jin et al., 2009).

Lastly, the canonical nucleosome itself is subject to dynamic assembly and disassembly. This is most obvious during transcription and DNA replication where the elongating polymerase complexes can disrupt or even displace nucleosomes (Belotserkovskaya et al., 2003). Several polymerase-associating histone chaperones (Huang et al., 2015; Yang et al., 2016) subsequently facilitate the reassembly of nucleosomes in the wake of the polymerases. This remarkable process would be expected to have effects on larger-scale chromatin structure, since such disruption of nucleosome structure would perturb inter-nucleosomal interactions. It would also alter the torsional stress of the DNA thereby affecting neighboring nucleosomes indirectly (Gupta et al., 2009; Yang et al., 2014). Even in the absence of a traversing polymerase, the H2A-H2B dimers dissociate and reassociate with nucleosomes forming transient tetrasomes (Kimura and Cook, 2001; Park et al., 2005), or possibly hexasomes. The consequence of such dynamic association likely impacts the ability of transcription factors and other proteins to recognize and bind their target DNA sequences. Although evidence suggests this dynamic behavior happens quite often (Kimura and Cook, 2001), it is unclear whether H2A-H2B assembly/disassembly occurs equally

at all nucleosomes in a genome. Where it does occur frequently, however, it also would be expected to disrupt higher-order chromatin structure.

### *1.4.4 Chromatin fibers*

Nucleosomes across a genome are separated by lengths of "naked" DNA termed linker DNA. In mammals, the average linker DNA length can be as high as ~45 bp whereas in yeast, linker lengths are on average only ~20 bp (Perisic et al., 2010) which conversely means that nucleosomes are packed more densely in yeast chromatin compared to mammals. This interesting inter-species difference not only affects the ability of DNA-binding proteins to access and bind their target sequences, since a higher nucleosome density decreases the probability that any given sequence is found in the linker DNA; but it also affects the ability of nearby nucleosomes to interact with each other and form higher order structures along an array of nucleosomes. One of the main reasons for this is the inherent stiffness of naked DNA (Grigoryev, 2012; Perisic et al., 2010). Shorter linker DNA restricts the bending angles between adjacent nucleosomes, in turn restricting the types and geometries of interactions among groups of neighboring nucleosomes (Perisic et al., 2010; Stehr et al., 2008). The types of structures that nucleosome arrays can form are called chromatin fibers, the archetypal one being the 30 nm fiber which can be formed from *in vitro*-assembled nucleosomal arrays (Huynh et al., 2005). Computational simulations have further revealed the structural properties of chromatin fibers, and notably, they predict different types of chromatin fibers formed when certain nucleosome parameters are altered, such as the linker length (Grigoryev, 2012; Perisic et al., 2010).

In addition to the core histones, an additional highly basic DNA binding protein associated with nearly all nucleosomes, at least in human chromatin, is the histone H1 protein (Hergeth and Schneider, 2015). Also called the linker histone, this protein binds to the linker DNA immediately

adjacent to the core nucleosome particle (Song et al., 2014). The linker histone strongly induces formation of chromatin fibers *in vitro*, possibly by favoring distortion of the linker DNA itself (Song et al., 2014), and thus its presence at nearly all nucleosomes in nuclei suggests that chromatin is organized into fibers throughout the length of chromosomes (Cutter and Hayes, 2015). However, current evidence does not suggest such widespread formation of fibers *in vivo*, although they may be more likely to form in some genomic regions more than others (Eltsov et al., 2008; Risca et al., 2017). The reason chromatin fiber structures are not prevalent *in vivo* may simply have to do with the dynamic nature of nucleosomes as described above. Chromatin fibers formed *in vitro*, and simulated *in silico*, depend entirely on arrays of precisely positioned and invariant nucleosomes (Collepardo-Guevara and Schlick, 2014). While some regions of genomes may contain such arrays, such as the highly repetitive heterochromatin regions, this is not likely to be the case in other regions where DNA-based processes often occur.

### *1.4.5 Histone N-terminal domains*

The four core histones also have extended and unstructured N-terminal tails and histone H2A also has an extended C-terminal tail (Figures 1-1 and 1-3). The importance of these extended tails in a variety of nuclear functions cannot be understated and determining their contributions to chromatin biology has been a defining focus of the field. Much of the research of the histone tails concerns their high degree of post-translational modification (PTM) (Bowman and Poirier, 2015; Lawrence et al., 2016; Nadal et al., 2018). Most histone PTMs have uncharacterized functions, but many are now well-known to play significant roles in the regulation of gene expression and chromatin structure. Of these, the lysines of histone H3 and H4 in particular are special for their ability to be reversibly and dynamically acetylated, methylated, and more (Lawrence et al., 2016). In general, histone lysine acetylation is associated with disruption of compact nucleosome and

chromatin structure (Lee et al., 1993; Tse et al., 1998; Xu et al., 2005) and acetylated nucleosomes tend to occur in genomic regions with transcriptional activity (Birney et al., 2007). The mechanism by which acetylation assists in activating transcription can be as simple as by neutralizing the positive charge of lysines and thereby disrupting the interactions with DNA and destabilizing chromatin structure (Bowman and Poirier, 2015). Alternatively, acetylation of specific H3 and H4 lysines, alone or in combination with other histone PTMs, can serve as platforms for the recruitment of other histone binding proteins to specific genomic loci (Dhalluin et al., 1999; Ruthenburg et al., 2007). In turn, these lysine acetylation "readers" can participate in the assembly and activation of the RNA polymerase complex (Li and Shogren-Knaak, 2009) or in recruiting chromatin remodeling enzymes to displace nucleosomes to facilitate binding of the transcriptional machinery (Hassan et al., 2002; Kasten et al., 2004). It is unclear the extent to which each of these types of mechanisms accounts for the effect of lysine acetylation on transcriptional activation.

Histone lysine methylation may have similar roles, although this PTM does not negate the positive charge of lysines and is therefore not likely to disrupt chromatin structure in the same manner. Notably, the various lysine methylation modifications in nucleosomes segregate to different regions of the genome and participate in forming different structural states of chromatin (Allshire and Madhani, 2017; Campos and Reinberg, 2009; Ruthenburg et al., 2007). For example, histone H3 lysine 9 trimethylation is prevalent in nucleosomes of the constitutive heterochromatin regions of genomes (Allshire and Madhani, 2017; Lachner et al., 2001). This modification mediates the local compaction of chromatin, which restricts the accessibility of DNA binding proteins and represses transcriptional activity (Lachner et al., 2001; Maison et al., 2002). Histone H3 lysine 27 trimethylation on the other hand tends to occur on nucleosomes in facultative heterochromatin, which also represses transcriptional activity (Bernstein et al., 2006; Campos and

Reinberg, 2009; Cao et al., 2002) but is structurally distinct (Boettiger et al., 2016) and localized to different genomic regions than the constitutive heterochromatin.

## 1.5 Do histones have functions in addition to regulation of DNA-based processes?

Histones are strong DNA-binding proteins, and their ability to bind DNA without strong sequence specificity makes them ideal for genome compaction. This strong DNA-binding capability has also been exploited as a means to regulate the binding of other proteins to DNA. The ability of nucleosomes to compete with other proteins, such as transcription factors, is a crucial component of the regulation of DNA-based processes (Bowman and Poirier, 2015). In turn, the regulation of the structural stability of nucleosomes or their DNA binding affinity is the mechanistic basis for this type of function. Alternatively, nucleosomes can also act as signaling modules, primarily via allosteric interactions between post-translationally modified residues and effector proteins (Ruthenburg et al., 2007). The aggregation of the various histone PTMs is thought to be decoded by other protein complexes to activate or inhibit transcription, replication or other processes. Regulation of this type of function has less to do with the nucleosome structure itself and is based on the enzymes that deposit the PTMs and the proteins that specifically recognize them. Together, these mechanisms give cells many options by which to control DNA-based processes and chromatin structure. But might histones and nucleosomes, have molecular and cellular functions beyond the canonical regulation of such processes?

### *1.5.1 Histone acetylation participates in regulation of intracellular pH*

Previous work in our lab considered the possibility that the global levels of histone acetylation were regulated in response to various cellular perturbations often experienced by cancer cells in tumors. These perturbations include restriction of certain nutrients, changes in osmolality, decreased oxygen, and increased acidity (Pavlova and Thompson, 2016). Intriguingly,

it was observed that decreases in pH resulted in significant decreases of the levels of several histone acetylation PTMs across the genome and not in a gene-specific manner (McBrian et al., 2013). Further investigation revealed that active deacetylation was induced in response to the acidity, which increases the generation of acetate ions, one of the products of deacetylation reactions (Seto and Yoshida, 2014). Consequently, acetate ions are cotransported with protons out of the cytoplasm, thereby decreasing the proton load and participating in maintaining intracellular pH. The global state of histone acetylation, and the histone acetyltransferase and deacetylase enzymes that control its levels, therefore assist in buffering intracellular pH independently of the canonical functions of histones in gene regulation (McBrian et al., 2013).

### *1.5.2 Unexplained conservation of histone sequences*

These findings highlight the importance of considering basic biochemical properties of the cellular milieu and the interactions that histones may have with its components, such as metabolites, salts, metal ions, pH, temperature, and macromolecular crowding. Like the ability to regulate pH, could the histones have other biochemical functions in addition to DNA binding and structural stabilization of the nucleosome? Using a computational modeling approach, Ramachandran and colleagues (Ramachandran et al., 2011) calculated the energetic consequences of mutation of each residue of histones H3 and H4 that are buried in the nucleosome core structure. As expected, many of those simulated mutations resulted in substantial changes in stability, indicative of their importance for nucleosome structure (Ramachandran et al., 2011). Many of these same residues are also highly conserved across eukaryotes and the degree of conservation of individual residues correlated significantly with their computed contribution to stability. However, several of the buried residues of histone H3 are more highly conserved than expected given their contribution to the thermodynamic stability of the nucleosome. Those residues, including H3Q93,

H3L100, and H3A114, are not known to be post-translationally modified. Thus, their conservation for reasons other than maintaining nucleosome stability suggests that they contribute to an important and alternative biochemical function of the histones and nucleosome in eukaryotes.

### *1.5.3 Coordination of transition metals by histones*

A few separate observations raise an unexpected possibility for an uncharacterized function of histones. Since the original determination of the nucleosome structure, it was noted that the region where the two histone H3 proteins dimerize contains a cluster of residues, including H3C110 and H3H113, that are often involved in coordination of biologically-relevant transition metals, such as zinc and copper (Saavedra, 1986) (Figure 1-4). Could it be that the nucleosome interacts with one or more of these metals in cells, and if so, would such binding have functional relevance in regulating nucleosome structure? Conversely, could the nucleosome participate in regulating metal homeostasis in a similar manner as its ability to regulate pH? Indeed, *in vitro*-assembled nucleosomes have been observed to interact with zinc and cobalt ions. Furthermore, examination of the histone-metal interactions with various spectroscopic techniques implicated the dimerization region of histone H3 as the site of metal coordination (Adamczyk et al., 2007). Whether such interactions occur *in vivo* with the same or other "preferred" metals, and whether histone-metal interactions are functionally relevant was not examined in this study (Adamczyk et al., 2007). The work presented in Chapters 4 and 5 of this dissertation explore such a function for the nucleosome.

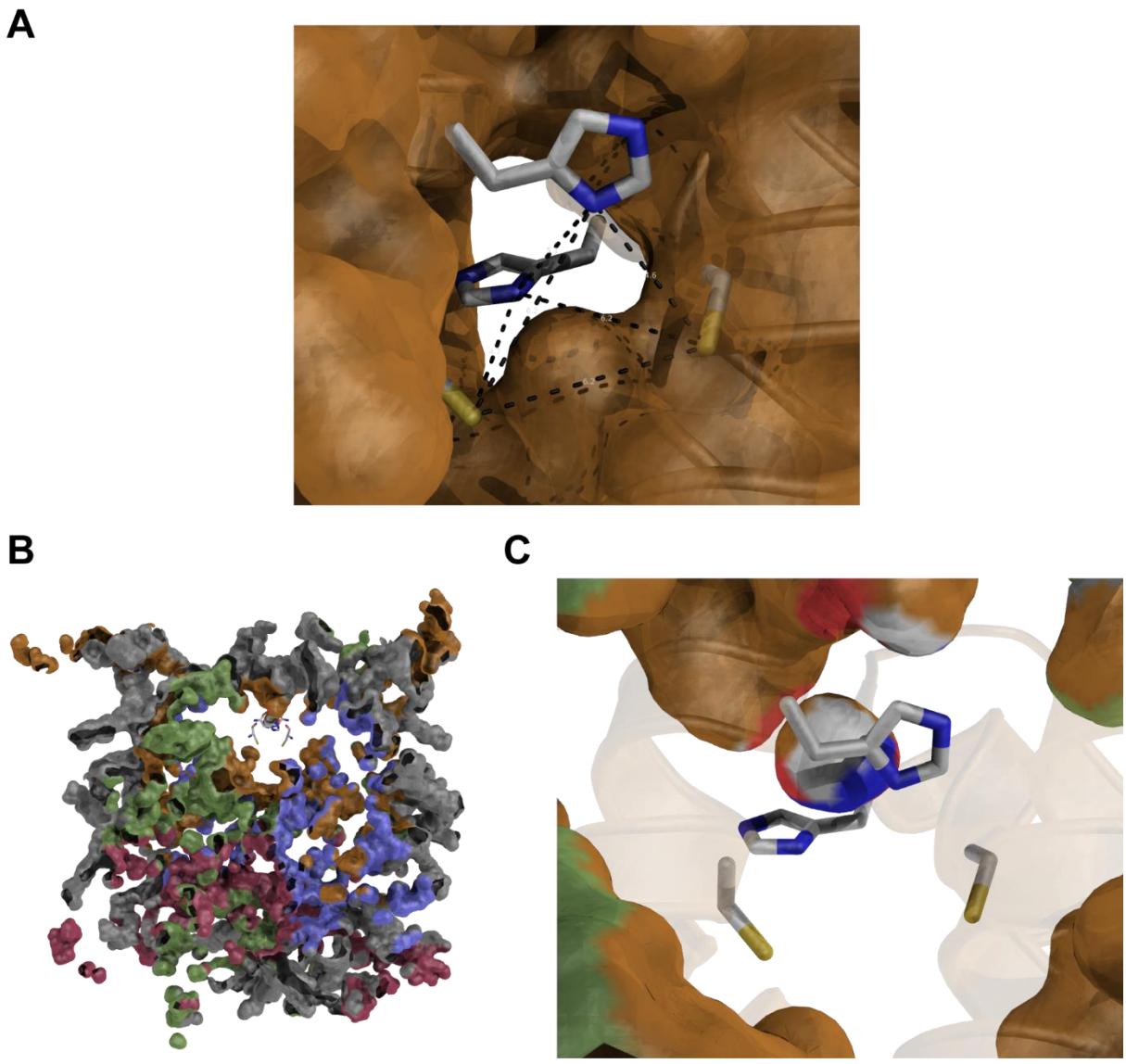


**Figure 1-4: A potential metal-binding site at dimerization interface of the two H3 molecules in the nucleosome. (A)** Stick representations of histone H3 residues histidine 113 and cysteine 110 buried in the core of the nucleosome. Other residues are shown as surface representation. The dotted lines represent a network of potentially interacting atoms that may coordinate a metal ion. This should not be confused with a predicted metal-coordinating geometry. **(B and C)** Same representation as in (A) but instead, the buried cavities of the nucleosome were rendered using PyMol. Even regions that are buried have some space to potentially accommodate other molecules or ions. A close-up view of the potential metal-binding site **(C)** reveals a small cavity that could spatially accommodate a metal ion. Representation generated using the 1KX5 structure (Davey et al., 2002).

PART II – REGULATING COPPER DISTRIBUTION AND REDOX STATUS

## 1.6 Copper utilization

### *1.6.1 The cuproproteins*

The amino acids provide a great range of properties for proteins but their abilities are far from limitless. Many enzymes use additional organic and inorganic cofactors to extend their biochemical capabilities and catalyze a greater range of chemical reactions, which has been absolutely essential for life in many instances. The smallest cofactors are the metal ions and many of them are used for a wide range of functions, from magnesium ions in DNA polymerases, to cobalt as the metal component of vitamin $B_{12}$. Transition metals of the d-Block of the periodic table have also been exploited by all organisms for their unique chemical properties. Arguably, the most important of these have been iron and copper because of their ability to exist in different oxidation states in biologically relevant conditions. This property has been used by proteins to mediate the majority of electron transfer processes that ultimately drive all metabolism. Iron is typically utilized in cells as either $Fe^{2+}$ (ferrous) or $Fe^{3+}$ (ferric) ions and is widely used to catalyze many reactions making it essential for all organisms. Copper similarly exists as either $Cu^{+}$ (cuprous) or $Cu^{2+}$ (cupric) ions, and while it is essential for many organisms, it appears to be utilized in fewer cellular processes compared to iron. In the budding yeast, copper ions are only known to be utilized as functional cofactors by five enzymes in three separate but interconnected biological processes. These are 1) subunits I and II of cytochrome *c* oxidase (C*c*O) of the mitochondrial electron transport chain, encoded by the COX1 and COX2 genes, respectively; 2) cytosolic copper-zinc superoxide dismutase (SOD), encoded by the SOD1 gene; and 3) two multicopper ferroxidases associated with the plasma and vacuolar membranes, encoded by the

FET3 and FET5 genes, respectively. These enzymes are found across the eukaryotic domain, in one form or another.

Cytochrome *c* oxidase, complex IV of the electron transport chain of the inner mitochondrial membrane, utilizes three copper ions in two cofactor groups to transfer electrons to molecular oxygen (Horn and Barrientos, 2008). The two copper sites occupy cytochrome *c* oxidase subunits Cox1 and Cox2 and mediate the four electron transfer to oxygen (Lucas et al., 2011). Depletion of copper ions from cytochrome *c* oxidase prevents proper electron transfer and consequently decreases the flux through the rest of the electron transport chain, decreases oxygen consumption, the proton gradient, and ATP production by the mitochondria. Interestingly, yeast cells can survive the loss of electron transport despite the disruption of the mitochondrial membrane potential—due to a smaller proton gradient—and abolishment of mitochondrial ATP production, as long as they can make full use of glycolysis (Dunn et al., 2006).

The yeast copper-zinc superoxide dismutase (Sod1) is distributed throughout the cytoplasm, nucleus, and the inter-membrane space of the mitochondria (Sturtz et al., 2001). Sod1, which dimerizes in its active form, binds a single copper ion which mediates the transfer of two electrons from two superoxide radicals in a disproportionation reaction to produce molecular oxygen and hydrogen peroxide (Tainer et al., 1983). Coupled with catalase or other peroxidases to subsequently detoxify $H_2O_2$, Sod1 plays a critical role in protecting biomolecules from the potential damage from reactive oxygen species. Interestingly, certain biological processes are particularly susceptible to superoxide-mediated damage (Liu et al., 1992; Schleit et al., 2013; Slekar et al., 1996) and loss of function of Sod1 results in several specific defects that reflect this underlying vulnerability. One example is the lysine biosynthetic pathway in yeast, where loss of Sod1 function renders cells auxotrophic for lysine (Klomp et al., 1997; Liu et al., 1992). Although

not confirmed, the likely reason for a defect in lysine production is that the homoaconitase enzyme of the lysine biosynthetic pathway is especially susceptible to superoxide damage since it depends on an iron-sulfur cluster cofactor for its catalytic mechanism (Wallace et al., 2004). Iron-sulfur clusters that are solvent exposed in certain proteins are known to be particularly sensitive to reactive oxygen species damage (Fridovich, 1995). Sod1 also has unexpected roles in various cell processes. These include stabilizing the yeast casein kinase Yck1 which in turn regulates glucose repression of the metabolism of other carbon sources (Reddi and Culotta, 2013). Sod1 is also involved in the activation of the Mac1 transcription factor (Wood and Thiele, 2009), which as will be described in more detail below, is the main copper regulatory transcription factor that activates genes in response to cellular copper depletion (Jungmann et al., 1993). Lastly, not only does Sod1 indirectly protect DNA from oxidative damage (Keyer et al., 1995) but its activity is involved in activating the signaling mechanisms in response to DNA damage (Dong et al., 2013).

The two multicopper oxidase enzymes in yeast function as ferrous iron oxidases and are both coupled to iron transport across cell membranes (Askwith et al., 1994; Desilva et al., 1995; Spizzo et al., 1997). Fet3 and Fet5 are both part of large family of multicopper oxidases. They utilize four copper ions in two copper sites to transfer four electrons from four $Fe^{2+}$ ions to oxygen (Taylor et al., 2005). This reaction produces four oxidized $Fe^{3+}$ ions, and as with cytochrome *c* oxidase, one water molecule. Fet3 and Fet5 are membrane-associated and occur in complexes with a ferric ion permease, Ftr1 and Fth1, on the plasma membrane (Stearman et al., 1996) and vacuolar membrane (Urbanowski and Piper, 1999), respectively. These ferroxidase-permease complexes function to transport iron ions into the cytoplasm and are transcriptionally induced in low-iron conditions (Rutherford et al., 2003; Yamaguchi-Iwai et al., 1995). Interestingly, the complexing is required for iron import as the permeases cannot utilize free $Fe^{3+}$ ions as substrates and must

receive $Fe^{3+}$ from the associated ferroxidase (Wang et al., 2003). The Fet3-Ftr1 complex is not the only iron import mechanism in yeast and loss of copper loading of Fet3, resulting in loss of its function, does not impact growth in rich media conditions often used in the laboratory. However, the Fet3-Ftr1 system is part of the high-affinity and high-specificity iron transport system and is essential for iron uptake and growth in low iron conditions. The fact that copper ions are utilized for iron oxidation and its eventual transport necessarily links the homeostasis of both elements (Chang and Fink, 1994; Taylor et al., 2005). Indeed, loss of Fet3 function due to disruption of copper utilization secondarily affects iron homeostasis and the functioning of iron-dependent processes (De Freitas et al., 2004), including probably mitochondrial respiration.

Two notable aspects are common between the three copper-dependent cellular processes in yeast. First, all three depend on the redox capability of copper ions. The cycling changes in copper ion oxidation and charge during the catalytic reactions likely necessitates that the copper-coordinating sites of each of the proteins has the unique feature of maintaining high affinity for copper ions despite the transient changes. Second, all three of these processes are dependent on, or are only biologically relevant in, the presence of oxygen. The electron transfer reactions of cytochrome *c* oxidase and the ferroxidases utilize oxygen as an electron acceptor, whereas Sod1 detoxifies superoxide radicals. Thus, when yeast cells are grown in hypoxia, their cell biology might be independent of copper utilization. This possibility has not been carefully examined but remains an interesting question that could lead to discovery of new copper-dependent processes.

The three copper-dependent processes described above are operational in all eukaryotes, although some of the specific mechanisms have diverged. In humans for example, cytochrome *c* oxidase and copper-zinc superoxide dismutase function in essentially the same way, but an additional extracellular copper-zinc superoxide dismutase is present (Serra et al., 2003; Zelko et

al., 2002). Homologous multicopper ferroxidases Hephaestin and Ceruloplasmin function in iron mobilization in humans. Like Fet3, Hephaestin is membrane-associated (Vulpe et al., 1999) while Ceruloplasmin is not, instead being secreted into the blood stream (Hellman and Gitlin, 2002). Both oxidize ferrous ions that are subsequently bound by the transferrin ferric ion binding protein in the bloodstream (Dlouhy and Outten, 2013; Gkouvatsos et al., 2012). Although most of the iron in the blood is bound to hemoglobin, the source of usable iron for other cells of the body is in the form of iron bound to transferrin.

### *1.6.2 Other copper-dependent cellular processes*

In addition to the three copper-dependent cellular processes and associated enzymes described above, additional proteins have uniquely evolved in animals that also bind and utilize copper ions. One of these is the enzyme dopamine β-hydroxylase which catalyzes the conversion of dopamine to norepinephrine in neurons. This enzyme is a member of a small family of copper-binding hydroxylases and utilizes copper for electron transfer (Vendelboe et al., 2016). Recently, copper ions have also been observed to interact with, and be necessary for the activation of, the MEK1/2 protein kinases involved in the Ras signaling cascade (Brady et al., 2014; Turski et al., 2012). Unlike most of the other known copper-dependent processes in eukaryotes, the function of copper in modulating this signaling pathway appears to depend only on binding to the kinases as an allosteric activator. Signaling mediated by MEK1/2 is therefore unexpectedly linked to copper homeostasis. An analogous copper-dependent kinase has not been identified in other organisms, such as in the budding yeast, but such a possibility is intriguing and unique as it does not depend on the redox capabilities of copper.

## 1.7 Copper import and trafficking

### *1.7.1 Transmembrane transport of copper*

While each of the copper-dependent processes described above are not strictly essential in yeast grown in rich laboratory media, their importance is readily apparent in several biologically relevant situations, such as in the presence of oxidants or when iron is depleted. Therefore, precise regulation of copper abundance and provision to the copper-utilizing enzymes of these processes is crucial in such instances. In addition, copper ions can be toxic further requiring organisms to properly handle and distribute them to appropriate cellular locations.

In typical laboratory rich media conditions, where the demand for copper is low and copper concentrations of about 1 μM are more than sufficient, copper ions in the environment typically enter the cell via the low-affinity and low-specificity metal permease Fet4 on the plasma membrane (Hassett et al., 2000; Portnoy et al., 2001). Originally thought to only be an iron transporter, Fet4 also transports copper and zinc ions. Copper transport mechanisms change however, when the need for copper utilization increases, such as when cells rely on mitochondrial respiration for ATP production, or when the copper concentrations in the environment significantly decrease. To enhance copper uptake under such conditions, yeast express the high-affinity and high-specificity copper transporter Ctr1 (Dancis et al., 1994a; Dancis et al., 1994b; Nevitt et al., 2012). This transporter forms homotypic complexes on the plasma membrane and forms a transmembrane channel lined with methionine residues that readily and selectively bind to $Cu^{+}$ ions (Puig et al., 2002). A second, high affinity $Cu^{+}$ transporter exists in the yeast genome, which is encoded by the CTR3 gene and has the same function as Ctr1 (Pena et al., 2000). Interestingly, Ctr3 is effectively lost in the commonly used S288C laboratory yeast strain due to its gene promoter being interrupted by a Ty2 transposon (Knight et al., 1996). In addition to greater binding affinity for copper

compared to Fet4, it is possible that Ctr1 enhances the effectiveness of copper utilization by coupling the transmembrane transport of copper ions to the copper trafficking systems (Levy et al., 2016; Pope et al., 2013; Xiao and Wedd, 2002), instead of simply providing copper ions to a general cytoplasmic pool.

Passage of copper ions across organelle membranes also requires transporters. Notably, the movement of copper ions into the endomembrane system and secretory pathway is accomplished by members of a large family of active pumps, the P-type ATPases (Inesi et al., 2014). In yeast, copper transport into the secretory pathway is mediated by Ccc2 which localizes mostly to late and post-Golgi compartments (Fu et al., 1995). Although the endomembrane system connects the endoplasmic reticulum, Golgi body, vacuole, and extracellular environment via vesicle transport, there is no evidence yet that copper transported into this system by Ccc2 diffuses to all of these compartments. Instead, Ccc2-mediated transport is tightly linked to the loading of copper ions into the Fet3 and Fet5 ferroxidases (Yuan et al., 1997; Yuan et al., 1995). Indeed, loss of Ccc2 function results in the same disruption of iron uptake as Fet3 loss of function (Lin et al., 1997). Mammals also express homologous copper-transporting P-type ATPases, ATP7A and ATP7B, and these similarly export copper out of the cytoplasm and into the secretory pathway or to the extracellular environment (Linz and Lutsenko, 2007).

Despite the fact that Ccc2 does not mediate the entry of copper into the yeast vacuole, nor is there an established mechanism for doing so, it is clear that the vacuole contains a regulated pool of copper ions (Szczypka et al., 1997). This is made evident by the presence of a copper-specific transporter, encoded by the CTR2 gene, localized on the vacuolar membrane which transports copper into the cytoplasm (Rees et al., 2004). The Ctr2 transporter, however, is not

transcriptionally induced when the cells experience copper deficiency as a mechanism to mobilize copper to the copper dependent processes (Portnoy et al., 2001).

It is important to note that the copper transporters Ctr1 and Ctr3 bind to cuprous ions specifically (Lee et al., 2002). This has presented an obstacle for yeast and other eukaryotes ever since the accumulation of oxygen 1-2 billion years ago that has caused the majority of copper in the environment to exist in the oxidized form. Eukaryotes have, however, evolved mechanisms to reduce copper ions extracellularly which would be predicted to facilitate copper import. Yeast express several metalloreductases on the cell surface which have varying degrees of specificity for both ferric and cupric ions. Cupric ions are apparently mostly reduced by the Fre1 reductase (Georgatsou et al., 1997; Hassett and Kosman, 1995). However, it is unclear whether Fre1 function is actually necessary for copper import or whether copper reduction and transport are physically coupled, as in the case of Fet3 and Ftr1 for iron. A similar metalloreductase, Fre6, localizes to the vacuolar membrane and catalyzes cupric ion reduction in the vacuolar lumen prior to transport of cuprous ions into the cytoplasm via Ctr2 (Rees et al., 2004).

### *1.7.2 Copper chaperones mediate intracellular trafficking of cuprous ions*

Following transport into the cytoplasm, cuprous ions must be properly distributed to the copper-utilizing enzymes of the various cellular processes described above. This distribution is in part handled by other intracellular transporters, like Ccc2, but it is also controlled by small copper-binding proteins termed copper chaperones. Dedicated copper chaperone systems have been identified, each of which mediates the insertion of copper into the copper-coordinating sites of Sod1, Cox1 and 2, and Fet3 and 5. The copper chaperone for Sod1, encoded by the CCS1 gene in yeast, is a small protein that binds a single $Cu^{+}$ ion (Culotta et al., 1997; Lamb et al., 1999). Delivery of copper to Sod1 is not thought to occur in any particular compartment since, like Sod1,

Ccs1 is diffusely distributed in the cytoplasm, nucleus, and intermembrane space of the mitochondria (Nevitt et al., 2012). Intriguingly, copper-zinc superoxide dismutase in *C. elegans* does not require a copper chaperone for acquiring its copper ion (Jensen and Culotta, 2005), and presumably acquires it directly from the available intracellular copper pool. In the budding yeast, Ccs1 has been described as being essential for Sod1 copper delivery and activation (Schmidt et al., 2000), although this is not entirely accurate. While loss of function of Ccs1 drastically reduces Sod1 activity, the loss of Ccs1 can be partially bypassed by increasing total cellular copper content (Schmidt et al., 2000). The mechanism by which Sod1 acquires copper in the absence of Ccs1 is unclear, although some evidence suggests that a small molecule ligand of cuprous ions, such as glutathione, might accomplish this (Carroll et al., 2004).

A copper chaperone has been identified for the delivery of copper to Ccc2 transporter and ultimately for copper loading on Fet3 and Fet5 (Lin et al., 1997). This copper chaperone, encoded by the ATX1 gene, is homologous to domain I of Ccs1 and a part of the cytosolic region of Ccc2 (Robinson and Winge, 2010; Stasser et al., 2007). It also utilizes a similar copper binding motif to bind a single cuprous ion. Atx1 physically interacts with both Ctr1 and Ccc2 (Banci et al., 2007; Xiao and Wedd, 2002) which presumably facilitates the transfer of copper between these compartments. Although Atx1 has been associated to the delivery of copper ions to the multicopper ferroxidases, its presence throughout the cytoplasm and nucleus raises questions as to whether it may regulate copper trafficking to other as-yet-unknown target proteins. Interestingly, the mammalian homolog, Atox1, has been observed to traffic copper into the nucleus and in turn affect expression of certain genes (Kahra et al., 2015), although the mechanism by which it does so is not known.

Unlike Sod1 and the ferroxidases, which have single copper chaperones involved in the majority of copper delivery, the trafficking of copper to cytochrome *c* oxidase is more complex and involves a chain of copper chaperones (Horn and Barrientos, 2008; Nevitt et al., 2012; Robinson and Winge, 2010). The most well-characterized of these chaperones are Cox17 (Glerum et al., 1996), Cox11 (Khalimonchuk et al., 2005) and Sco1 and 2 (Lode et al., 2002; Rentzsch et al., 1999). Cox17, having received a copper ion from an upstream chaperone, transfers a cuprous ion to either Cox11 or Sco1/2 (Horng et al., 2004), each of which subsequently delivers cuprous ions to the Cox1 and Cox2 subunits of cytochrome *c* oxidase, respectively (Horn and Barrientos, 2008). Loss of function of any of these chaperones prevents proper copper delivery to at least one of the copper sites of cytochrome *c* oxidase and renders cells unable to utilize mitochondrial respiration. As with Ccs1, some Cox17-independent delivery of copper is possible by substantially increasing the cellular copper content (Glerum et al., 1996) but it may only be achieved in certain laboratory strains that can tolerate extremely high copper concentrations.

Several notable properties of the known copper chaperones have implications for general cellular copper homeostasis. First, biochemical analyses of the copper transporters and chaperones has led to the proposal that the trafficking pathways of cuprous ions from Ctr1 to the chaperones to the cuproproteins is driven by a gradient of increasing copper binding affinities (Banci et al., 2010a). The proteins with the highest copper binding affinities include Sod1 and Cox2 and this elegant biochemical mechanism can account for the directionality of copper trafficking. Several aspects of copper homeostasis are not adequately addressed by this scenario, however. For example, it is unclear how, or even if, the copper-sensing transcription factors would fit in the gradient of increasing copper binding affinities. The model relies on the copper-binding affinities of each protein determined in *in vitro* experiments, but it is also unclear how the proteins and the

pathways would be affected by post-translational modifications or by binding to other protein partners. Likewise, it is unclear how different localizations, altering their local abundances, or possibly regulating local copper concentrations via other proteins or small molecules might affect the copper trafficking pathways. Furthermore, this affinity gradient-based model implies that only a fraction of the total copper pool of the cell would be "accessible" by the chaperones in situations where the cell needs to re-direct the use of copper ions in response to changing demands. For example, the copper ions bound by Sod1 are not likely to be accessible to Fet3/5 or cytochrome *c* oxidase, and vice versa. It is unclear therefore if recovery of the copper associated with Sod1 would require its degradation. Ultimately, this is predicted to result in a degree of competition between the different copper-utilizing pathways (Rae et al., 1999), which could become physiologically relevant under copper-starved conditions.

Second, biochemical analyses of the various copper-binding proteins have revealed that they all have very high binding affinities for copper ions, with dissociation constants in the range $10^{-13}$ to $10^{-16}$ M (Banci et al., 2010a). Such strong binding affinities implies that there are essentially no free copper ions present in cells (Rae et al., 1999), at least in regular environmental conditions with "normal" copper abundances. All copper ions are likely bound in one way or another and exchange of copper between different pools necessarily involves competition between binding factors. In addition to the known copper chaperones, other small molecules are also thought to participate in binding copper ions, including the highly abundant glutathione (Ciriolo et al., 1990; White and Cappai, 2003). Although it has a modest binding affinity relative to the dedicated copper chaperones (Banci et al., 2010a), the high abundance of glutathione in cells predicts that a relevant fraction of the total copper content is associated with and regulated by glutathione binding . Lastly, the copper chaperones and copper transporters appear to bind

exclusively to $Cu^{+}$ ions. Therefore, mechanisms to maintain the reduced state of copper ions are expected to be important for the trafficking of copper and its general homeostasis.

### *1.7.3 Unknown pathways for the mitochondrial and nuclear copper pools*

Despite the depth of knowledge of the mechanisms of copper trafficking, several important aspects remain to be understood. One of the unanswered questions in current models of cellular copper distribution regards the mechanism by which copper ions are transported from Ctr1, or other copper pools, to the mitochondria and the chaperone system present there. Whereas Ccs1 and Atx1 can physically interact with the cytoplasmic domain of Ctr1, Cox17 has not been observed to do so. Furthermore, restricting Cox17's localization to the mitochondria by tethering it to the inner mitochondrial membrane does not abolish copper trafficking to cytochrome *c* oxidase (Maxfield et al., 2004). Perhaps Cox17 does normally acquire copper ions in the cytosol and transports them into the mitochondrial inter-membrane space, but such an ability does not fully account for all copper trafficking to cytochrome *c* oxidase. Does another uncharacterized copper chaperone mediate this transport or could it involve non-protein copper ligands? Intriguingly, fractionation of yeast cells to isolate mitochondria and biochemical analysis of the mitochondrial copper content identified the presence of an anionic copper-ligand complex (CuL) in the mitochondrial matrix (Cobine et al., 2004). The exact nature of the ligand is not yet known but it is not a protein chaperone. Interestingly, the CuL is in dynamic equilibrium with cytoplasmic copper content and it was observed that restriction of the matrix CuL impedes copper loading on cytochrome *c* oxidase (Vest et al., 2013). Transport of the CuL appears to be mediated by non-copper-specific mitochondrial transporters Pic2 and Mrs3 (Vest et al., 2013; Vest et al., 2016). It is unlikely that these transporters account for all of the copper trafficking into mitochondria as loss of function of both genes does not completely abolish copper trafficking to cytochrome *c* oxidase

(Vest et al., 2016), as loss of Cox17 function does. Furthermore, although identification of the CuL provides additional knowledge of the copper trafficking pathway to cytochrome *c* oxidase, it is still not clear how the copper subsequently enters the inter-membrane space to be accessed by Cox17.

A significant fraction of the total copper content is also localized in the cell nucleus (McRae et al., 2013; Yang et al., 2005) but it is unclear how, or even if, transport of copper ions into or out of the nucleus is regulated. It is known that both Ccs1 and Sod1, as well as Atox1 in mammalian cells, and also the copper-responsive transcription factors are present in the nucleus. In fact, the copper-binding transcription factor Mac1 has only been measurably localized to the nucleus (Serpe et al., 1999), necessitating a means to import copper into this compartment. Perhaps some these proteins do participate in copper transport in or out of the nucleus, although studies carefully examining this possibility have not been carried out. Interestingly, Sod1 function in the nucleus is necessary for Mac1 activation since excluding it from the nucleus impairs the ability of Mac1 to sense and respond to copper depletion (Wood and Thiele, 2009). It is unclear if this dependency is due to Sod1's superoxide dismutase activity. Alternatively, and in an unprecedented manner, could Sod1 act as a "chaperone" to deliver copper ions to Mac1 and generally regulate copper distribution in the nucleus? Lastly, knockout of the ATP7A/B copper exporters in mammalian cells causes hyper-accumulation of copper in cells, but the accumulation occurs disproportionately in the cell nucleus (Huster et al., 2006). This suggests that the copper content of the nucleus is not in a simple 1:1 equilibrium with the cytoplasm, which in turn suggests that there are factors that influence this distribution in different circumstances. A detailed understanding of such factors is missing.

### *1.7.4 Transcriptional control of copper homeostasis*

The mechanisms described above for mobilizing copper to the cuproproteins are not constitutively active but are regulated in different circumstances and conditions. One of the mechanisms of this regulation occurs at the level of gene transcription, where two copper-sensing transcriptional activators have been identified in the budding yeast. These are the Mac1 (Jungmann et al., 1993) and Cup2 (Thiele, 1988) transcription factors. Mac1 activates the expression of the Ctr1 and Ctr3 transporters as well as the Fre1 and Fre7 metalloreductases in response to copper depletion (Gross et al., 2000), and does so by binding to a pair of copper response element DNA sequences in the promoters of its target genes (Labbe et al., 1997; Yamaguchi-Iwai et al., 1997). Importantly, Mac1 binds several $Cu^{+}$ ions and its activity is repressed by this binding (Heredia et al., 2001) giving it the ability to directly "sense" cellular copper content. However, given Mac1's restricted localization to the nucleus, depletion of copper concentrations from the extracellular environment are presumably only sensed if such depletion leads to local depletion of copper concentrations accessible by Mac1 in the nucleus. This raises an unanswered question in situations where copper demand increases, and in which Ctr1 function is required, but in which no change in total copper content occurs. Such would be the case when mitochondrial respiration is enhanced, for example. The mechanism by which Mac1 is activated in this scenario is unclear but perhaps an initial intracellular redistribution of copper pools to support increasing cytochrome *c* oxidase activity leads to local depletion of copper content elsewhere. If such depletion affects copper content of the nucleus, Mac1 could conceivably "interpret" it as a loss of copper availability and activate expression of its target genes.

Cup2 on the other hand, activates transcription of genes that allow the cell to tolerate high copper concentrations that would otherwise be toxic (Thiele, 1988). It also directly binds several

$Cu^+$ ions but in contrast with Mac1, transcriptional activity is activated by copper ion binding (Buchman et al., 1989). Cup2 activates the expression of two high copper-binding capacity metallothionein proteins, Cup1 and Crs5 (Buchman et al., 1989; Culotta et al., 1994), and interestingly, also Sod1 (Gralla et al., 1991). Direct copper binding by Cup2 alters its conformation allowing it to bind to response elements in the promoters of its target genes (Huibregtse et al., 1989). Loss of Cup2 function renders cells highly sensitive to elevations in environmental copper concentrations.

## 1.8 Regulation of the oxidation state of copper

### *1.8.1 Copper redox in cuproproteins*

While many factors regulating copper homeostasis and utilization have been characterized, most of the regulatory mechanisms involve control of copper transport, binding, and compartmentalization. Less is known, however, about how and to what extent the oxidation state of copper ions is regulated in cells. The states of copper ions that exist in biologically-relevant conditions are $Cu^+$ and $Cu^{2+}$, and the copper-dependent enzymes necessarily have strong binding affinity to both states, as they cycle between them in electron transfer reactions without losing the cofactor.

### *1.8.2 Cuprous ion binding in chaperones and its biousability*

Binding of copper ions by the known chaperones, transcription factors, metallothioneins, and transporters, however, appears to be selective for the cuprous ion. Therefore, unless cells contain undiscovered $Cu^{2+}$ binding proteins that also participate in copper homeostasis, the ability to sense, traffic and utilize copper properly ought to depend on the ability cells to maintain the reduced state of $Cu^+$ ions. This should especially be the case given the presence of oxygen in the environment and the propensity for metal ions like $Cu^+$ to be oxidized (Anbar, 2008). Indeed,

organisms utilize the Fre1, 6, and 7 metalloreductases, as described above, to facilitate and ensure the transmembrane transport of the biousable $Cu^{+}$ ions. Notably, these membrane-bound reductases catalyze copper reduction on the extracellular or vacuolar sides of the membrane prior to their transport into the cytoplasm (Georgatsou et al., 1997). It has not been definitively determined, however, how the cuprous ions are maintained in the cytoplasm, nucleus, or mitochondria.

### *1.8.3 Do cytoplasmic copper reduction mechanisms exist?*

It is somewhat surprising that the cellular regulation of copper reduction has not been adequately characterized in the field. It has been assumed that there is no need for regulated copper reduction in the cytoplasm since copper ions may be constitutively and non-specifically maintained in the reduced state due to the highly reducing environment of the cell cytoplasm. Spontaneously oxidized copper ions, perhaps by reacting with hydrogen peroxide (Gunther et al., 1995), could be almost immediately reduced back to the $Cu^{+}$ state by the abundant glutathione molecule, which is known to have modest affinity for copper ions (Banci et al., 2010a) and readily reduces copper *in vitro* (Ngamchuea et al., 2016; Speisky et al., 2009). While this prediction is reasonable, direct evidence of such a glutathione-mediated, non-enzymatic copper reduction occurring in cells is lacking. Furthermore, a similar prediction could be made regarding the presence of disulfide bridges in cytoplasmic proteins, yet there are several examples of stable cysteine-cysteine bonds in cytoplasmic and mitochondrial proteins despite the highly positive reduction potential established by glutathione (Lim et al., 2006; Mesecke et al., 2005). For such proteins, including the copper transporters ATP7A and ATP7B, the reduction of disulfide bridges is indeed driven ultimately by the glutathione-based reduction potential but is catalyzed by other

enzymes, such as the glutaredoxin Grx1 (Lim et al., 2006). Thus, the idea that regulation of the cuprous state would not be required deserves experimental observations to confirm or deny.

Unfortunately, current technical limitations have precluded investigation of this topic as there is a lack of reliable experimental tools to measure the oxidation state of copper ions in cells. One potential tool is the development of fluorescent copper ligands that can selectively bind to $Cu^{+}$ ions to indicate their localization and abundance (Yang et al., 2005; Zeng et al., 2006). Several limitations however, such as possible biases in their localization and ability to compete for copper binding with endogenous copper-binding factors, currently raise questions as to how accurately such fluorescent copper ligands can be used to measure copper contents, let alone oxidation states. Alternatively, techniques based on X-ray absorption spectroscopy are able to detect spectroscopic signatures corresponding to $Cu^{+}$ and $Cu^{2+}$ coordinating geometries in copper-binding sites in cells (Yang et al., 2005). However, such technology is not yet easily accessible to many labs and therefore progress has been slow. More importantly, the identities of the copper-ligand geometries observed are not clear and other than the mere observation that $Cu^{2+}$ ions are coordinated by some ligand in cells, no further experimentation has been done to determine if such a copper-ligand species can be altered or regulated in any way.

## 1.9 Interactions with copper ions

### *1.9.1 Copper binding sites*

Known copper-binding proteins exhibit a variety of different structures and copper-coordinating sites are also diverse. Yet, many share common attributes owing to the chemical constraints imposed by copper-ligand interactions in the aqueous environments of cells, and indeed, copper sites in proteins can be grouped into various classes (Katz et al., 2003; Palumaa, 2013). In general, the copper-binding sites of the cuproproteins have catalytic copper ions with

high coordination numbers, with four to six atoms binding the central copper ion (Katz et al., 2003). The interacting ligands vary between different proteins but preferentially involve sulfur, nitrogen, and oxygen atoms provided by cysteine, methionine, and histidine residues, and sometimes carbonyls of polypeptide backbones, and even water molecules (Katz et al., 2003). Active site copper-coordination environments alter various properties of the copper ions, perhaps most notably changing reduction potentials (Holm et al., 1996). This is obviously advantageous for the function of these copper ions for the electron transfer reactions that they perform.

The copper-coordinating sites of the known eukaryotic copper chaperones, such as Ccs1, Atx1 and their homologs, and also of the copper-transporting P-type ATPases are somewhat different than those in cuproproteins (Palumaa, 2013). The chaperone copper-binding domains are distantly related to bacterial copper chaperones and more generally to ferredoxin fold-containing proteins (Rosenzweig et al., 1999; Rosenzweig and O'Halloran, 2000). These copper chaperones and transporters tend to coordinate $Cu^{+}$ ions specifically using a pair of cysteines in near-linear geometry (Rosenzweig et al., 1999), although tetrahedral-like coordination geometries also occur with additional sulfur atoms provided by non-protein free thiols or even by dimerization of two copper-binding sites, as in the case of human Atox1 (Wernimont et al., 2000). The copper chaperone Cox17 also utilizes sulfur atoms from cysteines but its copper coordination structures are different. In a fully reduced form, Cox17 forms a tetracopper-thiolate cluster of four $Cu^{+}$ ions coordinated by six cysteine sulfurs, whereas in a the partially oxidized form, it only coordinates a single $Cu^{+}$ ion with two sulfur atoms (Palumaa et al., 2004). It is interesting that the cuproproteins generally bind to catalytically-active copper ions with a greater complexity of coordinating structures compared to the chaperones (Banci et al., 2010b), and this could be indicative of the need for stable binding to both $Cu^{+}$ and $Cu^{2+}$ ions. Chaperones on the other hand, while they must

stably bind $Cu^{+}$ ions, must also be able to release the cuprous ions when transferring them to the target cuproproteins. Perhaps, lower complexity coordination structures allow more efficient copper ion exchange between proteins without requiring drastic protein conformational rearrangements. Lastly, the metallothioneins like Cup1, also have unique structural motifs that depend on clusters of many cysteine sulfurs binding many $Cu^{+}$ ions with very high affinity (Winge et al., 1985).

### *1.9.2 Cupric ion reduction by transmembrane metalloreductases*

The cuproproteins alter reducing potential of the copper ions they bind, and the other known copper-binding proteins favor the binding of the reduced cuprous ions, but these proteins are not recognized as copper reductases *per se*. The cuproproteins instead utilize the ability of copper redox activity to catalyze oxidation and reduction reactions of other substrates. For example, the multicopper ferroxidase Fet3 in the budding yeast oxidizes $Fe^{2+}$ by extracting an electron and transferring it to the cluster of oxidized copper ions (Jones and Solomon, 2015; Taylor et al., 2005). This extraction of four electrons from four $Fe^{2+}$ ions effectively and transiently reduces the multicopper cluster. Of course, electrons extracted from iron and "stored" by the copper cluster ultimately reduce molecular oxygen, thereby restoring the oxidized copper ions.

As mentioned in previous sections however, there is a class of metalloreductases found in all three kingdoms of life that catalyze copper, and iron, reduction (Schroder et al., 2003). These eukaryotic membrane-bound metal reductases are NAD(P)H-dependent ferric and cupric ion reductases and interestingly, are homologous to the human NADPH oxidase in phagocytes (Shatwell et al., 1996). Enzymes like the yeast Fre1 transfer electrons from the cytoplasmic side of the membrane, using NAD(P)H as an electron donor, across the membrane via a series of electron transfer reactions involving heme *b* and probably FAD (Finegold et al., 1996). The Flavin

nucleotide ultimately reduces the $Cu^{2+}$, or $Fe^{3+}$, substrates on the extracellular or vacuolar lumen side (Schroder et al., 2003). Unlike the other copper-binding proteins, however, the copper reductases like Fre1 and Fre6 have not been shown to have specific metal coordinating regions. It is unclear therefore how electrons are specifically transferred to these metals, and it has been proposed that these class of enzymes are really just Flavin reductases that have been adapted for diverse substrates (Schroder et al., 2003). Notably, the yeast metalloreductases are exclusively membrane bound and catalyze copper and iron reduction on the extracytoplasmic side. There are no known copper reductases that function inside the eukaryotic cytoplasm or nucleus. The work presented in Chapters 4 and 5 of this dissertation propose the first of such a class of enzymes.

## 1.10 References


Adamczyk, M., Poznanski, J., Kopera, E., and Bal, W. (2007). A zinc-finger like metal binding site in the nucleosome. Febs Lett *581*, 1409-1416.

Allshire, R.C., and Madhani, H.D. (2017). Ten principles of heterochromatin formation and function. Nat Rev Mol Cell Biol.

Anbar, A.D. (2008). Oceans. Elements and evolution. Science *322*, 1481-1483.

Anderson, J.D., and Widom, J. (2000). Sequence and position-dependence of the equilibrium accessibility of nucleosomal DNA target sites. J Mol Biol *296*, 979-987.

Antoniacci, L.M., Kenna, M.A., and Skibbens, R.V. (2007). The nuclear envelope and spindle pole body-associated Mps3 protein bind telomere regulators and function in telomere clustering. Cell Cycle *6*, 75-79.

Arents, G., and Moudrianakis, E.N. (1995). The histone fold: a ubiquitous architectural motif utilized in DNA compaction and protein dimerization. Proceedings of the National Academy of Sciences of the United States of America *92*, 11170-11174.

Askwith, C., Eide, D., Van Ho, A., Bernard, P.S., Li, L., Davis-Kaplan, S., Sipe, D.M., and Kaplan, J. (1994). The FET3 gene of S. cerevisiae encodes a multicopper oxidase required for ferrous iron uptake. Cell *76*, 403-410.

Banci, L., Bertini, I., Chasapis, C.T., Rosato, A., and Tenori, L. (2007). Interaction of the two soluble metal-binding domains of yeast Ccc2 with copper(I)-Atx1. Biochem Biophys Res Commun *364*, 645-649.

Banci, L., Bertini, I., Ciofi-Baffoni, S., Kozyreva, T., Zovo, K., and Palumaa, P. (2010a). Affinity gradients drive copper to cellular destinations. Nature *465*, 645-648.

Banci, L., Bertini, I., McGreevy, K.S., and Rosato, A. (2010b). Molecular recognition in copper trafficking. Nat Prod Rep *27*, 695-710.

Barbieri, M., Chotalia, M., Fraser, J., Lavitas, L.M., Dostie, J., Pombo, A., and Nicodemi, M. (2012). Complexity of chromatin folding is captured by the strings and binders switch model. Proceedings of the National Academy of Sciences of the United States of America *109*, 16173-16178.

Belotserkovskaya, R., Oh, S., Bondarenko, V.A., Orphanides, G., Studitsky, V.M., and Reinberg, D. (2003). FACT facilitates transcription-dependent nucleosome alteration. Science *301*, 1090-1093.

Bernstein, B.E., Mikkelsen, T.S., Xie, X., Kamal, M., Huebert, D.J., Cuff, J., Fry, B., Meissner, A., Wernig, M., Plath, K., *et al.* (2006). A bivalent chromatin structure marks key developmental genes in embryonic stem cells. Cell *125*, 315-326.

Bickmore, W.A. (2013). The spatial organization of the human genome. Annu Rev Genomics Hum Genet *14*, 67-84.

Birney, E., Stamatoyannopoulos, J.A., Dutta, A., Guigo, R., Gingeras, T.R., Margulies, E.H., Weng, Z., Snyder, M., Dermitzakis, E.T., Thurman, R.E., *et al.* (2007). Identification and analysis of functional elements in 1% of the human genome by the ENCODE pilot project. Nature *447*, 799-816.

Boettiger, A.N., Bintu, B., Moffitt, J.R., Wang, S., Beliveau, B.J., Fudenberg, G., Imakaev, M., Mirny, L.A., Wu, C.T., and Zhuang, X. (2016). Super-resolution imaging reveals distinct chromatin folding for different epigenetic states. Nature *529*, 418-422.

Bowman, G.D., and Poirier, M.G. (2015). Post-Translational Modifications of Histones That Influence Nucleosome Dynamics. Chem Rev *115*, 2274-2295.

Brackley, C.A., Johnson, J., Kelly, S., Cook, P.R., and Marenduzzo, D. (2016). Simulated binding of transcription factors to active and inactive regions folds human chromosomes into loops, rosettes and topological domains. Nucleic Acids Res *44*, 3503-3512.

Brady, D.C., Crowe, M.S., Turski, M.L., Hobbs, G.A., Yao, X.J., Chaikuad, A., Knapp, S., Xiao, K.H., Campbell, S.L., Thiele, D.J., *et al.* (2014). Copper is required for oncogenic BRAF signalling and tumorigenesis. Nature *509*, 492-+.

Buchman, C., Skroch, P., Welch, J., Fogel, S., and Karin, M. (1989). The Cup2 Gene-Product, Regulator of Yeast Metallothionein Expression, Is a Copper-Activated DNA-Binding Protein. Mol Cell Biol *9*, 4091-4095.

Buenrostro, J.D., Giresi, P.G., Zaba, L.C., Chang, H.Y., and Greenleaf, W.J. (2013). Transposition of native chromatin for fast and sensitive epigenomic profiling of open chromatin, DNA-binding proteins and nucleosome position. Nat Methods *10*, 1213-1218.

Burgess, R.J., and Zhang, Z. (2013). Histone chaperones in nucleosome assembly and human disease. Nat Struct Mol Biol *20*, 14-22.

Buschbeck, M., and Hake, S.B. (2017). Variants of core histones and their roles in cell fate decisions, development and cancer. Nat Rev Mol Cell Bio *18*, 299-314.

Campos, E.I., and Reinberg, D. (2009). Histones: annotating chromatin. Annu Rev Genet *43*, 559-599.

Cao, R., Wang, L., Wang, H., Xia, L., Erdjument-Bromage, H., Tempst, P., Jones, R.S., and Zhang, Y. (2002). Role of histone H3 lysine 27 methylation in Polycomb-group silencing. Science *298*, 1039-1043.

Carroll, M.C., Girouard, J.B., Ulloa, J.L., Subramaniam, J.R., Wong, P.C., Valentine, J.S., and Culotta, V.C. (2004). Mechanisms for activating Cu- and Zn-containing superoxide dismutase in the absence of the CCSCu chaperone. P Natl Acad Sci USA *101*, 5964-5969.

Chang, A., and Fink, G.R. (1994). Metal ion metabolism. The copper-iron connection. Curr Biol *4*, 532-533.

Choy, J.S., and Lee, T.H. (2012). Structural dynamics of nucleosomes at single-molecule resolution. Trends Biochem Sci *37*, 425-435.

Ciriolo, M.R., Desideri, A., Paci, M., and Rotilio, G. (1990). Reconstitution of Cu,Zn-superoxide dismutase by the Cu(I).glutathione complex. J Biol Chem *265*, 11030-11034.

Cobine, P.A., Ojeda, L.D., Rigby, K.M., and Winge, D.R. (2004). Yeast contain a non-proteinaceous pool of copper in the mitochondrial matrix. J Biol Chem *279*, 14447-14455.

Collepardo-Guevara, R., and Schlick, T. (2014). Chromatin fiber polymorphism triggered by variations of DNA linker lengths. Proceedings of the National Academy of Sciences of the United States of America *111*, 8061-8066.

Cremer, T., and Cremer, M. (2010). Chromosome territories. Cold Spring Harb Perspect Biol *2*, a003889.

Culkin, J., de Bruin, L., Tompitak, M., Phillips, R., and Schiessel, H. (2017). The role of DNA sequence in nucleosome breathing. Eur Phys J E Soft Matter *40*, 106.

Culotta, V.C., Howard, W.R., and Liu, X.F. (1994). CRS5 encodes a metallothionein-like protein in Saccharomyces cerevisiae. J Biol Chem *269*, 25295-25302.

Culotta, V.C., Klomp, L.W.J., Strain, J., Casareno, R.L.B., Krems, B., and Gitlin, J.D. (1997). The copper chaperone for superoxide dismutase. J Biol Chem *272*, 23469-23472.

Cutter, A.R., and Hayes, J.J. (2015). A brief review of nucleosome structure. Febs Lett *589*, 2914-2922.

Dancis, A., Haile, D., Yuan, D.S., and Klausner, R.D. (1994a). The Saccharomyces cerevisiae copper transport protein (Ctr1p). Biochemical characterization, regulation by copper, and physiologic role in copper uptake. J Biol Chem *269*, 25660-25667.

Dancis, A., Yuan, D.S., Haile, D., Askwith, C., Eide, D., Moehle, C., Kaplan, J., and Klausner, R.D. (1994b). Molecular characterization of a copper transport protein in S. cerevisiae: an unexpected role for copper in iron transport. Cell *76*, 393-402.

Davey, C.A., Sargent, D.F., Luger, K., Maeder, A.W., and Richmond, T.J. (2002). Solvent mediated interactions in the structure of the nucleosome core particle at 1.9 angstrom resolution. J Mol Biol *319*, 1097-1113.

De Freitas, J.M., Kim, J.H., Poynton, H., Su, T., Wintz, H., Fox, T., Holman, P., Loguinov, A., Keles, S., van der Laan, M., *et al.* (2004). Exploratory and confirmatory gene expression profiling of mac1Delta. J Biol Chem *279*, 4450-4458.

Dekker, J., and Mirny, L. (2016). The 3D Genome as Moderator of Chromosomal Communication. Cell *164*, 1110-1121.

Dekker, J., Rippe, K., Dekker, M., and Kleckner, N. (2002). Capturing chromosome conformation. Science *295*, 1306-1311.

Derenzini, M., Olins, A.L., and Olins, D.E. (2014). Chromatin structure in situ: the contribution of DNA ultrastructural cytochemistry. Eur J Histochem *58*, 2307.

Desilva, D.M., Askwith, C.C., Eide, D., and Kaplan, J. (1995). The Fet3 Gene-Product Required for High-Affinity Iron Transport in Yeast Is a Cell-Surface Ferroxidase. J Biol Chem *270*, 1098-1101.

Dhalluin, C., Carlson, J.E., Zeng, L., He, C., Aggarwal, A.K., and Zhou, M.M. (1999). Structure and ligand of a histone acetyltransferase bromodomain. Nature *399*, 491-496.

Dixon, J.R., Gorkin, D.U., and Ren, B. (2016). Chromatin Domains: The Unit of Chromosome Organization. Mol Cell *62*, 668-680.

Dixon, J.R., Jung, I., Selvaraj, S., Shen, Y., Antosiewicz-Bourget, J.E., Lee, A.Y., Ye, Z., Kim, A., Rajagopal, N., Xie, W., *et al.* (2015). Chromatin architecture reorganization during stem cell differentiation. Nature *518*, 331-336.

Dixon, J.R., Selvaraj, S., Yue, F., Kim, A., Li, Y., Shen, Y., Hu, M., Liu, J.S., and Ren, B. (2012). Topological domains in mammalian genomes identified by analysis of chromatin interactions. Nature *485*, 376-380.

Dlouhy, A.C., and Outten, C.E. (2013). The iron metallome in eukaryotic organisms. Met Ions Life Sci *12*, 241-278.

Dong, K.Z., Addinall, S.G., Lydall, D., and Rutherford, J.C. (2013). The Yeast Copper Response Is Regulated by DNA Damage. Mol Cell Biol *33*, 4041-4050.

Draker, R., Ng, M.K., Sarcinella, E., Ignatchenko, V., Kislinger, T., and Cheung, P. (2012). A Combination of H2A.Z and H4 Acetylation Recruits Brd2 to Chromatin during Transcriptional Activation. Plos Genet *8*.

Duan, Z., Andronescu, M., Schutz, K., McIlwain, S., Kim, Y.J., Lee, C., Shendure, J., Fields, S., Blau, C.A., and Noble, W.S. (2010). A three-dimensional model of the yeast genome. Nature *465*, 363-367.

Dultz, E., and Ellenberg, J. (2010). Live imaging of single nuclear pores reveals unique assembly kinetics and mechanism in interphase. J Cell Biol *191*, 15-22.

Dunn, C.D., Lee, M.S., Spencer, F.A., and Jensen, R.E. (2006). A genomewide screen for petite-negative yeast strains yields a new subunit of the i-AAA protease complex. Mol Biol Cell *17*, 213-226.

Edens, L.J., White, K.H., Jevtic, P., Li, X., and Levy, D.L. (2013). Nuclear size regulation: from single cells to development and disease. Trends Cell Biol *23*, 151-159.

Eltsov, M., Maclellan, K.M., Maeshima, K., Frangakis, A.S., and Dubochet, J. (2008). Analysis of cryo-electron microscopy images does not support the existence of 30-nm chromatin fibers in mitotic chromosomes in situ. Proceedings of the National Academy of Sciences of the United States of America *105*, 19732-19737.

Eser, U., Chandler-Brown, D., Ay, F., Straight, A.F., Duan, Z., Noble, W.S., and Skotheim, J.M. (2017). Form and function of topologically associating genomic domains in budding yeast. Proceedings of the National Academy of Sciences of the United States of America *114*, E3061-E3070.

Eslami-Mossallam, B., Schiessel, H., and van Noort, J. (2016). Nucleosome dynamics: Sequence matters. Adv Colloid Interface Sci *232*, 101-113.

Finegold, A.A., Shatwell, K.P., Segal, A.W., Klausner, R.D., and Dancis, A. (1996). Intramembrane bis-heme motif for transmembrane electron transport conserved in a yeast iron reductase and the human NADPH oxidase. J Biol Chem *271*, 31021-31024.

Fridovich, I. (1995). Superoxide radical and superoxide dismutases. Annu Rev Biochem *64*, 97-112.

Fu, D.D., Beeler, T.J., and Dunn, T.M. (1995). Sequence, Mapping and Disruption of Ccc2, a Gene That Cross-Complements the Ca2+-Sensitive Phenotype of Csg1 Mutants and Encodes a P-Type Atpase Belonging to the Cu2+-Atpase Subfamily. Yeast *11*, 283-292.

Gaspar-Maia, A., Alajem, A., Meshorer, E., and Ramalho-Santos, M. (2011). Open chromatin in pluripotency and reprogramming. Nat Rev Mol Cell Biol *12*, 36-47.

Georgatsou, E., Mavrogiannis, L.A., Fragiadakis, G.S., and Alexandraki, D. (1997). The yeast Fre1p/Fre2p cupric reductases facilitate copper uptake and are regulated by the copper-modulated Mac1p activator. J Biol Chem *272*, 13786-13792.

Ghirlando, R., and Felsenfeld, G. (2016). CTCF: making the right connections. Genes Dev *30*, 881-891.

Gkouvatsos, K., Papanikolaou, G., and Pantopoulos, K. (2012). Regulation of iron transport and the role of transferrin. Biochim Biophys Acta *1820*, 188-202.

Glerum, D.M., Shtanko, A., and Tzagoloff, A. (1996). Characterization of COX17, a yeast gene involved in copper metabolism and assembly of cytochrome oxidase. J Biol Chem *271*, 14504-14509.

Gralla, E.B., Thiele, D.J., Silar, P., and Valentine, J.S. (1991). ACE1, a copper-dependent transcription factor, activates expression of the yeast copper, zinc superoxide dismutase gene. Proceedings of the National Academy of Sciences of the United States of America *88*, 8558-8562.

Grigoryev, S.A. (2012). Nucleosome spacing and chromatin higher-order folding. Nucleus *3*, 493-499.

Gross, C., Kelleher, M., Iyer, V.R., Brown, P.O., and Winge, D.R. (2000). Identification of the copper regulon in Saccharomyces cerevisiae by DNA microarrays. J Biol Chem *275*, 32310-32316.

Grunstein, M., and Gasser, S.M. (2013). Epigenetics in Saccharomyces cerevisiae. Cold Spring Harb Perspect Biol *5*.

Guacci, V., Hogan, E., and Koshland, D. (1997). Centromere position in budding yeast: evidence for anaphase A. Mol Biol Cell *8*, 957-972.

Guelen, L., Pagie, L., Brasset, E., Meuleman, W., Faza, M.B., Talhout, W., Eussen, B.H., de Klein, A., Wessels, L., de Laat, W., *et al.* (2008). Domain organization of human chromosomes revealed by mapping of nuclear lamina interactions. Nature *453*, 948-951.

Gunther, M.R., Hanna, P.M., Mason, R.P., and Cohen, M.S. (1995). Hydroxyl radical formation from cuprous ion and hydrogen peroxide: a spin-trapping study. Arch Biochem Biophys *316*, 515-522.

Gupta, P., Zlatanova, J., and Tomschik, M. (2009). Nucleosome assembly depends on the torsion in the DNA molecule: a magnetic tweezers study. Biophys J *97*, 3150-3157.

Haase, K., Macadangdang, J.K., Edrington, C.H., Cuerrier, C.M., Hadjiantoniou, S., Harden, J.L., Skerjanc, I.S., and Pelling, A.E. (2016). Extracellular Forces Cause the Nucleus to Deform in a Highly Controlled Anisotropic Manner. Scientific reports *6*, 21300.

Hassan, A.H., Prochasson, P., Neely, K.E., Galasinski, S.C., Chandy, M., Carrozza, M.J., and Workman, J.L. (2002). Function and selectivity of bromodomains in anchoring chromatin-modifying complexes to promoter nucleosomes. Cell *111*, 369-379.

Hassett, R., Dix, D.R., Eide, D.J., and Kosman, D.J. (2000). The Fe(II) permease Fet4p functions as a low affinity copper transporter and supports normal copper trafficking in Saccharomyces cerevisiae. Biochem J *351*, 477-484.

Hassett, R., and Kosman, D.J. (1995). Evidence for Cu(Ii) Reduction as a Component of Copper Uptake by Saccharomyces-Cerevisiae. J Biol Chem *270*, 128-134.

Hecht, A., Laroche, T., Strahl-Bolsinger, S., Gasser, S.M., and Grunstein, M. (1995). Histone H3 and H4 N-termini interact with SIR3 and SIR4 proteins: a molecular model for the formation of heterochromatin in yeast. Cell *80*, 583-592.

Hediger, F., Neumann, F.R., Van Houwe, G., Dubrana, K., and Gasser, S.M. (2002). Live imaging of telomeres: yKu and Sir proteins define redundant telomere-anchoring pathways in yeast. Curr Biol *12*, 2076-2089.

Hellman, N.E., and Gitlin, J.D. (2002). Ceruloplasmin metabolism and function. Annu Rev Nutr *22*, 439-458.

Heredia, J., Crooks, M., and Zhu, Z. (2001). Phosphorylation and Cu+ coordination-dependent DNA binding of the transcription factor Mac1p in the regulation of copper transport. J Biol Chem *276*, 8793-8797.

Hergeth, S.P., and Schneider, R. (2015). The H1 linker histones: multifunctional proteins beyond the nucleosomal core particle. Embo Rep *16*, 1439-1453.

Heun, P., Laroche, T., Shimada, K., Furrer, P., and Gasser, S.M. (2001). Chromosome dynamics in the yeast interphase nucleus. Science *294*, 2181-2186.

Holm, R.H., Kennepohl, P., and Solomon, E.I. (1996). Structural and Functional Aspects of Metal Sites in Biology. Chem Rev *96*, 2239-2314.

Horn, D., and Barrientos, A. (2008). Mitochondrial copper metabolism and delivery to cytochrome c oxidase. Iubmb Life *60*, 421-429.

Horng, Y.C., Cobine, P.A., Maxfield, A.B., Carr, H.S., and Winge, D.R. (2004). Specific copper transfer from the Cox17 metallochaperone to both Sco1 and Cox11 in the assembly of yeast cytochrome c oxidase. J Biol Chem *279*, 35334-35340.

Huang, H.D., Stromme, C.B., Saredi, G., Hodl, M., Strandsby, A., Gonzalez-Aguilera, C., Chen, S., Groth, A., and Patel, D.J. (2015). A unique binding mode enables MCM2 to chaperone histones H3-H4 at replication forks. Nature Structural & Molecular Biology *22*, 618-626.

Huibregtse, J.M., Engelke, D.R., and Thiele, D.J. (1989). Copper-induced binding of cellular factors to yeast metallothionein upstream activation sequences. Proceedings of the National Academy of Sciences of the United States of America *86*, 65-69.

Huster, D., Finegold, M.J., Morgan, C.T., Burkhead, J.L., Nixon, R., Vanderwerf, S.M., Gilliam, C.T., and Lutsenko, S. (2006). Consequences of copper accumulation in the livers of the Atp7b(-/-) (Wilson disease gene) knockout mice. Am J Pathol *168*, 423-434.

Hutchison, C.J. (2002). Lamins: building blocks or regulators of gene expression? Nat Rev Mol Cell Biol *3*, 848-858.

Huynh, V.A.T., Robinson, P.J.J., and Rhodes, D. (2005). A method for the in vitro reconstitution of a defined "30 nm" chromatin fibre containing stoichiometric amounts of the linker histone. J Mol Biol *345*, 957-968.

Inesi, G., Pilankatta, R., and Tadini-Buoninsegni, F. (2014). Biochemical characterization of P-type copper ATPases. Biochem J *463*, 167-176.

Ishii, K., Arib, G., Lin, C., Van Houwe, G., and Laemmli, U.K. (2002). Chromatin boundaries in budding yeast: the nuclear pore connection. Cell *109*, 551-562.

Jensen, L.T., and Culotta, V.C. (2005). Activation of CuZn superoxide dismutases from Caenorhabditis elegans does not require the copper chaperone CCS. J Biol Chem *280*, 41373-41379.

Jin, C.Y., Zang, C.Z., Wei, G., Cui, K.R., Peng, W.Q., Zhao, K.J., and Felsenfeld, G. (2009). H3.3/H2A.Z double variant-containing nucleosomes mark 'nucleosome-free regions' of active promoters and other regulatory regions. Nat Genet *41*, 941-U112.

Jin, Q.W., Fuchs, J., and Loidl, J. (2000). Centromere clustering is a major determinant of yeast interphase nuclear organization. J Cell Sci *113*, 1903-1912.

Jones, S.M., and Solomon, E.I. (2015). Electron transfer and reaction mechanism of laccases. Cell Mol Life Sci *72*, 869-883.

Jungmann, J., Reins, H.A., Lee, J.W., Romeo, A., Hassett, R., Kosman, D., and Jentsch, S. (1993). Mac1, a Nuclear Regulatory Protein Related to Cu-Dependent Transcription Factors Is Involved in Cu/Fe Utilization and Stress Resistance in Yeast. Embo J *12*, 5051-5056.

Kagey, M.H., Newman, J.J., Bilodeau, S., Zhan, Y., Orlando, D.A., van Berkum, N.L., Ebmeier, C.C., Goossens, J., Rahl, P.B., Levine, S.S., *et al.* (2010). Mediator and cohesin connect gene expression and chromatin architecture. Nature *467*, 430-435.

Kahra, D., Mondol, T., Niemiec, M.S., and Wittung-Stafshede, P. (2015). Human Copper Chaperone Atox1 Translocates to the Nucleus but does not Bind DNA In Vitro. Protein Peptide Lett *22*, 532-538.

Kasten, M., Szerlong, H., Erdjument-Bromage, H., Tempst, P., Werner, M., and Cairns, B.R. (2004). Tandem bromodomains in the chromatin remodeler RSC recognize acetylated histone H3 Lys14. Embo J *23*, 1348-1359.

Katz, A.K., Shimoni-Livny, L., Navon, O., Navon, N., Bock, C.W., and Glusker, J.P. (2003). Copper-binding motifs: Structural and theoretical aspects. Helv Chim Acta *86*, 1320-1338.

Keyer, K., Gort, A.S., and Imlay, J.A. (1995). Superoxide and the production of oxidative DNA damage. Journal of bacteriology *177*, 6782-6790.

Khalimonchuk, O., Ostermann, K., and Rodel, G. (2005). Evidence for the association of yeast mitochondrial ribosomes with Cox11p, a protein required for the Cu(B) site formation of cytochrome c oxidase. Curr Genet *47*, 223-233.

Kimura, H., and Cook, P.R. (2001). Kinetics of core histones in living human cells: little exchange of H3 and H4 and some rapid exchange of H2B. J Cell Biol *153*, 1341-1353.

Klomp, L.W., Lin, S.J., Yuan, D.S., Klausner, R.D., Culotta, V.C., and Gitlin, J.D. (1997). Identification and functional expression of HAH1, a novel human gene involved in copper homeostasis. J Biol Chem *272*, 9221-9226.

Knight, S.A., Labbe, S., Kwon, L.F., Kosman, D.J., and Thiele, D.J. (1996). A widespread transposable element masks expression of a yeast copper transport gene. Genes Dev *10*, 1917-1929.

Labbe, S., Zhu, Z.W., and Thiele, D.J. (1997). Copper-specific transcriptional repression of yeast genes encoding critical components in the copper transport pathway. J Biol Chem *272*, 15951-15958.

Lachner, M., O'Carroll, D., Rea, S., Mechtler, K., and Jenuwein, T. (2001). Methylation of histone H3 lysine 9 creates a binding site for HP1 proteins. Nature *410*, 116-120.

Lamb, A.L., Wernimont, A.K., Pufahl, R.A., Culotta, V.C., O'Halloran, T.V., and Rosenzweig, A.C. (1999). Crystal structure of the copper chaperone for superoxide dismutase. Nat Struct Biol *6*, 724-729.

Laroche, T., Martin, S.G., Gotta, M., Gorham, H.C., Pryde, F.E., Louis, E.J., and Gasser, S.M. (1998). Mutation of yeast Ku genes disrupts the subnuclear organization of telomeres. Curr Biol *8*, 653-656.

Lawrence, M., Daujat, S., and Schneider, R. (2016). Lateral Thinking: How Histone Modifications Regulate Gene Expression. Trends Genet *32*, 42-56.

Lee, D.Y., Hayes, J.J., Pruss, D., and Wolffe, A.P. (1993). A positive role for histone acetylation in transcription factor access to nucleosomal DNA. Cell *72*, 73-84.

Lee, J., Pena, M.M., Nose, Y., and Thiele, D.J. (2002). Biochemical characterization of the human copper transporter Ctr1. J Biol Chem *277*, 4380-4387.

Levy, A.R., Nissim, M., Mendelman, N., Chill, J., and Ruthstein, S. (2016). Ctr1 Intracellular Loop Is Involved in the Copper Transfer Mechanism to the Atox1 Metallochaperone. J Phys Chem B *120*, 12334-12345.

Li, G., Levitus, M., Bustamante, C., and Widom, J. (2005). Rapid spontaneous accessibility of nucleosomal DNA. Nat Struct Mol Biol *12*, 46-53.

Li, S., and Shogren-Knaak, M.A. (2009). The Gcn5 bromodomain of the SAGA complex facilitates cooperative and cross-tail acetylation of nucleosomes. J Biol Chem *284*, 9411-9417.

Lieberman-Aiden, E., van Berkum, N.L., Williams, L., Imakaev, M., Ragoczy, T., Telling, A., Amit, I., Lajoie, B.R., Sabo, P.J., Dorschner, M.O., *et al.* (2009). Comprehensive mapping of long-range interactions reveals folding principles of the human genome. Science *326*, 289-293.

Light, W.H., Brickner, D.G., Brand, V.R., and Brickner, J.H. (2010). Interaction of a DNA zip code with the nuclear pore complex promotes H2A.Z incorporation and INO1 transcriptional memory. Mol Cell *40*, 112-125.

Lim, C.M., Cater, M.A., Mercer, J.F., and La Fontaine, S. (2006). Copper-dependent interaction of glutaredoxin with the N termini of the copper-ATPases (ATP7A and ATP7B) defective in Menkes and Wilson diseases. Biochem Biophys Res Commun *348*, 428-436.

Lin, S.J., Pufahl, R.A., Dancis, A., O'Halloran, T.V., and Culotta, V.C. (1997). A role for the Saccharomyces cerevisiae ATX1 gene in copper trafficking and iron transport. J Biol Chem *272*, 9215-9220.

Linz, R., and Lutsenko, S. (2007). Copper-transporting ATPases ATP7A and ATP7B: cousins, not twins. J Bioenerg Biomembr *39*, 403-407.

Liu, X.F., Elashvili, I., Gralla, E.B., Valentine, J.S., Lapinskas, P., and Culotta, V.C. (1992). Yeast lacking superoxide dismutase. Isolation of genetic suppressors. J Biol Chem *267*, 18298-18302.

Lode, A., Paret, C., and Rodel, G. (2002). Molecular characterization of Saccharomyces cerevisiae Sco2p reveals a high degree of redundancy with Sco1p. Yeast *19*, 909-922.

Lucas, M.F., Rousseau, D.L., and Guallar, V. (2011). Electron transfer pathways in cytochrome c oxidase. Biochim Biophys Acta *1807*, 1305-1313.

Luger, K., Mader, A.W., Richmond, R.K., Sargent, D.F., and Richmond, T.J. (1997). Crystal structure of the nucleosome core particle at 2.8 A resolution. Nature *389*, 251-260.

Macadangdang, B.R., Oberai, A., Spektor, T., Campos, O.A., Sheng, F., Carey, M.F., Vogelauer, M., and Kurdistani, S.K. (2014). Evolution of histone 2A for chromatin compaction in eukaryotes. Elife *3*.

Maison, C., Bailly, D., Peters, A.H., Quivy, J.P., Roche, D., Taddei, A., Lachner, M., Jenuwein, T., and Almouzni, G. (2002). Higher-order structure in pericentric heterochromatin involves a distinct pattern of histone modification and an RNA component. Nat Genet *30*, 329-334.

Marshall, W.F., Straight, A., Marko, J.F., Swedlow, J., Dernburg, A., Belmont, A., Murray, A.W., Agard, D.A., and Sedat, J.W. (1997). Interphase chromosomes undergo constrained diffusional motion in living cells. Curr Biol *7*, 930-939.

Maxfield, A.B., Heaton, D.N., and Winge, D.R. (2004). Cox17 is functional when tethered to the mitochondrial inner membrane. J Biol Chem *279*, 5072-5080.

McBrian, M.A., Behbahan, I.S., Ferrari, R., Su, T., Huang, T.W., Li, K., Hong, C.S., Christofk, H.R., Vogelauer, M., Seligson, D.B., *et al.* (2013). Histone acetylation regulates intracellular pH. Mol Cell *49*, 310-321.

McRae, R., Lai, B., and Fahrni, C.J. (2013). Subcellular redistribution and mitotic inheritance of transition metals in proliferating mouse fibroblast cells. Metallomics *5*, 52-61.

Meluh, P.B., Yang, P.R., Glowczewski, L., Koshland, D., and Smith, M.M. (1998). Cse4p is a component of the core centromere of Saccharomyces cerevisiae. Cell *94*, 607-613.

Mendiburo, M.J., Padeken, J., Fulop, S., Schepers, A., and Heun, P. (2011). Drosophila CENH3 Is Sufficient for Centromere Formation. Science *334*, 686-690.

Mesecke, N., Terziyska, N., Kozany, C., Baumann, F., Neupert, W., Hell, K., and Herrmann, J.M. (2005). A disulfide relay system in the intermembrane space of mitochondria that mediates protein import. Cell *121*, 1059-1069.

Nadal, S., Raj, R., Mohammed, S., and Davis, B.G. (2018). Synthetic post-translational modification of histones. Curr Opin Chem Biol *45*, 35-47.

Neumann, F.R., and Nurse, P. (2007). Nuclear size control in fission yeast. J Cell Biol *179*, 593-600.

Nevitt, T., Ohrvik, H., and Thiele, D.J. (2012). Charting the travels of copper in eukaryotes from yeast to mammals. Biochim Biophys Acta *1823*, 1580-1593.

Ngamchuea, K., Batchelor-McAuley, C., and Compton, R.G. (2016). The Copper(II)-Catalyzed Oxidation of Glutathione. Chemistry *22*, 15937-15944.

Ngo, T.T., Zhang, Q., Zhou, R., Yodh, J.G., and Ha, T. (2015). Asymmetric unwrapping of nucleosomes under tension directed by DNA local flexibility. Cell *160*, 1135-1144.

Olmo, E. (1983). Nucleotype and cell size in vertebrates: a review. Basic Appl Histochem *27*, 227-256.

Palladino, F., Laroche, T., Gilson, E., Axelrod, A., Pillus, L., and Gasser, S.M. (1993). SIR3 and SIR4 proteins are required for the positioning and integrity of yeast telomeres. Cell *75*, 543-555.

Palumaa, P. (2013). Copper chaperones. The concept of conformational control in the metabolism of copper. Febs Lett *587*, 1902-1910.

Palumaa, P., Kangur, L., Voronova, A., and Sillard, R. (2004). Metal-binding mechanism of Cox17, a copper chaperone for cytochrome c oxidase. Biochem J *382*, 307-314.

Park, Y.J., Chodaparambil, J.V., Bao, Y., McBryant, S.J., and Luger, K. (2005). Nucleosome assembly protein 1 exchanges histone H2A-H2B dimers and assists nucleosome sliding. J Biol Chem *280*, 1817-1825.

Pavlova, N.N., and Thompson, C.B. (2016). The Emerging Hallmarks of Cancer Metabolism. Cell Metab *23*, 27-47.

Pena, M.M., Puig, S., and Thiele, D.J. (2000). Characterization of the Saccharomyces cerevisiae high affinity copper transporter Ctr3. J Biol Chem *275*, 33244-33251.

Perisic, O., Collepardo-Guevara, R., and Schlick, T. (2010). Modeling Studies of Chromatin Fiber Structure as a Function of DNA Linker Length. J Mol Biol *403*, 777-802.

Pope, C.R., De Feo, C.J., and Unger, V.M. (2013). Cellular distribution of copper to superoxide dismutase involves scaffolding by membranes. Proceedings of the National Academy of Sciences of the United States of America *110*, 20491-20496.

Portnoy, M.E., Schmidt, P.J., Rogers, R.S., and Culotta, V.C. (2001). Metal transporters that contribute copper to metallochaperones in Saccharomyces cerevisiae. Mol Genet Genomics *265*, 873-882.

Prakash, K. (2017). A Condensed History of Chromatin Research. Springer Theses-Reco, 1-24.

Puig, S., Lee, J., Lau, M., and Thiele, D.J. (2002). Biochemical and genetic analyses of yeast and human high affinity copper transporters suggest a conserved mechanism for copper uptake. J Biol Chem *277*, 26021-26030.

Rae, T.D., Schmidt, P.J., Pufahl, R.A., Culotta, V.C., and O'Halloran, T.V. (1999). Undetectable intracellular free copper: The requirement of a copper chaperone for superoxide dismutase. Science *284*, 805-808.

Ramachandran, S., Vogel, L., Strahl, B.D., and Dokholyan, N.V. (2011). Thermodynamic stability of histone H3 is a necessary but not sufficient driving force for its evolutionary conservation. PLoS Comput Biol *7*, e1001042.

Rao, S.S., Huntley, M.H., Durand, N.C., Stamenova, E.K., Bochkov, I.D., Robinson, J.T., Sanborn, A.L., Machol, I., Omer, A.D., Lander, E.S., *et al.* (2014). A 3D map of the human genome at kilobase resolution reveals principles of chromatin looping. Cell *159*, 1665-1680.

Reddi, A.R., and Culotta, V.C. (2013). SOD1 integrates signals from oxygen and glucose to repress respiration. Cell *152*, 224-235.

Rees, E.M., Lee, J., and Thiele, D.J. (2004). Mobilization of intracellular copper stores by the ctr2 vacuolar copper transporter. J Biol Chem *279*, 54221-54229.

Rentzsch, A., Krummeck-Weiss, G., Hofer, A., Bartuschka, A., Ostermann, K., and Rodel, G. (1999). Mitochondrial copper metabolism in yeast: mutational analysis of Sco1p involved in the biogenesis of cytochrome c oxidase. Curr Genet *35*, 103-108.

Richmond, T.J., Finch, J.T., Rushton, B., Rhodes, D., and Klug, A. (1984). Structure of the nucleosome core particle at 7 A resolution. Nature *311*, 532-537.

Risca, V.I., Denny, S.K., Straight, A.F., and Greenleaf, W.J. (2017). Variable chromatin structure revealed by in situ spatially correlated DNA cleavage mapping. Nature *541*, 237-241.

Risca, V.I., and Greenleaf, W.J. (2015). Unraveling the 3D genome: genomics tools for multiscale exploration. Trends Genet *31*, 357-372.

Robinson, N.J., and Winge, D.R. (2010). Copper metallochaperones. Annu Rev Biochem *79*, 537-562.

Rosenzweig, A.C., Huffman, D.L., Hou, M.Y., Wernimont, A.K., Pufahl, R.A., and O'Halloran, T.V. (1999). Crystal structure of the Atx1 metallochaperone protein at 1.02 A resolution. Structure *7*, 605-617.

Rosenzweig, A.C., and O'Halloran, T.V. (2000). Structure and chemistry of the copper chaperone proteins. Curr Opin Chem Biol *4*, 140-147.

Rudnizky, S., Bavly, A., Malik, O., Pnueli, L., Melamed, P., and Kaplan, A. (2016). H2A.Z controls the stability and mobility of nucleosomes to regulate expression of the LH genes. Nat Commun *7*, 12958.

Ruthenburg, A.J., Li, H., Patel, D.J., and Allis, C.D. (2007). Multivalent engagement of chromatin modifications by linked binding modules. Nat Rev Mol Cell Biol *8*, 983-994.

Rutherford, J.C., Jaron, S., and Winge, D.R. (2003). Aft1p and Aft2p mediate iron-responsive gene expression in yeast through related promoter elements. J Biol Chem *278*, 27636-27643.

Saavedra, R.A. (1986). Histones and Metal-Binding Domains. Science *234*, 1589-1589.

Sauer, P.V., Timm, J., Liu, D.N., Sitbon, D., Boeri-Erba, E., Velours, C., Mucke, N., Langowski, J., Ochsenbein, F., Almouzni, G., *et al.* (2017). Insights into the molecular architecture and histone H3-H4 deposition mechanism of yeast Chromatin assembly factor 1. Elife *6*.

Schardin, M., Cremer, T., Hager, H.D., and Lang, M. (1985). Specific staining of human chromosomes in Chinese hamster x man hybrid cell lines demonstrates interphase chromosome territories. Hum Genet *71*, 281-287.

Schleit, J., Johnson, S.C., Bennett, C.F., Simko, M., Trongtham, N., Castanza, A., Hsieh, E.J., Moller, R.M., Wasko, B.M., Delaney, J.R., *et al.* (2013). Molecular mechanisms underlying genotype-dependent responses to dietary restriction. Aging Cell *12*, 1050-1061.

Schmidt, P.J., Kunst, C., and Culotta, V.C. (2000). Copper activation of superoxide dismutase 1 (SOD1) in vivo. Role for protein-protein interactions with the copper chaperone for SOD1. J Biol Chem *275*, 33771-33776.

Schones, D.E., Cui, K., Cuddapah, S., Roh, T.Y., Barski, A., Wang, Z., Wei, G., and Zhao, K. (2008). Dynamic regulation of nucleosome positioning in the human genome. Cell *132*, 887-898.

Schroder, I., Johnson, E., and de Vries, S. (2003). Microbial ferric iron reductases. FEMS Microbiol Rev *27*, 427-447.

Serpe, M., Joshi, A., and Kosman, D.J. (1999). Structure-function analysis of the protein-binding domains of Mac1p, a copper-dependent transcriptional activator of copper uptake in Saccharomyces cerevisiae. J Biol Chem *274*, 29211-29219.

Serra, V., von Zglinicki, T., Lorenz, M., and Saretzki, G. (2003). Extracellular superoxide dismutase is a major antioxidant in human fibroblasts and slows telomere shortening. J Biol Chem *278*, 6824-6830.

Seto, E., and Yoshida, M. (2014). Erasers of histone acetylation: the histone deacetylase enzymes. Cold Spring Harb Perspect Biol *6*, a018713.

Sexton, T., Yaffe, E., Kenigsberg, E., Bantignies, F., Leblanc, B., Hoichman, M., Parrinello, H., Tanay, A., and Cavalli, G. (2012). Three-dimensional folding and functional organization principles of the Drosophila genome. Cell *148*, 458-472.

Shatwell, K.P., Dancis, A., Cross, A.R., Klausner, R.D., and Segal, A.W. (1996). The FRE1 ferric reductase of Saccharomyces cerevisiae is a cytochrome b similar to that of NADPH oxidase. J Biol Chem *271*, 14240-14244.

Slekar, K.H., Kosman, D.J., and Culotta, V.C. (1996). The yeast copper/zinc superoxide dismutase and the pentose phosphate pathway play overlapping roles in oxidative stress protection. J Biol Chem *271*, 28831-28836.

Song, F., Chen, P., Sun, D., Wang, M., Dong, L., Liang, D., Xu, R.M., Zhu, P., and Li, G. (2014). Cryo-EM study of the chromatin fiber reveals a double helix twisted by tetranucleosomal units. Science *344*, 376-380.

Speisky, H., Gomez, M., Burgos-Bravo, F., Lopez-Alarcon, C., Jullian, C., Olea-Azar, C., and Aliaga, M.E. (2009). Generation of superoxide radicals by copper-glutathione complexes: redox-consequences associated with their interaction with reduced glutathione. Bioorg Med Chem *17*, 1803-1810.

Spizzo, T., Byersdorfer, C., Duesterhoeft, S., and Eide, D. (1997). The yeast FET5 gene encodes a FET3-related multicopper oxidase implicated in iron transport. Mol Gen Genet *256*, 547-556.

Stasser, J.P., Siluvai, G.S., Barry, A.N., and Blackburn, N.J. (2007). A multinuclear copper(I) cluster forms the dimerization interface in copper-loaded human copper chaperone for superoxide dismutase. Biochemistry *46*, 11845-11856.

Stearman, R., Yuan, D.S., Yamaguchi-Iwai, Y., Klausner, R.D., and Dancis, A. (1996). A permease-oxidase complex involved in high-affinity iron uptake in yeast. Science *271*, 1552-1557.

Stehr, R., Kepper, N., Rippe, K., and Wedemann, G. (2008). The effect of internucleosomal interaction on folding of the chromatin fiber. Biophys J *95*, 3677-3691.

Sturtz, L.A., Diekert, K., Jensen, L.T., Lill, R., and Culotta, V.C. (2001). A fraction of yeast Cu,Zn-superoxide dismutase and its metallochaperone, CCS, localize to the intermembrane space of mitochondria. A physiological role for SOD1 in guarding against mitochondrial oxidative damage. J Biol Chem *276*, 38084-38089.

Sullivan, T., Escalante-Alcalde, D., Bhatt, H., Anver, M., Bhat, N., Nagashima, K., Stewart, C.L., and Burke, B. (1999). Loss of A-type lamin expression compromises nuclear envelope integrity leading to muscular dystrophy. J Cell Biol *147*, 913-920.

Symmons, O., Uslu, V.V., Tsujimura, T., Ruf, S., Nassari, S., Schwarzer, W., Ettwiller, L., and Spitz, F. (2014). Functional and topological characteristics of mammalian regulatory domains. Genome Res *24*, 390-400.

Szczypka, M.S., Zhu, Z., Silar, P., and Thiele, D.J. (1997). Saccharomyces cerevisiae mutants altered in vacuole function are defective in copper detoxification and iron-responsive gene transcription. Yeast *13*, 1423-1435.

Tachiwana, H., Kagawa, W., Osakabe, A., Kawaguchi, K., Shiga, T., Hayashi-Takanaka, Y., Kimura, H., and Kurumizaka, H. (2010). Structural basis of instability of the nucleosome containing a testis-specific histone variant, human H3T. Proceedings of the National Academy of Sciences of the United States of America *107*, 10454-10459.

Tainer, J.A., Getzoff, E.D., Richardson, J.S., and Richardson, D.C. (1983). Structure and mechanism of copper, zinc superoxide dismutase. Nature *306*, 284-287.

Taylor, A.B., Stoj, C.S., Ziegler, L., Kosman, D.J., and Hart, P.J. (2005). The copper-iron connection in biology: structure of the metallo-oxidase Fet3p. Proceedings of the National Academy of Sciences of the United States of America *102*, 15459-15464.

Thiele, D.J. (1988). ACE1 regulates expression of the Saccharomyces cerevisiae metallothionein gene. Mol Cell Biol *8*, 2745-2752.

Towbin, B.D., Gonzalez-Aguilera, C., Sack, R., Gaidatzis, D., Kalck, V., Meister, P., Askjaer, P., and Gasser, S.M. (2012). Step-Wise Methylation of Histone H3K9 Positions Heterochromatin at the Nuclear Periphery. Cell *150*, 934-947.

Tse, C., Sera, T., Wolffe, A.P., and Hansen, J.C. (1998). Disruption of higher-order folding by core histone acetylation dramatically enhances transcription of nucleosomal arrays by RNA polymerase III. Mol Cell Biol *18*, 4629-4638.

Turski, M.L., Brady, D.C., Kim, H.J., Kim, B.E., Nose, Y., Counter, C.M., Winge, D.R., and Thiele, D.J. (2012). A novel role for copper in Ras/mitogen-activated protein kinase signaling. Mol Cell Biol *32*, 1284-1295.

Urbanowski, J.L., and Piper, R.C. (1999). The iron transporter Fth1p forms a complex with the Fet5 iron oxidase and resides on the vacuolar membrane. J Biol Chem *274*, 38061-38070.

van Steensel, B., and Belmont, A.S. (2017). Lamina-Associated Domains: Links with Chromosome Architecture, Heterochromatin, and Gene Repression. Cell *169*, 780-791.

Vendelboe, T.V., Harris, P., Zhao, Y., Walter, T.S., Harlos, K., El Omari, K., and Christensen, H.E. (2016). The crystal structure of human dopamine beta-hydroxylase at 2.9 A resolution. Sci Adv *2*, e1500980.

Vest, K.E., Leary, S.C., Winge, D.R., and Cobine, P.A. (2013). Copper Import into the Mitochondrial Matrix in Saccharomyces cerevisiae Is Mediated by Pic2, a Mitochondrial Carrier Family Protein. J Biol Chem *288*, 23884-23892.

Vest, K.E., Wang, J., Gammon, M.G., Maynard, M.K., White, O.L., Cobine, J.A., Mahone, W.K., and Cobine, P.A. (2016). Overlap of copper and iron uptake systems in mitochondria in Saccharomyces cerevisiae. Open Biol *6*, 150223.

Vlijm, R., Lee, M., Lipfert, J., Lusser, A., Dekker, C., and Dekker, N.H. (2015). Nucleosome Assembly Dynamics Involve Spontaneous Fluctuations in the Handedness of Tetrasomes. Cell Rep *10*, 216-225.

Vulpe, C.D., Kuo, Y.M., Murphy, T.L., Cowley, L., Askwith, C., Libina, N., Gitschier, J., and Anderson, G.J. (1999). Hephaestin, a ceruloplasmin homologue implicated in intestinal iron transport, is defective in the sla mouse. Nat Genet *21*, 195-199.

Wal, M., and Pugh, B.F. (2012). Genome-Wide Mapping of Nucleosome Positions in Yeast Using High-Resolution MNase ChIP-Seq. Nucleosomes, Histones & Chromatin, Pt B *513*, 233-250.

Wallace, M.A., Liou, L.L., Martins, J., Clement, M.H., Bailey, S., Longo, V.D., Valentine, J.S., and Gralla, E.B. (2004). Superoxide inhibits 4Fe-4S cluster enzymes involved in amino acid biosynthesis. Cross-compartment protection by CuZn-superoxide dismutase. J Biol Chem *279*, 32055-32062.

Wang, D., Ulyanov, N.B., and Zhurkin, V.B. (2010). Sequence-dependent Kink-and-Slide deformations of nucleosomal DNA facilitated by histone arginines bound in the minor groove. J Biomol Struct Dyn *27*, 843-859.

Wang, T.P., Quintanar, L., Severance, S., Solomon, E.I., and Kosman, D.J. (2003). Targeted suppression of the ferroxidase and iron trafficking activities of the multicopper oxidase Fet3p from Saccharomyces cerevisiae. J Biol Inorg Chem *8*, 611-620.

Weintraub, A.S., Li, C.H., Zamudio, A.V., Sigova, A.A., Hannett, N.M., Day, D.S., Abraham, B.J., Cohen, M.A., Nabet, B., Buckley, D.L., *et al.* (2017). YY1 Is a Structural Regulator of Enhancer-Promoter Loops. Cell *171*, 1573-1588 e1528.

Wernimont, A.K., Huffman, D.L., Lamb, A.L., O'Halloran, T.V., and Rosenzweig, A.C. (2000). Structural basis for copper transfer by the metallochaperone for the Menkes/Wilson disease proteins. Nature structural biology *7*, 766-771.

White, A.R., and Cappai, R. (2003). Neurotoxicity from glutathione depletion is dependent on extracellular trace copper. J Neurosci Res *71*, 889-897.

White, C.L., Suto, R.K., and Luger, K. (2001). Structure of the yeast nucleosome core particle reveals fundamental changes in internucleosome interactions. Embo J *20*, 5207-5218.

Winge, D.R., Nielson, K.B., Gray, W.R., and Hamer, D.H. (1985). Yeast metallothionein. Sequence and metal-binding properties. J Biol Chem *260*, 14464-14470.

Wood, L.K., and Thiele, D.J. (2009). Transcriptional activation in yeast in response to copper deficiency involves copper-zinc superoxide dismutase. J Biol Chem *284*, 404-413.

Xiao, Z., and Wedd, A.G. (2002). A C-terminal domain of the membrane copper pump Ctr1 exchanges copper(I) with the copper chaperone Atx1. Chem Commun (Camb), 588-589.

Xu, F., Zhang, K., and Grunstein, M. (2005). Acetylation in histone H3 globular domain regulates gene expression in yeast. Cell *121*, 375-385.

Yamaguchi-Iwai, Y., Dancis, A., and Klausner, R.D. (1995). AFT1: a mediator of iron regulated transcriptional control in Saccharomyces cerevisiae. Embo J *14*, 1231-1239.

Yamaguchi-Iwai, Y., Serpe, M., Haile, D., Yang, W., Kosman, D.J., Klausner, R.D., and Dancis, A. (1997). Homeostatic regulation of copper uptake in yeast via direct binding of MAC1 protein to upstream regulatory sequences of FRE1 and CTR1. J Biol Chem *272*, 17711-17718.

Yang, F., Teves, S.S., Kemp, C.J., and Henikoff, S. (2014). Doxorubicin, DNA torsion, and chromatin dynamics. Biochim Biophys Acta *1845*, 84-89.

Yang, J., Zhang, X., Feng, J., Leng, H., Li, S., Xiao, J., Liu, S., Xu, Z., Xu, J., Li, D., *et al.* (2016). The Histone Chaperone FACT Contributes to DNA Replication-Coupled Nucleosome Assembly. Cell Rep *14*, 1128-1141.

Yang, L.C., McRae, R., Henary, M.M., Patel, R., Lai, B., Vogt, S., and Fahrni, C.J. (2005). Imaging of the intracellular topography of copper with a fluorescent sensor and by synchrotron x-ray fluorescence microscopy. P Natl Acad Sci USA *102*, 11179-11184.

Yuan, D.S., Dancis, A., and Klausner, R.D. (1997). Restriction of copper export in Saccharomyces cerevisiae to a late Golgi or post-Golgi compartment in the secretory pathway. J Biol Chem *272*, 25787-25793.

Yuan, D.S., Stearman, R., Dancis, A., Dunn, T., Beeler, T., and Klausner, R.D. (1995). The Menkes/Wilson disease gene homologue in yeast provides copper to a ceruloplasmin-like oxidase required for iron uptake. Proceedings of the National Academy of Sciences of the United States of America *92*, 2632-2636.

Zelko, I.N., Mariani, T.J., and Folz, R.J. (2002). Superoxide dismutase multigene family: a comparison of the CuZn-SOD (SOD1), Mn-SOD (SOD2), and EC-SOD (SOD3) gene structures, evolution, and expression. Free Radic Biol Med *33*, 337-349.

Zeng, L., Miller, E.W., Pralle, A., Isacoff, E.Y., and Chang, C.J. (2006). A selective turn-on fluorescent sensor for imaging copper in living cells. J Am Chem Soc *128*, 10-11.

Zhang, H.Y., Roberts, D.N., and Cairns, B.R. (2005). Genome-wide dynamics of Htz1, a histone H2A variant that poises repressed/basal promoters for activation through histone loss. Cell *123,* 219-231.

Zimmer, C., and Fabre, E. (2011). Principles of chromosomal organization: lessons from yeast. J Cell Biol *192*, 723-733.

# Chapter 2

## Evolution of histone 2A for chromatin compaction in eukaryotes

## 2.1 Summary

During eukaryotic evolution, genome size has increased disproportionately to nuclear volume, necessitating greater degrees of chromatin compaction in higher eukaryotes which have evolved several mechanisms for genome compaction. However, it is unknown whether histones themselves have also evolved to regulate chromatin compaction. Analysis of histone sequences from 160 eukaryotes revealed that the H2A N-terminus has systematically acquired arginines as genomes expanded. Insertion of arginines into their evolutionary-conserved position in H2A of a small-genome organism increased linear compaction by as much as 40%, while their absence markedly diminished compaction in cells with large genomes. This effect was recapitulated *in vitro* with nucleosomal arrays using unmodified histones, indicating that H2A N-terminus directly modulates the chromatin fiber likely through intra- and inter-nucleosomal arginine-DNA contacts to enable tighter nucleosomal packing. Our findings reveal a novel evolutionary mechanism for regulation of chromatin compaction and may explain the frequent mutations of the H2A N-terminus in cancer.

## 2.2 Introduction

Genome size, defined as the haploid DNA content of a cell, has increased as eukaryotes evolved from single-cell species to more complex, multicellular organisms. Within the same evolutionary timeframe, nuclear volume has also increased but at a slower rate than genome size expansion (Maul and Deaven, 1977; Olmo, 1982). While the ratio of nuclear to cell size has remained essentially constant in eukaryotes (Cavalier-Smith, 2005), the disproportional increase in genome size relative to the nuclear volume has required organisms with larger genomes to compact their chromatin to greater extents than organisms with small sized genomes. Indeed there is a positive correlation between genome size and native chromatin compaction as measured by

dye incorporation into chromatin (Vinogradov, 2005). In most eukaryotes, the genome is organized into chromatin by the repeating nucleosomal structure (Luger et al., 1997). The nucleosomes stack and fold into higher order structures, serving to systematically compact the genome (Duan et al., 2010; Lieberman-Aiden et al., 2009) and to regulate molecular processes that are based on DNA (Celeste et al., 2002; Fischle et al., 2005; Fussner et al., 2011; Kouzarides, 2007; Vogelauer et al., 2002).

The surface of the histone octamer has fourteen DNA interaction sites. Each interaction is mediated by an arginine residue that intercalates into the minor groove of the DNA to stabilize the nucleosomal structure (Luger et al., 1997; West et al., 2010). Arginine is the most commonly used amino acid for interaction with DNA due to its positive charge and the lower energetic cost compared to lysine for displacing water when intercalating into the minor groove (Rohs et al., 2009). Nucleosomes mediate chromatin compaction through a variety of mechanisms. For instance, nucleosomes form higher order structures through inter-nucleosomal contacts between the histone H4 N-terminal domain (NTD) and the acidic patch of H2A and between two H2B C-terminal domains (CTD) (Dorigo et al., 2003; Dorigo et al., 2004; Gordon et al., 2005; Luger et al., 1997; Schalch et al., 2005). Histone variants, such as H2A.Z or H2A.Bbd, as well as post-translational modifications of histones, such as H4K16ac, can further regulate the degree of compaction (Bao et al., 2004; Chandrasekharan et al., 2009; Fierz et al., 2011; Kim et al., 2009; Shogren-Knaak et al., 2006; Suto et al., 2000; Zhou et al., 2007). Polycomb complexes compact large domains of chromatin (Eskeland et al., 2010) and are important for proper development. Histones of the H1 family promote additional compaction by binding between nucleosomes to linker DNA near the DNA entry/exit site on nucleosomes and stabilize the intrinsic ability of nucleosomal arrays to fold *in vitro* (Carruthers et al., 1998; Robinson et al., 2008; Szerlong and

Hansen, 2010). Linker histones may affect chromatin compaction globally (Fan et al., 2005), at specific stages of the cell cycle such as mitosis (Maresca et al., 2005) or at specific regions of the genome (Li et al., 2012). In contrast to canonical histones, the sequence of linker histones are much less conserved (Caterino and Hayes, 2010) and ectopic expression of human linker histones in the budding yeast even at low levels is lethal for the cell (Miloshev et al., 1994). Finally, structural proteins such as condensin also contribute to chromatin condensation (Tada et al., 2011). Many of these modulatory mechanisms are dynamic in nature (Luger et al., 2012) and may help explain why multicellular organisms can compact chromatin to different degrees in different cell types. However, despite the existence of these mechanisms for genome compaction in higher eukaryotes, it has not been known whether the canonical histones themselves have evolved sequence features that also contribute to the generally increased chromatin compaction observed in organisms with larger genomes.

Here we provide evidence from analysis of 160 fully-sequenced eukaryotic genomes that arginine (R) residues at specific positions in the N-terminal tail of histone H2A—which protrudes from the nucleosome on the opposite side of DNA entry/exit site—have co-evolved with increasing genome size with a concomitant decrease in serine/threonines. Although increases in genome size are associated with phylogenetic evolution from protozoa to fungi to more complex plants and animals, we present genetic and molecular evidence from the budding yeast and human cells as well as *in vitro* biochemical data to demonstrate that the evolutionary changes in H2A directly regulate chromatin compaction *in vivo* and *in vitro* with consequences for the nuclear volume. The evolutionary changes in H2A regulate chromatin compaction in yeast and human cells, revealing a surprising flexibility in the dynamics of the chromatin fiber that has been conserved across distant eukaryotes. This previously unrecognized structural feature of the

nucleosome has evolved to enable greater chromatin compaction when genome size is disproportionately larger than the nuclear volume. Our findings also suggest that the reported mutations in histone H2A NTD may contribute to the altered chromatin compaction that is commonly observed in cancer cells (Zink et al., 2004).

## 2.3 Results

### 2.3.1 H2A acquires specifically positioned arginines as genome size increases

To determine whether specific residues in the four core histones have co-evolved with increasing genome size, we performed residue composition analysis of canonical histone protein sequences from 160 fully sequenced eukaryotes with genome sizes ranging from 8-5600 Mbp encompassing protozoa, fungi, plants and animals. The canonical histone proteins for each organism were defined based on at least 90% overlap and 35% identity with the histone fold domain of the corresponding human sequence (see Methods). Each organism was categorized as having a small (<100 Mbp), medium (100-1000 Mbp), or large (>1000 Mbp) genome (Fig 2-2A). Of the canonical histones, the H2A NTD showed the most statistically significant variability in amino acid residues, where the number of arginines increased with increasing genome size (Fig 2-1A), while the number of serines (S) and threonines (T) decreased (Fig 2-1B). Other amino acid residues in the H2A NTD, including lysines (K), did not correlate with genome size (Fig 2-2B).

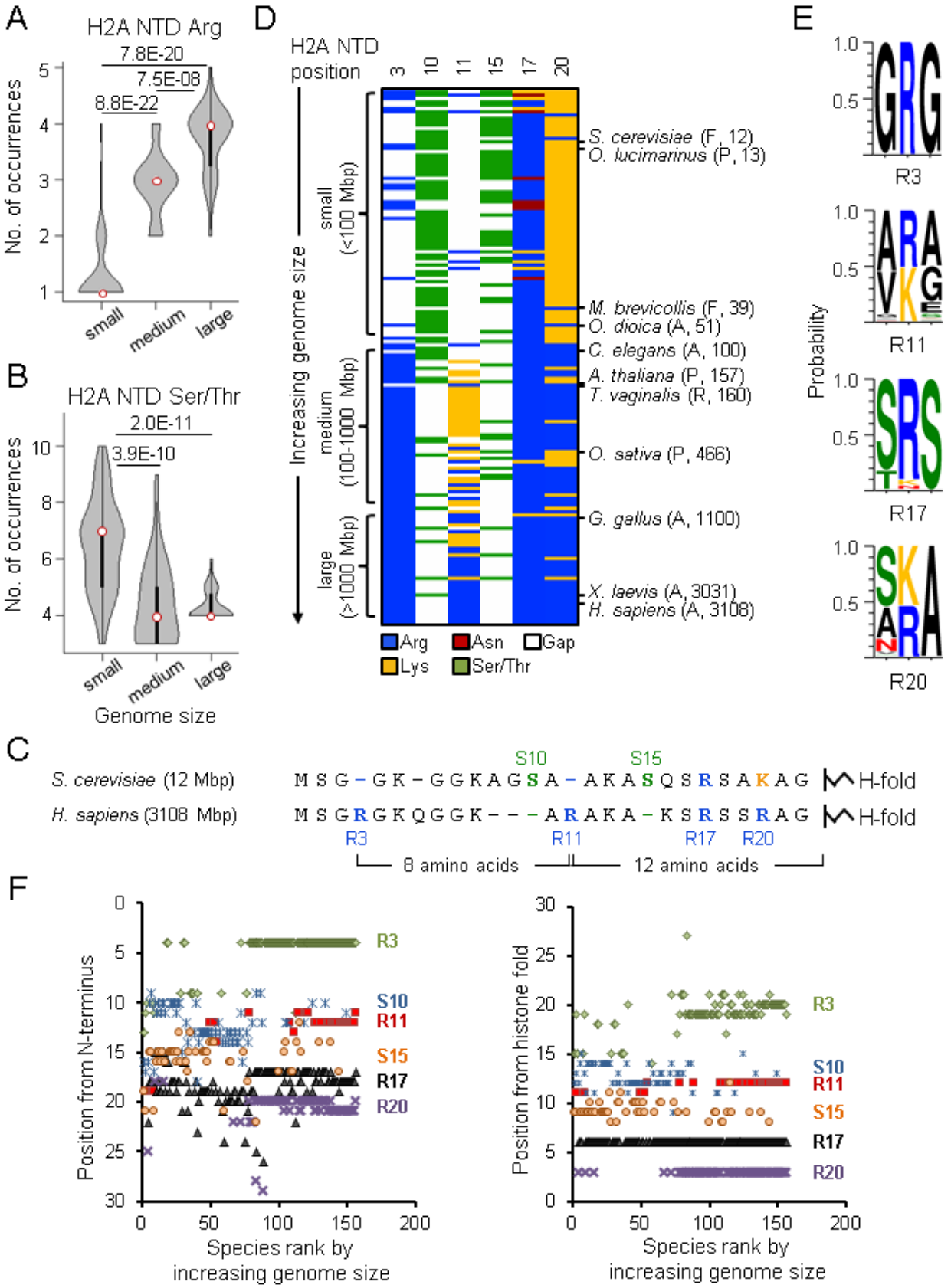
A
H2A NTD Arg
7.8E-20
7.5E-08
8.8E-22
No. of occurrences
small
medium
large
B
H2A NTD Ser/Thr
2.0E-11
3.9E-10
No. of occurrences
small
medium
large
Genome size
D
H2A NTD position
3
10
11
15
17
20
Increasing genome size
small (<100 Mbp)
medium (100-1000 Mbp)
large (>1000 Mbp)
S. cerevisiae (F, 12)
O. lucimarinus (P, 13)
M. brevicollis (F, 39)
O. dioica (A, 51)
C. elegans (A, 100)
A. thaliana (P, 157)
T. vaginalis (R, 160)
O. sativa (P, 466)
G. gallus (A, 1100)
X. laevis (A, 3031)
H. sapiens (A, 3108)
Arg
Asn
Gap
Lys
Ser/Thr
E
Probability
R3
R11
R17
R20
C
S10
S15
S. cerevisiae (12 Mbp)
M S G – G K – G G K A G S A – A K A S Q S R S A K A G
H-fold
H. sapiens (3108 Mbp)
M S G R G K Q G G K – – – A R A K A – K S R S S R A G
H-fold
R3
R11
R17
R20
8 amino acids
12 amino acids
F
Position from N-terminus
R3
S10
R11
S15
R17
R20
Species rank by increasing genome size
Position from histone fold
R3
S10
R11
S15
R17
R20
Species rank by increasing genome size

**Figure 2-1: Histone H2A N-terminal sequence has co-evolved with genome size.** Violin plots of the number of (**A**) arginines or (**B**) serines/threonines in the H2A NTD for species with small, medium, and large genomes. Plot widths correspond to species frequency within each group. (**C**) H2A NTD sequences for *S. cerevisiae* and *H. sapiens*. (**D**) Heat map of H2A NTD residue composition at the indicated positions ordered by genome size. Example species are shown with kingdom and genome size information. (**E**) Protein sequence motifs surrounding the four H2A NTD arginine residues. (**F**) Positioning of evolutionarily variable residues relative to the H2A N-terminus (left) or histone fold (right).

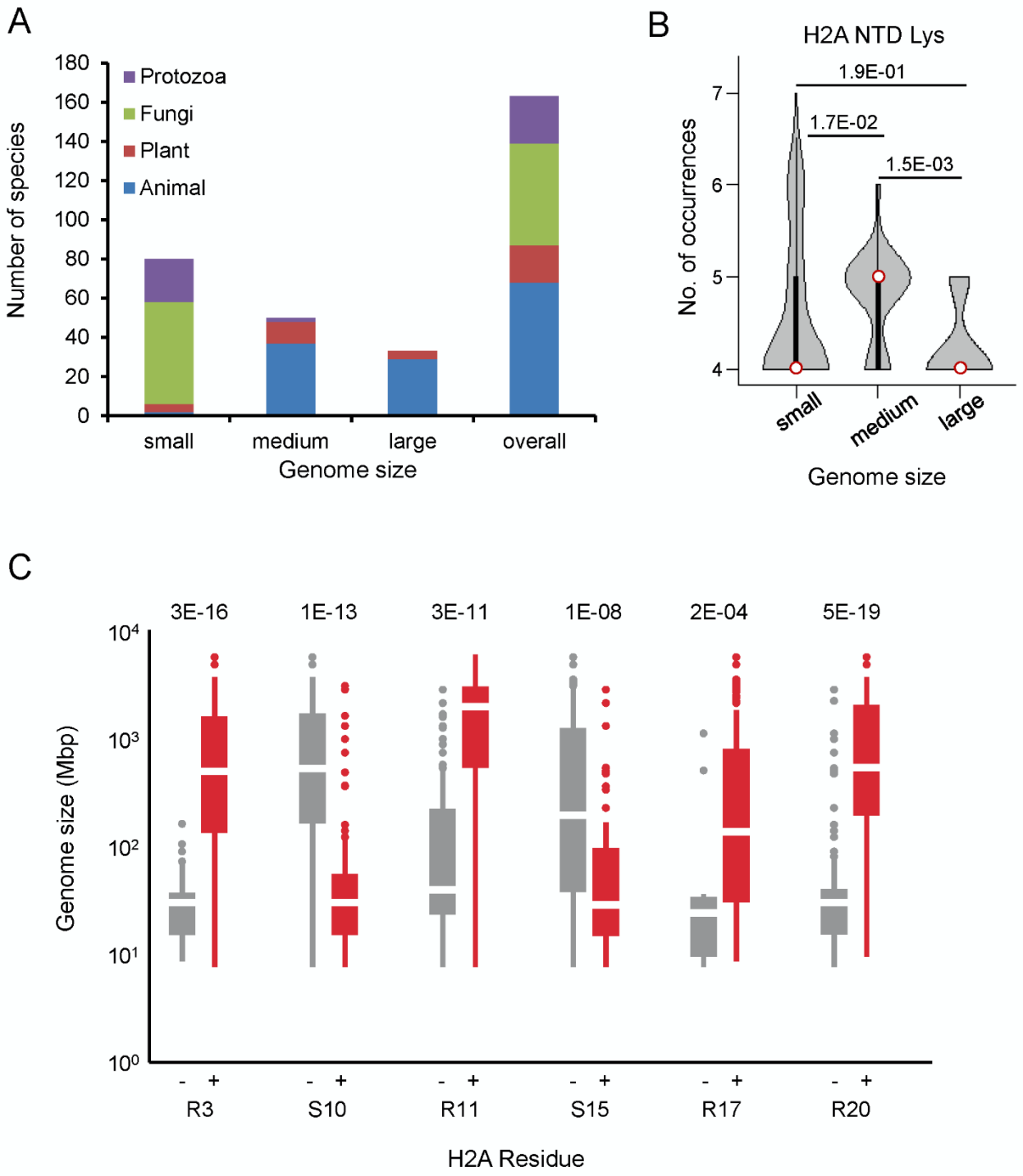


**Figure 2-2: Phylogenetic distribution of species analyzed in this study.** (**A**) The bar graph indicates the number and proportion of organisms in our dataset that belong to the indicated phylogenetic kingdoms for each genome size category. (**B**) Violin plots of the number of lysines in the H2A NTD grouped by genome size as in figure 1. (**C**) Boxplot of genome sizes of the organisms which have an H2A without (left) or with (right) the indicated residue. P-values (Mann-Whitney U test) of the difference in means between the absence or presence of the indicated residue are indicated.

The acquisition of arginines and loss of serines/threonines in the H2A NTD with increasing genome size occur at specific positions and in sequential order. For instance, the human H2A NTD contains arginine residues at positions 3 and 11 that are absent in yeast and at position 20 which is correspondingly a lysine in yeast (Fig 2-1C). In contrast, the human sequence lacks S10 and S15 that are observed in the yeast H2A NTD (Fig 2-1C). Alignment of all H2A NTD sequences also revealed similar trends across all eukaryotes studied here. The heat map in figure 2-1D shows the occurrence of arginines and serines/threonines in the H2A NTD as a function of genome size (see Fig 2-2C for statistical analysis). At position 3, an arginine (R3) is predominantly present in medium and large species but lacking in small species. At position 11, a lysine (K11) is observed in species with medium genomes which evolves to an arginine (R11) mainly in organisms with large genomes. R17 is present in most organisms examined, suggesting a very conserved function for this residue (Zheng et al., 2010). At position 20, small genomes contain predominantly a lysine residue, which converts to arginine in medium and large genomes. In contrast, serines/threonines at positions 10 and 15 are found primarily in organisms with small genomes and much less so in organisms with medium and large genomes (Fig 2-1D). Additionally, each of the four H2A NTD arginines is surrounded by a conserved motif (Fig 2-1E). The residues surrounding R3 and R17 are mainly glycine and serine respectively. At position 11, the motif varies based on genome size. Species with medium sized genomes contain VKG and those with large genomes contain ARA. The same is true of position 20, where AKA is present in organisms with small genomes and (S/T)RA in larger genome species (Fig 2-1E).

Interestingly, except for R3, the positions of all the other evolutionarily varying residues in the H2A NTD are strongly conserved relative to the histone fold domain and not the N-terminus (Fig 2-1F). When counting conventionally from the N-terminus, amino acids R11, R17 and R20—

which are numbered based on the human sequence—were not observed consistently at the same positions in other organisms. However, these residues are respectively 12, 6 and 3 amino acids away from the histone fold in most species (note the vertical axes in Fig 2-1F). S10 and S15—which are numbered based on the yeast sequence—also show more uniform positioning when counted from the histone fold. Altogether, as genome size increases, arginines appear in conserved positions within the H2A NTD relative to the histone fold and serines and threonines are lost.

### 2.3.2 Arginines 3 and 11 in the H2A NTD increase chromatin compaction

To determine whether arginines and serines/threonines of the H2A NTD affect chromatin compaction *in vivo,* we took advantage of a strain of *S. cerevisiae*, that has both chromosomal copies of H2A deleted and carries a single copy of H2A on a plasmid (TSY107) to construct mutant strains containing single or multiple insertions of arginines into their conserved motifs, deletions of serines, or combinations thereof (see Table 2-1 for specific amino acid changes and Table 2-6 for a description of the mutant strains). Two mutants, R3(ΔGS10)R11 and R11ΔS15, were also designed such that the spacing between R3 and R11 or R11 and the histone fold, respectively, is the same as in the H2A NTD of organisms with large genomes (Fig 2-1C, 2-1F). As a control for positive charge, mutant strains with lysines inserted in the same positions as arginines were also generated.

**Table 2-1: List of H2A mutations, sequence changes and their effects on chromatin compaction and nuclear volume..**

| Yeast | | | | | |
|---|---|---|---|---|---|
| | | FISH | | Nuclear volume | |
| H2A Mutant | H2A NTD Protein sequence | % change | p-val | % change | p-val |
| WT | SG-GKG-GKAGSA-AKASQSRSAKAG | - | 1.0E+00 | - | 1.0E+00 |
| R3 | SG**R**GKG-GKAGSA-AKASQSRSAKAG | **-18** | 9.5E-04 | -5 | 4.1E-01 |
| R11 | SG-GKG-GKAGSA**R**AKASQSRSAKAG | **-15** | 8.6E-04 | **-20** | 5.9E-05 |
| R3R11 | SG**R**GKG-GKAGSA**R**AKASQSRSAKAG | **-22** | 8.2E-06 | **-16** | 3.0E-03 |
| R3(ΔGS10)R11 | SG**R**GKG-GKA··A**R**AKASQSRSAKAG | **-30** | 2.1E-06 | +6 | 3.7E-01 |
| R11ΔS15 | SG-GKG-GKAGSA**R**AKA·QSRSAKAG | **-41** | 3.9E-08 | **-9**† | 4.7E-04 |
| K3 | SG**K**GKG-GKAGSA-AKASQSRSAKAG | +9 | 8.6E-01 | **+13** | 9.4E-03 |
| K11 | SG-GKG-GKAGSA**K**AKASQSRSAKAG | +16 | 3.1E-01 | +3 | 2.6E-01 |
| K3K11 | SG**K**GKG-GKAGSA**K**AKASQSRSAKAG | +6 | 8.3E-01 | **+31** | 5.4E-08 |
| K11ΔS15 | SG-GKG-GKAGSA**K**AKA·QSRSAKAG | -7 | 9.2E-02 | +2 | 6.6E-01 |
| ΔGS10 | SG-GKG-GKA··A-AKASQSRSAKAG | -6 | 3.2E-02 | +10 | 3.0E-02 |
| ΔS15 | SG-GKG-GKAGSA-AKA·QSRSAKAG | +3 | 9.4E-02 | **+9** | 9.7E-03 |
| R6 | SG-GKG**R**GKAGSA-AKASQSRSAKAG | -5 | 5.6E-02 | **+10** | 1.0E-03 |
| K20R | SG-GKG-GKAGSA-AKASQSRSA**R**AG | -3 | 3.0E-01 | +7 | 1.5E-02 |
| R17K | SG-GKG-GKAGSA-AKASQS**K**SAKAG | -1 | 7.9E-01 | 0 | 2.7E-01 |
| **Human – HA Tag** | | | | | |
| WT | SGRGKQGGKTRAKAKSRSSRAG | - | 1.0E+00 | - | 1.0E+00 |
| ΔR3 | SG·GKQGGKTRAKAKSRSSRAG | **+39** | 8.3E-03 | **+42** | 1.3E-08 |
| R11K | SGRGKQGGKT**K**AKAKSRSSRAG | **+20** | 2.3E-02 | **+14** | 1.2E-03 |
| R11A | SGRGKQGGKT**A**AKAKSRSSRAG | **+43** | 1.0E-05 | **+21** | 5.7E-07 |
| ΔR3R11A | SG·GKQGGKT**A**AKAKSRSSRAG | **+35** | 3.5E-03 | **+18** | 5.9E-04 |
| **Human – FLAG Tag** | | | | | |
| WT | SGRGKQGGKARAKAKSRSSRAG | - | 1.0E+00 | - | 1.0E+00 |
| Δ1-12 | ·····KAKSRSSRAG | **+47** | 4.9E-03 | **+18** | 2.8E-04 |

- The – marks indicate spacing for sequence alignment purposes. The inserted residues are bold typed and underlined. Deletions are indicated by ·.
- Percent (%) change refers to the difference in median values relative to WT unless otherwise indicated; the statistically significant differences are bold typed. P-values were calculated using the t-test (yeast) and Mann-Whitney U test (human).
- †percent change was calculated relative to isogenic WT control (ΔS15).

To test the effects of H2A NTD changes on chromatin compaction, the physical distance between two probes on chromosome XVI spaced 275 kb apart was assessed in each of the H2A mutants using fluorescent *in situ* hybridization (FISH) (Fig 2-3A) (Bystricky et al., 2004; Guacci

et al., 1997). The probes were differentially labeled and visualized by confocal microscopy. The distance between the probes was measured in a single plane in which both probes were present within each nucleus (Bystricky et al., 2004). When compared to the isogenic wild type (WT), addition of a single arginine at position 3 (R3) or 11 (R11) to the H2A NTD was sufficient to significantly decrease the average interprobe distance by 18% and 15%, respectively (Fig 2-2B-C, Table 2-1). The average interprobe distance was further decreased by 22% when both arginines were present (R3R11) and even more so (30%) in R3(ΔGS10)R11. Deleting G9S10 (ΔGS10) alone caused slightly increased compaction with low statistical significance (Table 2-1). The largest decrease in interprobe distance (41%) was observed in the R11ΔS15 mutant, which places R11 twelve amino acids from the histone fold, the same position as in organisms with large genomes. Removal of S15 (ΔS15) alone had no effect. The effect of arginines was not simply due to increasing the positive charge of the H2A NTD, as insertions of lysines at positions 3 and 11 did not significantly affect the interprobe distances (Fig 2-3C and Table 2-2). Although lysines are found at these positions in certain species (Fig 2-1D), the lack of potential compaction by lysines may be due to the absence of other evolutionary changes in yeast histones (see Fig 2-1E). Additionally, R17K or K20R mutations did not affect compaction, nor did a randomly inserted arginine at position 6 (R6) (Fig 2-3C and Table 2-2), suggesting that not every arginine in the H2A NTD contributes to chromatin compaction.

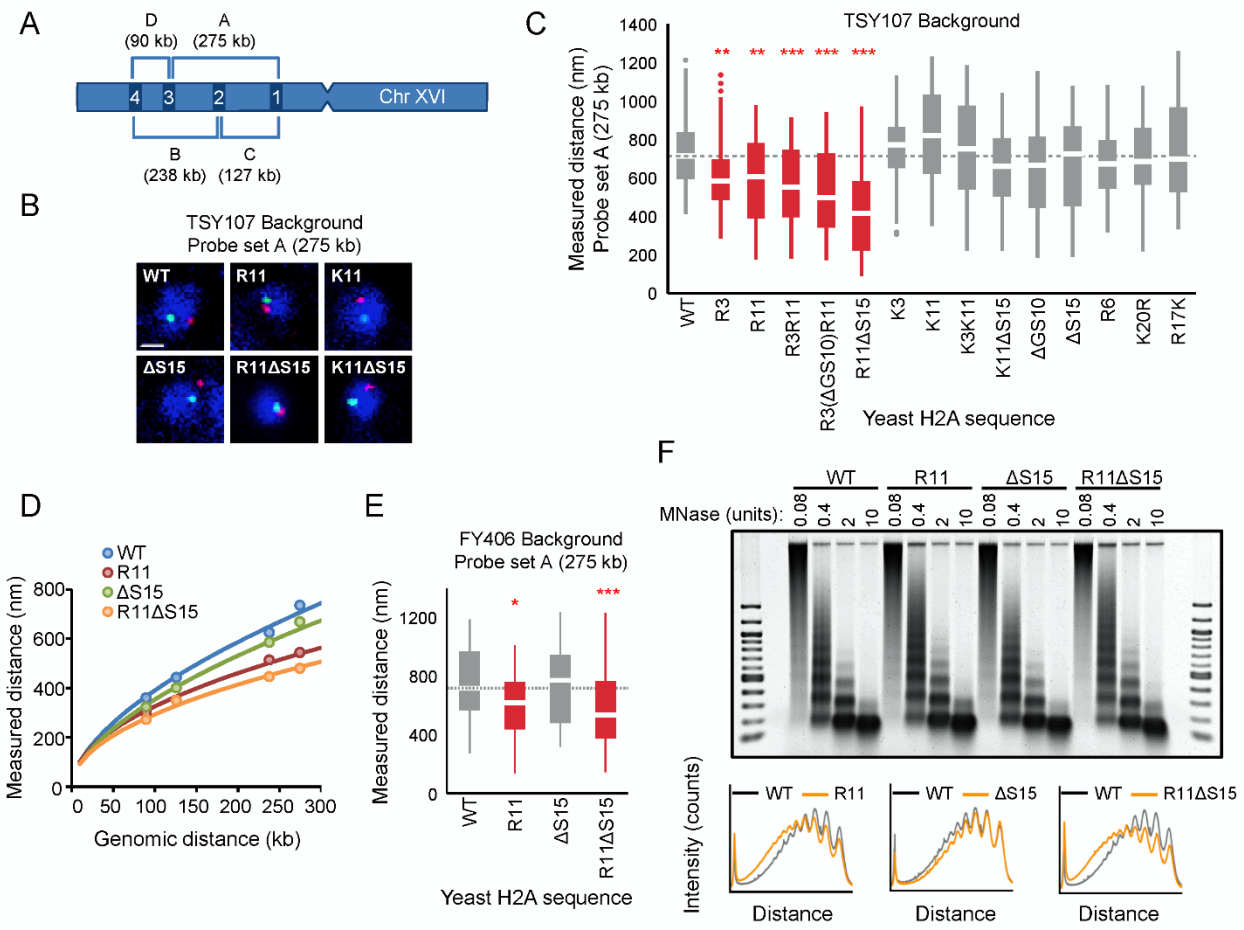


**Figure 2-3: Ectopic expression of H2A NTD arginines causes compaction in yeast.** (**A**) Schematic position of probes on chromosome XVI that were used for FISH. The letters correspond to the probe sets. (**B**) FISH images and (**C**) boxplot of the distributions of interprobe distances for probe set A in the indicated strains. (**D**) The mean interprobe distances for the indicated yeast strains for probe sets A, B, C, and D are plotted as a function of genomic distance. Solid lines are best fit equations. (**E**) Boxplot of the distributions of interprobe distances for probe set A in the indicated strains. Dashed lines mark the median value for the WT strain. The boxplot whiskers contain 90% of the data. All scale bars are 1 μm. Boxes are colored if the mean of the indicated strain is significantly different from WT. Red stars denote level of significance: * $p<0.01$; ** $p<0.001$; *** $p<0.0001$. (**F**) Agarose gel electrophoresis of MNase-digested chromatin in the indicated strains including the densitometric profiles comparing the WT to each of the mutant H2A strains for a given amount of enzyme.

**Table 2-2: Yeast FISH data**

| Yeast FISH - Probe Set A | | | | | | | |
|---|---|---|---|---|---|---|---|
| Strain | nm | | | | % change | p-value | No. cells |
| | Minimum | Maximum | Mean | Median | | | |
| WT | 364 | 1487 | 757 | 714 | 0 | 1.0E+00 | 63 |
| R3 | 178 | 1377 | 619 | 584 | -18 | 9.5E-04 | 90 |
| R11 | 22 | 1101 | 584 | 605 | -23 | 8.6E-04 | 49 |
| R3R11 | 79 | 1102 | 557 | 553 | -26 | 8.2E-06 | 72 |
| R3(ΔGS10)R11 | 107 | 1410 | 516 | 497 | -32 | 2.1E-06 | 51 |
| R11ΔS15 | 67 | 1378 | 455 | 415 | -40 | 3.9E-08 | 57 |
| K3 | 272 | 1378 | 749 | 772 | -1 | 8.6E-01 | 64 |
| K11 | 236 | 1421 | 808 | 820 | 7 | 3.1E-01 | 56 |
| K3K11 | 164 | 1430 | 747 | 751 | -1 | 8.3E-01 | 71 |
| K11ΔS15 | 124 | 1355 | 665 | 659 | -12 | 9.2E-02 | 42 |
| ΔGS10 | 66 | 1084 | 649 | 666 | -14 | 3.2E-02 | 60 |
| ΔS15 | 30 | 1236 | 668 | 726 | -12 | 9.4E-02 | 49 |
| R6 | 106 | 1410 | 674 | 672 | -11 | 5.6E-02 | 73 |
| K20R | 205 | 1539 | 708 | 686 | -6 | 3.0E-01 | 64 |
| R17K | 230 | 1598 | 743 | 699 | -2 | 7.9E-01 | 54 |
| **Yeast FISH - Probe Set B** | | | | | | | |
| WT | 259 | 1372 | 626 | 599 | 0 | 1.0E+00 | 59 |
| R11 | 64 | 1231 | 514 | 476 | -18 | 1.4E-02 | 60 |
| ΔS15 | 88 | 1452 | 586 | 549 | -6 | 2.8E-01 | 53 |
| R11ΔS15 | 66 | 934 | 446 | 433 | -29 | 2.3E-05 | 51 |
| **Yeast FISH - Probe Set C** | | | | | | | |
| WT | 91 | 1192 | 493 | 485 | 0 | 1.0E+00 | 75 |
| R11 | 74 | 1481 | 399 | 349 | -19 | 1.4E-03 | 50 |
| ΔS15 | 153 | 896 | 456 | 437 | -8 | 1.9E-01 | 55 |
| R11ΔS15 | 89 | 925 | 398 | 410 | -19 | 5.4E-03 | 48 |
| **Yeast FISH - Probe Set D** | | | | | | | |
| WT | 65 | 1029 | 361 | 342 | 0 | 1.0E+00 | 85 |
| R11 | 41 | 802 | 299 | 261 | -17 | 4.8E-05 | 70 |
| ΔS15 | 33 | 648 | 323 | 324 | -11 | 8.7E-02 | 51 |
| R11ΔS15 | 16 | 748 | 273 | 237 | -24 | 1.6E-07 | 62 |
| **Yeast (FY406) FISH - Probe Set A** | | | | | | | |
| WT | 172 | 1318 | 728 | 723 | 0 | 1.0E+00 | 80 |
| R11 | 56 | 1158 | 609 | 617 | -16 | 7.5E-03 | 86 |
| ΔS15 | 165 | 1379 | 730 | 766 | 0 | 9.7E-01 | 62 |
| R11ΔS15 | 23 | 1225 | 532 | 512 | -27 | 8.5E-05 | 61 |

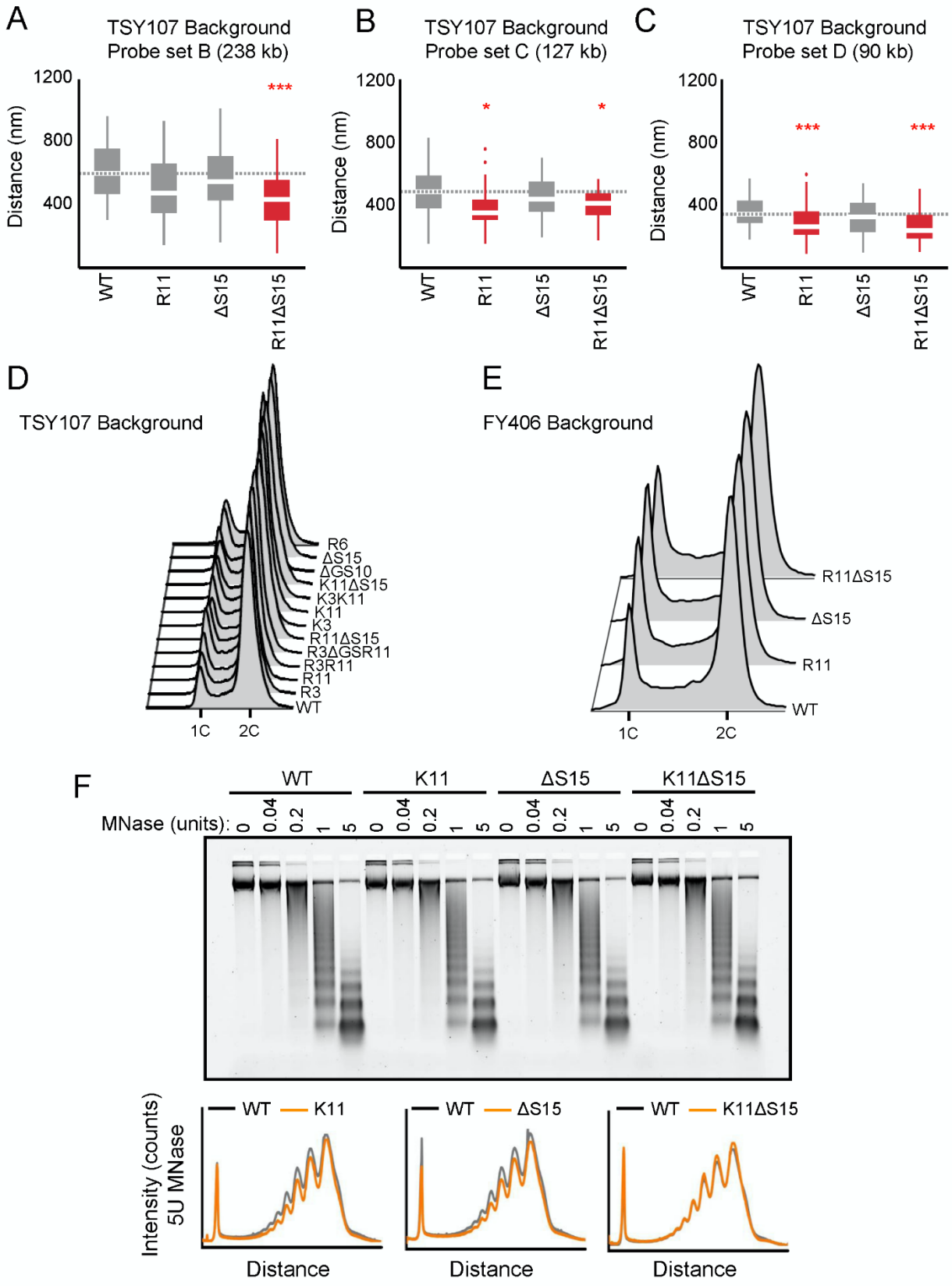
A
TSY107 Background
Probe set B (238 kb)
Distance (nm)
1200
800
400
***
WT
R11
ΔS15
R11ΔS15
B
TSY107 Background
Probe set C (127 kb)
Distance (nm)
1200
800
400
*
*
WT
R11
ΔS15
R11ΔS15
C
TSY107 Background
Probe set D (90 kb)
Distance (nm)
1200
800
400
***
***
WT
R11
ΔS15
R11ΔS15
D
TSY107 Background
R6
ΔS15
ΔGS10
K11ΔS15
K3K11
K11
K3
R11ΔS15
R3ΔGSR11
R3R11
R11
R3
WT
1C
2C
E
FY406 Background
R11ΔS15
ΔS15
R11
WT
1C
2C
F
WT
K11
ΔS15
K11ΔS15
MNase (units): 0 0.04 0.2 1 5 0 0.04 0.2 1 5 0 0.04 0.2 1 5 0 0.04 0.2 1 5
Intensity (counts)
5U MNase
WT K11
WT ΔS15
WT K11ΔS15
Distance
Distance
Distance

**Figure 2-4: Ectopic expression of H2A NTD arginines causes compaction in yeast.** (**A-C**). Boxplot of the distributions of interprobe distances in the indicated H2A mutant strains for probe sets B, C, and D as shown in figure 3A. Boxes are colored if the mean of the indicated strain is significantly different from WT. Red stars denote level of significance: * $p<0.01$; ** $p<0.001$; *** $p<0.0001$. Cell cycle analysis of yeast strains in the TSY107 (**D**) or FY406 (**E**) background. 1C and 2C refer to G1 and G2 DNA content, respectively. Note that the WT strains (TSY107, FY406) carry one copy of the H2A gene on a plasmid with the two chromosomal copies deleted (Hirschhorn et al., 1995; Schuster et al., 1986). Dosage alterations of the H2A protein cause G2/M arrest (Sopko et al., 2006) which is evident in our WT strains. Nonetheless, all the mutants display highly similar cell cycle profiles. (**F**) Agarose gel electrophoresis of MNase-digested chromatin in the indicated strains. The amount of enzyme used to digest chromatin is indicated. Also shown are the densitometric profiles of the agarose gel that compares WT to each of the indicated mutant H2A strains for a given amount of enzyme.

We further confirmed the effects of R11 on chromatin compaction using three additional probe sets (Fig 2-3A). The level of compaction seen in our WT strain is similar to what has been previously reported in yeast using a different strain background (Bystricky et al., 2004). The interprobe distances for all probe sets were significantly decreased in R11 compared to WT and even more so in R11ΔS15 but not ΔS15 alone (Fig 2-4A-C and Table 2-2). Plotting the physical vs. genomic distances for all probe sets revealed uniform compaction across large genomic distances (Fig 2-3D). The effect of R11 on chromatin compaction was not strain-specific as H2A R11 and R11ΔS15, but not ΔS15, caused chromatin compaction in a different strain background (Fig 2-3E; Table 2-2). We therefore conclude that H2A arginines at positions 3 and 11, especially when R11 is placed at the evolutionarily-conserved position relative to the histone fold, increase the degree of chromatin compaction.

Chromatin is differentially compacted at different cell cycle stages (Guacci et al., 1997). Cell cycle profile analysis showed little difference between the strain harboring WT H2A and any of the mutant strains (Fig 2-4D-E), indicating that the observed differences in chromatin compaction are not due to altered cell cycle profiles. Chromatin compaction may also be influenced by nucleosomal spacing; indeed the linker DNA length is larger in human cells than in yeast (Grigoryev, 2012). We find that there are essentially no differences in nucleosomal density

in H2A arginine mutants using Micrococcal Nuclease (MNase) digestion (Fig 2-3F, Fig 2-4F), indicating that the average nucleosomal spacing is not affected by these mutations. But the more compact mutants displayed decreased accessibility to MNase as indicated by the delayed appearance of nucleosomal digestion pattern (Fig 2-3F, Fig 2-4F).

### 2.3.3 H2A arginines and serines affect nuclear volume in yeast

Since chromatin structure may influence volume of the nucleus (Cavalier-Smith, 2005), we asked whether nuclear volume was affected by H2A-mediated chromatin compaction. We tagged a nuclear pore protein, Nup49, in its chromosomal locus with GFP to visualize the nuclear membrane and used confocal microscopy to capture three-dimensional images of the nucleus to quantify volumes of ≥150 cells per H2A mutant (Fig 2-5A-B, Table 2-1, Table 2-3, see Methods for volume calculations). As compared to WT cells, H2A mutants containing R11 or R3R11, both of which contain more compact chromatin, displayed significantly decreased nuclear volumes. The average nuclear volume in the R3 mutant was also less than WT but did not reach statistical significance. Interestingly, H2A mutants from which serines 10 and 15 were removed displayed larger nuclear volumes. Simultaneous insertions of arginines into these strains (R3(ΔGS10)R11 and R11ΔS15) decreased their nuclear volume (R11ΔS15 $p<0.001$ compared to ΔS15), restoring them to levels similar to WT. The control strains with either lysines or R6 had nuclear volumes similar to or larger than WT. Neither arginines nor serines had any effect on total cell size as measured by concanavalin A staining (Fig 2-6A-B, Table 2-3). In the FY406 strain background, ΔS15 did not cause an increase in nuclear volume; and thus both R11 and R11ΔS15 strains exhibited smaller nuclear volumes than isogenic WT (Fig 2-5C, Table 2-3). These data suggest that modulation of chromatin compaction through the H2A NTD, especially in presence of R11, affects the nuclear volume but this effect may be indirect (see human data below).

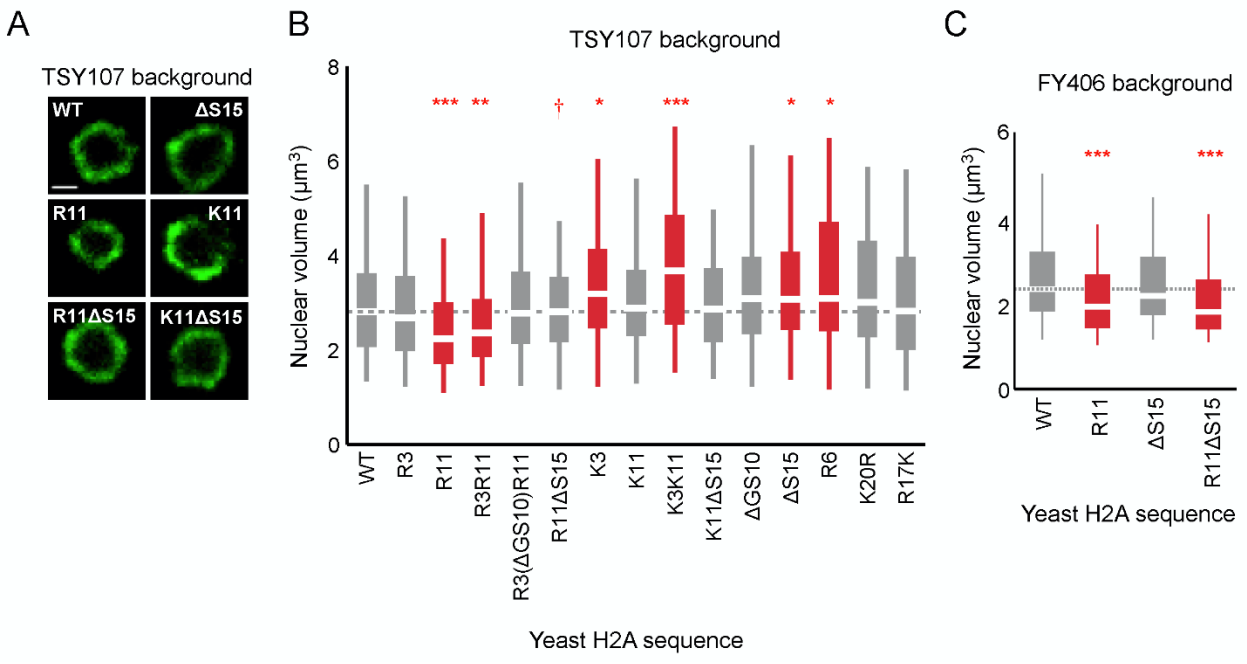


**Figure 2-5: Ectopic expression of H2A NTD arginines decreases nuclear volume in yeast.** (**A**) Images of the nuclear envelope, as visualized by Nup49p-GFP, and boxplot of the distributions of nuclear volumes in the indicated strains in the TSY107 background (**B**) or the FY406 background (**C**). Dashed lines mark the median value for the WT strain. The boxplot whiskers contain 90% of the data. All scale bars are 1 μm. Boxes are colored if the mean of the indicated strain is significantly different from WT. Red stars denote level of significance: * $p<0.01$; ** $p<0.001$; *** $p<0.0001$. Red dagger (†) indicates that mean nuclear volume of R11ΔS15 is significantly smaller than its isogenic WT strain (ΔS15; $p<0.001$).

**Table 2-3: Yeast nuclear and cellular volume data**

| Yeast nuclear volume (TSY107 Background) | | | | | | | |
|---|---|---|---|---|---|---|---|
| Nuclear Vol | $\mu m^3$ | | | | % change | p-value | No. cells |
| | Minimum | Maximum | Mean | Median | | | |
| WT | 0.6 | 6.9 | 2.9 | 2.8 | 0 | 1.0E+00 | 188 |
| R3 | 0.6 | 6.5 | 2.8 | 2.6 | -5 | 4.1E-01 | 177 |
| R11 | 0.7 | 7.0 | 2.3 | 2.1 | -20 | 5.9E-05 | 201 |
| R3R11 | 0.4 | 6.9 | 2.5 | 2.3 | -16 | 3.0E-03 | 180 |
| R3(ΔGS10)R11 | 0.7 | 8.1 | 3.1 | 3.0 | 6 | 3.7E-01 | 196 |
| R11ΔS15 | 0.8 | 6.2 | 2.8 | 2.7 | 0 | 4.2E-01 | 150 |
| K3 | 0.5 | 9.1 | 3.3 | 3.1 | 13 | 9.4E-03 | 181 |
| K11 | 0.7 | 10.8 | 3.2 | 2.9 | 3 | 2.6E-01 | 191 |
| K3K11 | 1.0 | 9.3 | 3.8 | 3.6 | 31 | 5.4E-08 | 172 |
| K11ΔS15 | 0.8 | 8.9 | 3.0 | 2.9 | 2 | 6.6E-01 | 186 |
| ΔGS10 | 0.8 | 12.6 | 3.5 | 3.1 | 10 | 3.0E-02 | 198 |
| ΔS15 | 0.8 | 8.8 | 3.3 | 3.0 | 9 | 9.7E-03 | 202 |
| R6 | 0.8 | 10.3 | 3.4 | 3.1 | 10 | 1.0E-03 | 201 |
| K20R | 0.7 | 9.3 | 3.3 | 3.0 | 7 | 1.5E-02 | 199 |
| R17K | 0.7 | 8.3 | 3.0 | 2.5 | 0 | 2.7E-01 | 199 |
| **Yeast nuclear volume (FY406 Background)** | | | | | | | |
| WT | 1.0 | 5.1 | 2.5 | 2.3 | 0 | 1.0E+00 | 268 |
| R11 | 1.0 | 3.9 | 2.0 | 1.9 | -17 | 7.0E-07 | 195 |
| ΔS15 | 1.0 | 5.0 | 2.4 | 2.1 | -3 | 4.9E-01 | 194 |
| R11ΔS15 | 1.0 | 4.2 | 2.0 | 1.8 | -19 | 1.9E-07 | 191 |
| **Yeast cellular volume (TSY107 Background)** | | | | | | | |
| WT | 11.4 | 92.8 | 46.1 | 42.6 | 0 | 1.0E+00 | 178 |
| R11 | 12.1 | 155.9 | 48.2 | 43.4 | 4 | 2.9E-01 | 199 |
| K11 | 10.7 | 114.1 | 44.2 | 44.2 | -4 | 5.0E-01 | 209 |
| ΔS15 | 13.7 | 123.5 | 47.0 | 47.0 | 2 | 5.0E-01 | 83 |
| R11ΔS15 | 13.0 | 99.5 | 46.0 | 46.0 | 0 | 4.3E-01 | 104 |

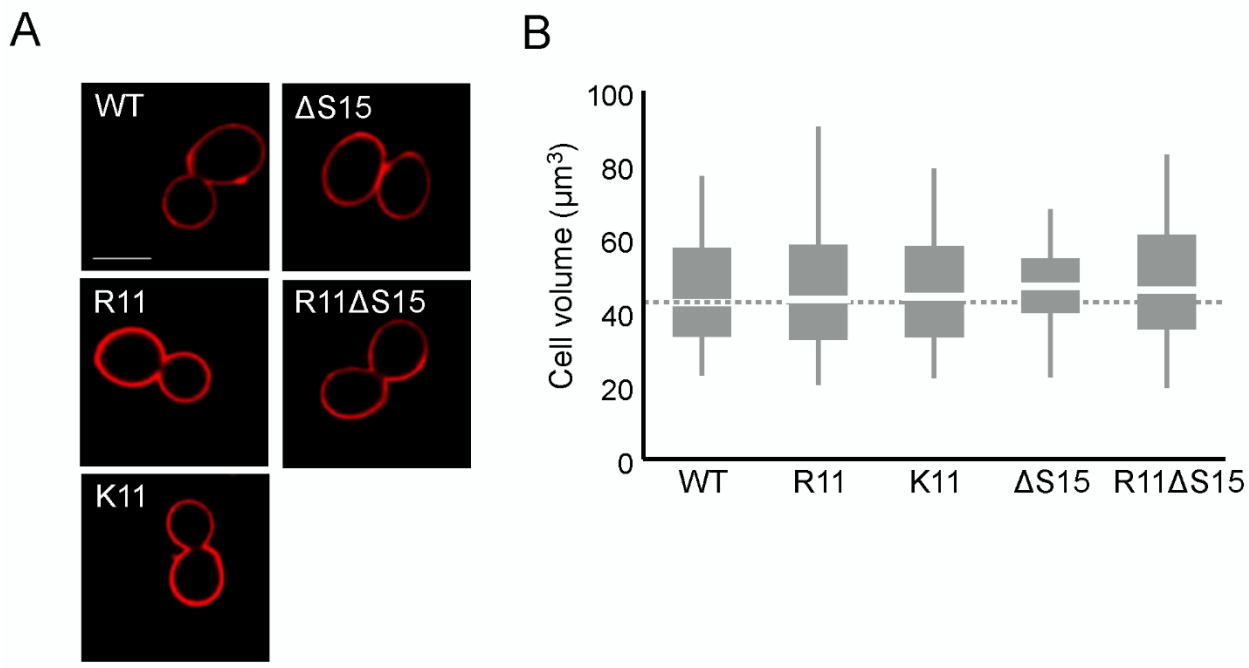


**Figure 2-6: H2A arginines do not affect cell size.** (**A**) Images of the cell wall, as visualized by concanavalin A staining, and (**B**) boxplot of the distributions of cellular volumes in the indicated yeast strains. The scale bar is 5 μm. Boxes are colored if the mean of the indicated strain is significantly different from WT. Red stars denote level of significance: * $p<0.01$; ** $p<0.001$; *** $p<0.0001$.

### 2.3.4 Loss of H2A arginines causes de-compaction of chromatin in human cells

Since the H2A NTD in large genomes contains both R3 and R11, we expected that their removal would cause de-compaction of chromatin. To test this prediction, we ectopically expressed WT or mutant H2A in several human cell lines and measured the distances between probes 0.49 Mbp apart on chromosome 1 by FISH, as well as the largest nuclear cross-sectional areas (see Methods). The H2A gene was HA-tagged and mutated to remove R3 (ΔR3), to replace R11 with alanine (R11A) or lysine (R11K), or to combine two mutations (ΔR3R11A). The H2A constructs were overexpressed using the strong CMV promoter in the normal human IMR90 fibroblasts, the breast cancer cell line MDA-MB-453, or the HEK293 cells. Cells overexpressing ΔR3, R11A, or ΔR3R11A H2A mutants had increased interprobe distances, indicating de-compaction of chromatin. Expression of H2A R11K had modest effects on chromatin de-

compaction with marginal statistical significance (Fig 2-7A-B, Fig 2-8A-B, Table 2-4). Cells expressing any of the H2A mutants displayed larger nuclear areas, suggesting that nuclear size is increased (Fig 2-7C-D, Fig 2-8C-F, Table 2-5). Equal degrees of overexpression were confirmed by immunofluorescence analysis with an anti-HA antibody and detection of HA-H2A by western blotting (Fig 2-7D, Fig 2-8G). Ectopic expression of a C-terminally FLAG-tagged H2A mutant missing residues 1-12 (Δ1-12) also caused significant de-compaction of chromatin and increased nuclear area despite being expressed at a lower level than WT (Fig 2-7E-F). These data demonstrate that consistent with our predictions, the H2A NTD, especially arginines 3 and 11, function to compact chromatin in human cells.

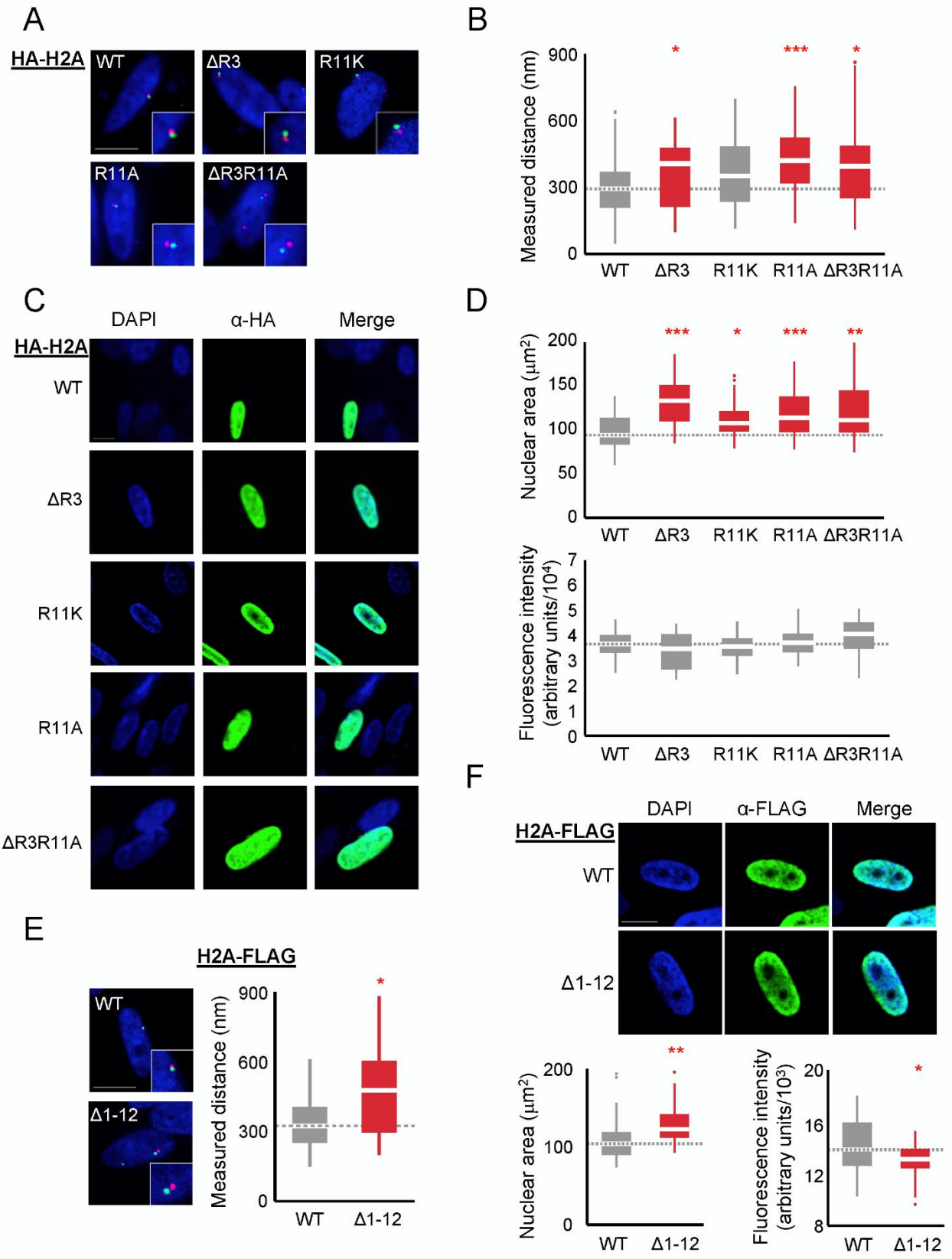
A
HA-H2A
WT
ΔR3
R11K
R11A
ΔR3R11A
B
Measured distance (nm)
900
600
300
0
*
***
*
WT
ΔR3
R11K
R11A
ΔR3R11A
C
DAPI
α-HA
Merge
HA-H2A
WT
ΔR3
R11K
R11A
ΔR3R11A
D
Nuclear area (μm²)
200
150
100
50
0
***
*
***
**
WT
ΔR3
R11K
R11A
ΔR3R11A
Fluorescence intensity (arbitrary units/10⁴)
7
6
5
4
3
2
1
0
WT
ΔR3
R11K
R11A
ΔR3R11A
E
H2A-FLAG
WT
Δ1-12
Measured distance (nm)
900
600
300
0
*
WT
Δ1-12
F
DAPI
α-FLAG
Merge
H2A-FLAG
WT
Δ1-12
Nuclear area (μm²)
200
100
0
**
WT
Δ1-12
Fluorescence intensity (arbitrary units/10³)
20
16
12
8
*
WT
Δ1-12

**Figure 2-7: Loss of H2A NTD arginines decreases chromatin compaction in human cells.** (**A**) FISH images of probes on chromosome 1 in normal primary IMR90 fibroblasts with HA-tagged WT or mutant H2A overexpressed as indicated. (**B**) Boxplot of the distributions of inter-probe distances. Note that R11K was only marginally significant at p=0.023. (**C**) Immunofluorescence images of IMR90 cells overexpressing HA-tagged WT or mutant H2A as indicated. (**D**) Top: Boxplot of the distributions of largest nuclear cross-sectional areas in the indicated H2A overexpressing cells. Bottom: Boxplot of the distributions of α-HA fluorescence intensities. (**E**) Left: FISH images, as in (A), of IMR90 cells expressing a C-terminal FLAG-tagged WT or tailless (Δ1-12) H2A. Right: Boxplot of the distributions of inter-probe distances. (**F**) Top: Immunofluorescence images of IMR90 cells overexpressing FLAG-tagged WT or tailless H2A. Bottom: Boxplot of nuclear areas and fluorescence intensities, as indicated. Dashed lines mark the median value for the WT strain. All scale bars are 10 μm. Boxes are colored if the mean of the indicated strain is significantly different from WT. Red stars denote level of significance: * $p<0.01$; ** $p<0.001$; *** $p<0.0001$.

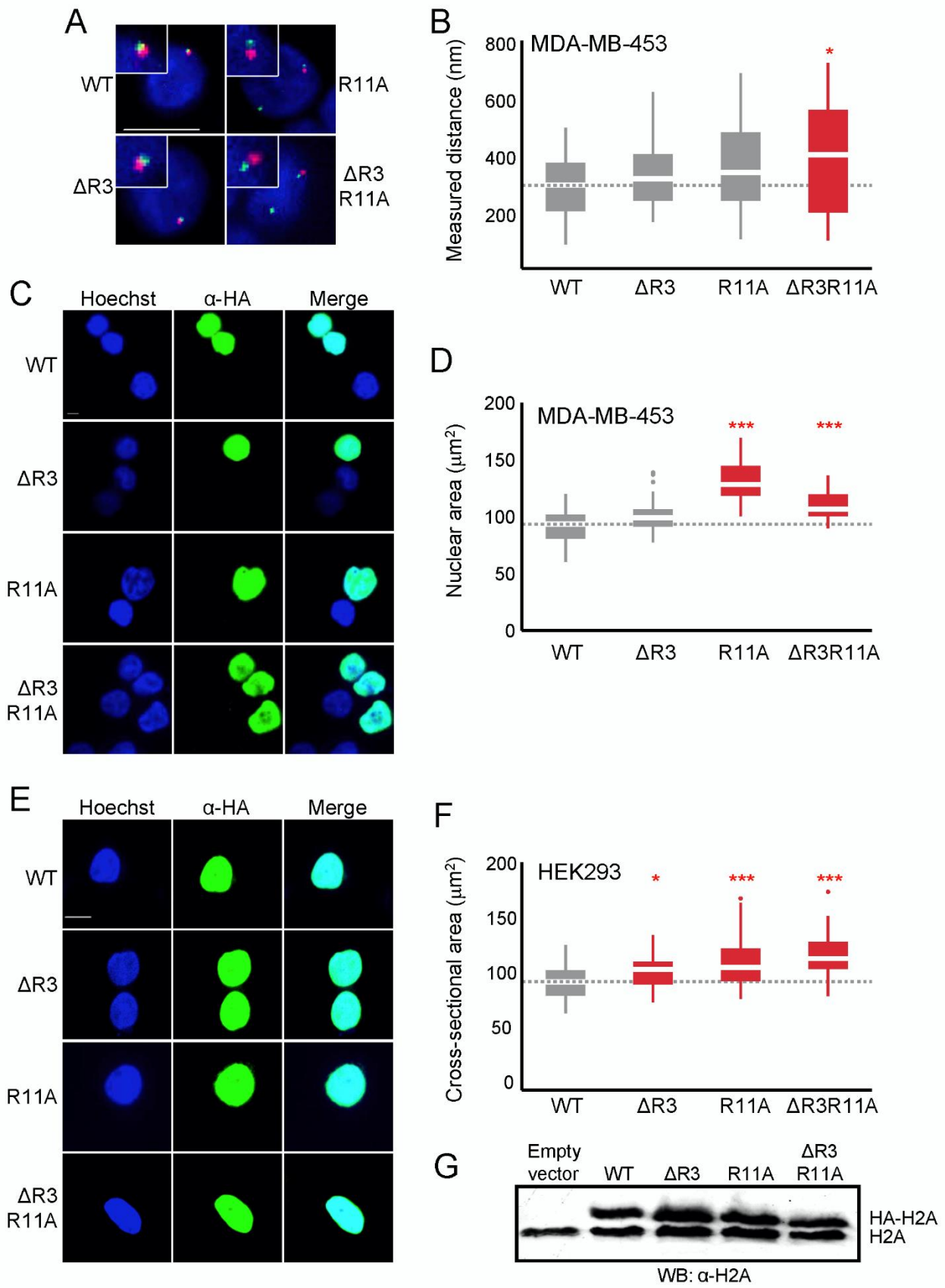
A
WT
R11A
ΔR3
ΔR3 R11A
B
MDA-MB-453
Measured distance (nm)
800
600
400
200
*
WT
ΔR3
R11A
ΔR3R11A
C
Hoechst
α-HA
Merge
WT
ΔR3
R11A
ΔR3 R11A
D
MDA-MB-453
Nuclear area (μm²)
200
150
100
50
0
***
***
WT
ΔR3
R11A
ΔR3R11A
E
Hoechst
α-HA
Merge
WT
ΔR3
R11A
ΔR3 R11A
F
HEK293
Cross-sectional area (μm²)
200
150
100
50
0
*
***
***
WT
ΔR3
R11A
ΔR3R11A
G
Empty vector
WT
ΔR3
R11A
ΔR3 R11A
HA-H2A
H2A
WB: α-H2A

**Figure 2-8: Loss of H2A NTD arginines decreases chromatin compaction in human cells.** (**A**) FISH images of probes on chromosome 1 in MDA-MB-453 cells with either WT or mutant HA-tagged H2A overexpressed. (**B**) Boxplot of the distributions of interprobe distances. Immunofluorescence images of (**C**) MDA-MB-453 or (**E**) HEK293 cells overexpressing WT or mutant HA-tagged H2A. Boxplot of the distributions of largest nuclear cross-sectional areas in (**D**) MDA-MB-453 or (**F**) HEK293 for the indicated H2A over-expressing cells. (**G**) Western blot of lysates from HEK293 cells overexpressing the indicated WT or mutant HA-tagged H2A. All scale bars are 10 μm. Dashed lines mark the median value for the WT strain. Boxes are colored if the mean of the indicated strain is significantly different from WT. Red stars denote level of significance: * $p<0.01$; *** $p<0.0001$.

**Table 2-4: Human FISH data**

| Human FISH – IMR90 cells – HA Tag | | | | | | | |
|---|---|---|---|---|---|---|---|
| IMR90 | nm | | | | % change | p-value | No. cells |
| | Minimum | Maximum | Mean | Median | | | |
| WT | 35 | 1079 | 312 | 293 | 0 | 1.0E+00 | 94 |
| ΔR3 | 57 | 702 | 363 | 406 | 16 | 8.3E-03 | 53 |
| R11K | 90 | 975 | 382 | 351 | 23 | 2.3E-02 | 40 |
| R11A | 28 | 1087 | 437 | 420 | 40 | 1.05E-05 | 62 |
| ΔR3R11A | 70 | 1161 | 420 | 394 | 43 | 3.5E-03 | 54 |
| R11H | 71 | 892 | 399 | 325 | 28 | 1.1E-02 | 52 |
| R11C | 84 | 1138 | 417 | 389 | 34 | 4.4E-04 | 53 |
| R11P | 74 | 1047 | 485 | 460 | 56 | 5.9E-06 | 50 |
| **Human FISH – IMR90 cells – FLAG Tag** | | | | | | | |
| WT | 53 | 1080 | 354 | 324 | 0 | 1.0E+00 | 40 |
| Δ1-12 | 148 | 977 | 481 | 478 | 36 | 4.9E-03 | 39 |
| **Human FISH – MDA-MB-453 cells** | | | | | | | |
| WT | 33 | 745 | 296 | 293 | 0 | 1.0E+00 | 49 |
| ΔR3 | 42 | 740 | 341 | 315 | 15 | 1.9E-01 | 45 |
| R11A | 97 | 793 | 362 | 338 | 22 | 1.7E-02 | 60 |
| ΔR3R11A | 46 | 764 | 388 | 399 | 31 | 5.9E-03 | 35 |

**Table 2-5: Human largest cross-sectional nuclear area data**

| Human nuclear area - IMR90 cells - HA Tag | | | | | | |
|---|---|---|---|---|---|---|
| IMR90 | μm² | | | % change | p-value | No. cells |
| | Minimum | Maximum | Mean | | | |
| WT | 52 | 179 | 99 | 0 | 1.0E+00 | 93 |
| ΔR3 | 73 | 372 | 142 | 43 | 1.3E-08 | 42 |
| R11K | 69 | 182 | 113 | 14 | 1.2E-03 | 64 |
| R11A | 64 | 239 | 121 | 22 | 5.6E-07 | 121 |
| ΔR3R11A | 63 | 379 | 133 | 34 | 5.9E-04 | 40 |
| R11H | 68 | 184 | 104 | 5 | 6.8E-02 | 67 |
| R11C | 53 | 153 | 98 | -1 | 4.1E-01 | 67 |
| R11P | 50 | 220 | 105 | 6 | 3.4E-01 | 67 |
| **Human nuclear area - IMR90 cells - FLAG Tag** | | | | | | |
| WT | 63 | 223 | 114 | 0 | 1.0E+00 | 50 |
| Δ1-12 | 92 | 240 | 131 | 15 | 2.8E-04 | 57 |
| **Human nuclear area - HEK293 cells** | | | | | | |
| WT | 58 | 158 | 96 | 0 | 1.0E+00 | 52 |
| ΔR3 | 65 | 161 | 106 | 10 | 7.0E-03 | 60 |
| R11A | 68 | 231 | 116 | 21 | 4.4E-05 | 65 |
| ΔR3R11A | 76 | 251 | 121 | 26 | 4.6E-07 | 52 |
| **Human nuclear area - MDA-MB-453 cells** | | | | | | |
| WT | 57 | 137 | 92 | 0 | 1.0E+00 | 36 |
| ΔR3 | 67 | 165 | 103 | 12 | 3.0E-02 | 34 |
| R11A | 92 | 172 | 132 | 43 | 4.8E-11 | 33 |
| ΔR3R11A | 78 | 154 | 111 | 21 | 3.1E-05 | 33 |

### 2.3.5 H2A R11 regulates compaction of nucleosomal arrays *in vitro*

Because R11 compacts chromatin *in vivo*, we investigated whether this effect is directly on the chromatin fiber. We used step-wise salt dialysis to assemble nucleosomal arrays with a DNA template containing twelve copies of the 177 bp "601" nucleosome positioning sequence (601-177-12) and recombinant *X. laevis* histone octamers that contain either WT H2A or one with R11 deleted (ΔR11). We assembled nucleosomal arrays at different octamer-to-template ratios (0.9, 1, and 1.1 octamer to 1 template) and monitored the quality of the arrays by $MgCl_2$ precipitation and restriction digest analysis using ScaI. We found that a 1:1 octamer-to-template ratio gave the best results as the ScaI digest demonstrated well assembled arrays compared to the 5% free DNA loaded as a comparison (Fig 2-9A). We used analytical ultracentrifugation to determine the

sedimentation velocity combined with van Holde–Weischet analysis (Weischet et al., 1978) to ascertain the distribution of sedimentation coefficients (S) for each nucleosomal array in the absence or presence of 0.8 mM $MgCl_2$, a concentration of the divalent cation that promotes intra-molecular folding of nucleosomal arrays (Schwarz and Hansen, 1994). In the absence of $Mg^{2+}$, arrays containing WT H2A sedimented with a coefficient of 33.1, which is a value that has been previously shown for similar arrays (Dorigo et al., 2003; Shogren-Knaak et al., 2006; Zhou et al., 2007). In contrast, arrays missing R11 adopted a more extended conformation with a smaller sedimentation coefficient of 31.0 (Fig 2-9B). Addition of $Mg^{2+}$ increased compaction of both arrays and shifted the sedimentation coefficients to 39.3 and 37.4 for WT and ΔR11 H2A, respectively (Fig 2-9B). A second independent chromatin assembly and ultracentrifugation analysis confirmed these results (Fig 2-10). Thus, in the absence of R11 in the H2A NTD, nucleosomal arrays adopt a less compact conformation even in the presence of divalent cations, showing that R11 directly increases chromatin compaction.

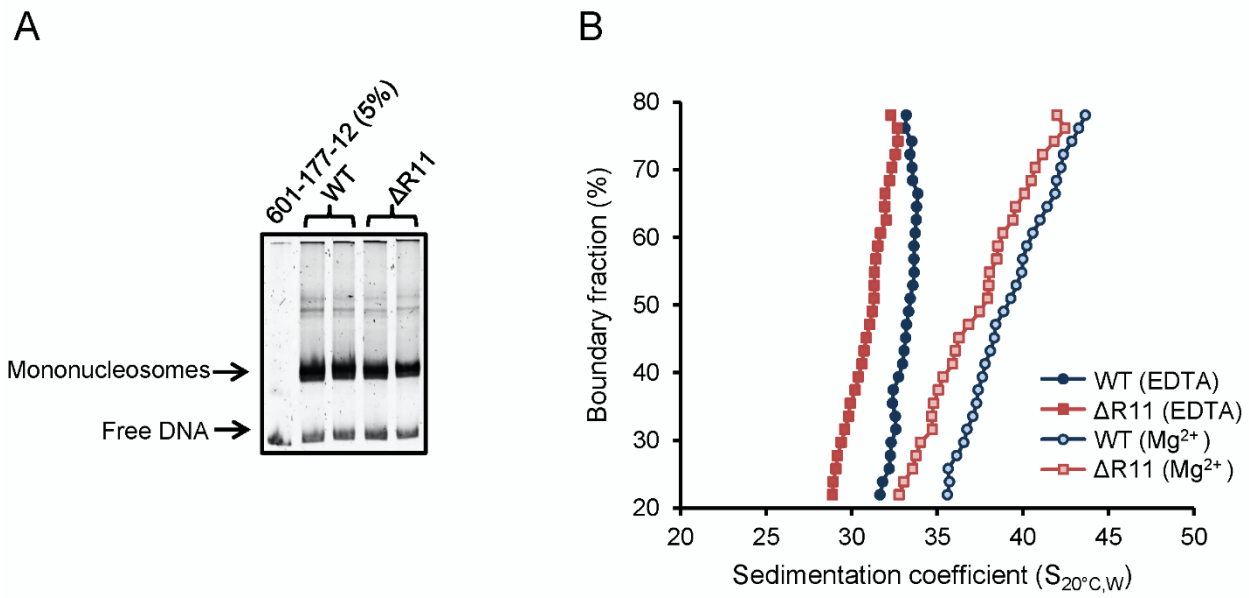


**Figure 2-9: H2A NTD R11 directly modulates the compaction of chromatin fibers *in vitro*.** (**A**) Polyacrylamide gel electrophoresis (PAGE) of ScaI-digested 601-177-12 DNA template assembled with octamers containing recombinant WT or ΔR11 H2A. As a control, 5% of the 601-177-12 DNA without octamers was also digested. (**B**) The distribution of sedimentation coefficients determined by von-Holde Weischet analysis plotted against the percent boundary fraction in the absence or presence of 0.8 mM $MgCl_2$ as indicated. $S_{20°C,W}$ is the sedimentation coefficient corrected to water at 20°C.

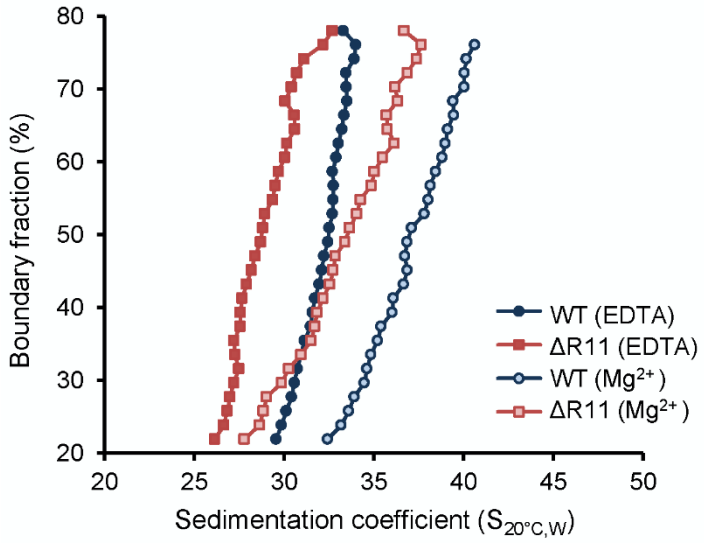


**Figure 2-10: H2A NTD R11 directly modulates the compaction of chromatin fibers *in vitro*.** The distribution of sedimentation coefficients determined by von-Holde Weischet analysis plotted against the percent boundary fraction in absence or presence of 0.6 mM $MgCl_2$ as indicated. $S_{20°C,W}$ is the sedimentation coefficient corrected to water at 20°C.

### 2.3.6. Compaction of chromatin by H2A NTD arginines does not alter global gene expression in yeast

To determine whether chromatin compaction through H2A arginines interferes with transcription regulation, we examined gene expression patterns in the H2A yeast mutants. Remarkably, there was a high level of correlation (≥0.99) between all strains examined (Fig 2-11A), and no specific gene ontology was found among the genes that were differentially expressed by two-fold or more. The expression levels of the histone genes were similar, indicating that altered levels of histone genes expression do not account for the changes in chromatin compaction. These data indicate that compaction of chromatin by H2A does not significantly alter global gene expression in exponentially growing cells.

All strains also showed similar growth rates in rich media (Fig 2-11B) and no significant differences in sensitivity to hydroxyurea, methyl methanesulfonate (MMS), bleomycin, 4-nitroquinoline 1-oxide (4NQO), cycloheximide, and rapamycin, indicating no major defects with DNA replication or repair, protein synthesis, or the TOR signaling pathways (Fig 2-11C). But in competition growth assays in which equal amounts of WT and H2A mutant cells harboring the PGK1 gene fused to either GFP or RFP were co-cultured, the H2A mutants regardless of any effect on chromatin compaction, were outcompeted (Fig 2-11D). This suggests that changes in the H2A NTD sequence can affect the overall fitness of the cell.

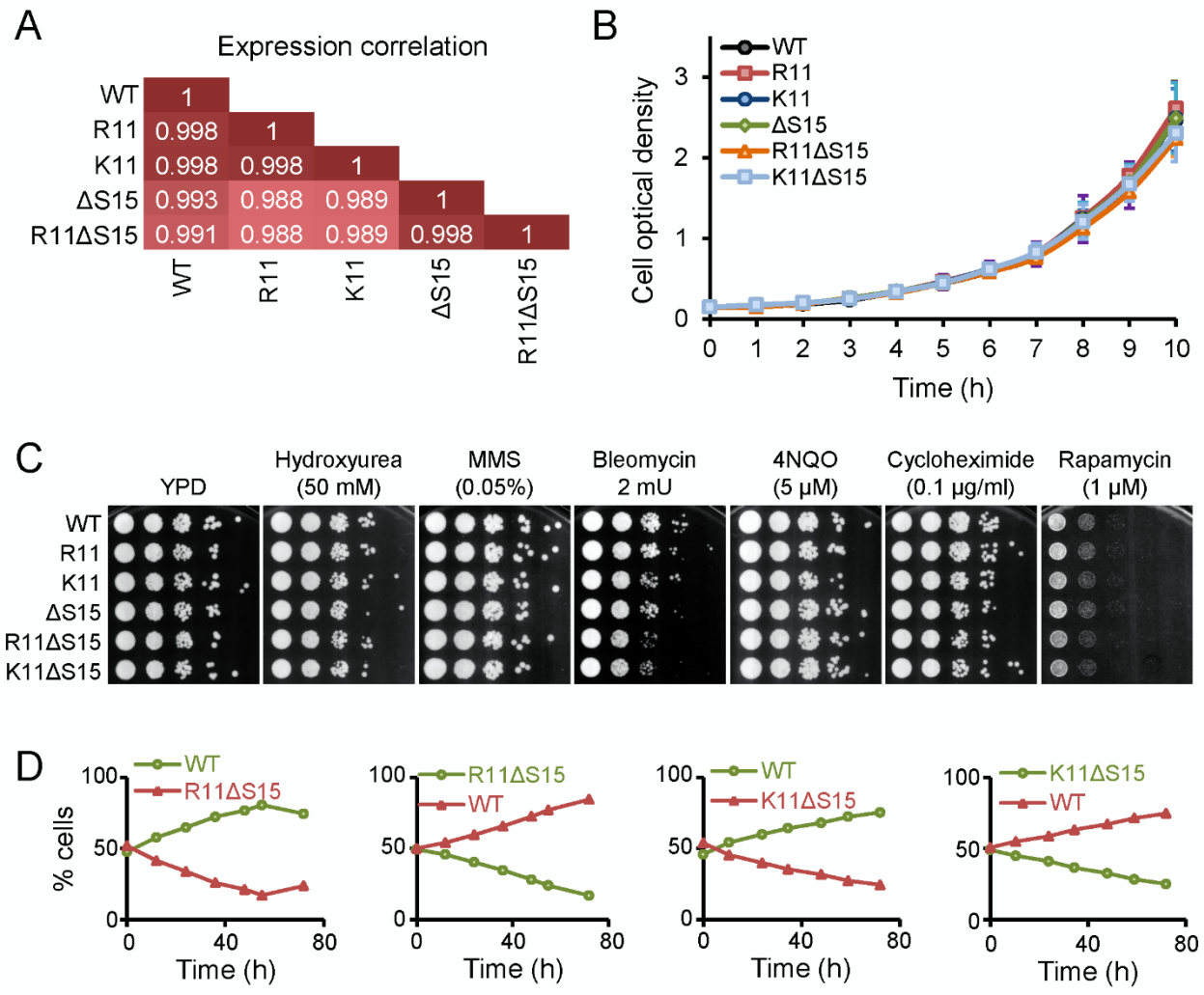


**Figure 2-11: Mutations to H2A NTD decrease the fitness of yeast.** (**A**) Pearson correlations between the global gene expressions of the indicated strains grown in YPD. Correlations are calculated from an average of at least two experiments. (**B**) Growth curves of the indicated H2A yeast strains over 10 hrs in YPD. (**C**) Spot tests with ten-fold serial dilutions for the indicated strains in the presence of different drugs. (**D**) The proportion of yeast cells in a co-culture of WT and the indicated mutant H2A carrying Pgk1 gene fusion to GFP (green) or RFP (red) as indicated by color.

### 2.3.7 H2A NTD arginines and their surrounding residues are mutated in cancer and affect chromatin compaction

Deregulated chromatin compaction is often a pathological hallmark of cancer cells (Edens et al., 2012), although the underlying mechanisms are not well-understood. A survey of the COSMIC database (Forbes et al., 2011), as of the time of writing, revealed 41 documented

missense mutations within the H2A NTD with 29 (71%) affecting a residue within one of the four arginine motifs (Fig 2-12A). R11, which had the strongest effect of any single arginine residue on chromatin compaction, is the most commonly mutated residue in the H2A NTD. We tested the effects of three of these mutations, R11C, H and P, and found that ectopic expression of each in normal human fibroblasts decreases chromatin compaction significantly with R11P having the strongest effect (Fig 2-12B-C). These cancer mutations have little effect on increasing nuclear area, however (Fig 2-12D-E), in contrast to R11A (Fig 2-7D). It is unclear to what extent the H2A mutants have to be expressed in cancer cells relative to the seventeen canonical H2A genes in the human genome to affect chromatin compaction. But our data suggest that over-expression of an H2A mutant has the potential to disrupt chromatin compaction in cancer.

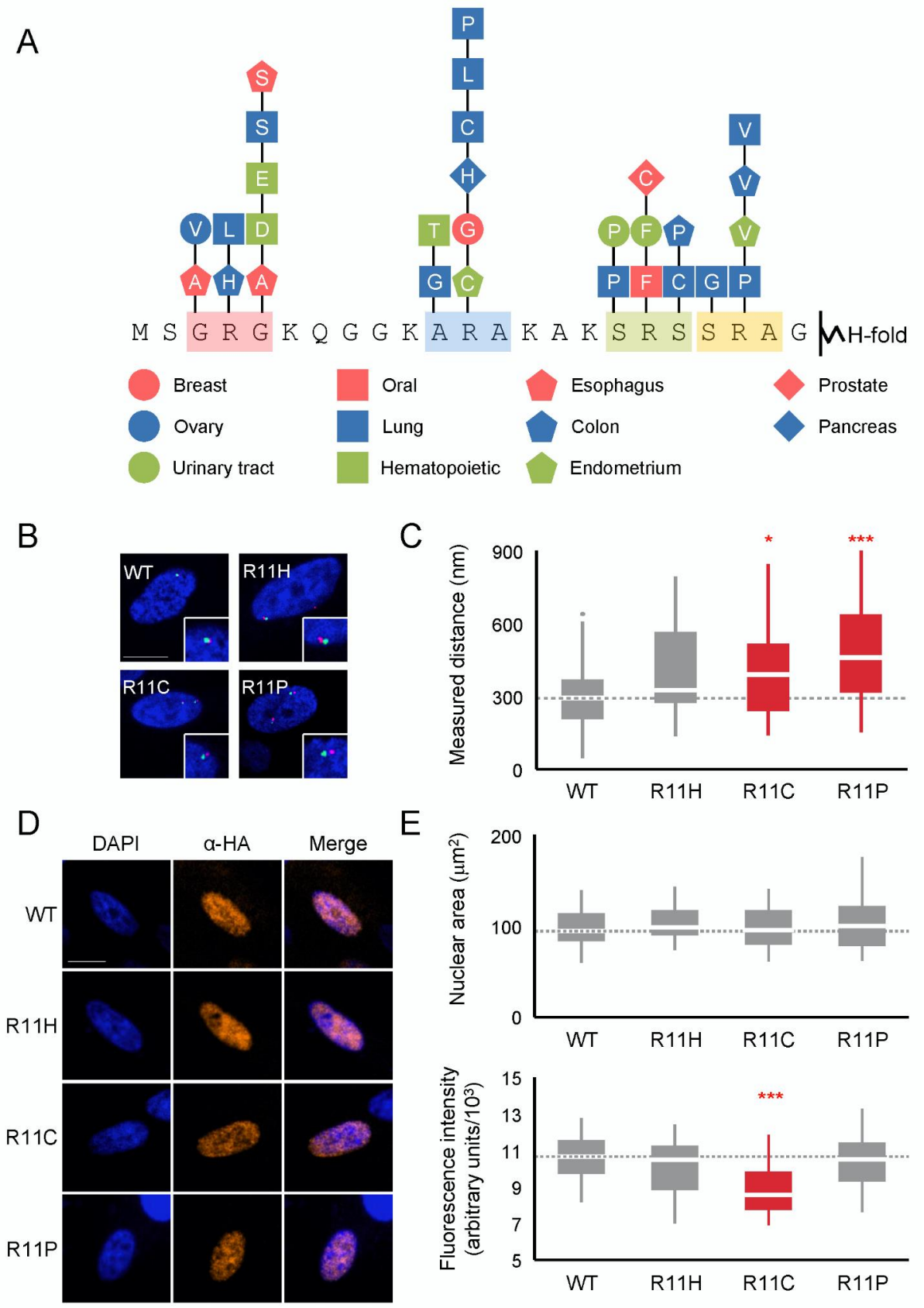
A
M S G R G K Q G G K A R A K A K S R S S R A G
H-fold
Breast
Ovary
Urinary tract
Oral
Lung
Hematopoietic
Esophagus
Colon
Endometrium
Prostate
Pancreas
B
WT
R11H
R11C
R11P
C
Measured distance (nm)
900
600
300
0
*
***
WT
R11H
R11C
R11P
D
DAPI
α-HA
Merge
WT
R11H
R11C
R11P
E
Nuclear area (μm²)
200
100
0
WT
R11H
R11C
R11P
Fluorescence intensity (arbitrary units/10³)
15
13
11
9
7
5
***
WT
R11H
R11C
R11P

**Figure 2-12: Mutations of H2A NTD found in cancers decreases chromatin compaction in human cells.** (**A**) Schematic of the H2A NTD showing only the mutations within the arginine motifs found in various cancers as indicated by the colored shapes (Forbes et al., 2011). The letter within each shape represents the mutated amino acid. (**B**) FISH images of probes on chromosome 1 in normal primary IMR90 fibroblasts with HA-tagged WT or mutant H2A overexpressed as indicated. (**C**) Boxplot of the distributions of inter-probe distances. (**D**) Immunofluorescence images of IMR90 cells overexpressing HA-tagged WT or mutant H2A as indicated. Anti-HA primary and Alexa Fluor 647-conjugated secondary antibodies were used to determine expression in FISH images and for measurement of nuclear areas. (**E**) Top: Boxplot of the distributions of largest nuclear cross-sectional areas in the indicated H2A overexpressing cells. (**F**) Boxplot of the distributions of α-HA fluorescence intensities. Dashed lines mark the median value for the WT strain. All scale bars are 10 μm. Boxes are colored if the mean of the indicated strain is significantly different from WT. Red stars denote level of significance: * $p<0.01$; *** $p<0.0001$.

## 2.4 Discussion

In this study we describe evolutionary adaptations of the histone H2A whereby single arginines in the NTD function to dramatically affect the degree of genome compaction. This mechanism is distinct from several other known chromatin compaction mechanisms in higher eukaryotes (Bednar et al., 1998; Dorigo et al., 2003; Fierz et al., 2011; Shogren-Knaak et al., 2006; Zhou et al., 2007) in that it involves the histone proteins themselves. The H2A-mediated chromatin compaction thus provides a novel but potentially complementary mechanism for genome compaction. Organisms with small genomes but also very small cell size may face similar physical constraints as those with larger genomes, and may therefore use arginine-containing H2A as a means for chromatin compaction. For instance, *Ostreococcus tauri* which possesses an R3-containing H2A, is a free-living unicellular algae that has a very small genome of 12.6 Mbp but a cell diameter of 0.8 μm (Palenik et al., 2007). *S. cerevisiae*, which does not contain an H2A with R3, has a similarly sized genome but has a cell diameter that is approximately five times larger. Furthermore, certain organisms such as *Oikopleura dioica*, which has one of the smallest genomes in animals, have distinctive life cycles and possess H2A genes with and without arginines, which may enable them to dynamically regulate genome compaction at different stages of their life cycles

(Moosmann et al., 2011) (for species with H2A isoforms see attached spreadsheet). So, the H2A arginines may have evolved in circumstances when the genome size became disproportionately large compared to nuclear volume. Interestingly, the toad, *Bufo gargarizans,* which has a genome size that is twice as large as the human genome, possesses an H2A gene with not only R3 and R11 but also glutamine 6 replaced with an arginine, suggesting that additional arginines in the H2A tail may enable further compaction in organisms with even larger genomes.

To better understand the three dimensional positions of the H2A NTD arginines, we examined a crystal structure of the mono-nucleosome in which R3, R11, R17, and R20 were all simultaneously crystalized, and visualized interactions between nucleosomes within the crystal lattice (Davey et al., 2002). Interestingly, while R17 and R20 are more buried within the octamer, R3 and R11 are situated close to the DNA backbone. R3 is at 2.87 Å from the DNA and could potentially bind the DNA gyre as DNA wraps around the histone octamer. R11 forms close contacts with the DNA phosphate backbone of self and neighboring nucleosomes (4.09, 2.90 Å, respectively). Although these interactions may have helped form the crystal lattice, they also suggest a possible mechanism for tighter nucleosomal stacking *in vivo* through shielding of the DNA negative charge (Fig 2-13A-B) (Davey et al., 2002). Thus, the evolutionary appearance of arginines in the H2A NTD sequence at positions 3 and 11 corresponds to strategic positioning of R3 and R11 within the nucleosome structure that may enable interactions with the DNA, leading to more compact chromatin.

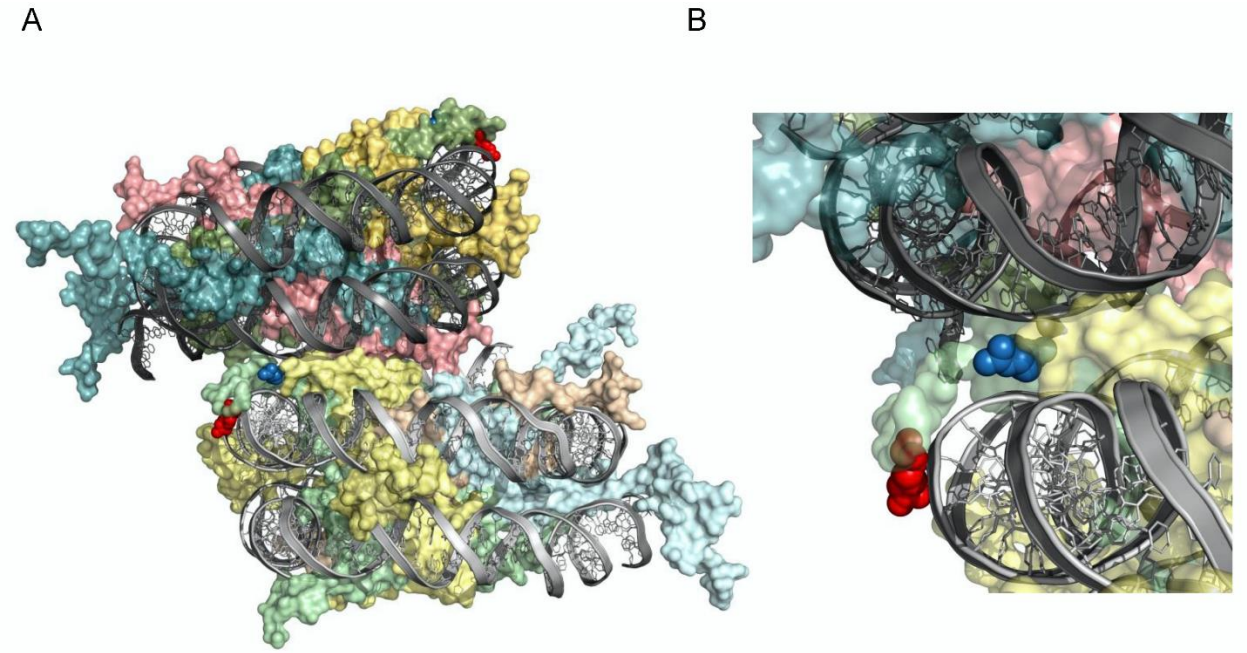


**Figure 2-13: H2A arginines 3 and 11 are situated adjacent to DNA within the nucleosome.** Structure of a di-nucleosome obtained from the crystal lattice of a mono-nucleosome structure is shown from (**A**) the side or (**B**) close up highlighting potential intra- and inter-nucleosomal interactions between arginines and DNA backbone. Green is H2A, yellow is H2B, cyan is H3, and salmon is H4. The red and blue spheres are R3 and R11, respectively, both of which are in chain C (Davey et al., 2002).

Our *in vivo* data in yeast cells demonstrate that interprobe distances shorten in the presence of the H2A arginines R3 and R11. While the mechanism of this shortening is still unknown, the two most likely explanations are due to linear chromosomal compaction or increased chromatin looping (Bohn and Heermann, 2010). However, our data is more consistent with increased linear compaction due to several reasons. First, our analysis of multiple probes along Chr XVI in yeast demonstrates a uniform compaction between all probe pairs examined. Second, our *in vivo* data within human cells lines shows de-compaction of chromatin in the absence of R11. If chromatin looping was the mechanism, loops would have to be disassembled in human nuclei independent of factors such as CTCF and condensin. Third, our *in vitro* data show that R11 alone affects chromatin compaction even in absence of divalent cations. Because the *in vitro* experiments were

performed with unmodified histones in arrays with equal linker lengths, this strongly points to a direct effect of H2A NTD arginines on chromatin compaction that occurs in short arrays. Both R3 and R11 are at contact distances from the DNA, and R11 may also contact the DNA backbone of the neighboring nucleosome (Fig 2-13). These intra- and inter-nucleosomal interactions with the arginines and the DNA may serve to neutralize the negative charge of the DNA backbone, leading to enhanced stacking of nucleosomes and hence increased compaction. Consistent with this model, the other two arginine residues in the H2A NTD, R17 and R20, which are more buried from the surface, do not affect compaction by themselves. However, their functions may be to modulate the effects of the surrounding residues. Although all canonical H2A genes contain R3 and R11 in humans, the cell may still be able to dynamically regulate chromatin compaction by these arginines. For instance, arginines may be subject to posttranslational modifications, such a methylation which makes the arginine residue bulkier, or citrullination which removes the positive charge (Di Lorenzo and Bedford, 2011; Hagiwara et al., 2005; Waldmann et al., 2011; Wang et al., 2001). Interestingly, the H2A NTD is situated in close proximity to the H2B CTD which when ubiquitylated, disrupts chromatin compaction *in vitro* (Fierz et al., 2011), lending support to the ability of this region of the nucleosome to modulate chromatin compaction.

The inability of lysines, especially at position 11, to increase chromatin compaction suggests exquisite structural constraints for H2A-mediated chromatin compaction. Although lysines and arginines both are positively charged, the positive charge of arginine is due to the presence of a guanidinium group which is structurally different from the positive charge of an amino group of a lysine residue. In this regard, it is interesting to note that only arginines contact DNA as it wraps around the nucleosome core (Luger et al., 1997); and arginines preferentially bind the minor groove of DNA compared to lysines (Rohs et al., 2009). The context in which

lysines appear in evolution may be important as well. We did not observe a lysine at position 3 in our list of organisms, and K11 was present in organisms with medium sized genomes and surrounded mainly by the motif VKG (Fig 2-1D-E). When tested in our *S. cerevisiae* strains, K11 was in the context of AKA. So, it is conceivable that additional amino acid changes would be required for lysines in the H2A NTD to increase genome compaction.

The nucleoskeletal theory proposes that chromatin structure influences the shape of the nucleus and thus is a major determinant of nuclear volume (Cavalier-Smith, 2005), although the amount of DNA *per se* does not affect nuclear volume (Neumann and Nurse, 2007). Non-chromatin components such as nuclear import factors from the cytoplasm may also modulate nuclear size (Levy and Heald, 2010). Our data suggest that in particular cases, the effects of H2A NTD mutations on chromatin compaction are linked to nuclear volume, although not in a straightforward relationship. While arginines at positions 3 and 11 increase chromatin compaction and reduce nuclear volume, lysines at the same positions have no effect on chromatin compaction yet increase nuclear volume. Removal of serines at positions 10 or 15 has little effect on compaction but also increase nuclear volume. In human cells, expression of all R11 mutants (R11A, C, H, and P) decreased compaction but only R11A also affected nuclear area. Although we do not observe a clear-cut relationship between nuclear volume and chromatin compaction, our data identify a region of the nucleosome that is directly or indirectly linked to nuclear volume control mechanisms.

Since alterations in chromatin structure often cause changes in transcription (Parra and Wyrick, 2007), we were surprised that mutant H2A-containing yeast had very similar gene expression profiles as WT cells, grew at similar rates, did not have altered cell cycle profiles, and were not sensitive to DNA damaging drugs or environmental challenges. These data raise the

possibility that H2A-mediated compaction of chromatin may have evolved as a mechanism to enable regulation of chromatin compaction without having to make compensatory changes to all other processes that are also based on DNA such as transcription. Nevertheless, it remains to be determined what molecular or cellular processes govern the optimal level of chromatin compaction and nuclear volume for an organism. The stable alterations of chromatin compaction in eukaryotic model organisms through genetic manipulation of H2A should facilitate further experiments to uncover these processes.

## 2.5 Materials and Methods

### Strains and media

The yeast strains used in this study are listed in Table 2-6. Yeast cells were grown in YPD at 30°C unless otherwise noted. C-terminal tagging of yeast proteins was performed as described previously (Longtine et al., 1998). Mammalian cell lines were maintained at 37°C and 5% $CO_2$ and cultured with 10% fetal bovine serum (FBS) and DMEM (Gibco).

**Table 2-6: List of yeast strains used in this study**

| Name | Mutant name | Description | Reference |
|---|---|---|---|
| FLY142 | | *Matα, hta1-1, hta2-1, ura3-52, his3,* pFL142-*HIS3* | Lefant et al., 1996 |
| TSY107 | Parental | *Mat*a, *hta1-1*, *hta2-1*, *ura3-52*, *his3*, pJC102-*URA3* | Schuster et al., 1986 |
| FY406 | Parental | *Mat*a, *(hta1-htb1)Δ::LEU2, (hta2-htb2)Δ::TRP1, pSAB6* | Hirschhorn et al., 1995 |
| AOY001 | WT | *Mat*a, *hta1-1*, *hta2-1*, *ura3-52*, *his3*, pFL142-*HIS3* | this study |
| AOY002 | R3 | *Mat*a, *hta1-1*, *hta2-1*, *ura3-52*, *his3*, pR3-*HIS3* | this study |
| AOY004 | R11 | *Mat*a, *hta1-1*, *hta2-1*, *ura3-52*, *his3*, pR11-*HIS3* | this study |
| AOY005 | K3 | *Mat*a, *hta1-1*, *hta2-1*, *ura3-52*, *his3*, pK3-*HIS3* | this study |
| AOY009 | K20R | *Mat*a, *hta1-1*, *hta2-1*, *ura3-52*, *his3*, pK20R-*HIS3* | this study |
| AOY011 | R17K | *Mat*a, *hta1-1*, *hta2-1*, *ura3-52*, *his3*, pR17K-*HIS3* | this study |
| AOY013 | K11 | *Mat*a, *hta1-1*, *hta2-1*, *ura3-52*, *his3*, pK11-*HIS3* | this study |
| AOY014 | K3K11 | *Mat*a, *hta1-1*, *hta2-1*, *ura3-52*, *his3*, pK3K11-*HIS3* | this study |
| AOY015 | R3R11 | *Mat*a, *hta1-1*, *hta2-1*, *ura3-52*, *his3*, pR3R11-*HIS3* | this study |
| AOY020 | R6 | *Mat*a, *hta1-1*, *hta2-1*, *ura3-52*, *his3*, pR6-*HIS3* | this study |
| AOY022 | ΔGS10 | *Mat*a, *hta1-1*, *hta2-1*, *ura3-52*, *his3*, pΔGS10-*HIS3* | this study |
| AOY023 | R3(ΔGS10)R11 | *Mat*a, *hta1-1*, *hta2-1*, *ura3-52*, *his3*, pR3Δ(GS)R11-*HIS3* | this study |
| AOY024 | ΔS15 | *Mat*a, *hta1-1*, *hta2-1*, *ura3-52*, *his3*, pΔS15-*HIS3* | this study |

| | | | |
|---|---|---|---|
| AOY025 | R11ΔS15 | *Mat*a, *hta1-1*, *hta2-1*, *ura3-52*, *his3*, pR11ΔS15-*HIS3* | this study |
| AOY029 | K11ΔS15 | *Mat*a, *hta1-1*, *hta2-1*, *ura3-52*, *his3*, pK11ΔS15-*HIS3* | this study |
| BBY011 | WT | *Mat*a, *(hta1-htb1)Δ::LEU2, (hta2-htb2)Δ::TRP1, pJH55* | this study |
| BBY013 | ΔS15 | *Mat*a, *(hta1-htb1)Δ::LEU2, (hta2-htb2)Δ::TRP1, pΔS15* | this study |
| BBY022 | R11 | *Mat*a, *(hta1-htb1)Δ::LEU2, (hta2-htb2)Δ::TRP1, pR11* | this study |
| BBY023 | R11ΔS15 | *Mat*a, *(hta1-htb1)Δ::LEU2, (hta2-htb2)Δ::TRP1, pR11ΔS15* | this study |
| BMY003 | Parental | *Mat*a, *hta1-1*, *hta2-1*, *ura3-52*, *his3*, *Nup49-GFP(kanMX6)*, pJC102-*URA3* | this study |
| BMY004 | WT | *Mat*a, *hta1-1*, *hta2-1*, *ura3-52*, *his3*, *Nup49-GFP(kanMX6)*, pFL142-*HIS3* | this study |
| BMY005 | R3 | *Mat*a, *hta1-1*, *hta2-1*, *ura3-52*, *his3*, *Nup49-GFP(kanMX6)*, pR3-*HIS3* | this study |
| BMY007 | R11 | *Mat*a, *hta1-1*, *hta2-1*, *ura3-52*, *his3*, *Nup49-GFP(kanMX6)*, pR11-*HIS3* | this study |
| BMY008 | K3 | *Mat*a, *hta1-1*, *hta2-1*, *ura3-52*, *his3*, *Nup49-GFP(kanMX6)*, pK3-*HIS3* | this study |
| BMY012 | K20R | *Mat*a, *hta1-1*, *hta2-1*, *ura3-52*, *his3*, *Nup49-GFP(kanMX6)*, pK20R-*HIS3* | this study |
| BMY014 | R17K | *Mat*a, *hta1-1*, *hta2-1*, *ura3-52*, *his3*, *Nup49-GFP(kanMX6)*, pR17K-*HIS3* | this study |
| BMY016 | K11 | *Mat*a, *hta1-1*, *hta2-1*, *ura3-52*, *his3*, *Nup49-GFP(kanMX6)*, pK11-*HIS3* | this study |
| BMY017 | K3K11 | *Mat*a, *hta1-1*, *hta2-1*, *ura3-52*, *his3*, *Nup49-GFP(kanMX6)*, pK3K11-*HIS3* | this study |
| BMY018 | R3R11 | *Mat*a, *hta1-1*, *hta2-1*, *ura3-52*, *his3*, *Nup49-GFP(kanMX6)*, pR3R11-*HIS3* | this study |
| BMY038 | R6 | *Mat*a, *hta1-1*, *hta2-1*, *ura3-52*, *his3*, *Nup49-GFP(kanMX6)*, pR6-*HIS3* | this study |
| BMY039 | ΔS15 | *Mat*a, *hta1-1*, *hta2-1*, *ura3-52*, *his3*, *Nup49-GFP(kanMX6)*, pΔS15-*HIS3* | this study |
| BMY040 | ΔGS10 | *Mat*a, *hta1-1*, *hta2-1*, *ura3-52*, *his3*, *Nup49-GFP(kanMX6)*, pΔGS10-*HIS3* | this study |
| BMY041 | R3(ΔGS10)R11 | *Mat*a, *hta1-1*, *hta2-1*, *ura3-52*, *his3*, *Nup49-GFP(kanMX6)*, pR3ΔGS10R11-*HIS3* | this study |
| BMY043 | R11ΔS15 | *Mat*a, *hta1-1*, *hta2-1*, *ura3-52*, *his3*, *Nup49-GFP(kanMX6)*, pR11ΔS15-*HIS3* | this study |
| BMY045 | K11ΔS15 | *Mat*a, *hta1-1*, *hta2-1*, *ura3-52*, *his3*, *Nup49-GFP(kanMX6)*, pK11ΔS15-*HIS3* | this study |
| BMY501 | WT | *Mat*a, *hta1-1*, *hta2-1*, *ura3-52*, *his3*, *Pgk1-GFP(kanMX6)*, pFL142-*HIS3* | this study |
| BMY502 | R11 | *Mat*a, *hta1-1*, *hta2-1*, *ura3-52*, *his3*, *Pgk1-GFP(kanMX6)*, pR11-*HIS3* | this study |
| BMY503 | ΔS15 | *Mat*a, *hta1-1*, *hta2-1*, *ura3-52*, *his3*, *Pgk1-GFP(kanMX6)*, pΔS15-*HIS3* | this study |
| BMY504 | R11ΔS15 | *Mat*a, *hta1-1*, *hta2-1*, *ura3-52*, *his3*, *Pgk1-GFP(kanMX6)*, pR11ΔS15-*HIS3* | this study |
| BMY505 | K11 | *Mat*a, *hta1-1*, *hta2-1*, *ura3-52*, *his3*, *Pgk1-GFP(kanMX6)*, pK11-*HIS3* | this study |
| BMY509 | K11ΔS15 | *Mat*a, *hta1-1*, *hta2-1*, *ura3-52*, *his3*, *Pgk1-GFP(kanMX6)*, pK11ΔS15-*HIS3* | this study |
| BMY511 | WT | *Mat*a, *hta1-1*, *hta2-1*, *ura3-52*, *his3*, *Pgk1-RFP(kanMX6)*, pFL142-*HIS3* | this study |

| | | | |
|---|---|---|---|
| BMY512 | R11 | *Mat*a, *hta1-1, hta2-1, ura3-52, his3, Pgk1-RFP(kanMX6),* pR11-*HIS3* | this study |
| BMY513 | ΔS15 | *Mat*a, *hta1-1, hta2-1, ura3-52, his3, Pgk1-RFP(kanMX6),* pΔS15-*HIS3* | this study |
| BMY514 | R11ΔS15 | *Mat*a, *hta1-1, hta2-1, ura3-52, his3, Pgk1-RFP(kanMX6),* pR11ΔS15-*HIS3* | this study |
| BMY515 | K11 | *Mat*a, *hta1-1, hta2-1, ura3-52, his3, Pgk1-RFP(kanMX6),* pK11-*HIS3* | this study |
| BMY519 | K11ΔS15 | *Mat*a, *hta1-1, hta2-1, ura3-52, his3, Pgk1-RFP(kanMX6),* pK11ΔS15-*HIS3* | this study |

**Histone sequence database construction and analysis**

Sequences were initially extracted from the Entrez database using a keyword search for "histone", and removing non-histone sequences by using keyword searches such as "histone-like", "ubiquitin", and "acetyl", yielding 54,646 results. Blast 2.0 (Camacho et al., 2009) was used to align the sequences against the highly conserved histone fold region of the four core histones from *H. sapiens*. Thresholds for true hits were set at >35% identity match and >90% overlap match with the histone fold globular domain region. All duplicate sequences were removed, and further sequence comparisons were made for histone H3 and H2A sequences to filter variants within them. The canonical sequence datasets comprised 672 sequences for histone H3, 357 sequences for histone H4, 518 sequences for histone H2B, and 435 sequences for histone H2A. To further select one canonical sequence for a species among isotypes and variants when annotation was missing, the sequences were compared to the canonical *H. sapiens* and *S. cerevisiae* sequence, and the sequence with highest similarity was selected. Using only completely sequenced species, the final histone sequence dataset included canonical sequences for 160 species from plants, fungi, protozoa, and animals, with genome sizes ranging from 8 to 5600 Mbp.

Sequences for the four core histones were subsequently split into the N-terminal tail, globular domain, and C-terminal tail (in the case of H2A and H2B) sub-sequences. For discovery of patterns of residue changes according to genome size, each of the sub-sequences was further

sub-grouped into small (<100 Mbp), medium (100-1000 Mbp), and large (>1000 Mbp) genome sizes. The frequency of the amino acid residues in each sequence in the sub-groups was determined, and a p-value for the comparison between sub groups was obtained using a Mann-Whitney U Test. Multiple sequence alignment profiles were created using the Muscle sequence comparison tool from Embl-EBI (Edgar, 2004a, b). Weblogo3 (Crooks et al., 2004; Schneider and Stephens, 1990) was used for motif discovery. Heat maps for residue positions were constructed using Cluster 3.0 (de Hoon et al., 2004) and Java Treeview(Saldanha, 2004).

**Yeast H2A mutagenesis**

Site directed mutagenesis was performed using the QuickChange Lightning kit (Agilent) on the pFL142 plasmid. Table 2-7 contains all the plasmids that were used and constructed in this study. The sequences of primers are listed in Table 2-8. The correct mutation was verified by sequencing.

**Table 2-7: List of yeast plasmids used in this study**

| Name | Description | Reference |
|---|---|---|
| pFL142 | *CEN6, ARSH4, HIS3, HTA1* | Lefant et al., 1996 |
| pR3 | *CEN6, ARSH4, HIS3, hta1-R3* | this study |
| pR11 | *CEN6, ARSH4, HIS3, hta1-R11* | this study |
| pK3 | *CEN6, ARSH4, HIS3, hta1-K3* | this study |
| pK11 | *CEN6, ARSH4, HIS3, hta1-K11* | this study |
| pK3K11 | *CEN6, ARSH4, HIS3, hta1-K3K11* | this study |
| pR3R11 | *CEN6, ARSH4, HIS3, hta1-R3R11* | this study |
| pR6 | *CEN6, ARSH4, HIS3, hta1-R6* | this study |
| pΔGS10 | *CEN6, ARSH4, HIS3, hta1-ΔG9ΔS10* | this study |
| pR3ΔGSR11 | *CEN6, ARSH4, HIS3, hta1-R3ΔG9ΔS10R11* | this study |
| pΔS15 | *CEN6, ARSH4, HIS3, hta1-ΔS15* | this study |
| pR11ΔS15 | *CEN6, ARSH4, HIS3, hta1-R11ΔS15* | this study |
| pK11ΔS15 | *CEN6, ARSH4, HIS3, hta1-K11ΔS15* | this study |
| pR3ΔS10R11ΔS15 | *CEN6, ARSH4, HIS3, hta1-R3 ΔS10R11ΔS15* | this study |

**Table 2-8: List of oligonucleotides used in this study**

| Name | Sequence |
|---|---|
| R3_f | CATACATATAAAATATAAAATGTCCGGTAGAGGTAAAGGTGGTAAAGCTGGTT CAGCTGCTAAAGC |
| R3_r | ACCGGACATTTTATATTTTATATGTATGAAATTTGTTTGTTTTGAAGTTG |

| | |
|---|---|
| R11_f | GTGGTAAAGCTGGTTCAGCTAGAGCTAAAGCTTCTCAATCTAG |
| R11_r | AGCTGAACCAGCTTTACCACCTTTACCACCGGAC |
| R6_f | GTCCGGTGGTAAAGGTAGAGGTAAAGCTGGTTCAGC |
| R6_r | GCTGAACCAGCTTTACCTCTACCTTTACCACCGGAC |
| K3_f | CATACATATAAAATATAAAATGTCCGGTAAAGGTAAAGGTGGTAAAGCTGGTTC |
| K11_f | GTGGTAAAGCTGGTTCAGCTAAAGCTAAAGCTTCTCAATCTAG |
| R3R11_f | CATACATATAAAATATAAAATGTCCGGTAGAGGTAAAGGTGGTAAAGCTGGTTCAGCTAGAGCTAAAGC |
| R3R11_r | AGCTGAACCAGCTTTACCACCTTTACCTC |
| K3K11_f | CATACATATAAAATATAAAATGTCCGGTAAAGGTAAAGGTGGTAAAGCTGGTTCAGCTAAAGCTAAAGCTTC |
| ΔGS10_f | GTAAAGGTGGTAAAGCTGCTGCTAAAGCTTCTC |
| ΔGS10_r | GAGAAGCTTTAGCAGCAGCTTTACCACCTTTAC |
| R3ΔGS10R11_f | GTAAAGGTGGTAAAGCTGCTAGAGCTAAAGCTTCTC |
| R3ΔGS10R11_r | GAGAAGCTTTAGCTCTAGCAGCTTTACCACCTTTAC |
| ΔS15_f | CAGCTGCTAAAGCTCAATCTAGATCTGC |
| ΔS15_r | GCAGATCTAGATTGAGCTTTAGCAGCTG |
| R11ΔS15_f | GGTAAAGCTGGTTCAGCTAGAGCTAAAGCTCAATCTAGATCTGCTAAGGC |
| R11ΔS15_r | GCCTTAGCAGATCTAGATTGAGCTTTAGCTCTAGCTGAACCAGCTTTACC |
| K11ΔS15_f | GGTAAAGCTGGTTCAGCTAAAGCTAAAGCTCAATCTAGATCTGCTAAGGC |
| K11ΔS15_r | GCCTTAGCAGATCTAGATTGAGCTTTAGCTTTAGCTGAACCAGCTTTACC |
| R3ΔS10R11ΔS15_f | GTAAAGGTGGTAAAGCTGGTGCTAGAGCTAAAGCTCAATCTAGATCTGCTAAG |
| R3ΔS10R11ΔS15_r | CTTAGCAGATCTAGATTGAGCTTTAGCTCTAGCACCAGCTTTACCACCTTTAC |
| Probe2_P1_f | CTCGTCCTCTGAACCAAAGC |
| Probe2_P1_r | ACCACATCGTTGTCCTCACA |
| Probe2_P2_f | TGACGAGCCATCTTTGTCAG |
| Probe2_P2_r | CCAGTAGGCGGTTGAATGTT |
| Probe2_P3_f | AGTGGAAACCACCGTTTCTG |
| Probe2_P3_r | CACTAGCGGCAGTTGATTGA |
| H2A_dR3_f | GAGATATACATATGTCAGGAGGCAAACAAGGCGG |
| H2A_dR3_r | CCGCCTTGTTTGCCTCCTGACATATGTATATCTC |
| H2A_dR11_f | ACAAGGCGGTAAAACCGCTAAGGCCAAGACTC |
| H2A_dR11_r | GAGTCTTGGCCTTAGCGGTTTTACCGCCTTGT |
| H2A_R11A_f | CAAGGCGGTAAAACCGCCGCTAAGGCCAAGAC |
| H2A_R11A_r | GTCTTGGCCTTAGCGGCGGTTTTACCGCCTTG |
| H2A_R11K_f | CAAACAAGGCGGTAAAACCAAGGCTAAGGCCAAGACTCGCT |
| H2A_R11K_r | AGCGAGTCTTGGCCTTAGCCTTGGTTTTACCGCCTTGTTTG |
| H2A_Δ1-12_f | CCGAGGAGATCTGCCGCCGCGATCGCCATGAAGGCCAAGTCGCGCTCGTCCCGCGCTGGCCT |
| H2A_Δ1-12_r | AGGCCAGCGCGGGACGAGCGCGACTTGGCCTTCATGGCGATCGCGGCGGCAGATCTCCTCGG |
| F_H2A_wt_EcoRI | GGCCCGAATTCTCTCAGGAAGAGGCAAACAAGGCGG |
| F_H2AdelR3_EcoRI | GGCCCGAATTCTCTCAGGAGGCAAACAAGGCGG |

| | |
|---|---|
| R_H2A_NotI | TTACAGTCTGCGGCCGCCTATCACTTGCTCTTGGCCGACTTG |

**Measurement of yeast nuclear volume**

Yeast strains were generated that contained a C-terminally tagged Nup49p-GFP fusion. Cells were grown in rich medium to 0.6-0.8x$10^7$ cells/mL, fixed in growth medium with 4% paraformaldehyde for 15 min at room temperature, washed twice in PBS, and mounted on a poly-L-lysine-coated slide with mounting medium (Vector Labs). Z-stacks were obtained as described in the microscopy imaging section, and GFP excitation was achieved at 488 nm. Resulting z-stack images were de-convolved using a constrained iterative algorithm from SlideBook 5.0 software and nuclear volumes were measured by masking the inside of each nucleus, which were delineated by the GFP signal. The resulting mask was used to calculate volumes through the SlideBook software. Statistical analysis was performed using the Student's t-test.

**Measurement of yeast cellular volume**

Yeast strains were grown in rich medium to 0.6-0.8x$10^7$ cells/mL, fixed in growth medium with 4% paraformaldehyde for 15 min at room temperature, washed twice in PBS, and stained with a 1:50 dilution of concanavalin A conjugated with tetramethylrhodamine (Invitrogen) for 15 min at room temperature. Cells were washed twice in PBS, once in water, and mounted on a poly-L-lysine-coated slide with mounting medium. Z-stacks were obtained as described in the microscopy imaging with mRFP excitation. Cell volume was measured by masking the inside of the RFP signal as described in measurement of yeast nuclear volume.

**FISH probes**

For yeast FISH analysis, DNA templates for probes 1, 3, and 4 came from ATCC cosmids 71042, 70912, and 70982 as described elsewhere (Guacci et al., 1994). DNA templates for Probe 2 were obtained by PCR amplification of a 10kb region starting at coordinate 364647 of chromosome 16 using three primer pairs (Probe2_P1, Probe2_P2, Probe2_P3, Table 2-8). All

DNA templates were digested to smaller fragments using Sau3a (NEB). Fragments were directly labeled using BioPrime labeling kit (Invitrogen) with either ChromaTide Alexa Fluor 488-5-dUTP or ChromaTide Alexa Fluor 568-5-dUTP (Invitrogen).

For human cell FISH analysis, DNA templates for probes came from BACS RP11-252L24 and RP11-195J4 spaced 0.488 Mb apart on chromosome 1. Each BAC was digested into smaller fragments using Sau3a and fragments were directly labeled using BioPrime labeling kit with either ChromaTide Alexa Fluor 488-5-dUTP or ChromaTide Alexa Fluor 568-5-dUTP, as described above.

**Fluorescent *in-situ* hybridization analysis in yeast**

Yeast strains were grown in rich medium to 0.6-0.8x$10^7$ cells/mL and fixed in growth medium with 4% paraformaldehyde for 15 min at room temperature. Cells were then washed twice in growth medium and re-suspended in 2 mL of EDTA-KOH (0.1 M, pH 8.0) and 10 mM DTT and incubated for 10 min shaking at 30°C. Cells were spun down and re-suspended in 2 mL of YPD + 1.2 M sorbitol with 50 µg/mL of Zymolyase 100-T (Sunrise Science) and 400 U/mL of lyticase (Sigma) and incubated at 30°C for 16 min with shaking. Spheroblasts were then washed twice in YPD + 1.2 M sorbitol and transferred to a poly-L-lysine-coated slide. After settling for 5 min, excess liquid was aspirated away and slides were allowed to air dry for 5 additional min. Slides were washed in methanol for 10 min and then acetone for 30 sec before air drying. Cells were then dehydrated in a series of cold ethanol washes (70%, 80%, 90%, 100%, 1 min each) and allowed to air dry. Denaturing solution (70% deionized formamide, 2x SSC) was added to the slide and cells were denatured at 75°C for 7-10 min. Slides were immediately put through another cold ethanol dehydration series and allowed to air dry. Hybridization solution (50% deionized formamide, 2x SSC, 10% dextran sulfate, 100 ng/µL salmon sperm DNA) containing fresh probes

was added to the slide and the probes were hybridized for 40-48 hours at 37°C. Slides were then washed in two 5 min washes in 0.05x SSC at 48°C and washed twice in BT Buffer (0.15 M NaHCO3 pH 7.5, 0.1% Tween) for 5 min at room temperature. Mounting medium containing DAPI was added to the slides and a coverslip was sealed with nail polish.

Inter-probe distances were measured in single projections as described elsewhere (Bystricky et al., 2004) by finding the pixel distance between weighted centers of the green signal and red signal and converted to nm by the appropriate factor.

**Microscopy imaging**

A 3i Marianas SDC confocal microscope equipped with a Zeiss AxioObserver Z1 with a 100×/1.45 NA objective and Yokogawa CSU-22 confocal head was used. Images were captured by a Hamamatsu EMCCD C9100-13 camera controlled by Slidebook 5.5. DAPI, GFP, mRFP, and Far-red images were acquired by excitation at 360 nm, 488 nm, 561 nm, and 640 nm from a high-speed AOTF laser launch line. A step size of 0.3 (yeast) or 0.5 (human) µm was used for z-stack acquisition.

**Micrococcal nuclease digestion**

Micrococcal nuclease (MNase) digestions were performed on exponentially growing yeast cells as described previously, except that the enzyme was obtained from Sigma-Aldrich (Sigma-Aldrich)(Rando, 2010).

**RNA expression analysis**

RNA was extracted from exponentially growing yeast as described previously(Schmitt et al., 1990). PolyA-RNA was prepared, labeled and hybridized to Affymetrix Gene ChIP Yeast Genome 2.0 array by the UCLA clinical microarray core facility and data normalized according to

manufacturer's indications. The data are accessible at Gene Expression Omnibus with accession number GSE50440.

**DNA template and histone preparation for *in vitro* studies**

A plasmid containing 12 tandem 177 bp repeats of the high affinity 601 sequence was obtained from Craig L. Peterson's laboratory (Shogren-Knaak et al., 2006). DNA arrays were prepared as described previously (Luger et al., 1999). After excision with EcoRV, the arrays were gel purified. QuikChange Lightning Site-Directed Mutagenesis (Agilent) was used to create H2A ΔR11 using primers as listed in Table 2-8. Recombinant *X. laevis* histones were expressed in bacteria and purified as described previously (Luger et al., 1999). Equimolar amounts of all histones were co-folded to form octamers. Intact octamers were purified from aggregates and free H2A-H2B dimers using Pharmacia Superdex 200 gel filtration column.

**Nucleosome array assembly**

Recombinant histone octamers and the 601-177-12 DNA template (Lowary and Widom, 1998) were combined in stoichiometric amounts where 1.0 equivalent of histone octamers and 1.0 equivalents of DNA template were mixed in 2.0 M NaCl. Nucleosome arrays were assembled by step-wise salt dialysis in decreasing NaCl concentration: 1.6 M, 1.2 M, 1.0 M, 0.6 M, 0.4 M, 0.1 M and 0.025 M (in 10 mM Tris pH 8.0, 0.25 mM EDTA), followed by exchanges with 2.5 mM NaCl and 10 mM Tris pH 8.0 without EDTA. Each dialysis step was performed at 4°C for 4 hr to overnight. Partially assembled chromatin was eliminated by precipitation in 4.0 mM $MgCl_2$(Dorigo et al., 2003). The extent of array saturation was assessed by ScaI digestion (200 ng total DNA/chromatin, 3 units ScaI, 50 mM NaCl, 50 mM Tris pH 7.4, 0.5 mM $MgCl_2$), performed for 16 hrs at room temperature followed by 1 hr at 37°C, and subsequent analysis using a 5% native polyacrylamide gel (Luger et al., 1999).

**Analytical ultracentrifugation**

Nucleosome arrays were allowed to equilibrate at room temperature in buffer (2.5 mM NaCl, 10 mM Tris-HCl pH 8.0) containing either 0.1 mM EDTA or 0.6 and 0.8 mM $MgCl_2$. Samples were centrifuged at 20,000 RPM on a Beckman Optima XL-I analytical ultracentrifuge using an An60 Ti rotor after a 1 hr equilibration at 20°C under vacuum. Time-dependent sedimentation was monitored at 260 nm. Boundaries were analyzed by the method of van Holde and Weichet (Hansen and Turgeon, 1999; Weischet et al., 1978).

**Combined immunofluorescence and fluorescent *in-situ* hybridization in human cells**

N-terminally HA-tagged WT H2A of *X. laevis* was cloned by PCR into mammalian expression vector pCMV-HA (Clontech) between EcoRI and NotI sites. C-terminally Myc-FLAG-tagged human H2A, in a mammalian expression vector, was obtained from OriGene (RC200688). Site directed mutagenesis was performed using the QuickChange Lightning kit (Agilent) on these expression plasmids. Human cells (HEK293, IMR90 and MDA-MB-453) were grown on glass coverslips in 24-well plates in DMEM containing 10% fetal bovine serum and transfected with the indicated H2A expression plasmids using BioT transfection reagent (Bioland Scientific) or Lipofectamine LTX with Plus reagent (Life Technologies). Cells were grown for 48 hrs post-transfection. For immunofluorescence only, transfected cells were fixed with ice-cold methanol for 15 min at -20°C followed by washing with PBS-T. For combined immunofluorescence and FISH, transfected cells were fixed with 4% paraformaldehyde in PBS for 10 min at room temperature followed by washing with PBS. Cells were then permeabilized in 0.5% Triton X-100 in PBS for 10 min at room temperature followed by washing with PBS. Cells were blocked in 5% BSA and incubated with anti-HA antibody (1:250 dilution, Abcam, ab9110) or anti-FLAG antibody (1:1000 dilution, Sigma F1804). Cells were washed and incubated with secondary

antibody (1:500 Alexa Fluor 488 goat anti-rabbit, Invitrogen, A11008, 1:250 Alexa Fluor 647 goat anti-rabbit, Invitrogen, A21245, 1:500 Alexa Fluor 488 goat anti-mouse, Invitrogen, A11001, or 1:100 Alexa Fluor 647 goat anti-mouse, Invitrogen, A21235). For immunofluorescence, cells were washed and then incubated with Hoechst stain (0.001 mg/mL in PBS). After final washes, cover slips were mounted and imaged. Fluorescence was visualized as above except with the use of 63X magnification.

For FISH, cells were washed, following secondary antibody incubation, in CSK buffer (100 mM NaCl, 300 mM sucrose, 3mM $MgCl_2$, 10 mM PIPES pH 6.8) and permeabilized in CSKT buffer (CSK+0.5% Triton X-100) before being fixed for 10 min in 4% paraformaldehyde in PBS at room temperature. Cells were immediately put through a cold ethanol dehydration series (5 min each at 85%, 95%, and 100%) and allowed to air dry. Cells were rehydrated in 2x SSC for 5 min and then RNase-treated for 30 min at 37°C in a humid chamber. Cells were washed with 2x SSC, and denatured at 80°C for 15-20 min with 70% deionized formamide and 2x SSC. They were immediately cooled with cold 2x SSC, and put through another cold ethanol dehydration series. Probes were added to cells and allowed to hybridize for 48 hrs. After hybridization, cells were washed with 50% formamide in 2x SSC, 2x SSC, and 1x SSC containing DAPI. Slides were mounted, imaged, and analyzed as described above. Nuclear staining, in H2A-expressing cells, was used to measure lengths of the long and short orthogonal nuclear axes. Estimated nuclear cross-sectional area was calculated using the following formula: Area = $(D_1/2)*(D_2/2)*\pi$, where $D_1$ and $D_2$ are long and short axis lengths, respectively.

**Competition assays**

Two sets of yeast strains were generated in which Pgk1p was C-terminally fused with either GFP or RFP (Table 2-6). GFP-labeled WT H2A strains were co-cultured with RFP-labeled mutant

H2A strains at a 1:1 ratio and at an optical density of ~0.4. Corresponding co-cultures with switched fluorescent labels were also made. Cultures were incubated at 30°C for 72 hours and were diluted every 6-12 hrs to maintain cells in exponential growth phase. Samples were collected every 12 hrs for analysis by flow cytometry. Collected cells were fixed in 70% ethanol, washed and re-suspended in 50 mM sodium citrate, pH 7.0, and mildly sonicated to disrupt aggregates. GFP- and RFP- labeled cells were counted using a Becton Dickinson FACScan cytometer, and the proportion of each in the population was calculated.

**Cell cycle analysis**

Cell cycle analysis of exponentially growing cells was performed essentially as described previously (Zou et al., 1997), except that cells were stained with 1 μM SYTOX Green (Molecular Probes).

**Spot tests**

Approximately $1.0x10^7$ exponentially growing yeast cells were collected and re-suspended in 100 μl of $H_2O$ and 10-fold serially diluted. Subsequently, 5 μl were spotted on agar plates containing media and drugs as indicated in the figures and incubated at 30°C for 2-6 days.

## 2.6 References


Bao, Y., Konesky, K., Park, Y.-J., Rosu, S., Dyer, P.N., Rangasamy, D., Tremethick, D.J., Laybourn, P.J., and Luger, K. (2004). Nucleosomes containing the histone variant H2A. Bbd organize only 118 base pairs of DNA. The EMBO journal *23*, 3314-3324.

Bednar, J., Horowitz, R.A., Grigoryev, S.A., Carruthers, L.M., Hansen, J.C., Koster, A.J., and Woodcock, C.L. (1998). Nucleosomes, linker DNA, and linker histone form a unique structural motif that directs the higher-order folding and compaction of chromatin. Proceedings of the National Academy of Sciences *95*, 14173-14178.

Bohn, M., and Heermann, D.W. (2010). Diffusion-driven looping provides a consistent framework for chromatin organization. PLoS One *5*, e12218.

Bystricky, K., Heun, P., Gehlen, L., Langowski, J., and Gasser, S.M. (2004). Long-range compaction and flexibility of interphase chromatin in budding yeast analyzed by high-resolution imaging techniques. Proceedings of the National Academy of Sciences of the United States of America *101*, 16495-16500.

Camacho, C., Coulouris, G., Avagyan, V., Ma, N., Papadopoulos, J., Bealer, K., and Madden, T. (2009). BLAST+: architecture and applications. BMC bioinformatics *10*, 421.

Carruthers, L.M., Bednar, J., Woodcock, C.L., and Hansen, J.C. (1998). Linker histones stabilize the intrinsic salt-dependent folding of nucleosomal arrays: mechanistic ramifications for higher-order chromatin folding. Biochemistry *37*, 14776-14787.

Caterino, T.L., and Hayes, J.J. (2010). Structure of the H1 C-terminal domain and function in chromatin condensation This paper is one of a selection of papers published in a Special Issue entitled 31st Annual International Asilomar Chromatin and Chromosomes Conference, and has undergone the Journal's usual peer review process. Biochemistry and Cell Biology *89*, 35-44.

Cavalier-Smith, T. (2005). Economy, speed and size matter: evolutionary forces driving nuclear genome miniaturization and expansion. Annals of Botany *95*, 147-175.

Celeste, A., Petersen, S., Romanienko, P.J., Fernandez-Capetillo, O., Chen, H.T., Sedelnikova, O.A., Reina-San-Martin, B., Coppola, V., Meffre, E., and Difilippantonio, M.J. (2002). Genomic instability in mice lacking histone H2AX. Science Signaling *296*, 922.

Chandrasekharan, M.B., Huang, F., and Sun, Z.-W. (2009). Ubiquitination of histone H2B regulates chromatin dynamics by enhancing nucleosome stability. Proceedings of the National Academy of Sciences *106*, 16686-16691.

Crooks, G.E., Hon, G., Chandonia, J.-M., and Brenner, S.E. (2004). WebLogo: a sequence logo generator. Genome research *14*, 1188-1190.

Davey, C.A., Sargent, D.F., Luger, K., Maeder, A.W., and Richmond, T.J. (2002). Solvent mediated interactions in the structure of the nucleosome core particle at 1.9 Å resolution. Journal of molecular biology *319*, 1097-1113.

de Hoon, M.J., Imoto, S., Nolan, J., and Miyano, S. (2004). Open source clustering software. Bioinformatics *20*, 1453-1454.

Di Lorenzo, A., and Bedford, M.T. (2011). Histone arginine methylation. FEBS letters *585*, 2024-2031.

Dorigo, B., Schalch, T., Bystricky, K., and Richmond, T.J. (2003). Chromatin fiber folding: requirement for the histone H4 N-terminal tail. Journal of molecular biology *327*, 85-96.

Dorigo, B., Schalch, T., Kulangara, A., Duda, S., Schroeder, R.R., and Richmond, T.J. (2004). Nucleosome arrays reveal the two-start organization of the chromatin fiber. Science *306*, 1571-1573.

Duan, Z., Andronescu, M., Schutz, K., McIlwain, S., Kim, Y.J., Lee, C., Shendure, J., Fields, S., Blau, C.A., and Noble, W.S. (2010). A three-dimensional model of the yeast genome. Nature *465*, 363-367.

Edens, L.J., White, K.H., Jevtic, P., Li, X., and Levy, D.L. (2012). Nuclear size regulation: from single cells to development and disease. Trends in cell biology.

Edgar, R.C. (2004a). MUSCLE: a multiple sequence alignment method with reduced time and space complexity. BMC bioinformatics *5*, 113.

Edgar, R.C. (2004b). MUSCLE: multiple sequence alignment with high accuracy and high throughput. Nucleic acids research *32*, 1792-1797.

Eskeland, R., Leeb, M., Grimes, G.R., Kress, C., Boyle, S., Sproul, D., Gilbert, N., Fan, Y., Skoultchi, A.I., and Wutz, A. (2010). Ring1B compacts chromatin structure and represses gene expression independent of histone ubiquitination. Molecular cell *38*, 452-464.

Fan, Y., Nikitina, T., Zhao, J., Fleury, T.J., Bhattacharyya, R., Bouhassira, E.E., Stein, A., Woodcock, C.L., and Skoultchi, A.I. (2005). Histone H1 depletion in mammals alters global chromatin structure but causes specific changes in gene regulation. Cell *123*, 1199-1212.

Fierz, B., Chatterjee, C., McGinty, R.K., Bar-Dagan, M., Raleigh, D.P., and Muir, T.W. (2011). Histone H2B ubiquitylation disrupts local and higher-order chromatin compaction. Nature chemical biology *7*, 113-119.

Fischle, W., Tseng, B.S., Dormann, H.L., Ueberheide, B.M., Garcia, B.A., Shabanowitz, J., Hunt, D.F., Funabiki, H., and Allis, C.D. (2005). Regulation of HP1–chromatin binding by histone H3 methylation and phosphorylation. Nature *438*, 1116-1122.

Forbes, S.A., Bindal, N., Bamford, S., Cole, C., Kok, C.Y., Beare, D., Jia, M., Shepherd, R., Leung, K., and Menzies, A. (2011). COSMIC: mining complete cancer genomes in the Catalogue of Somatic Mutations in Cancer. Nucleic acids research *39*, D945-D950.

Fussner, E., Ching, R.W., and Bazett-Jones, D.P. (2011). Living without 30nm chromatin fibers. Trends in biochemical sciences *36*, 1-6.

Gordon, F., Luger, K., and Hansen, J.C. (2005). The core histone N-terminal tail domains function independently and additively during salt-dependent oligomerization of nucleosomal arrays. Journal of Biological Chemistry *280*, 33701-33706.

Grigoryev, S. (2012). Nucleosome spacing and chromatin higher-order folding. Nucleus *3*, 9-15.

Guacci, V., Hogan, E., and Koshland, D. (1994). Chromosome condensation and sister chromatid pairing in budding yeast. The Journal of cell biology *125*, 517-530.

Guacci, V., Koshland, D., and Strunnikov, A. (1997). A direct link between sister chromatid cohesion and chromosome condensation revealed through the analysis of MCD1 in S. cerevisiae. Cell *91*, 47.

Hagiwara, T., Hidaka, Y., and Yamada, M. (2005). Deimination of histone H2A and H4 at arginine 3 in HL-60 granulocytes. Biochemistry *44*, 5827-5834.

Hansen, J.C., and Turgeon, C.L. (1999). Analytical ultracentrifugation of chromatin. In Chromatin Protocols (Springer), pp. 127-141.

Hirschhorn, J.N., Bortvin, A.L., Ricupero-Hovasse, S.L., and Winston, F. (1995). A new class of histone H2A mutations in Saccharomyces cerevisiae causes specific transcriptional defects in vivo. Molecular and cellular biology *15*, 1999-2009.

Kim, J., Guermah, M., McGinty, R.K., Lee, J.-S., Tang, Z., Milne, T.A., Shilatifard, A., Muir, T.W., and Roeder, R.G. (2009). RAD6-Mediated transcription-coupled H2B ubiquitylation directly stimulates H3K4 methylation in human cells. Cell *137*, 459-471.

Kouzarides, T. (2007). Chromatin modifications and their function. Cell *128*, 693-705.

Levy, D.L., and Heald, R. (2010). Nuclear Size Is Regulated by Importin α and Ntf2 in Xenopus. Cell *143*, 288-298.

Li, J.-Y., Patterson, M., Mikkola, H.K., Lowry, W.E., and Kurdistani, S.K. (2012). Dynamic distribution of linker histone h1. 5 in cellular differentiation. PLoS genetics *8*, e1002879.

Lieberman-Aiden, E., van Berkum, N.L., Williams, L., Imakaev, M., Ragoczy, T., Telling, A., Amit, I., Lajoie, B.R., Sabo, P.J., and Dorschner, M.O. (2009). Comprehensive mapping of long-range interactions reveals folding principles of the human genome. science *326*, 289-293.

Longtine, M.S., McKenzie III, A., Demarini, D.J., Shah, N.G., Wach, A., Brachat, A., Philippsen, P., and Pringle, J.R. (1998). Additional modules for versatile and economical PCR-based gene deletion and modification in Saccharomyces cerevisiae. Yeast *14*, 953-961.

Lowary, P., and Widom, J. (1998). New DNA sequence rules for high affinity binding to histone octamer and sequence-directed nucleosome positioning. Journal of molecular biology *276*, 19-42.

Luger, K., Dechassa, M.L., and Tremethick, D.J. (2012). New insights into nucleosome and chromatin structure: an ordered state or a disordered affair? Nature Reviews Molecular Cell Biology *13*, 436-447.

Luger, K., Mäder, A.W., Richmond, R.K., Sargent, D.F., and Richmond, T.J. (1997). Crystal structure of the nucleosome core particle at 2.8 Å resolution. Nature *389*, 251-260.

Luger, K., Rechsteiner, T.J., and Richmond, T.J. (1999). Preparation of nucleosome core particle from recombinant histones. Methods in enzymology *304*, 3-19.

Maresca, T.J., Yan, J., Skoko, D., Heald, R., and Marco, J. (2005). Histone H1 is essential for mitotic chromosome architecture and segregation in Xenopus laevis egg extracts. Journal of Cell Biology *169*, 859-869.

Maul, G.G., and Deaven, L. (1977). Quantitative determination of nuclear pore complexes in cycling cells with differing DNA content. The Journal of cell biology *73*, 748-760.

Miloshev, G., Venkov, P., van Holde, K., and Zlatanova, J. (1994). Low levels of exogenous histone H1 in yeast cause cell death. Proceedings of the National Academy of Sciences *91*, 11567-11570.

Moosmann, A., Campsteijn, C., Jansen, P.W., Nasrallah, C., Raasholm, M., Stunnenberg, H.G., and Thompson, E.M. (2011). Histone variant innovation in a rapidly evolving chordate lineage. BMC evolutionary biology *11*, 208.

Neumann, F.R., and Nurse, P. (2007). Nuclear size control in fission yeast. The Journal of cell biology *179*, 593-600.

Olmo, E. (1982). Nucleotype and cell size in vertebrates: a review. Basic and applied histochemistry *27*, 227-256.

Palenik, B., Grimwood, J., Aerts, A., Rouzé, P., Salamov, A., Putnam, N., Dupont, C., Jorgensen, R., Derelle, E., and Rombauts, S. (2007). The tiny eukaryote Ostreococcus provides genomic insights into the paradox of plankton speciation. Proceedings of the National Academy of Sciences *104*, 7705-7710.

Parra, M.A., and Wyrick, J.J. (2007). Regulation of gene transcription by the histone H2A N-terminal domain. Molecular and cellular biology *27*, 7641-7648.

Rando, O.J. (2010). Genome-wide mapping of nucleosomes in yeast. Methods in enzymology *470*, 105-118.

Robinson, P.J., An, W., Routh, A., Martino, F., Chapman, L., Roeder, R.G., and Rhodes, D. (2008). 30 nm chromatin fibre decompaction requires both H4-K16 acetylation and linker histone eviction. Journal of molecular biology *381*, 816-825.

Rohs, R., West, S.M., Sosinsky, A., Liu, P., Mann, R.S., and Honig, B. (2009). The role of DNA shape in protein–DNA recognition. Nature *461*, 1248-1253.

Saldanha, A.J. (2004). Java Treeview—extensible visualization of microarray data. Bioinformatics *20*, 3246-3248.

Schalch, T., Duda, S., Sargent, D.F., and Richmond, T.J. (2005). X-ray structure of a tetranucleosome and its implications for the chromatin fibre. Nature *436*, 138-141.

Schmitt, M.E., Brown, T.A., and Trumpower, B.L. (1990). A rapid and simple method for preparation of RNA from Saccharomyces cerevisiae. Nucleic acids research *18*, 3091.

Schneider, T.D., and Stephens, R.M. (1990). Sequence logos: a new way to display consensus sequences. Nucleic acids research *18*, 6097-6100.

Schuster, T., Han, M., and Grunstein, M. (1986). Yeast histone H2A and H2B amino termini have interchangeable functions. Cell *45*, 445-451.

Schwarz, P.M., and Hansen, J.C. (1994). Formation and stability of higher order chromatin structures. Contributions of the histone octamer. Journal of Biological Chemistry *269*, 16284-16289.

Shogren-Knaak, M., Ishii, H., Sun, J.-M., Pazin, M.J., Davie, J.R., and Peterson, C.L. (2006). Histone H4-K16 acetylation controls chromatin structure and protein interactions. Science *311*, 844-847.

Sopko, R., Huang, D., Preston, N., Chua, G., Papp, B., Kafadar, K., Snyder, M., Oliver, S.G., Cyert, M., and Hughes, T.R. (2006). Mapping pathways and phenotypes by systematic gene overexpression. Molecular cell *21*, 319-330.

Suto, R.K., Clarkson, M.J., Tremethick, D.J., and Luger, K. (2000). Crystal structure of a nucleosome core particle containing the variant histone H2A. Z. Nature Structural & Molecular Biology *7*, 1121-1124.

Szerlong, H.J., and Hansen, J.C. (2010). Nucleosome distribution and linker DNA: connecting nuclear function to dynamic chromatin structure. Biochemistry and Cell Biology *89*, 24-34.

Tada, K., Susumu, H., Sakuno, T., and Watanabe, Y. (2011). Condensin association with histone H2A shapes mitotic chromosomes. Nature *474*, 477-483.

Vinogradov, A.E. (2005). Genome size and chromatin condensation in vertebrates. Chromosoma *113*, 362-369.

Vogelauer, M., Rubbi, L., Lucas, I., Brewer, B.J., and Grunstein, M. (2002). Histone acetylation regulates the time of replication origin firing. Molecular cell *10*, 1223-1233.

Waldmann, T., Izzo, A., Kamieniarz, K., Richter, F., Vogler, C., Sarg, B., Lindner, H., Young, N.L., Mittler, G.M.J., and Garcia, B.A. (2011). Methylation of H2AR29 is a novel repressive PRMT6 target (Bibliothek der Universität Konstanz).

Wang, H., Huang, Z.-Q., Xia, L., Feng, Q., Erdjument-Bromage, H., Strahl, B.D., Briggs, S.D., Allis, C.D., Wong, J., and Tempst, P. (2001). Methylation of histone H4 at arginine 3 facilitating transcriptional activation by nuclear hormone receptor. Science *293*, 853-857.

Weischet, W., Tatchell, K., Van Holde, K., and Klump, H. (1978). Thermal denaturation of nucleosomal core particles. Nucleic acids research *5*, 139-160.

West, S.M., Rohs, R., Mann, R.S., and Honig, B. (2010). Electrostatic interactions between arginines and the minor groove in the nucleosome. Journal of Biomolecular Structure and Dynamics *27*, 861-866.

Zheng, S., Wyrick, J.J., and Reese, J.C. (2010). Novel trans-tail regulation of H2B ubiquitylation and H3K4 methylation by the N terminus of histone H2A. Molecular and cellular biology *30*, 3635-3645.

Zhou, J., Fan, J.Y., Rangasamy, D., and Tremethick, D.J. (2007). The nucleosome surface regulates chromatin compaction and couples it with transcriptional repression. Nature structural & molecular biology *14*, 1070-1076.

Zink, D., Fischer, A.H., and Nickerson, J.A. (2004). Nuclear structure in cancer cells. Nature reviews cancer *4*, 677-687.

Zou, L., Mitchell, J., and Stillman, B. (1997). CDC45, a novel yeast gene that functions with the origin recognition complex and Mcm proteins in initiation of DNA replication. Molecular and cellular biology *17*, 553-563.

# Chapter 3

## Histones H2A and H2B co-evolved to enhance chromatin compaction

## 3.1 Summary

In the crystal structure of the nucleosome, the H2B C-terminal domain (CTD) is usually fully crystalized in an alpha helical formation, indicating that it has a well-defined structure(Davey et al., 2002; Luger et al., 1997). Residues within H2B CTD are known to influence chromatin structure through several mechanisms. H2B E110 is part of the H2A/H2B acidic patch that interacts with the H4 N-terminal tail to aid in compaction(Dorigo et al., 2003; Luger and Richmond, 1998; Shogren-Knaak et al., 2006). Ubiquitination of H2B K123 can disrupt *in vitro* chromatin fiber folding and oligomerization(Fierz et al., 2011) and internucleosomal interactions are directly mediated by the H2B CTDs in different nucleosomes interacting with each other(Schalch et al., 2005). Previously we reported that the H2A N-terminal domain (NTD) has evolved to aid in increased chromatin compaction as genome size increased. Here we demonstrate that residues near the H2B C-terminus have co-evolved with the H2A NTD residues during genome size expansion. The evolutionarily changed residues in H2B can mediate compaction of chromatin by themselves. However, compaction is further enhanced when combinations of evolutionarily changes within H2A and H2B are simultaneously present. We find that a physical region near the H2B C-terminus contains a cluster of residues in the H2A NTD and H2B CTD that change evolutionarily as well as mediate chromatin compaction. We term this region the H2A-H2B Compaction Domain (ABC Domain). Comparison of residues in this region between *S. cerevisiae*, an organism with a small genome, and *Xenopus laevis*, an organism with a large genome, shows that the evolutionary changes to the H2A NTD and H2B CTD have increased the positive charge of the nucleosomal surface as genome size has increased.

## 3.2 Results and Discussion

### 3.2.1 The H2B CTD changes in relation to genome size

Previously we found that arginine and serine/threonine residues in the H2A NTD have evolved with genome size to aid in eukaryotic genome compaction (ref). Specifically, H2A R3 and R11 are not found in many small genome sized organisms but appear in the H2A NTD of larger genome sized organisms while H2A S10 and S15 show the opposite trend. When these two arginines are added to the H2A of *S. cerevisiae*, a small genome organism, either by themselves or in combination with serine removal, we observe genome compaction. When H2A arginines are removed from large genome organisms, we observe decompaction of the genome. Because the H2A NTD has this strong effect on genome compaction and has a unique location on the surface of the nucleosome, we were interested to know if other parts of the nucleosome can coordinate with the H2A NTD.

Examination of the nucleosome crystal structure revealed that the H2A NTD is located physically close to the H2B CTD and that portions of the tails parallel each other as they protrude from the surface of the octamer (Figure 3-1A) (Davey et al., 2002; Luger et al., 1997). To determine if residues in the H2B CTD evolved with genome size in a matter similar to residues in the H2A NTD, we compared the H2B CTD protein sequences of 153 fully-sequenced eukaryotes spanning genome sizes of 8-3475 Mbp. We categorized each eukaryote in our dataset into one of four categories based on their genome size – extra-small (<25 Mbp), small (25-100 Mbp), medium (100-1000 Mbp), and large (>1000 Mbp). Residue composition analysis revealed that the number of lysines positively correlated to genome size whereby the average number of lysines in each genome size category increases with increasing genome size (Figure 3-1B). Besides single amino acid changes, we examined if classes of amino acids have changed together. This grouped analysis

revealed that towards the end of the H2B C-terminus, the number of amino acids with polar (serine, threonine, glutamine, asparagine) and small (glycine and alanine) side chains has decreased with increasing genome size (Figure 3-1C).

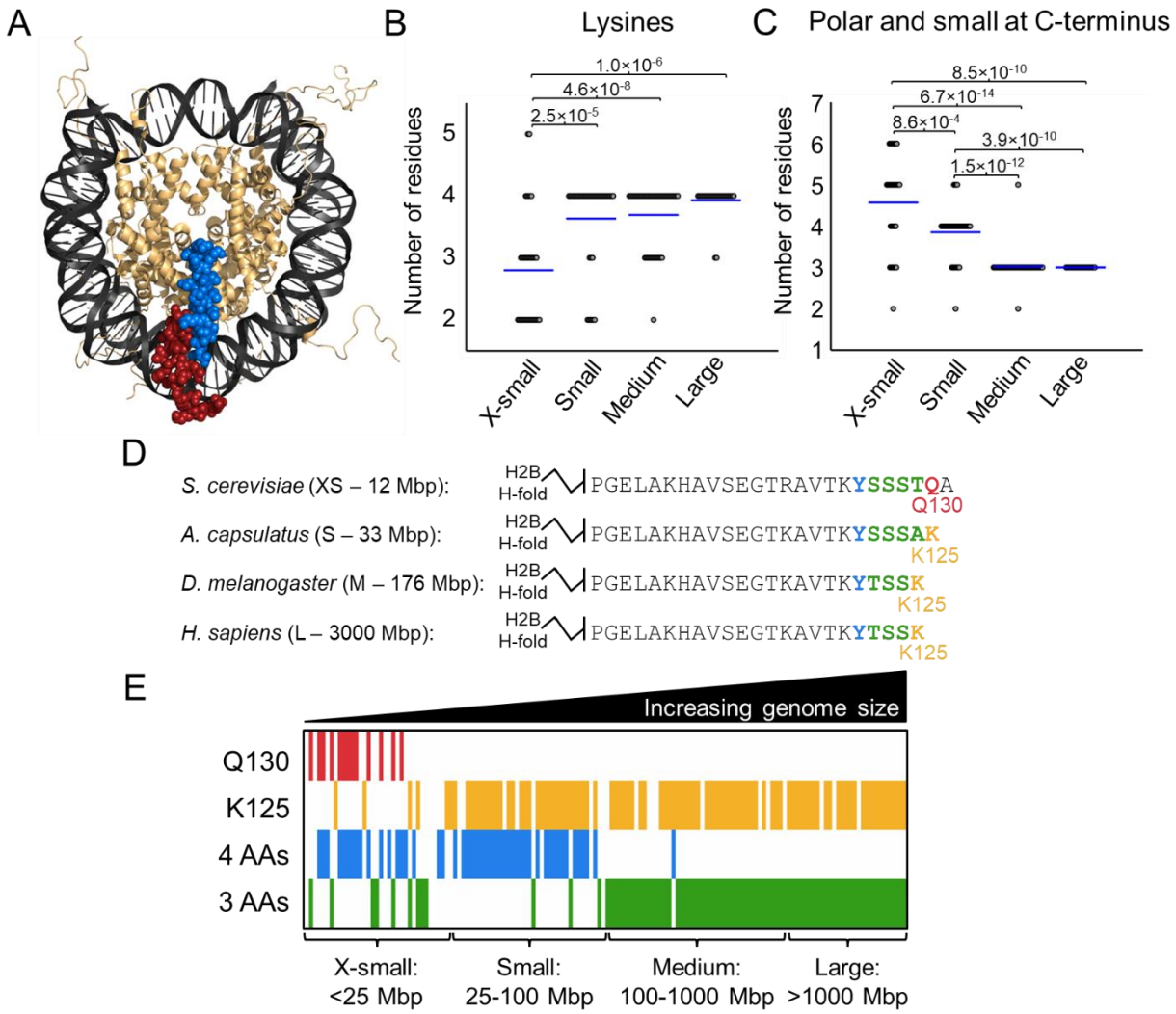


**Figure 3-1: Histone H2B C-terminal domain has co-evolved with genome size. (A)** Crystal structure view from the top of the nucleosome. Red is the H2A NTD. Blue is the H2B CTD (Davey et al., 2002). Distributions of the number of lysines **(B)** or the number of polar and small residues **(C)** in the H2B CTD. Polar residues include serines (S), threonines (T), asparagines (N), and glutamines (Q). Small residues include alanines (A) and glycines (G). Genome size categories are: X-small (<25 Mbp), Small (25-100 Mbp), Medium (100-1000 Mbp), and Large (>1000 Mbp). **(D)** H2B CTD protein sequences from the indicated species in each genome size category. **(E)** Heatmap of the H2B CTD residue composition at the indicated residue (Q130 or K126) or the presence of four amino acids or three amino acids (green highlight of part **(D)**) near the C-terminus. Species are ordered by increasing genome size.

Because the H2A NTD acquires precisely positioned residues throughout evolution, we investigated the possibility that a similar phenomenon occurs in the H2B CTD. We first examined representative H2B CTD protein sequences from an organism in each of the four genome size categories (Figure 3-1D). Inspection of these sequences revealed that a glutamine (Q130, yeast numbering) near the C-terminus of H2B in *S. cerevisiae* (yeast) is mutated to a lysine (K125, human numbering) in *A. capsulatus*, *D. melanogastger*, and *H. sapiens* (Figure 3-1D orange highlight). Located between the Q130/K125 residue and a conserved tyrosine residue (Figure 3-1D blue highlight) is a stretch of polar and small amino acids (Figure 3-1D, green highlight). In both *S. cerevisiae* and *A. capsulatus*, the stretch contains four residues but in *D. melanogaster* and *H. sapiens*, one amino acid is lost and the stretch only contains three residues.

To determine if similar patterns occur across all eukaryotes in our dataset, we created a heatmap to visualize the amino acid composition at these two regions in relation to genome size (Figure 3-1E). Like yeast, most extra-small genome sized organisms contain a glutamine at a similar position in the H2B CTD. This glutamine is mutated to a lysine (K125) in small, medium, and large genome sized organisms. Near the H2B C-terminus, most extra-small and small genome sized organisms contain a stretch of four polar and small amino acids that subsequently becomes a stretch of three in medium and large genome sized organisms.

### 3.2.2 Residues in the H2B CTD affect chromatin compaction in yeast and human cells

Because evolutionary changes to the H2B CTD correlated with genome size, we investigated whether those changes can compact chromatin. We used a strain of yeast (FY406) in which the genomic loci of H2A and H2B were disrupted and instead expresses H2A and H2B on a plasmid that includes the native promoter (Hirschhorn et al., 1995). We then mutated H2B to mimic the evolutionary patterns observed in Figure 3-1D and E. To investigate the role of the

terminal lysine, we created a Q130K mutant (note yeast numbering). We examined the effect of losing polar and small amino acids by creating ΔS127 and combined mutants together to create ΔS127Q130K.

To measure chromatin compaction, we performed fluorescence *in situ* hybridization (FISH) using probes along the long arm of Chr XVI(Bystricky et al., 2004; Guacci et al., 1997). We previously demonstrated using multiple probe pairs that this region of the chromosome compacts uniformly when arginines are added to the yeast H2A NTD. FISH analysis revealed that addition of a terminal lysine into the H2B CTD (Q130K) slightly decreases interprobe distances by 12% when compared to an isogenic WT (Figure 3-2A and 3-2B). Removal of polar amino acids (ΔS127) had little effect by decreasing interprobe distances by 1% when compared to WT. However, when combined (ΔS127Q130K), these mutations showed a synergistic chromatin compaction of 20% ($p<0.01$).

Because chromatin compaction may influence nuclear size(Cavalier-Smith, 1978; Cavalier-Smith, 2005; Jorgensen et al., 2007), we investigated whether changes to the H2B CTD regulate nuclear volume by tagging the nuclear pore protein Nup49 in its genomic locus with GFP. We then used confocal microscopy to measure the nuclear volumes in approximately 200 cells. Volume analysis revealed that none of the H2B CTD mutants showed a mean nuclear volume that was statistically different from an isogenic WT (Figure 3-2A and 3-2C).

We previously observed that histone H2A NTD arginines regulate chromatin and nuclear structure in human cells as well (Macadangdang et al., 2014) (see Chapter 2). Thus, we sought to determine if the corresponding evolutionary residues in the human histone H2B CTD also contribute to structural regulation of the nucleus. The H2B gene was HA-tagged and mutated to remove the C-terminal lysine 126 (ΔK126), or replace it with glutamine (K126Q), and to extend

the CTD by insertion of a serine (S125) in the string of serines/threonines, which make the human H2B CTD more similar to the yeast H2B. The combination of mutations (S125K126Q) was also generated. In contrast to the lack of an effect of the H2B CTD on nuclear volume in yeast, HEK293 cells ectopically overexpressing any of the H2B mutants displayed larger nuclear areas, suggesting that nuclear size is increased (Figure 3-2D and 3-2E). It is unclear why the H2B CTD may affect nuclear size only in the human cells, and possibly other animals, but it raises the interesting possibility that chromatin compaction and nuclear size are more tightly co-regulated in animal cells than in yeast, where the changes in either do not necessarily coincide. Overall, the changes in the histone H2B CTD, like the H2A NTD arginines, contribute to differential chromatin compaction in eukaryotes.

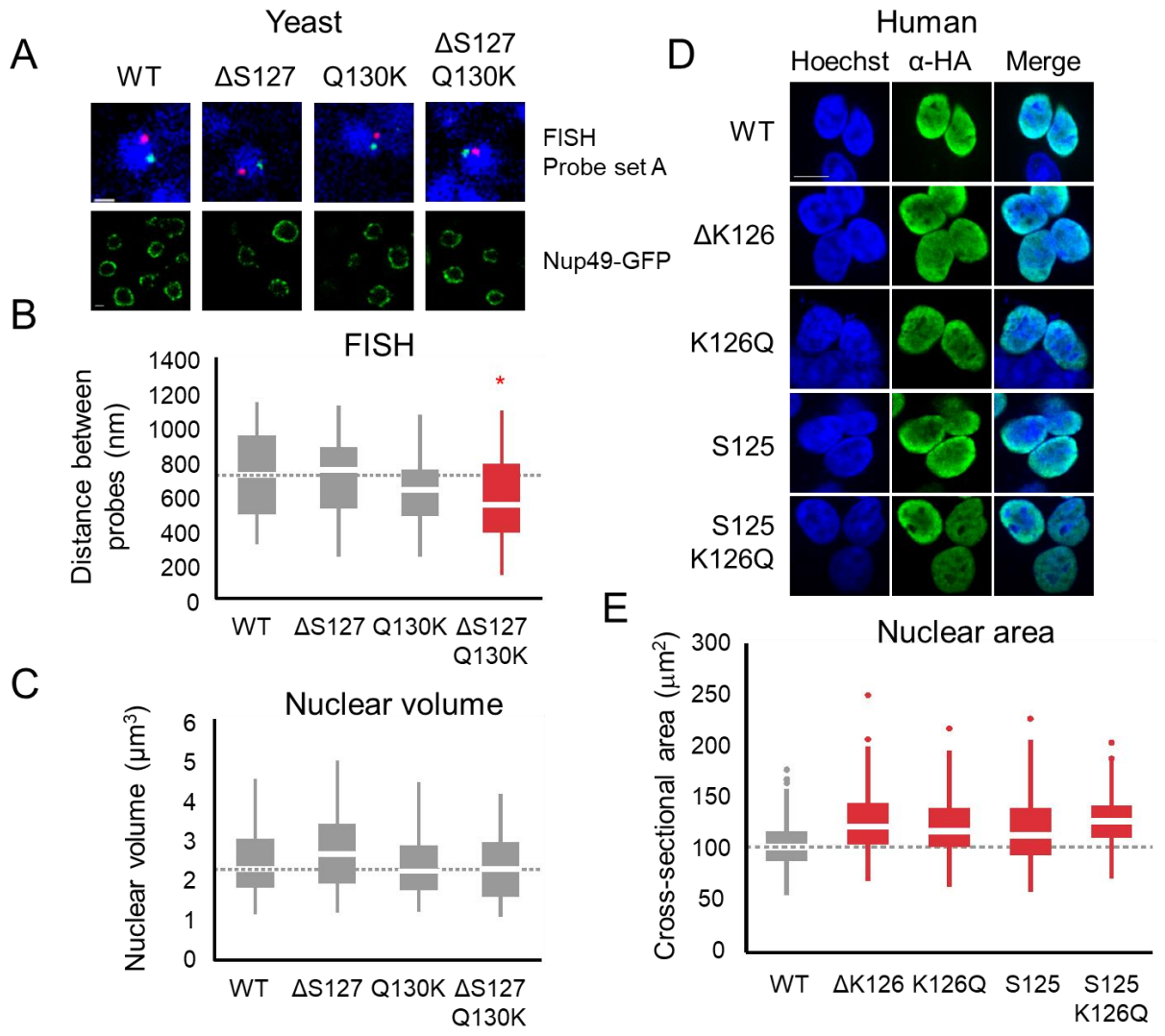


**Figure 3-2: Evolutionary residues in the H2B CTD affect chromatin compaction. (A)** Representative FISH images (top row) and nuclear envelope structure, imaged by Nup49-GFP fluorescence (bottom row), of the indicated strains. **(B)** Boxplot of the distributions of interprobe distances measured by FISH. **(C)** Boxplot of the distributions of nuclear volumes for the indicated strains. **(D)** Immunofluorescence images of human HEK293 cells overexpressing HA-tagged WT or mutant H2B genes as indicated. **(E)** Boxplot of the distributions of largest nuclear cross-sectional areas in the indicated H2B overexpressing cells. Boxes are colored red if the mean of the indicated strain or transiently-overexpressing cells is significantly different ($p<0.01$) from WT.

### 3.2.3 The H2A NTD and H2B CTD together aid in genome compaction

The co-evolution of the H2A NTD and H2B CTD with genome size as well as the physical proximity in the nucleosome structure to each other suggests that the H2A NTD and the H2B CTD

may function collectively to regulate genome compaction. To test this prediction, we created mutant yeast strains with simultaneous changes to H2A and H2B. Our previous work demonstrated that modifying yeast H2A in a way that renders is closer to large-genome H2A compacts chromatin. In particular, introduction or arginine in position 11 alone or in combination with the deletion of serine 15, but not deletion of serine 15 on its own, causes increased chromatin compaction. Therefore, to test simultaneous H2A and H2B changes, we combined each H2A mutation (R11, ΔS15, or R11ΔS15) with an H2B containing either a WT sequence or the mutations Q130K or ΔS127Q130K. To control for positive charge, we also included combinations with K11 and K11ΔS15.

FISH analysis confirmed that the H2A NTD and H2B CTD work cooperatively to regulate chromatin compaction. For instance, compaction mediated by only H2A R11 (15%) was further enhanced by simultaneous mutations in H2B, with R11-Q130K compacting chromatin by 22% and R11-ΔS127Q130K compacting chromatin by 32% (Figure 3-3A). This trend also occurs with other combination mutants. H2A ΔS15, by itself, did not have an effect on chromatin compaction but when combined with H2B Q130K (ΔS15-Q130K) or ΔS127Q130K (ΔS15-ΔS127Q130K), it compacted chromatin by a significant 17% and 22%, respectively (Figure 3-3A). The strongest levels of compaction were seen in the R11ΔS15-ΔS127Q130K mutant, which was able to compact chromatin by about 35%. An evolutionary change to H2A, K20 to R20, by itself does not affect chromatin compaction (Figure 3-4A – K20R mutant), but when combined with another H2A evolutionary change (R11, ΔS15, or R11ΔS15), it causes synergistic compaction (Figure 3-4A). However, when we combined H2A R11, H2A R20, and H2B K125 (R11K20R-ΔS127Q130K), we did not see further enhancement of compaction (Figure 3-4A).

Although the combination of H2A and H2B mutations results in stronger chromatin compaction than mutations of each single histone by themselves, they are not entirely additive. For instance, H2A R11ΔS15 decreases interprobe distances by 26% while H2B ΔS127Q130K decreases distances by 20%. If additive, the R11ΔS15-ΔS127Q130K mutant would decrease interprobe distances by 46% but instead only decreases by 35%. This observation together with the finding that chromatin compaction is not further enhanced by simultaneously expressing H2A R11, H2A R20, and H2B K125 (Figure 3-4A) suggests overlapping functions of these residues in compacting chromatin.

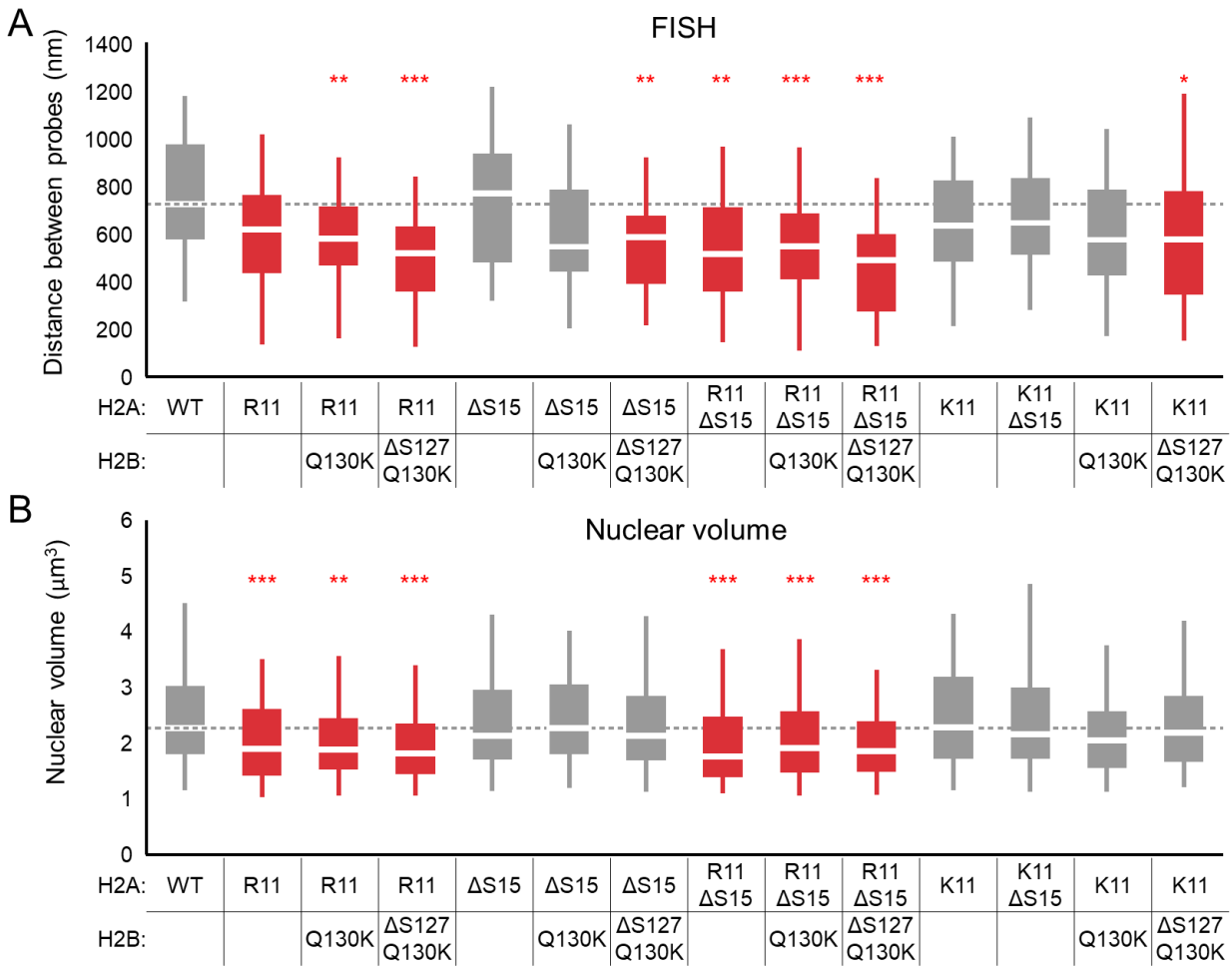


**Figure 3-3: Simultaneous expression of H2A NTD arginines and H2B CTD lysines compacts chromatin but only H2A R11 regulates nuclear size.** Boxplots of the distribution of **(A)** interprobe distances for FISH probes spaced 275 kbp apart and **(B)** nuclear volumes as measured Nup49-GFP imaging. The mutation within H2A and H2B are indicated below in the cells. Boxes are colored if the mean of the indicated strain is significantly different from WT. Red stars denote level of significance: * $p<0.01$; ** $p<0.001$; *** $p<0.0001$.

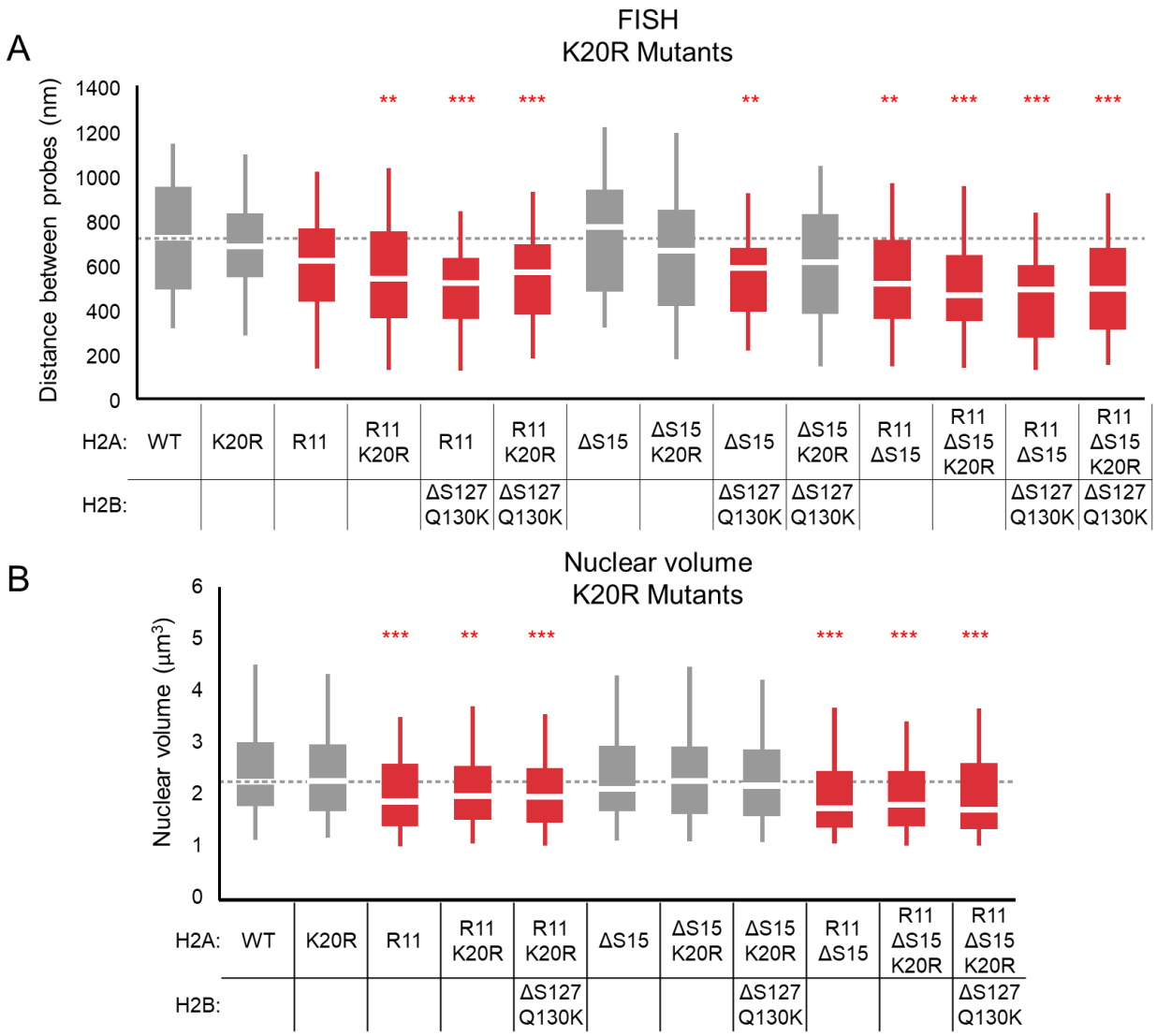


**Figure 3-4: Small contribution of H2A K20R to chromatin compaction modulation but not to nuclear volume in yeast.** Boxplots of the distribution of **(A)** interprobe distances for FISH probes spaced 275 kbp apart and **(B)** nuclear volumes as measured Nup49-GFP imaging. The mutation within H2A and H2B are indicated below in the cells. Boxes are colored if the mean of the indicated strain is significantly different from WT. Red stars denote level of significance: ** $p<0.001$; *** $p<0.0001$.

Because the H2A NTD and H2B CTD function mutually to regulate chromatin compaction, it is conceivable that these two domains also cooperate to regulate nuclear volume. We measured nuclear volume in yeast strains expressing H2A NTD- and H2B CTD- mutations, as described above. Volume analysis demonstrated that nuclear size in yeast is not altered by the presence of

mutations within the H2B CTD (Figure 3-3B, Figure 3-4B) unless H2A R11 was also present. The decrease in nuclear volumes mediated by H2A R11 ranged from 14%-20% (Figures 3-3, Figure 3-4B). We therefore conclude that changes in nuclear volume do not depend on the level of chromatin compaction but are to some extent regulated by the presence of H2A R11.

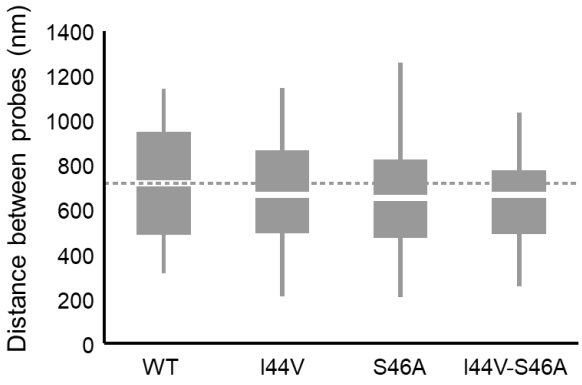


**Figure 3-5: Not all H2A residues that co-evolved with genome size affect chromatin compaction.** Boxplots of the distribution of interprobe distances for FISH probes spaced 275 kbp in the indicated strains expressing mutant H2A.

### 3.2.4 The H2A-H2B Compaction Domain (ABC Domain) is a cluster of residues that affect chromatin compaction

Not every evolutionary change to H2A or H2B affects chromatin compaction. In yeast, H2A ΔS15, H2A K11, and H2B ΔS127 do not significantly alter the interprobe distances measured by FISH (Figure 3-2B, 3-3A). In addition, some evolutionary changes in the H2A histone fold region also have no effect on chromatin compaction (Figure 3-5). Finally, there are residues that by themselves have no or little impact on compaction (H2A K20R) but when put in the correct context (H2A R11K20R), have greater effects on compaction (Figure 3-4A).

To give us a better understanding of how H2A R20 could have an effect only when combined with other mutations, we closely examined the crystal structure and discovered an interesting looping of the H2A NTD that forms a pocket of positively charged amino acids in three

dimensional space that is not evident from the one dimensional sequence. This region includes two of the evolutionarily changed H2A NTD arginines, R11 and R20, as well as the terminal lysine of the H2B CTD, K125 (Figure 3-6A). More comprehensive analysis revealed that there is a hotspot region of the nucleosome where there are simultaneously many residues that not only change evolutionarily but also affect chromatin compaction. Using the crystal structure where the H2A NTD and H2B CTD were fully crystalized(Davey et al., 2002), we calculated the nearest atom-to-atom distances for these residues (summarized in Table 3-1). This region, which we call the H2A-H2B Compaction Domain (ABC Domain), contains three out of the four H2A NTD arginines found in higher eukaryotes (R11, R17, and R20), as well as K125 and the stretch of three residues with polar/small side chains. Another residue found in this region is H2A K15 (Q16 in yeast). Interestingly, also contained in this region is H2B K120, whose ubiquitination was found to de-compact chromatin and hinder nucleosomal array oligomerization(Fierz et al., 2011).

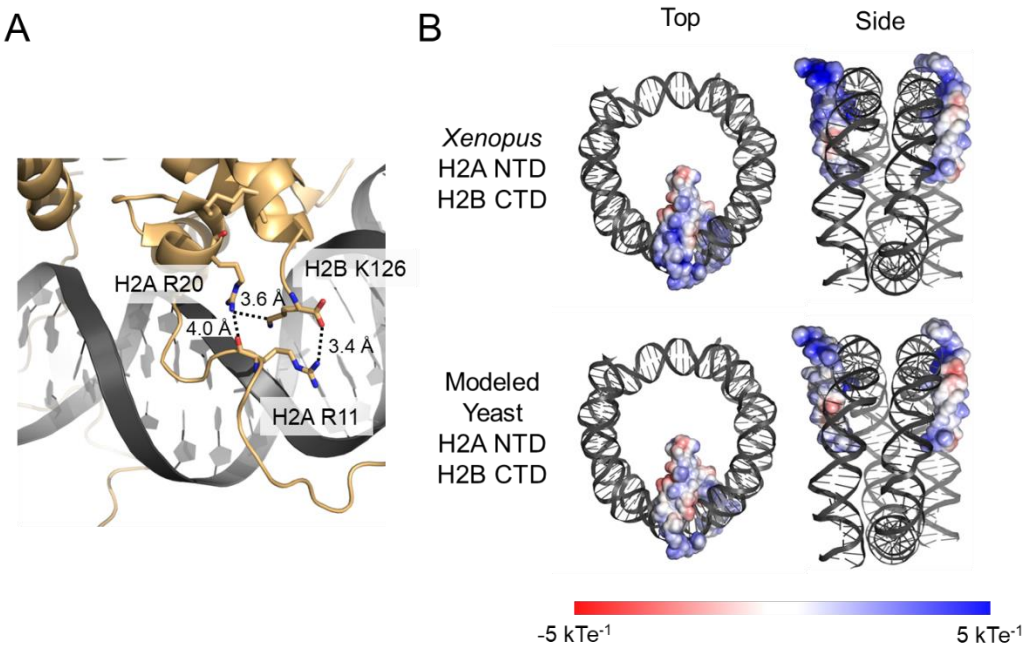


**Figure 3-6: The ABC Domain has increased positive charge in the nucleosome of *Xenopus laevis* compared to yeast. (A)** Close-up view of the ABC domain of X. laevis with the spatial distances of various residues in H2A and H2B shown. **(B)** View of the electrostatic potential of the H2A NTD and H2B CTD with the indicated orientation. The scale bar at the bottom shows the color representing the corresponding charge.

**Table** Error! No text of specified style in document.**-1: Distances between indicated residue and the H2B C-terminus and involvement in chromatin compaction.**

| Histone | Residue | Distance to H2B C-terminus (Å) | Part of evolutionary changes | Involved with compaction |
|---|---|---|---|---|
| H2B | K125 | 0.00 | ✓ | ✓ |
| H2B | S124 | 1.37 | ✓ | ✓ |
| H2A | R11 | 3.45 | ✓ | ✓ |
| H2A | R20 | 3.65 | ✓ | ✓ |
| H2B | S123 | 4.20 | ✓ | ✓ |
| H2A | A12 | 5.65 | | |
| H2B | T122 | 5.89 | ✓ | ✓ |
| H2B | Y121 | 5.91 | | |

| | | | | | |
|---|---|---|---|---|---|
| H2A | T10 | 6.78 | ✓ | | |
| H2A | K15 | 6.92 | ✓ | | |
| H2B | K120 | 6.96 | | | ✓ |
| H2A | R17 | 6.96 | | | |

We noticed that many of the residues within the ABC Domain contain side chains that are positively charged at physiological pH. To better understand how these changes may have affected the surface of the nucleosome, we took the crystal structure of the *Xenopus laevis* nucleosome where the H2A NTD and H2B CTD were mostly crystalized(Davey et al., 2002) and used PyMOL(DeLano, 2002) to mutate evolutionary changed residues back to the residue found in yeast (see Methods for exact mutagenesis changes). We then used the APBS toolkit(Unni et al., 2011) to calculate the electrostatic potential of the H2A NTD and H2B CTD in the original structure and in the mutated structure to resemble the yeast tails (Figure 3-6B). When compared to the yeast residues, the residues in the *Xenopus* structure, which represents higher eukaryotes, show an increase of positive charge density along the surface of the nucleosome. This increase in charge density along the surface has the potential to facilitate internucleosomal stacking interactions.

Because linker lengths can affect both higher-order fiber formation and linker histone binding(Robinson et al., 2006; Routh et al., 2008; Woodcock et al., 2006), we investigated the possibility that the mechanism of increased compaction mediated through residues within the ABC Domain involved rearrangement of nucleosomes throughout the genome. We used *Micrococcal* nuclease digestion followed by paired-end deep sequencing (MNase-Seq), to obtain the native positions of nucleosomes in our yeast strains that expressed ABC Domain mutations that exhibited greater chromatin compaction compared to strains whose mutations had no effect on compaction.

Analysis of the locations of nucleosomes genome-wide revealed that mutations within the ABC Domain had little effect on nucleosomal positioning. Figure 3-7A shows a genome browser view of a short segment of Chr II where both the spacing and intensity of the peaks is similar in all strains, and the same pattern occurred genome-wide. Meta-analysis of specific genomic features such as open reading frames (ORFs) (Figure 3-7B), tRNAs, autonomously replicating sequences (ARS), snRNAs, telomeres, ncRNAs, Y' elements, retrotransposons, and centromeres also revealed no differences between any of the mutants. Other measures besides occupancy, such as fuzziness and nucleosome shifts, were found to be unchanged as well. These data suggest that the increased compaction mediated by the residues in the ABC Domain does not occur through changes in linker lengths nor does it affect nucleosome positioning genomewide.

In addition to nucleosome spacing, we investigated the possibility that mutations within the ABC Domain interfered with transcription. Previously we demonstrated that H2A NTD mutations do not affect steady state mRNA levels, so to determine whether the H2B CTD mutations influence gene expression patterns, we performed mRNA extraction followed by deep sequencing (RNA-Seq). Similar to what was observed for H2A mutants, the levels of mRNA transcripts for each gene were unaltered by mutations in the H2B CTD, with all the correlations between strains > 0.995 (Figure 3-7C). On a strain-by-strain basis, very few genes were greater than two fold over- or under-expressed and those genes did not show any enriched gene ontology (Figure 3-7D). These data suggest that, just like H2A NTD mutations, H2B CTD mutations have evolved to aid in genome compaction without interfering with transcription.

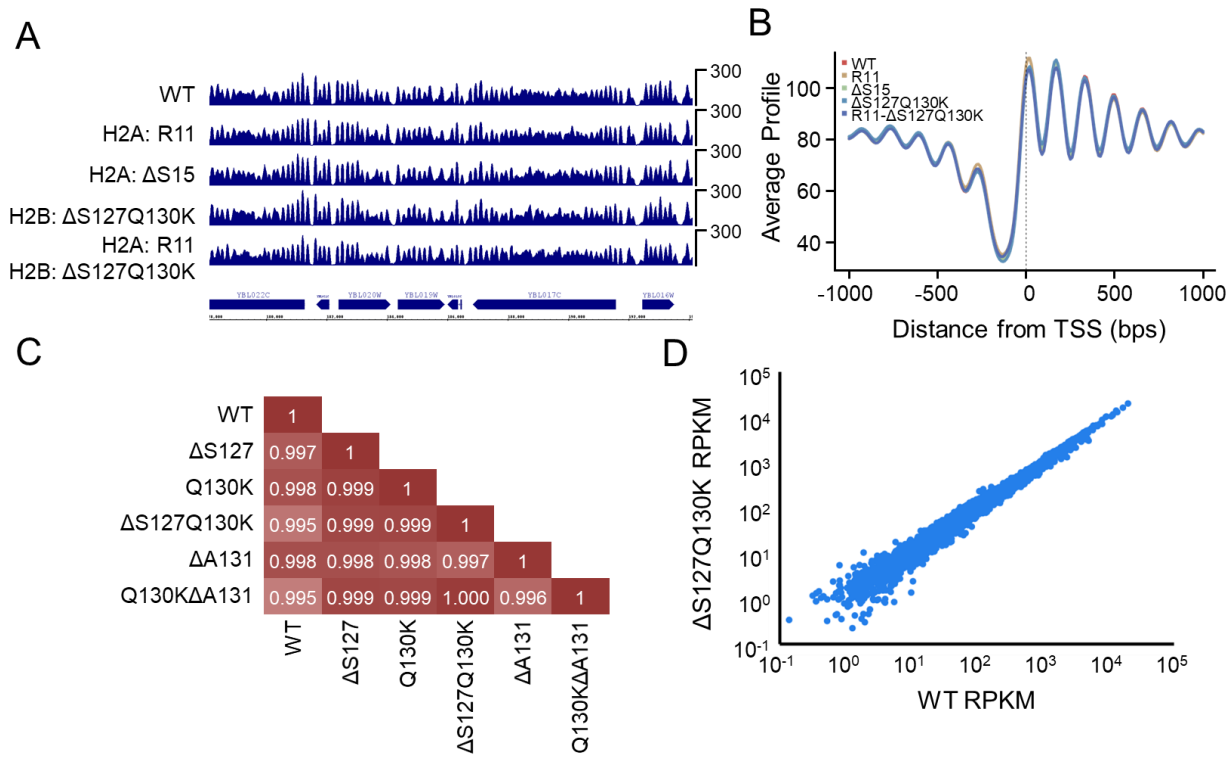


**Figure 3-7: Mutations within the ABC Domain do not affect nucleosomal occupancy or gene expression in yeast. (A)** Genome browser view of nucleosomal occupancy along a portion of Chr II in the indicated strains from deep sequencing after MNase digestion. **(B)** Average profile of nucleosome occupancy around open reading frames in the indicated strains. **(C)** Correlations of all RPKM values in the genome between the indicated strains. **(D)** Scatter plot of the RPKM values for individual genes between WT and ΔS127Q130K, which significantly increased chromatin compaction.

### 3.3 Conclusions

Eukaryotes have evolved several mechanisms for chromatin compaction, including linker histones, changes in linker length, and chromatin binding proteins(Bannister et al., 2001; Margueron and Reinberg, 2011; Routh et al., 2008; Tada et al., 2011). Although histones are thought to be conserved proteins throughout evolution, we previously demonstrated that the H2A NTD has evolved to increase chromatin compaction in species with large genomes. Here we report that the H2B CTD, which is in close physical proximity to the H2A NTD, has also co-evolved with increasing genome size. Changes to the H2B CTD can compact chromatin and can further enhance compaction in combination with H2A NTD evolutionary changes. A region of the

nucleosome near the H2B C-terminus that we termed the ABC Domain contains a cluster of physically proximal residues in the H2A NTD and H2B CTD that not only change evolutionarily but also affect chromatin compaction. The ABC Domain has evolved to increase the electrostatic potential of the nucleosomal surface on the side opposite of the DNA entry/exit points. Because ABC Domain residues have been shown to mediate nucleosome stacking(Davey et al., 2002; Schalch et al., 2005), our data explain how this previously unrecognized portion of the nucleosome is important as a structural determinant for chromatin.

## 3.4 Materials and Methods

### Strains and media

Yeast cells were grown in YPD at 30°C unless otherwise noted. C-terminal GFP tagging of the yeast nuclear pore protein Nup49 was performed as described previously (Longtine et al., 1998). The human HEK293 cell line was maintained at 37°C and 5% $CO_2$ and cultured with 10% fetal bovine serum (FBS) and DMEM (Gibco).

### Histone sequence database construction and analysis

The co-evolutionary histone sequence analysis relative to genome size changes across eukaryotes performed in this study is an extension of our work previously published, and presented in Chapter 2 of this dissertation (Macadangdang et al., 2014). The analysis of histone sequences and genome sizes involved the same data processing steps. Sequences were initially extracted from the Entrez database using a keyword search for "histone", and removing non-histone sequences by using keyword searches such as "histone-like", "ubiquitin", and "acetyl", yielding 54,646 results. Blast 2.0 (Camacho et al., 2009) was used to align the sequences against the highly conserved histone fold region of the four core histones from *H. sapiens*. Thresholds for true hits were set at >35% identity match and >90% overlap match with the histone fold globular domain region. All

duplicate sequences were removed, and further sequence comparisons were made for histone H3 and H2A sequences to filter variants within them. The canonical sequence datasets comprised 672 sequences for histone H3, 357 sequences for histone H4, 518 sequences for histone H2B, and 435 sequences for histone H2A. To further select one canonical sequence for a species among isotypes and variants when annotation was missing, the sequences were compared to the canonical *H. sapiens* and *S. cerevisiae* sequence, and the sequence with highest similarity was selected. Using only completely sequenced species, the final histone sequence dataset included canonical sequences for 160 species from plants, fungi, protozoa, and animals, with genome sizes ranging from 8 to 5600 Mbp.

Sequences for histone H2B were subsequently split into the N-terminal tail, globular domain, and C-terminal domain sub-sequences. For discovery of patterns of residue changes according to genome size, each of the sub-sequences was further sub-grouped into small (<100 Mbp), medium (100-1000 Mbp), and large (>1000 Mbp) genome sizes. The frequency of the amino acid residues in each sequence in the sub-groups was determined, and a p-value for the comparison between sub groups was obtained using a Mann-Whitney U Test. Multiple sequence alignment profiles were created using the Muscle sequence comparison tool from Embl-EBI (Edgar, 2004a, b). Weblogo3 (Crooks et al., 2004; Schneider and Stephens, 1990) was used for motif discovery. Heat maps for residue positions were constructed using Cluster 3.0 (de Hoon et al., 2004) and Java Treeview (Saldanha, 2004).

**Yeast H2B mutagenesis**

Site directed mutagenesis was performed using the QuickChange Lightning kit (Agilent) on the pJH55 plasmid which was a gift from Fred Winston (Hirschhorn et al., 1995).

**Measurement of yeast nuclear volume**

Yeast strains were generated that contained a C-terminally tagged Nup49p-GFP fusion. Cells were grown in rich medium to 0.6-0.8x$10^7$ cells/mL, fixed in growth medium with 4% paraformaldehyde for 15 min at room temperature, washed twice in PBS, and mounted on a poly-L-lysine-coated slide with mounting medium (Vector Labs). Z-stacks were obtained as described in the microscopy imaging section, and GFP excitation was achieved at 488 nm. Resulting z-stack images were de-convolved using a constrained iterative algorithm from SlideBook 5.0 software and nuclear volumes were measured by masking the inside of each nucleus, which were delineated by the GFP signal. The resulting mask was used to calculate volumes through the SlideBook software. Statistical analysis was performed using the Student's t-test.

**FISH probes**

For yeast FISH analysis, DNA templates for probes 1 and 3 came from ATCC cosmids 71042 and 70912 as described elsewhere (Guacci et al., 1994). All DNA templates were digested to smaller fragments using Sau3a (NEB). Fragments were directly labeled using BioPrime labeling kit (Invitrogen) with either ChromaTide Alexa Fluor 488-5-dUTP or ChromaTide Alexa Fluor 568-5-dUTP (Invitrogen).

**Fluorescent *in-situ* hybridization analysis in yeast**

Yeast strains were grown in rich medium to 0.6-0.8x$10^7$ cells/mL and fixed in growth medium with 4% paraformaldehyde for 15 min at room temperature. Cells were then washed twice in growth medium and re-suspended in 2 mL of EDTA-KOH (0.1 M, pH 8.0) and 10 mM DTT and incubated for 10 min shaking at 30°C. Cells were spun down and re-suspended in 2 mL of YPD + 1.2 M sorbitol with 50 µg/mL of Zymolyase 100-T (Sunrise Science) and 400 U/mL of lyticase (Sigma) and incubated at 30°C for 16 min with shaking. Spheroplasts were then washed

twice in YPD + 1.2 M sorbitol and transferred to a poly-L-lysine-coated slide. After settling for 5 min, excess liquid was aspirated away and slides were allowed to air dry for 5 additional min. Slides were washed in methanol for 10 min and then acetone for 30 sec before air drying. Cells were then dehydrated in a series of cold ethanol washes (70%, 80%, 90%, 100%, 1 min each) and allowed to air dry. Denaturing solution (70% deionized formamide, 2x SSC) was added to the slide and cells were denatured at 75°C for 7-10 min. Slides were immediately put through another cold ethanol dehydration series and allowed to air dry. Hybridization solution (50% deionized formamide, 2x SSC, 10% dextran sulfate, 100 ng/µL salmon sperm DNA) containing fresh probes was added to the slide and the probes were hybridized for 40-48 hours at 37°C. Slides were then washed in two 5 min washes in 0.05x SSC at 48°C and washed twice in BT Buffer (0.15 M NaHCO3 pH 7.5, 0.1% Tween) for 5 min at room temperature. Mounting medium containing DAPI was added to the slides and a coverslip was sealed with nail polish.

Inter-probe distances were measured in single Z-stacks as described elsewhere (Bystricky et al., 2004) by finding the pixel distance between weighted centers of the green signal and red signal and converted to nm by the appropriate scaling factor.

**Microscopy imaging**

A 3i Marianas SDC confocal microscope equipped with a Zeiss AxioObserver Z1 with a 100×/1.45 NA objective and Yokogawa CSU-22 confocal head was used. Images were captured by a Hamamatsu EMCCD C9100-13 camera controlled by Slidebook 5.5. DAPI, GFP, mRFP, and Far-red images were acquired by excitation at 360 nm, 488 nm, 561 nm, and 640 nm from a high-speed AOTF laser launch line. A step size of 0.3 (yeast) or 0.5 (human) µm was used for z-stack acquisition.

**Micrococcal nuclease digestion**

Micrococcal nuclease (MNase) digestions were performed on exponentially growing yeast cells as described previously, except that the enzyme was obtained from Sigma-Aldrich (Sigma-Aldrich)(Rando, 2010). For samples run on an agarose gel, increasing concentrations of MNase were used. For MNase-Seq, a concentration of MNase was used that gave approximately 80% mononucleosomes. The mononucleosomal DNA was gel extracted and libraries were prepared using NuGen Ovation Rapid DR Multiplex kits. Libraries were sequenced using an Illumina HIseq-2000 to obtain 50 bp paired-end reads. The reads were aligned back to the SacCer3 genome using Bowtie2(Langmead and Salzberg, 2012) and nucleosome occupancy was calculated using DANPOS(Chen et al., 2013).

**RNA expression analysis**

RNA was extracted from exponentially growing yeast as described previously(Schmitt et al., 1990). PolyA-RNA was prepared, labeled and hybridized to Affymetrix Gene ChIP Yeast Genome 2.0 array by the UCLA clinical microarray core facility and data normalized according to manufacturer's indications. The data are accessible at Gene Expression Omnibus with accession number GSE50440. For RNA-Seq, libraries were prepared and analyzed as previously described(Ferrari et al., 2012).

**Immunofluorescence in human cells**

N-terminally HA-tagged human H2B was cloned by PCR into mammalian expression vector pCMV-HA (Clontech). Site directed mutagenesis was performed using the QuickChange Lightning kit (Agilent) on the expression plasmid. Human HEK293 cells were grown on glass coverslips in 24-well plates in DMEM containing 10% fetal bovine serum and transfected with the indicated H2B expression plasmids using BioT transfection reagent (Bioland Scientific). Cells

were grown for 48 hrs post-transfection. Transfected cells were fixed with ice-cold methanol for 15 min at -20°C followed by washing with PBS-T. Cells were blocked in 5% BSA and incubated with anti-HA antibody (1:250 dilution, Abcam, ab9110). Cells were washed and incubated with secondary antibody (1:500 Alexa Fluor 488 goat anti-rabbit, Invitrogen, A11008). Cells were washed and then incubated with Hoechst stain (0.001 mg/mL in PBS). After final washes, cover slips were mounted and imaged. Fluorescence was visualized as above except with the use of 63X magnification.

### 3.5 References

Bannister, A.J., Zegerman, P., Partridge, J.F., Miska, E.A., Thomas, J.O., Allshire, R.C., and Kouzarides, T. (2001). Selective recognition of methylated lysine 9 on histone H3 by the HP1 chromo domain. Nature *410*, 120-124.

Bystricky, K., Heun, P., Gehlen, L., Langowski, J., and Gasser, S.M. (2004). Long-range compaction and flexibility of interphase chromatin in budding yeast analyzed by high-resolution imaging techniques. Proceedings of the National Academy of Sciences of the United States of America *101*, 16495-16500.

Camacho, C., Coulouris, G., Avagyan, V., Ma, N., Papadopoulos, J., Bealer, K., and Madden, T. (2009). BLAST+: architecture and applications. BMC bioinformatics *10*, 421.

Cavalier-Smith, T. (1978). Nuclear volume control by nucleoskeletal DNA, selection for cell volume and cell growth rate, and the solution of the DNA C-value paradox. Journal of Cell Science *34*, 247-278.

Cavalier-Smith, T. (2005). Economy, speed and size matter: evolutionary forces driving nuclear genome miniaturization and expansion. Annals of Botany *95*, 147-175.

Chen, K., Xi, Y., Pan, X., Li, Z., Kaestner, K., Tyler, J., Dent, S., He, X., and Li, W. (2013). DANPOS: Dynamic analysis of nucleosome position and occupancy by sequencing. Genome research *23*, 341-351.

Crooks, G.E., Hon, G., Chandonia, J.-M., and Brenner, S.E. (2004). WebLogo: a sequence logo generator. Genome research *14*, 1188-1190.

Davey, C.A., Sargent, D.F., Luger, K., Maeder, A.W., and Richmond, T.J. (2002). Solvent mediated interactions in the structure of the nucleosome core particle at 1.9 Å resolution. Journal of molecular biology *319*, 1097-1113.

de Hoon, M.J., Imoto, S., Nolan, J., and Miyano, S. (2004). Open source clustering software. Bioinformatics *20*, 1453-1454.

DeLano, W.L. (2002). The PyMOL molecular graphics system.

Dorigo, B., Schalch, T., Bystricky, K., and Richmond, T.J. (2003). Chromatin fiber folding: requirement for the histone H4 N-terminal tail. Journal of molecular biology *327*, 85-96.

Edgar, R.C. (2004a). MUSCLE: a multiple sequence alignment method with reduced time and space complexity. BMC bioinformatics *5*, 113.

Edgar, R.C. (2004b). MUSCLE: multiple sequence alignment with high accuracy and high throughput. Nucleic acids research *32*, 1792-1797.

Ferrari, R., Su, T., Li, B., Bonora, G., Oberai, A., Chan, Y., Sasidharan, R., Berk, A.J., Pellegrini, M., and Kurdistani, S.K. (2012). Reorganization of the host epigenome by a viral oncogene. Genome research *22*, 1212-1221.

Fierz, B., Chatterjee, C., McGinty, R.K., Bar-Dagan, M., Raleigh, D.P., and Muir, T.W. (2011). Histone H2B ubiquitylation disrupts local and higher-order chromatin compaction. Nature chemical biology *7*, 113-119.

Guacci, V., Hogan, E., and Koshland, D. (1994). Chromosome condensation and sister chromatid pairing in budding yeast. The Journal of cell biology *125*, 517-530.

Guacci, V., Koshland, D., and Strunnikov, A. (1997). A direct link between sister chromatid cohesion and chromosome condensation revealed through the analysis of MCD1 in S. cerevisiae. Cell *91*, 47.

Hirschhorn, J.N., Bortvin, A.L., Ricupero-Hovasse, S.L., and Winston, F. (1995). A new class of histone H2A mutations in Saccharomyces cerevisiae causes specific transcriptional defects in vivo. Mol Cell Biol *15*, 1999-2009.

Jorgensen, P., Edgington, N.P., Schneider, B.L., Rupeš, I., Tyers, M., and Futcher, B. (2007). The size of the nucleus increases as yeast cells grow. Molecular biology of the cell *18*, 3523-3532.

Langmead, B., and Salzberg, S.L. (2012). Fast gapped-read alignment with Bowtie 2. Nature methods *9*, 357-359.

Longtine, M.S., McKenzie III, A., Demarini, D.J., Shah, N.G., Wach, A., Brachat, A., Philippsen, P., and Pringle, J.R. (1998). Additional modules for versatile and economical PCR-based gene deletion and modification in Saccharomyces cerevisiae. Yeast *14*, 953-961.

Luger, K., Mäder, A.W., Richmond, R.K., Sargent, D.F., and Richmond, T.J. (1997). Crystal structure of the nucleosome core particle at 2.8 Å resolution. Nature *389*, 251-260.

Luger, K., and Richmond, T.J. (1998). The histone tails of the nucleosome. Current opinion in genetics & development *8*, 140-146.

Macadangdang, B.R., Oberai, A., Spektor, T., Campos, O.A., Sheng, F., Carey, M.F., Vogelauer, M., and Kurdistani, S.K. (2014). Evolution of histone 2A for chromatin compaction in eukaryotes. Elife *3*.

Margueron, R., and Reinberg, D. (2011). The Polycomb complex PRC2 and its mark in life. Nature *469*, 343-349.

Rando, O.J. (2010). Genome-wide mapping of nucleosomes in yeast. Methods in enzymology *470*, 105-118.

Robinson, P.J., Fairall, L., Huynh, V.A., and Rhodes, D. (2006). EM measurements define the dimensions of the "30-nm" chromatin fiber: evidence for a compact, interdigitated structure. Proceedings of the National Academy of Sciences *103*, 6506-6511.

Routh, A., Sandin, S., and Rhodes, D. (2008). Nucleosome repeat length and linker histone stoichiometry determine chromatin fiber structure. Proceedings of the National Academy of Sciences *105*, 8872-8877.

Saldanha, A.J. (2004). Java Treeview—extensible visualization of microarray data. Bioinformatics *20*, 3246-3248.

Schalch, T., Duda, S., Sargent, D.F., and Richmond, T.J. (2005). X-ray structure of a tetranucleosome and its implications for the chromatin fibre. Nature *436*, 138-141.

Schmitt, M.E., Brown, T.A., and Trumpower, B.L. (1990). A rapid and simple method for preparation of RNA from Saccharomyces cerevisiae. Nucleic acids research *18*, 3091.

Schneider, T.D., and Stephens, R.M. (1990). Sequence logos: a new way to display consensus sequences. Nucleic acids research *18*, 6097-6100.

Shogren-Knaak, M., Ishii, H., Sun, J.-M., Pazin, M.J., Davie, J.R., and Peterson, C.L. (2006). Histone H4-K16 acetylation controls chromatin structure and protein interactions. Science *311*, 844-847.

Tada, K., Susumu, H., Sakuno, T., and Watanabe, Y. (2011). Condensin association with histone H2A shapes mitotic chromosomes. Nature *474*, 477-483.

Unni, S., Huang, Y., Hanson, R.M., Tobias, M., Krishnan, S., Li, W.W., Nielsen, J.E., and Baker, N.A. (2011). Web servers and services for electrostatics calculations with APBS and PDB2PQR. Journal of computational chemistry *32*, 1488-1491.

Woodcock, C.L., Skoultchi, A.I., and Fan, Y. (2006). Role of linker histone in chromatin structure and function: H1 stoichiometry and nucleosome repeat length. Chromosome Research *14*, 17-25.

# Chapter 4

# The histone H3-H4 tetramer is a copper reductase

## 4.1 Summary

The histone H3-H4 tetramer forms a putative metal-binding region of unknown function at the interface of the two apposing H3 proteins. We report that mutating a highly conserved histidine residue in the H3-H3' interface impairs cellular activities such as mitochondrial respiration and Sod1 function that depend on availability of reduced copper. The impairment of copper homeostasis is not due to altered gene expression or total copper abundance but is consistent with decreased levels of cuprous ions, suggesting histones may directly affect copper's oxidation state. Indeed, the intact nucleosome or the H3-H4 tetramer assembled *in vitro* from recombinant histones exhibits robust copper reductase activity, catalyzing $Cu^{2+}$ to $Cu^{1+}$. We propose that eukaryotic chromatin is an oxidoreductase enzyme, which provides biousable copper for cellular and mitochondrial chemistry. As the emergence of eukaryotes coincided with increased oxidation and therefore decreased biousability of essential metals, the enzymatic function of histones could have facilitated eukaryogenesis.

## 4.2 Introduction

Eukaryotic genomes are nearly universally packaged in the form of chromatin, a nucleoprotein structure that protects the DNA and facilitates its compaction while also regulating DNA-based processes. The core histones H2A, H2B, H3 and H4—the main protein components of chromatin—evolved from histone-like proteins in archaea such as the HMf-1 and HMf-2 proteins of *Methanothermus fervidus* (Sandman et al., 1990). The H3-H4 tetramer bound to DNA, also known as a tetrasome, docks with two H2A-H2B dimers to form the canonical 146 bp eukaryotic nucleosome. Archaeal histones wrap only ~60 bp of DNA but otherwise form structures similar to the H3-H4 tetrasome (Pereira et al., 1997), with conserved geometry and protein-DNA interactions (Mattiroli et al., 2017). Unlike eukaryotic chromatin, archaeal histones lack extended

N-terminal tails and are typically devoid of post-translational modifications (Forbes et al., 2004); and thus could not contribute to gene regulation in the way that eukaryotes employ histone modifications. Although the archaeal nucleosomes could provide basic forms of regulation by restricting access of proteins to the DNA (Soares et al., 1998), the rationale for evolution of histones in certain archaeal species, with typically small genomes ranging from 1-3 Mbp, has been unclear. Histones may have evolved in archaea to maintain the integrity of the genome in the harsh environments in which they thrive (Li et al., 1998). But not all archaea that live in extreme environments contain nucleosome-like structures (Brochier-Armanet et al., 2011). Here we reveal a novel function of histones in copper homeostasis that could provide a basis for their evolutionary origin.

Eukaryotes derive from the merger of a histone-containing archaeon with a bacterium approximately 1.5-2 billion years ago (Koonin, 2015). A histone-based genome packaging system is thought to have been fortuitously present in the archaeal ancestor (Sandman and Reeve, 1998). In such a scenario, histones could only later have facilitated evolution of eukaryotic complexity in part by compacting an expanding genome size (Sandman and Reeve, 1998). It is possible, however, that the presence of histones in our archaeal ancestor was not incidental, rather essential for the emergence of early eukaryotes. So far, no viable scenario has been put forth to account for a possible contribution of histones to the development of early eukaryotes including the endosymbiotic evolution of mitochondria.

The emergence of eukaryotes coincided roughly with accumulation of molecular oxygen (Anbar, 2008), which resulted in significant alterations in the abundance and oxidation states of transition metals. Before the great oxidation event, iron (Fe) and copper (Cu) were present in their reduced and therefore biousable forms, with iron being much more prevalent than copper (Saito et

al., 2003). The earliest eukaryotes appeared when iron and copper were being increasingly oxidized and less biousable yet more toxic in the presence of oxygen (Saito et al., 2003). This presented a formidable challenge for acquisition or intracellular usage of these essential metals by organisms that had evolved in a previously reducing environment. That early eukaryotes may have relied partly on histones to meet this challenge has not been considered.

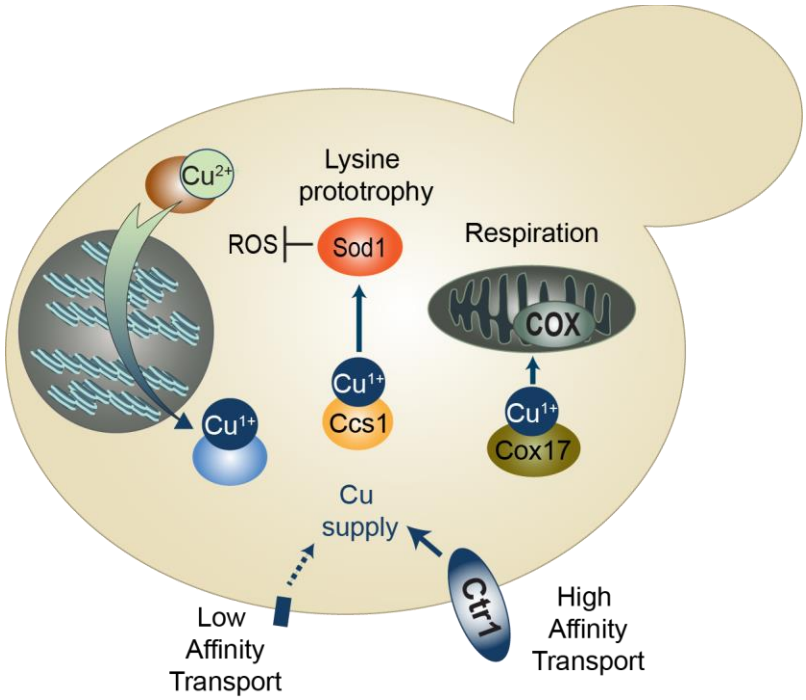


**Figure 4-1: Graphical representation of copper homeostasis in *S. cerevisiae*.** For the sake of simplicity, only processes relevant to this study are shown.

Copper is an essential element in eukaryotes and serves as a co-factor for numerous enzymes that function in key intra- and extra-cellular processes (Nevitt et al., 2012) (Figure 4-1). Copper is required for mitochondrial respiration as a co-factor for cytochrome *c* oxidase, the last enzyme (complex IV) in the mitochondrial electron transport chain (ETC), and for Cu, Zn-superoxide dismutase 1 (Sod1), which catalyzes disproportionation of superoxide radicals to prevent oxidative damage (Nevitt et al., 2012). Copper is imported through dedicated transporters

and distributed to its cellular destinations via protein chaperones. In *Saccharomyces cerevisiae*, *CTR1* (Copper Transport) encodes the main high-affinity copper transporter that mediate nearly all copper import in limited copper conditions (Dancis et al., 1994). Protein chaperones such as Ccs1 (Copper Chaperone for SOD1) and Cox17 (Cytochrome *c* Oxidase) are then required for delivery of copper to Sod1 or cytochrome *c* oxidase, respectively (Culotta et al., 1997; Glerum et al., 1996). Copper is also found in the nucleus but the dynamics of its entry and exit or its function(s) are unclear (McRae et al., 2013; Yang et al., 2005). Interestingly, absence of the ATPase copper transporting beta (ATP7B), the gene mutated in Wilson's disease, compromises copper efflux from the cell resulting in significant and disproportionate copper accumulation in the nucleus, reaching millimolar concentrations (Burkhead et al., 2011; Huster et al., 2006). As a co-factor, copper is utilized in its cupric ($Cu^{2+}$) or cuprous ($Cu^{1+}$) forms but only the latter is bound by chaperones, indicating that its oxidation state is important for proper intracellular trafficking (Pufahl et al., 1997). The intracellular ratio of oxidized vs. reduced copper and how this proportion is established are unknown, although evidence suggests that most, but not all, exists as $Cu^{1+}$ bound to protein and non-protein ligands (Rae et al., 1999; Yang et al., 2005). Copper may also serve as a signaling element to regulate specific biochemical pathways such as lipolysis (Krishnamoorthy et al., 2016). The utility of copper, however, must be balanced against its toxicity caused by displacement of other metals in proteins or its redox activity (Macomber and Imlay, 2009). Organisms have therefore evolved homeostatic mechanisms for careful provision of copper to meet specific demands. Several diseases in humans, including cancer, neurodegenerative diseases like Amyotrophic Lateral Sclerosis (ALS), Alzheimer's, Wilson's, Menkes and others, involve disruption of copper homeostasis (Bleackley and Macgillivray, 2011; Turski and Thiele, 2009).

As early as 1986, it was noted that the eukaryotic nucleosome has a potential metal-binding structure comprising amino acid residues in the C-terminal regions of the two apposing histone H3 proteins. These residues include cysteine 110 (H3C110) and histidine 113 (H3H113) (Saavedra, 1986) (Figure 4-2A). Several hydrogen bonds involving residues in and around the H3-H3' interface, including those that constitute the putative metal-binding pocket, form a 4-helix bundle that is also required for the assembly of the H3-H4 tetramer (Luger et al., 1997). Interestingly, the evolutionary conservation of individual or pairs of amino acids in this region is not readily explained by their contributions to the thermodynamic stability of the nucleosome alone. This observation suggests that "a novel function" provided by the H3-H3' interface is driving the surprising conservation (Ramachandran et al., 2011). The functional significance of a potential metal-binding structure in H3, and whether a metal-binding function could explain the evolutionary conservation, have not been investigated.

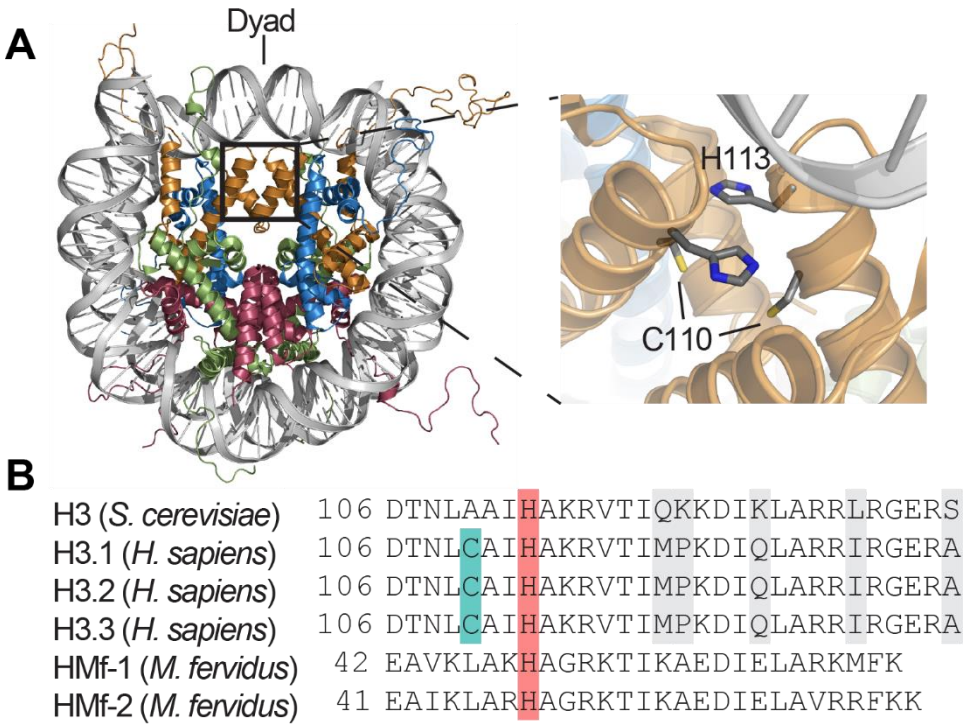


**Figure 4-2: A putative metal-binding site in the nucleosome. (A)** Left: *X. laevis* nucleosome core particle structure (PDB:1KX5) (Davey et al., 2002) viewed down the DNA superhelix axis. Histone H3, H4, H2A and H2B are shown in metallic orange, blue, green and red, respectively. The square box delineates the H3-H3' interface. Right: Interface residues H113 and C110, one from each of the histone H3 molecules, are highlighted. **(B)** Alignment of the C-terminal region of *S. cerevisiae* histone H3, human non-centromeric histone H3 variants, and M. *fervidus* HMf-1 and HMf-2.

Two lines of reasoning prompted us to investigate whether histone H3 may play a role in cellular copper homeostasis. First, the coincidence of eukaryotic emergence and geochemical alterations of transition metals raised the possibility of histones having a role in enhancing intracellular metal homeostasis. Second, a functioning complex IV in the ETC of the proto-mitochondria at the time of its merger may have depended on the intracellular provision of cuprous ions by the archaeal host—as it occurs today in eukaryotes. Here, we provide biochemical, molecular and genetic data that histone H3 is required for efficient use of copper inside cells. We show that recombinant H3-H4 tetramer catalyzes reduction of cupric to cuprous ions. Our data suggest that the catalytic site likely forms at the interface of the two histone H3 proteins as

mutations in this region alter or impair the *in vitro* enzymatic activity of the Xenopus H3-H4 tetramer; and cause defects in mitochondrial respiration and Sod1 activity—both of which depend on the availability of intracellular cuprous ions—in *S. cerevisiae*. Alterations in gene expression, nucleosome assembly, or total cellular copper quota could not explain these phenotypes. Rather, the phenotypes are consistent with decreased levels of $Cu^{+1}$ and can be recapitulated by decreasing intracellular reducing power. Our data reveal that eukaryotic DNA wraps around an enzyme that catalyzes reduction of copper for utilization by various cellular and mitochondrial proteins. This notion has a profound impact in the fields of evolution and the molecular biology of the eukaryotic cell and may be relevant to a range of human pathologies in which alterations of copper-dependent processes are implicated (Bleackley and Macgillivray, 2011; Turski and Thiele, 2009)

## 4.3 Results

### 4.3.1 Mutation of histone H3 histidine 113 to asparagine (H3H113N) has little effect on global chromatin accessibility or gene expression.

Since the H3-H3' interface contributes to the stability of the H3-H4 tetramer, we first determined the impact of mutating H3H113, a highly-conserved residue that is also found in archaeal histones (Figure 4-2B), on chromatin accessibility and global gene expression. Mutation of this residue to alanine (*H3H113A*) or glutamine (*H3H113Q*) is lethal in yeast for unknown reasons (Huang et al., 2009). However, we noticed that in the COSMIC (Forbes et al., 2015) and ExAC (Lek et al., 2016) databases H3H113 is mutated to asparagine (*H3H113N*) in certain cancers and individuals, suggesting that this mutation may be tolerated in yeast as well. We used CRISPR/Cas9 to generate a *S. cerevisiae* strain with H113N mutations in both copies of histone H3 genes (*HHT1* and *HHT2*) in their chromosomal loci under their natural promoters without any other genetic disruption. The H3H113N mutation is at least hypomorphic because when present

only in *HHT2* with wildtype *HHT1* expression shut off, it resulted in a more severe growth defect compared to the $H3^{H113N}$ strain in which both *HHT1* and *HHT2* are mutated and expressed (Figure 4-3A). The strain harboring mutations in both histone H3 copies, denoted as $H3^{H113N}$, exhibited a 2-fold increase in growth doubling time compared to wildtype (WT) in rich media (Figures 4-3A-C). Asf1 (Anti-Silencing Function) is a histone chaperone that binds to the H3-H4 dimer through interactions with H3H113 and other residues, and is required for nucleosome assembly and disassembly (Adkins et al., 2004; Agez et al., 2007). We also assessed the phenotype of an *ASF1* deletion strain (*asf1*Δ) to exclude potential disruption to Asf1-H3/H4 dimer interactions and consequent alteration in chromatin structure as underlying factors for the phenotypes of the $H3^{H113N}$ strain. Deletion of *ASF1* also increased doubling time (Figures 4-3B and 4-3C) but to a lesser extent than did the *H3H113N* mutation. Analysis of global chromatin structure by Micrococcal nuclease (MNase) revealed essentially similar digestion patterns for WT, $H3^{H113N}$ and *asf1*Δ strains, with the latter two being slightly less accessible at lower MNase concentrations (Figure 4-3D). Global gene expression patterns were also essentially similar between WT and $H3^{H113N}$ grown in yeast extract peptone dextrose (YPD) or in synthetic complete (SC) medium with no gene having a statistically significant difference at a Benjamini-Hochberg false discovery rate (FDR) of <10% (Figure 4-3E). Thus, the *H3H113N* mutation has no significant effect on steady state genome-wide gene expression or chromatin accessibility.

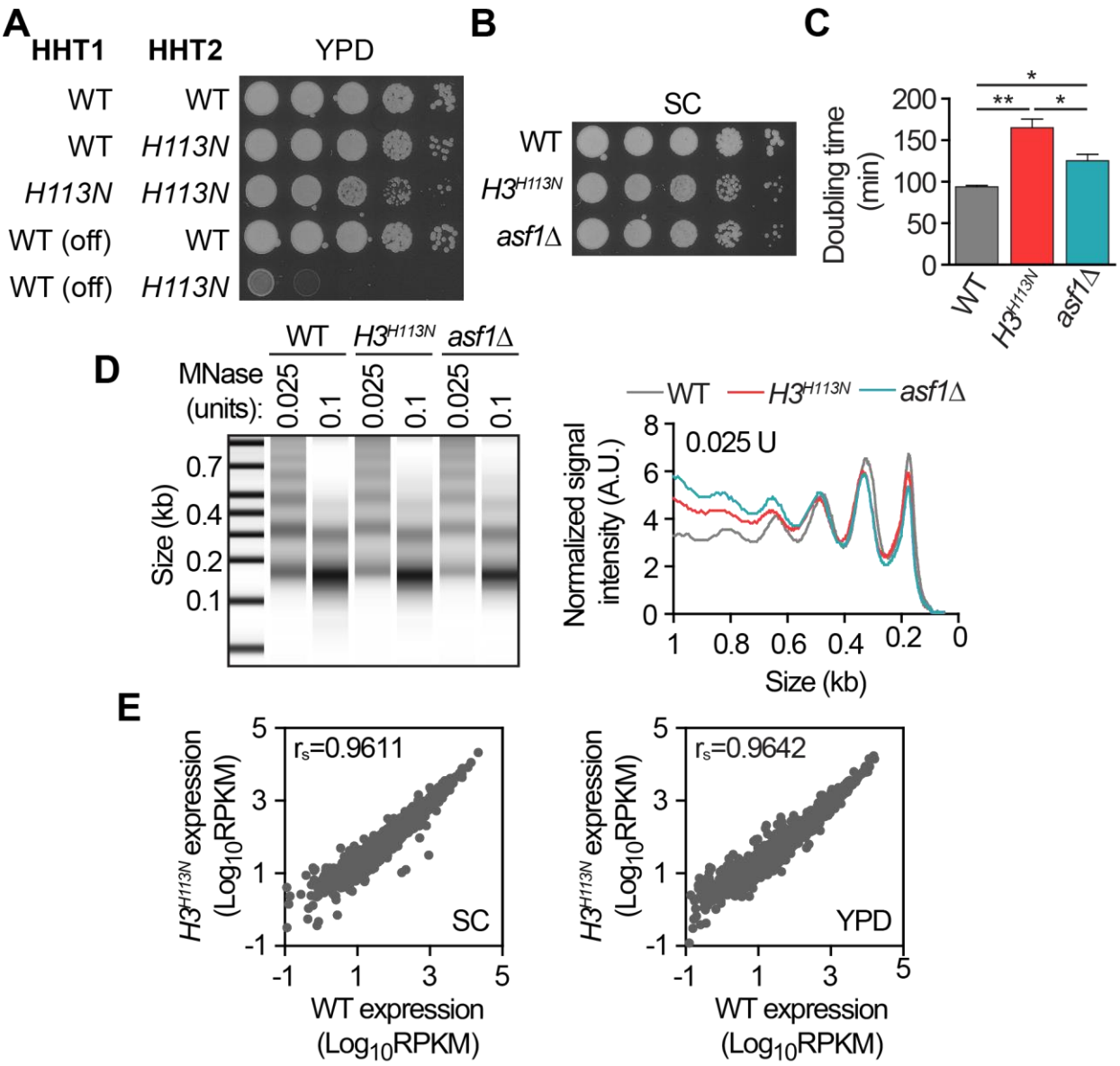


**Figure 4-3: Mutation of histone H3 histidine 113 to asparagine has little effect on global chromatin accessibility or gene expression in *S. cerevisiae*.** **(A)** Spot test assay of the indicated strains in fermentative media (YPD). Note that the *HHT1* gene in the bottom two strains was placed under the control of the *GAL1* promoter, which is repressed in YPD. Since one copy of H113N (bottom row) causes a more severe phenotype than two copies ($H3^{H113N}$ strain, third row), this suggests that H113N is likely a loss of function mutation. **(B)** Spot test growth assay and **(C)** average doubling times from steady-state growth in liquid SC media. Bar graphs show mean ± standard deviation (SD) from 3-6 replicate cultures. **(D)** Quantitative representation of the signal intensity profiles (right) from chromatin digested with the indicated amounts of MNase (left). A.U.: arbitrary units. **(E)** Scatterplots of average global gene expression values from exponentially growing cells in SC and YPD, with Spearman's rank correlation coefficient ($r_s$) as indicated. *P<0.05, **P≤0.01.

### 4.3.2 The H3H113 residue is required for efficient use of copper for mitochondrial respiration.

We reasoned that if the putative metal binding pocket at the H3-H3' interface is disrupted, the cell might suffer from aberrant metal ion homeostasis. To assess copper homeostasis, we examined the ability of $H3^{H113N}$ to grow on non-fermentable carbon sources and therefore rely on mitochondrial respiration for growth. Although $H3^{H113N}$ displayed a growth defect compared to WT in YPD, it did not display a further defect under respiratory conditions where non-fermentable ethanol and glycerol were substituted for dextrose (YPEG) (Figure 4-4A). In rich media conditions, abundant copper uptake might mask an underlying deficiency in copper utilization. We therefore deleted *CTR1*, the main copper importer in yeast, to disrupt copper availability in the context of WT and *H3H113N* histones. The *ctr1*Δ mutant was unable to grow on YPEG with baseline copper abundance (Figure 4-4A, lower panel). Addition of 20 μM copper rescued the *ctr1*Δ respiratory growth defect but only in the background of WT histone H3 (Figure 4-4A). Four times more exogenous copper was required to rescue the growth defect of *ctr1*Δ in the presence of *H3H113N* mutant histones (Figure 4-4A). The rescue of *asf1*Δ*ctr1*Δ was achieved at similar levels of copper as *ctr1*Δ alone, and therefore did not phenocopy $H3^{H113N}$*ctr1*Δ (Figure 4-4A). Combination of *H3H113N* mutation with deletion of *MAC1* ($H3^{H113N}$*mac1*Δ), a copper-sensing transcription factor required for expression of copper transport genes including *CTR1* (Graden and Winge, 1997), also increased the amount of exogenous copper required for growth on YPEG compared to *mac1*Δ alone (Figure 4-4B). Addition of iron, zinc, or manganese did not rescue the growth defects of strains with *ctr1*Δ, confirming the specific copper deficiency (Figure 4-4C).

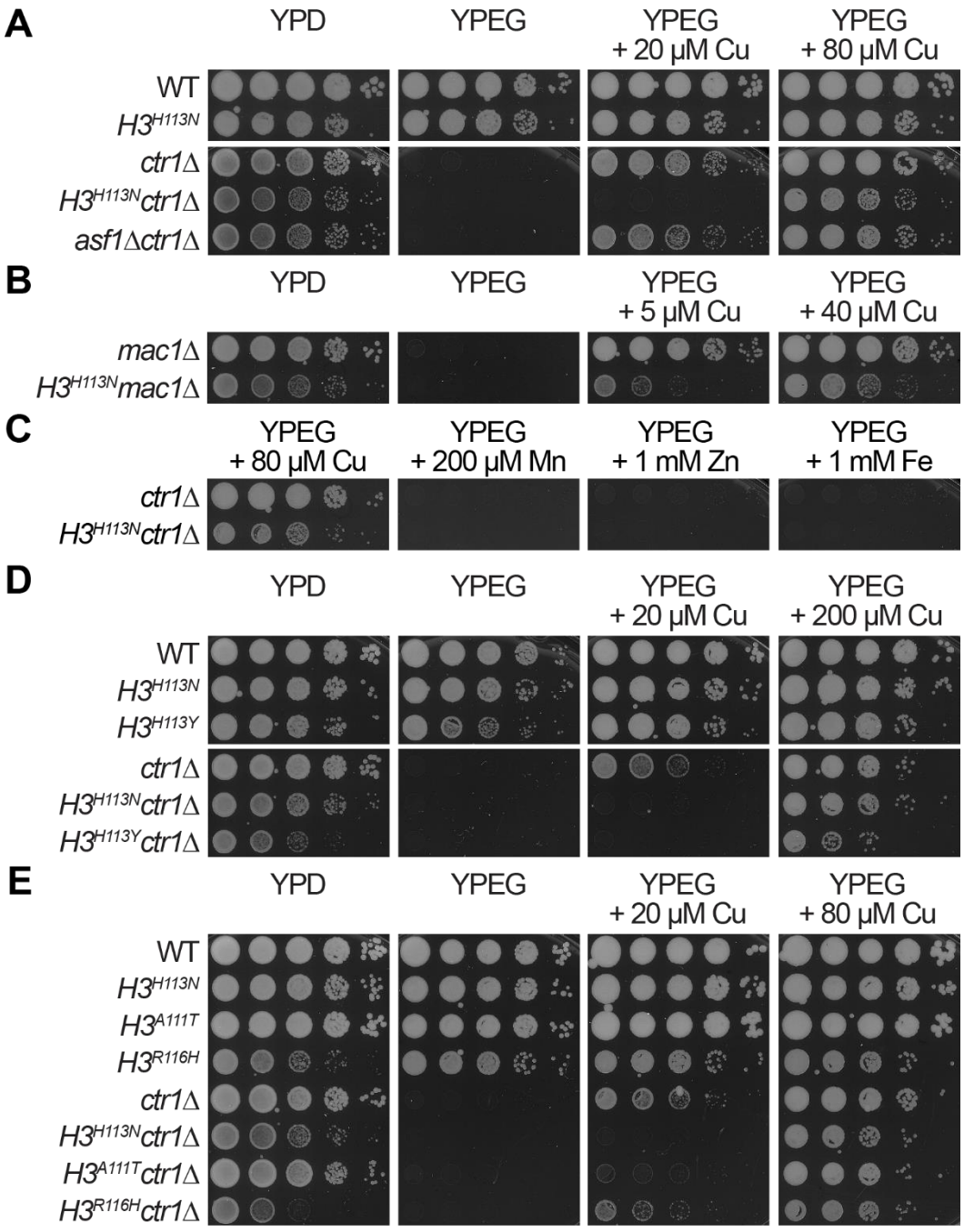


**Figure 4-4: *H3$^{H113N}$* diminishes copper utilization for respiratory growth. (A-E)** Spot test assays with the indicated strains in fermentative (YPD) or respiratory media (YPEG) with the indicated amounts of $CuSO_4$ or (C) $MnCl_2$, $ZnSO_4$ or $FeCl_3$. Baseline copper concentration in YP media is ~ 1 µM. Note that the *ctr1*Δ strain is respiratory deficient and cannot be rescued by exogenous manganese, zinc or iron.

We further tested the effect of loss of histidine 113 on the respiratory growth defect of *ctr1*Δ by replacing the same histidine 113 with tyrosine, a biochemically distinct amino acid compared to asparagine, using the same mutagenesis approach as described above. This strain, $H3^{H113Y}$, had a slightly more pronounced growth defect in rich media, and importantly, in combination with *ctr1*Δ also increased the requirement for copper for growth on YPEG (Figure 4-4D). While the H113 residue in the nucleosome structure is predicted to directly interact with copper ions, other residues in the vicinity of H113 may also contribute to this same function, either by also directly affecting copper ion interaction or by indirectly affecting the structural conformation of the H3-H3' dimerization interface. To examine whether other histone mutations also affect copper homeostasis, we generated two additional yeast strains harboring mutations in residues surrounding H113, in which alanine 111 was mutated to threonine ($H3^{A111T}$) and arginine 116 was mutated to histidine ($H3^{R116H}$). Interestingly, the H3A111T mutation also increased the requirement for copper for growth of *ctr1*Δ on YPEG (Figure 4-4E). However, taking into account that the H3R116H mutation resulted in the most drastic growth defect of these histone mutations, there was not a concomitant defect of copper utilization by the *ctr1*Δ strain for respiratory growth (Figure 4-4E).

In liquid YPEG culture, $H3^{H113N}$*ctr1*Δ also lagged behind *ctr1*Δ in growth and oxygen ($O_2$) consumption at several medium copper concentrations (Figure 4-5A). The copper-mediated rescue of growth in these mutants was indeed dependent on mitochondrial respiration because deletion of *COX17*, which functions downstream of Ctr1 for eventual delivery of copper to cytochrome *c* oxidase (Glerum et al., 1996) (Figure 4-1), prevented rescue even if >100-fold more exogenous copper was provided compared to *ctr1*Δ strains (Figure 4-5B). The inference that the copper-mediated effect was due to mitochondrial respiration is further supported by the inhibition of $O_2$

consumption in the presence of Antimycin A, a complex III inhibitor (Kim et al., 1999)(Figure 4-5C). These results indicate that the *H3H113N* mutation decreases copper availability for respiratory growth when copper is limiting.

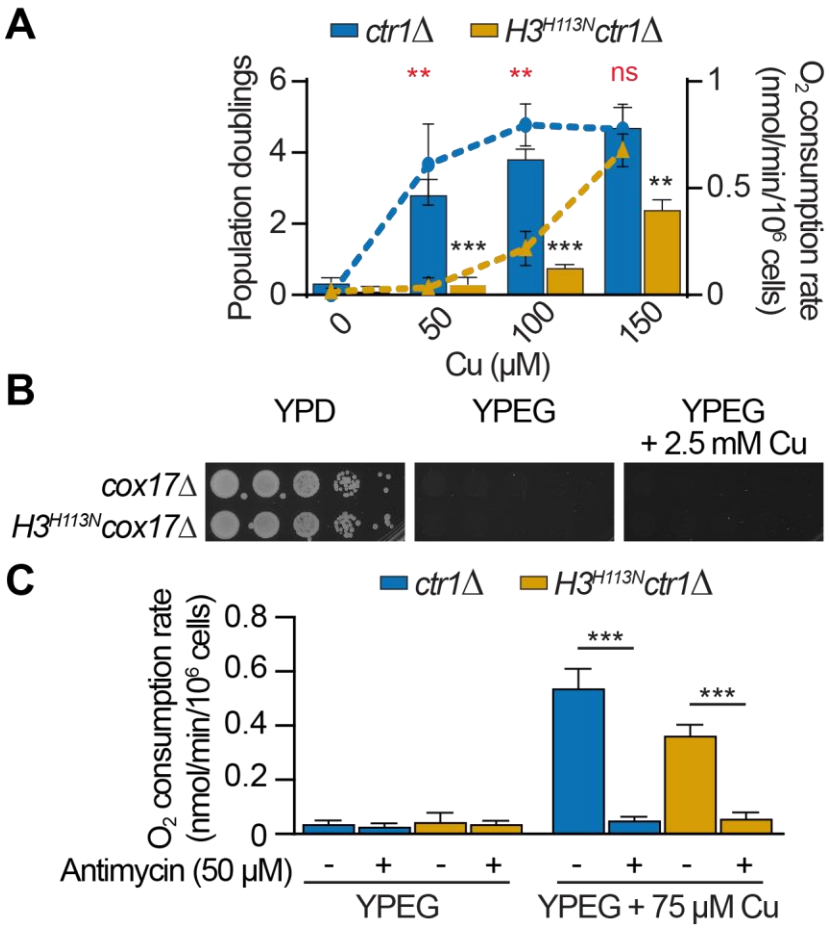


**Figure 4-5: *H3*$^{H113N}$ diminishes copper utilization for mitochondrial respiration. (A)** Growth and oxygen consumption assays in liquid YPEG with increasing amounts of $CuSO_4$. Bar and line graphs show mean population doublings ± SD and oxygen consumption rates after 24 hrs, respectively, from three independent experiments. P value representations are shown in black and red for growth and oxygen consumption measurements, respectively. **(B)** Spot test assay of the indicated strains in media as specified. **(C)** Bar graphs show mean oxygen consumption rates ± SD of the indicated strains from three independent experiments after 6 hrs in liquid YPEG with indicated amount of $CuSO_4$ in presence or absence of Antimycin A. Note that cells were pre-loaded with copper prior to growth in YPEG. **P≤0.01, ***P≤0.001.

### 4.3.3 The *H3$^{H113N}$ctr1*Δ respiratory deficiency is not due to copper buffering capacity, intracellular levels of copper or gene expression differences.

Cup1 is a metallothionein that binds and stores copper and thereby buffers the cytotoxic effects of high concentrations of copper (Jensen et al., 1996). *CUP1* is amplified to varying copy numbers in laboratory strains of yeast (Karin et al., 1984). To exclude the possibility that an increased Cup1 capacity for sequestering copper accounts for the inability of *H3$^{H113N}$ctr1*Δ to efficiently utilize copper for mitochondrial respiration, we introduced a stop codon (F8stop) in every copy of the *CUP1* gene using CRISPR/Cas9. As expected, loss of Cup1 sensitized cells to high concentrations of copper (data not shown) but the *cup1$^{F8stop}$H3$^{H113N}$ctr1*Δ strain still required more copper than did *cup1$^{F8stop}$ctr1*Δ to grow on YPEG (Figure 4-6A).

There were also no differences in intracellular levels of copper or iron between WT and *H3$^{H113N}$* strains in the same stage of growth in YPD (Figure 4-6B) or YPEG (Figure 4-6C) as measured by inductively coupled plasma mass spectrometry (ICP-MS). Deletion of *CTR1* lowered the intracellular levels of copper as expected and to the same extent with or without the *H3H113N* mutation (Figures 4-6B and 4-SC). Addition of excess copper to YPEG increased intracellular levels of copper to similar levels in both *ctr1*Δ and *H3$^{H113N}$ctr1*Δ strains (Figure 4-6C), suggesting that the *H3$^{H113N}$ctr1*Δ growth defect relative to *ctr1*Δ is not due to an inability to uptake copper through alternative routes (Hassett et al., 2000).

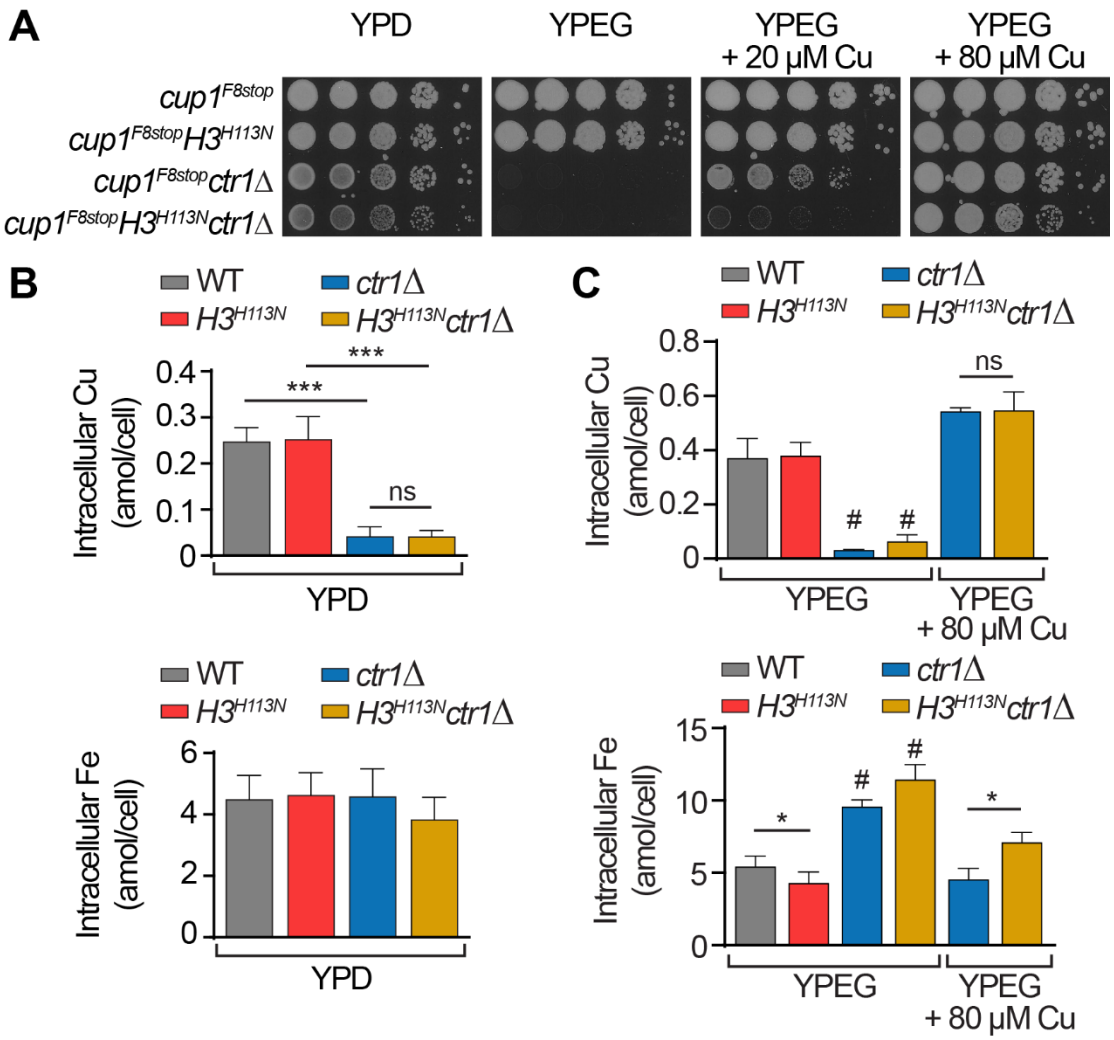


**Figure 4-6: The H3H113N mutation does not affect CUP1 buffering capacity or cellular metal content. (A)** Spot test assay of the indicated strains in media as specified. **(B)** Intracellular copper and iron content measured by ICP-MS for exponentially growing strains in YPD. Data are presented as mean ± SD from 3-6 replicate cultures. **(C)** Intracellular copper and iron content of cells grown in the indicated media for 3-4 doublings for WT and *H3*$^{H113N}$ and 12 hrs for *ctr1*Δ strains. Bar graphs represent mean ± SD from 3-6 replicate cultures. #The *ctr1*Δ strains, which do not grow in non-fermentable media, were incubated in YPEG and assessed for metal content for reference. *P<0.05, ***P≤0.001.

Analysis of gene expression by mRNA-seq revealed very similar global gene expression profiles in WT and *H3*$^{H113N}$ strains in YPEG (Figure 4-7A). The *H3*$^{H113N}$ strain showed comparable changes in gene expression as those observed in WT, including upregulation of genes that function in the ETC and the TCA cycle as well as copper or iron regulons, all of which are required for growth on YPEG (Figures 4-7B and 4-7C). Thus, the *H3H113N* mutation does not interfere with

either sensing of non-fermentable carbon sources or establishing the proper gene expression profiles for their metabolism. The inability of *H3*$^{H113N}$*ctr1*Δ to utilize copper for growth in non-fermentative media is therefore not caused by altered expression of genes important for respiratory growth.

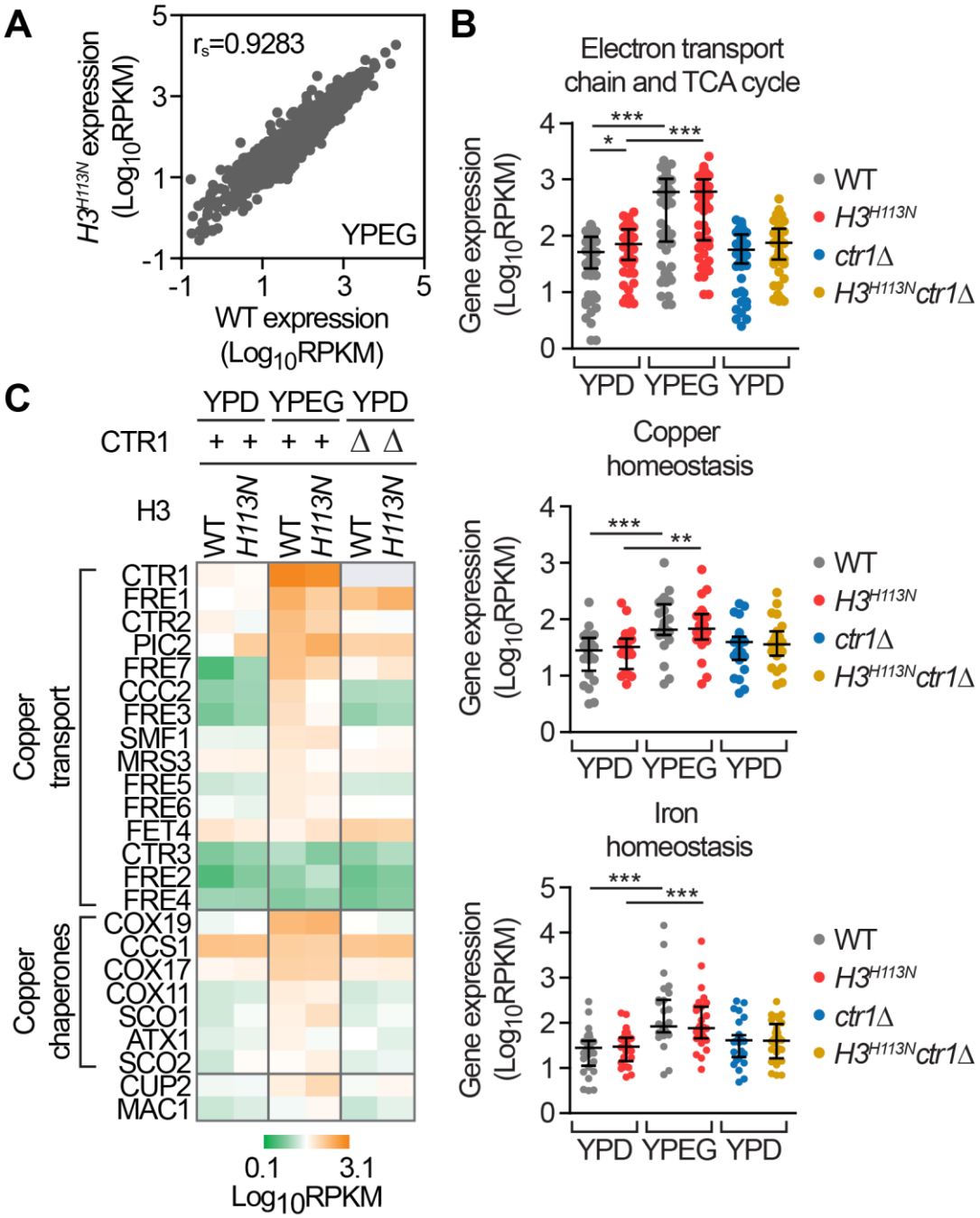


**Figure 4-7: The H3H113N mutation does not affect gene expression in fermentative or non-fermentative media**. **(A)** Scatterplot of average global gene expression values from exponentially growing cells in YPEG from two independent experiments, with Spearman's rank correlation coefficient ($r_s$) as indicated. **(B)** Average mRNA expression levels for three gene sets (Table 4-3) comparing fermentative (YPD) and respiratory (YPEG) growth conditions from two independent experiments. **(C)** Heat map of average mRNA expression levels for copper homeostasis genes (data summarized in Fig 4-2E) from two independent experiments. *P<0.05, **P≤0.01, ***P≤0.001.

### 4.3.4 Diminishing reducing power phenocopies the respiratory deficiency of *H3$^{H113N}$ctr1*Δ mutant.

The increased copper requirement of *H3$^{H113N}$ctr1*Δ for growth on YPEG despite having normal levels of intracellular copper raised the possibility that the levels of cuprous ions, which are required for cuproprotein assembly, is lower in *H3$^{H113N}$ctr1*Δ compared to *ctr1*Δ. However, there are difficulties associated with reliable determination of the oxidation state of intracellular copper in yeast. To indirectly address the effects of the copper oxidation state, we reasoned that decreasing cellular reducing power might phenocopy the respiratory deficiency of *H3$^{H113N}$ctr1*Δ by limiting the availability of electrons for reduction reactions. To disrupt the cellular redox state, we placed the expression of gamma glutamylcysteine synthetase (*GSH1*), which catalyzes the first step in glutathione (GSH) biosynthesis, under the control of the *GAL1* promoter in *ctr1*Δ to generate the *ctr1*Δ*p$^{(GAL1)}$-GSH1* strain. In media without galactose, the expression of *GSH1* is turned off, leading to decreased glutathione levels, a major source of reducing equivalents in the cell. The *ctr1*Δ*p$^{(GAL1)}$-GSH1* strain required more copper to grow on YPEG than *ctr1*Δ alone (Figure 4-8), reminiscent of the *H3$^{H113N}$ctr1*Δ phenotype (Figure 4-4). These data are consistent with decreased availability of cuprous ions, as opposed to decreased abundance of elemental copper, as an explanation for the respiratory deficiency of the *H3$^{H113N}$ctr1*Δ or *ctr1*Δ*p$^{(GAL1)}$-GSH1* strains compared to *ctr1*Δ alone.

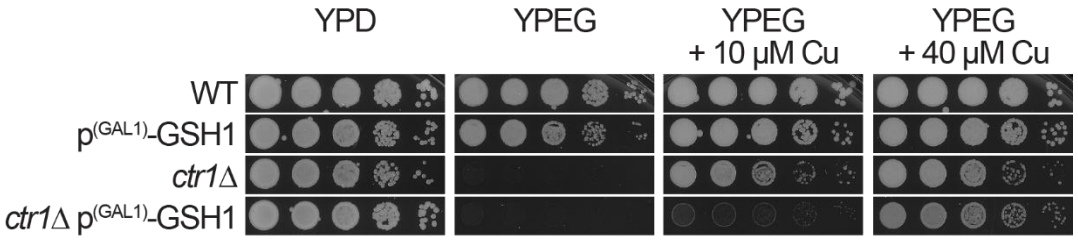


**Figure 4-8: Decreasing reducing power by depletion of glutathione diminishes copper utilization for respiratory growth.** Spot test assay of the indicated strains in media as specified.

### 4.3.5 The H3H113 residue is required for copper-dependent rescue of Sod1 activity and *ccs1*Δ lysine auxotrophy.

We next investigated whether the role of H3H113 residue in copper homeostasis is unique to mitochondrial function or if it more generally regulates copper utilization. Since Sod1 requires copper to function, we first analyzed the enzyme activity of Sod1 using an in-gel assay (Leitch et al., 2009). Sod1 showed a small decrease in activity in $H3^{H113N}$ compared to WT (Figure 4-9A). However, when combined with *ccs1*Δ, *H3H113N* substantially decreased the efficiency of copper utilization for Sod1 function. While *ccs1*Δ essentially abolished Sod1 enzyme activity in minimal media, addition of excess exogenous copper increasingly restored Sod1 activity but much less so in $H3^{H113N}$*ccs1*Δ compared to *ccs1*Δ (Figure 4-9B). This phenotype was not due to differential effects of *H3H113N* on an internal Sod1 disulfide bond that is required for its enzyme activity (Furukawa et al., 2004) (Figure 4-9C).

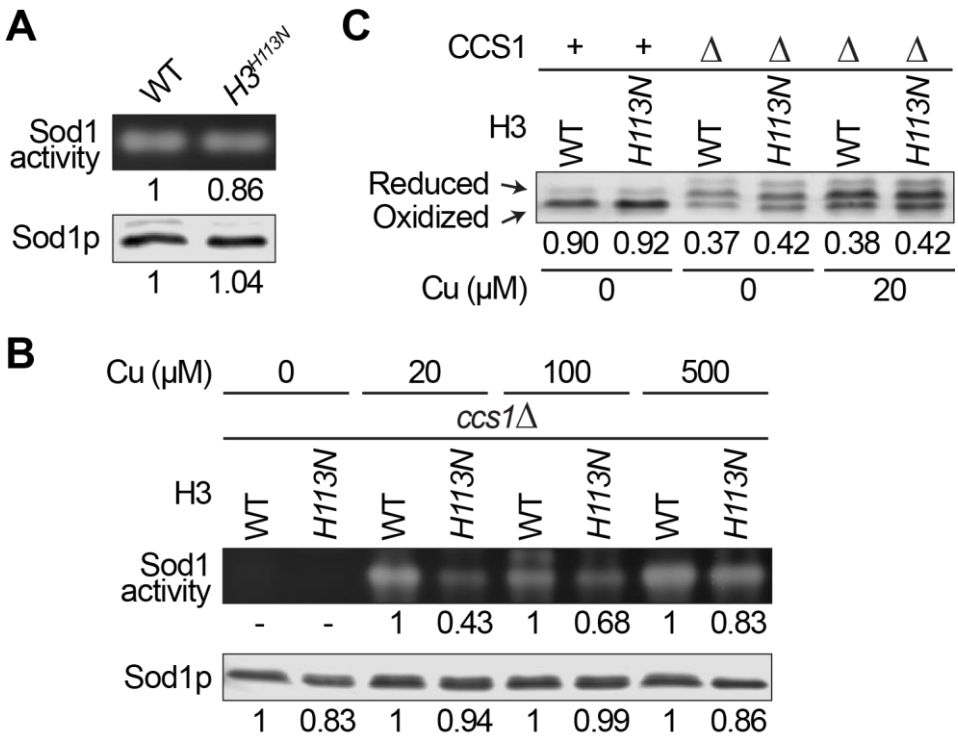


**Figure 4-9: *H3*$^{H113N}$ is deficient in utilizing copper to rescue Sod1 activity. (A)** Sod1 in-gel activity assay (top) and corresponding Sod1p western blot (bottom) for cells grown in SC. Numbers are relative signal intensities compared to WT. **(B)** Same as (A) but for cells grown in minimal medium with the indicated amounts of additional copper. Baseline copper concentration in minimal medium is ~ 0.25 μM. Numbers are relative signal intensities for each pair of bands. Gel and blot shown are representative of three independent experiments. **(C)** Sod1 disulfide bond assay for cells grown for 2 hrs in minimal media with the indicated amount of $CuSO_4$. The reduced Sod1 runs at a different molecular weight because of covalent bonding between iodoacetamide and sulfhydryl group of reduced cysteine residues. Numbers are relative amount of oxidized Sod1 compared to the total Sod1 protein.

Second, deletion of *SOD1* or *CCS1* results in lysine auxotrophy in yeast when grown in the presence of oxygen (Lin and Culotta, 1996) (Figures 4-1 and 4-10A). We found that while the lysine auxotrophy of *ccs1*Δ was rescued by addition of excess exogenous copper, the *H3*$^{H113N}$*ccs1*Δ growth in media lacking lysine was not fully restored even in presence of 500 μM copper (Figure 4-10A), consistent with reduced Sod1 activity in the histone mutant. Deletion of *ASF1* had no effect on copper-dependent rescue of *ccs1*Δ (Figure 4-10A). In stark contrast to the *H3H113N* mutation, reducing intracellular levels of copper by deletion of *CTR1* did not increase the requirement of *ccs1*Δ for exogenous copper (Figure 4-10B). This indicates that Ccs1-mediated

function(s) are more dependent on an intact H3-H3' interface than on total levels of intracellular copper. Addition of manganese, zinc or iron did not rescue *ccs1*Δ growth, confirming the specific disruption of copper utilization (Figure 4-10C). The rescue of *ccs1*Δ strains by exogenous copper is likely through recovering Sod1 function since similar amounts of copper did not rescue the lysine auxotrophy of *sod1*Δ with or without *H3H113N* mutation (Figure 4-10D).

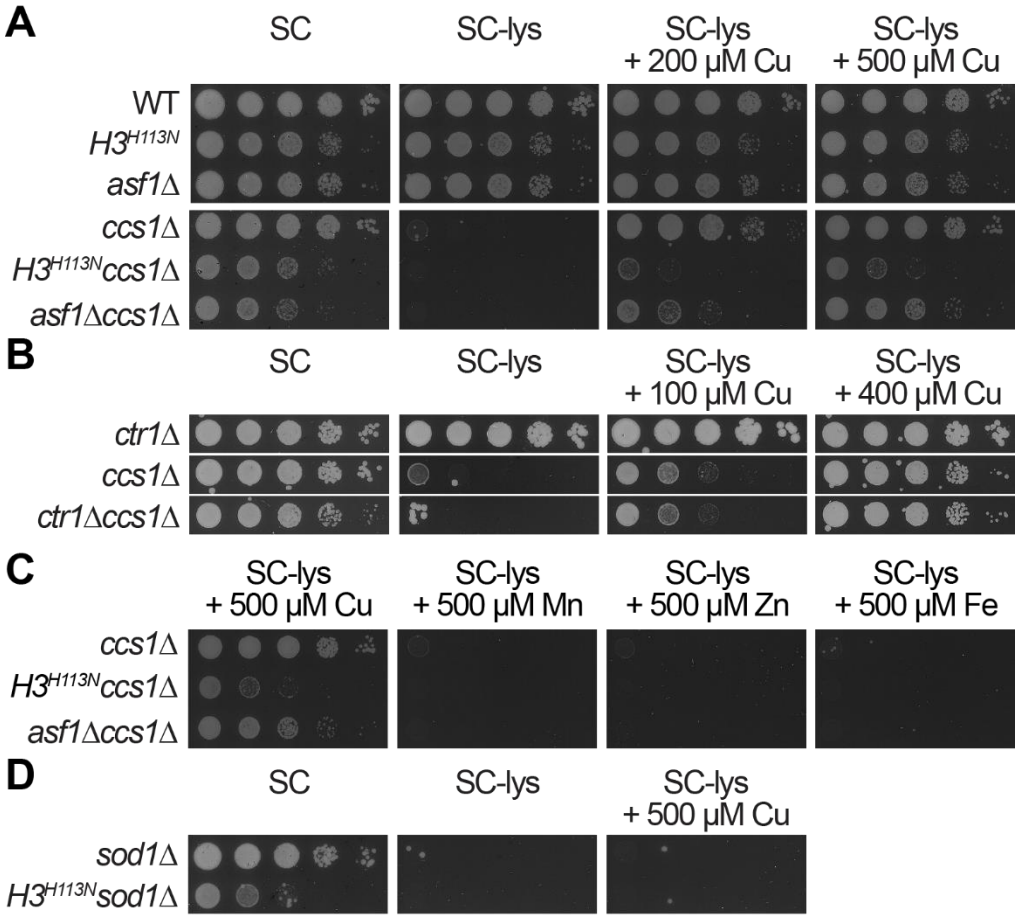


**Figure 4-10: *H3*$^{H113N}$ is deficient in utilizing copper to rescue *ccs1*Δ lysine auxotrophy**. **(A-D)** Spot test assays in the indicated media. Baseline copper concentration in SC medium is ~ 0.16 µM. Note that *ccs1*Δ and *sod1*Δ renders cells auxotrophic for lysine and cannot be rescued by exogenous manganese, zinc or iron.

Similar to growth on agar-plates, *H3*$^{H113N}$*ccs1*Δ showed little improvement in growth in lysine-deficient liquid media supplemented with copper compared to *ccs1*Δ alone (Figure 4-11A). The increased copper requirement of *H3*$^{H113N}$*ccs1*Δ was not due to decreases in intracellular copper

or iron levels (Figures 4-11B and 4-11C), or to increased Cup1 buffering capacity (Figure 4-11D). There were also no significant differences in global gene expression profiles of *ccs1*Δ versus $H3^{H113N}$*ccs1*Δ (Figure 4-12A) including genes involved in lysine biosynthesis, which were induced in lysine deficient media, copper homeostasis or antioxidant defense (Figures 4-12B and 4-12C). Hypoxic conditions restored the growth of *ccs1*Δ and *sod1*Δ in media lacking lysine, confirming the oxygen-dependent toxicity underlying the lysine auxotrophy. The *H3H113N* mutation had no effect on the rescue of *ccs1*Δ and *sod1*Δ lysine auxotrophy by hypoxic conditions (Figure 4-13), indicating that the *H3H113N* defect in lysine synthesis only manifests when copper-dependent Sod1 function is required. Altogether, these results indicate that extra copper can rescue *ccs1*Δ lysine auxotrophy, and that introduction of *H3H113N* mutation decreases the ability of *ccs1*Δ strain to use copper efficiently.

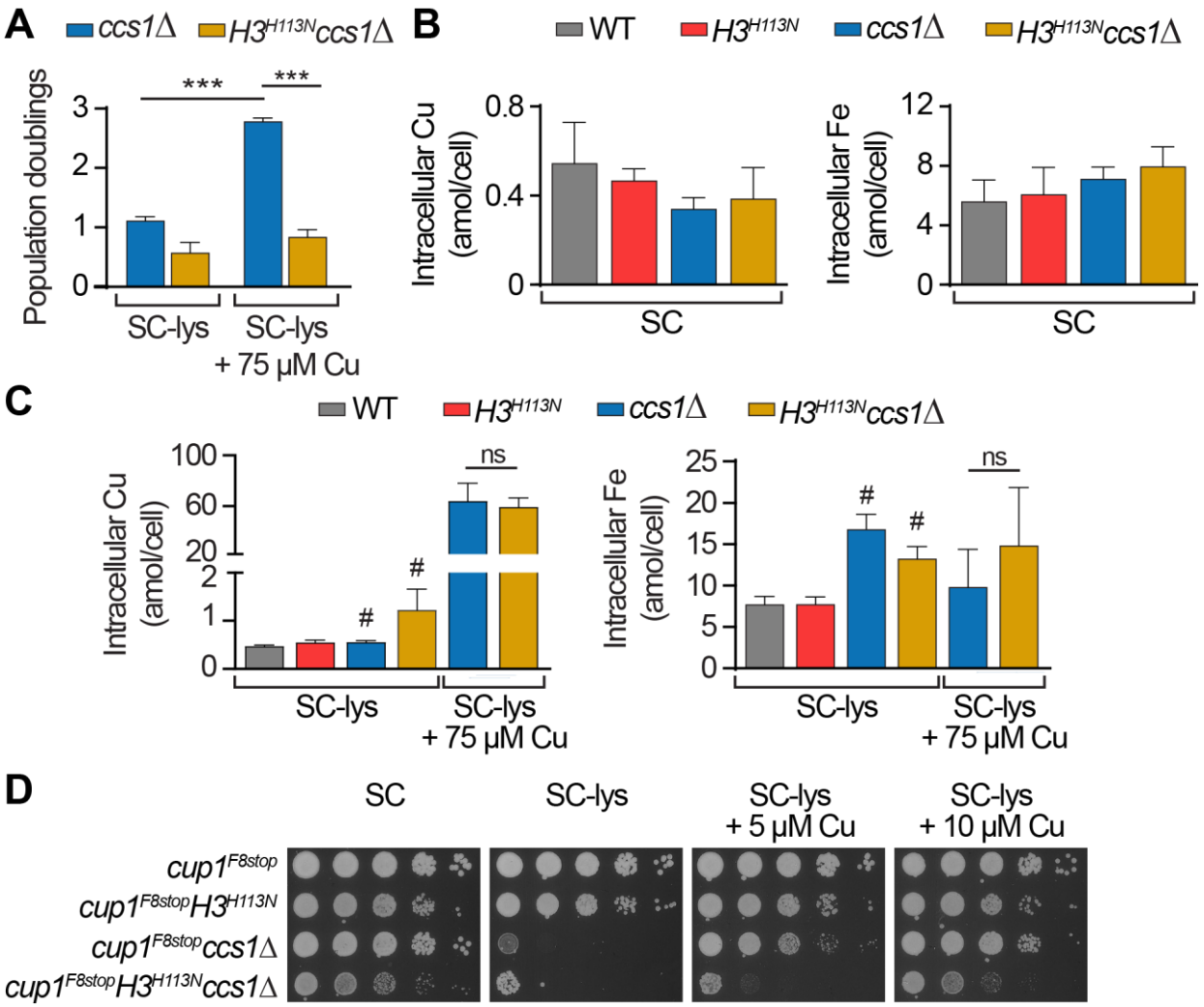


**Figure 4-11: The deficiency of *H3*$^{H113N}$ in utilizing copper to rescue *ccs1*Δ lysine auxotrophy is not due to defective cellular metal content or CUP1 buffering capacity. (A)** Growth assay in the indicated liquid media shown as average population doublings (± SD) after 24 hrs from three independent experiments. **(B)** Intracellular copper and iron content measured by ICP-MS for exponentially growing strains in SC. Data are presented as mean ± SD from 3-6 replicate cultures. **(C)** Intracellular copper and iron content of cells grown in the indicated media for 3-4 doublings for WT and *H3*$^{H113N}$ and 24 hrs for *ccs1*Δ strains. Bar graphs represent mean ± SD from 3-6 replicate cultures. #The *ccs1*Δ strains, which grow minimally in SC-lys media, were assessed for metal content for reference. **(D)** Spot test assay of the indicated strains in media as specified. ***P≤0.001.

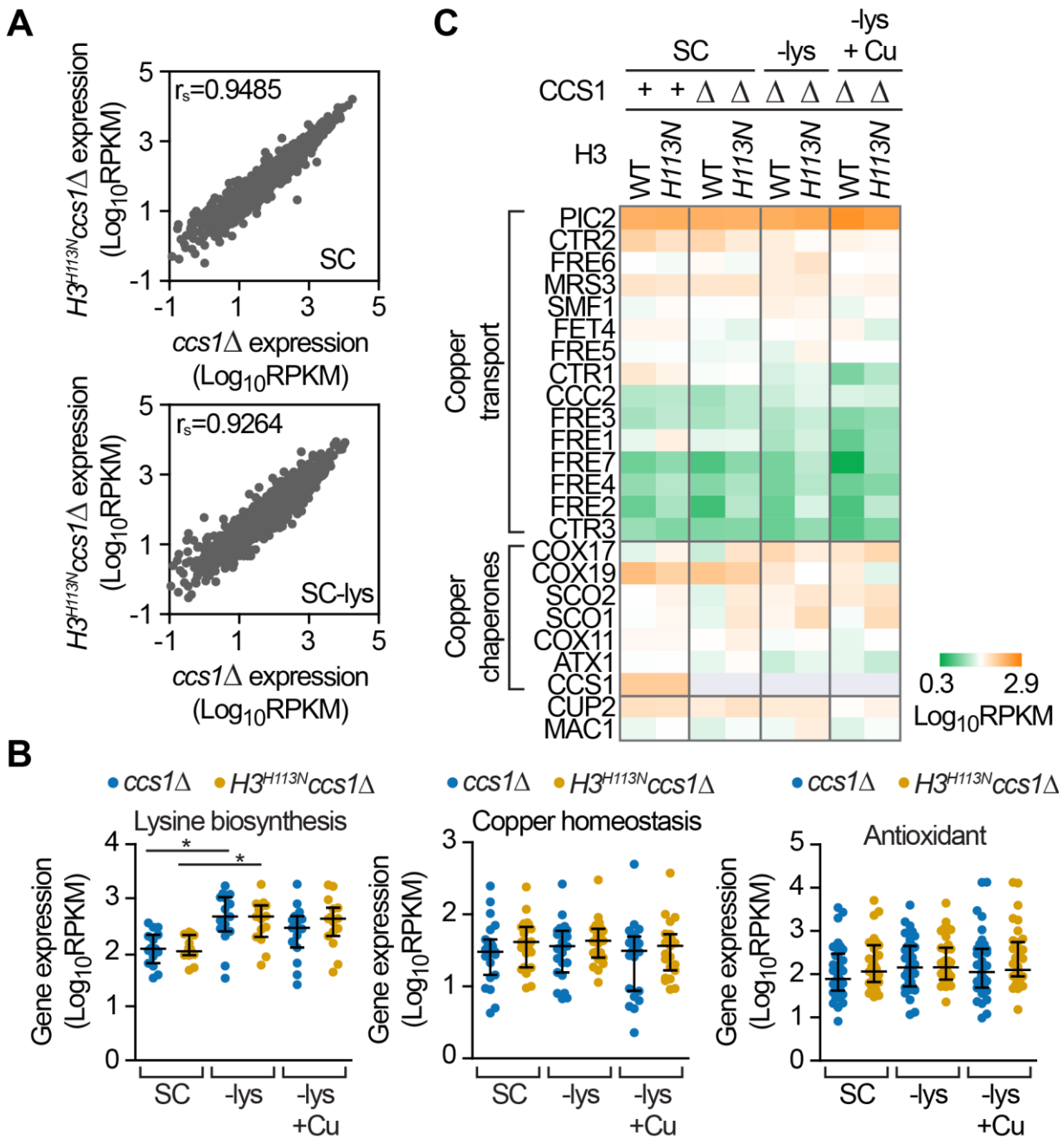


**Figure 4-12: The H3H113N mutation does not affect gene expression in lysine-deficient media**. **(A)** Scatterplot of average global gene expression values from exponentially growing cells in complete (SC) or lysine deficient (SC-lys) media from two independent experiments, with Spearman's rank correlation coefficient ($r_s$) as indicated. **(B)** Average mRNA expression levels for three gene sets (Table 4-3) in cells growing exponentially in the indicated media after 24 hrs from two independent experiments. **(C)** Heat map of average mRNA expression levels for copper homeostasis genes (data summarized in Fig 4-3E) from two independent experiments. *P<0.05.

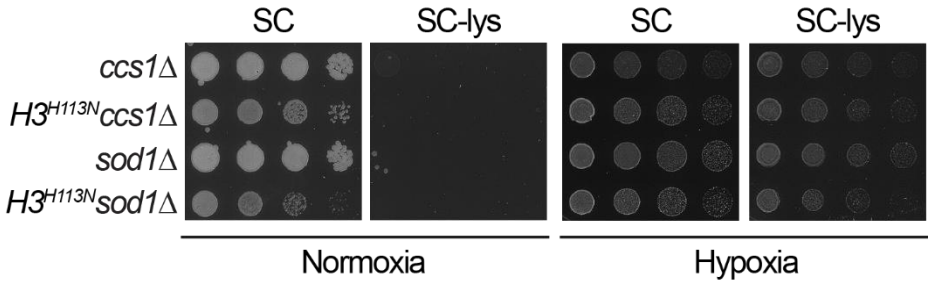


**Figure 4-13: The H3H113N mutation does not prevent the rescue of lysine auxotrophy by hypoxia**. Spot test assay of the indicated strains in SC or SC-lys grown in normoxic or hypoxic conditions.

Consistent with these results, we also found that the growth of $H3^{H113N}ctr1\Delta$ (*note that this is the copper transporter deletion*) on lysine deficient media was adversely affected relative to *ctr1*Δ (Figures 4-14A). Addition of the copper chelator bathocuproinedisulfonic acid (BCS) to decrease copper uptake exacerbated the growth defect of $H3^{H113N}ctr1\Delta$ on lysine-deficient media much more so than that of *ctr1*Δ (Figures 4-14A and 4-14B). This indicates that in limiting copper conditions the *H3H113N* mutation makes cells auxotrophic for lysine. Since as little as 2% of functional Sod1 is required for adequate lysine biosynthesis (Corson et al., 1998), our findings altogether suggest *H3H113N* significantly impairs efficiency of copper utilization for Sod1 function.

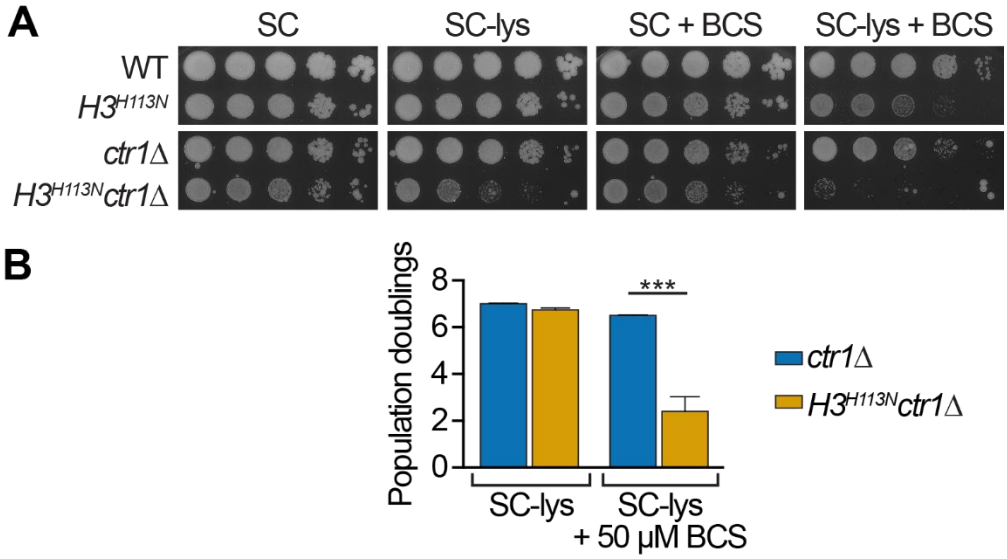


**Figure 4-14: *H3*$^{H113N}$ induces lysine auxotrophy in *ctr1*Δ when copper is limiting**. **(A)** Spot test assays on SC or SC-lys plates containing 1 mM and 10 μM copper chelator (BCS), respectively. **(B)** Average population doublings (±SD) for growth in the indicated media after 36 hrs from three independent experiments. ***P≤0.001.

### 4.3.6 Recombinant Xenopus histone H3-H4 tetramer is a copper reductase.

Since the phenotypes of strains with the *H3H113N* mutation were consistent with loss of the cuprous ion species, we hypothesized that histone H3 may be an enzyme that maintains cuprous ions for the cell by catalyzing reduction of $Cu^{2+}$ to $Cu^{1+}$. To test this hypothesis, we assembled and purified a histone H3-H4 tetramer from recombinant *Xenopus laevis* histones H3 and H4, which are identical to human H3.2 and H4 histones respectively, using the standard salt dialysis method (Figure 4-15A) (Luger et al., 1999). We also empirically developed a colorimetric assay to measure production of $Cu^{1+}$ based on the ability of the copper chelator neocuproine (NC) to chelate $Cu^{1+}$ quantitatively. The NC•$Cu^{1+}$ complex has a yellow color that absorbs light at 448 nm (Figure 4-15B). We used tris(2-carboxyethyl)phosphine (TCEP) as a source of electrons (i.e., reducing co-factor) because of its low rate of spontaneous copper reduction.

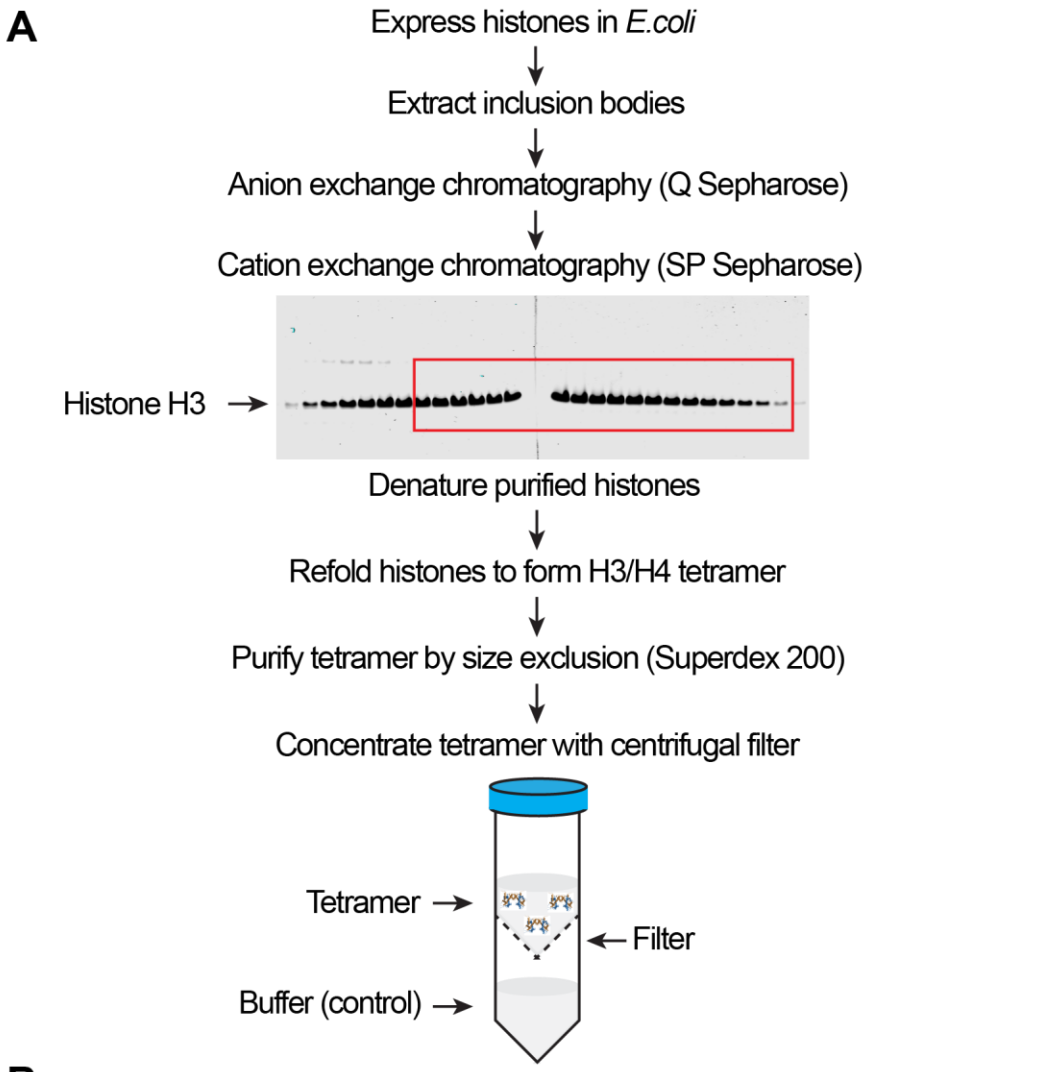
A
Express histones in E.coli
Extract inclusion bodies
Anion exchange chromatography (Q Sepharose)
Cation exchange chromatography (SP Sepharose)
Histone H3
Denature purified histones
Refold histones to form H3/H4 tetramer
Purify tetramer by size exclusion (Superdex 200)
Concentrate tetramer with centrifugal filter
Tetramer
Filter
Buffer (control)
B
TCEPred or Dihydrolipoic Acid
Tetramer
Neocuproine (NC)
NC•Cu1+
TCEPox
or
Lipoic Acid
Cu2+

**Figure 4-15: Experimental outline of H3.2/H4 tetramer formation and *in vitro* copper reductase assay. (A)** The procedure for preparation of histones and assembly of tetramer is outlined. **(B)** Graphical representation of the copper reductase assay.

We performed the assay by first mixing the tetramer, TCEP and NC in 100 mM NaCl and then adding cupric chloride ($CuCl_2$) in a sodium tricine buffer (pH=7.4). Upon addition of copper, we observed a time-dependent increase in production of $Cu^{1+}$ as indicated by increasing yellow coloration of the reaction mixture containing the H3-H4 tetramer but not the control buffer (Figure 4-16A). Figure 4-16B shows a typical reaction profile for a tetramer versus buffer alone. The earliest measurement is 2.2 seconds (s) after addition of copper by which time a significant fraction of copper is already reduced (Figure 4-16B). The reaction plateaus at later time points due to near full consumption of TCEP. Because ~75% of total $Cu^{1+}$ produced occurs within the first 30 seconds (Figure 4-16B inset), we focused on this time interval in subsequent experiments. The line and shadings represent the mean and standard deviations of at least three assays, respectively. We detected no significant activity in the absence of TCEP and increasing activity with increasing amounts of TCEP, indicating that TCEP provides the electrons for reduction of copper (Figure 4-17A). The enzymatic activity was specific to the tetramer since unassembled histone H3 or the yeast H2A did not show activity (Figure 4-17B). The tetramer's enzymatic activity was heat labile as boiling the tetramer prior to the assay abolished copper reduction (Figure 4-17C). The Xenopus/human tetramer can also utilize NADPH as a co-factor to catalyze copper reduction in an assay condition further optimized to prevent NADPH from reducing copper directly (see Methods)(Figure 4-17D). We did not detect iron reductase activity when using $FeCl_3$ and a ferrous ion chelator, indicating that the reaction is specific to copper under these conditions (data not shown).

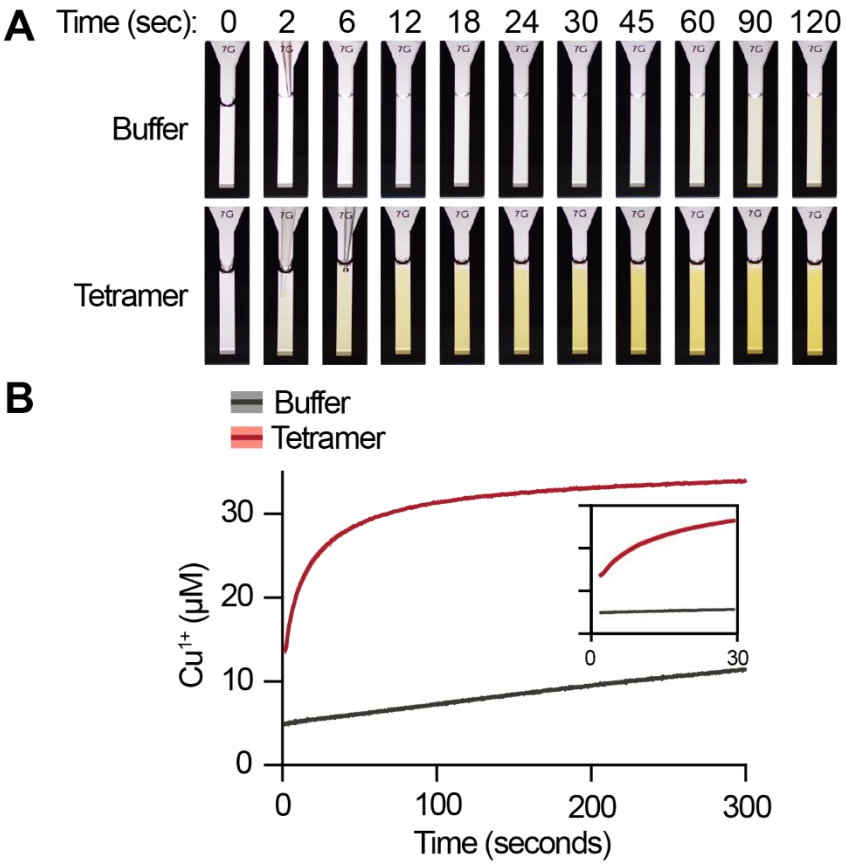


**Figure 4-16: The human H3.2/H4 tetramer enhances copper reduction**. **(A)** Photographic representation of *in vitro* copper reductase assay at indicated times. Control buffer or H3.2/H4 tetramer were reacted with 100 μM TCEP and 1 mM $CuCl_2$. Note that reduction of copper occurs as soon as it is added to the tetramer reaction mix. **(B)** Reaction profiles of 1 μM H3.2/H4 tetramer or buffer reacted with 1 mM $CuCl_2$ and 20 μM TCEP. Lines and shading represent the mean ± SD of 3-5 assays. Inset shows data from the initial 30 seconds of the same reaction.

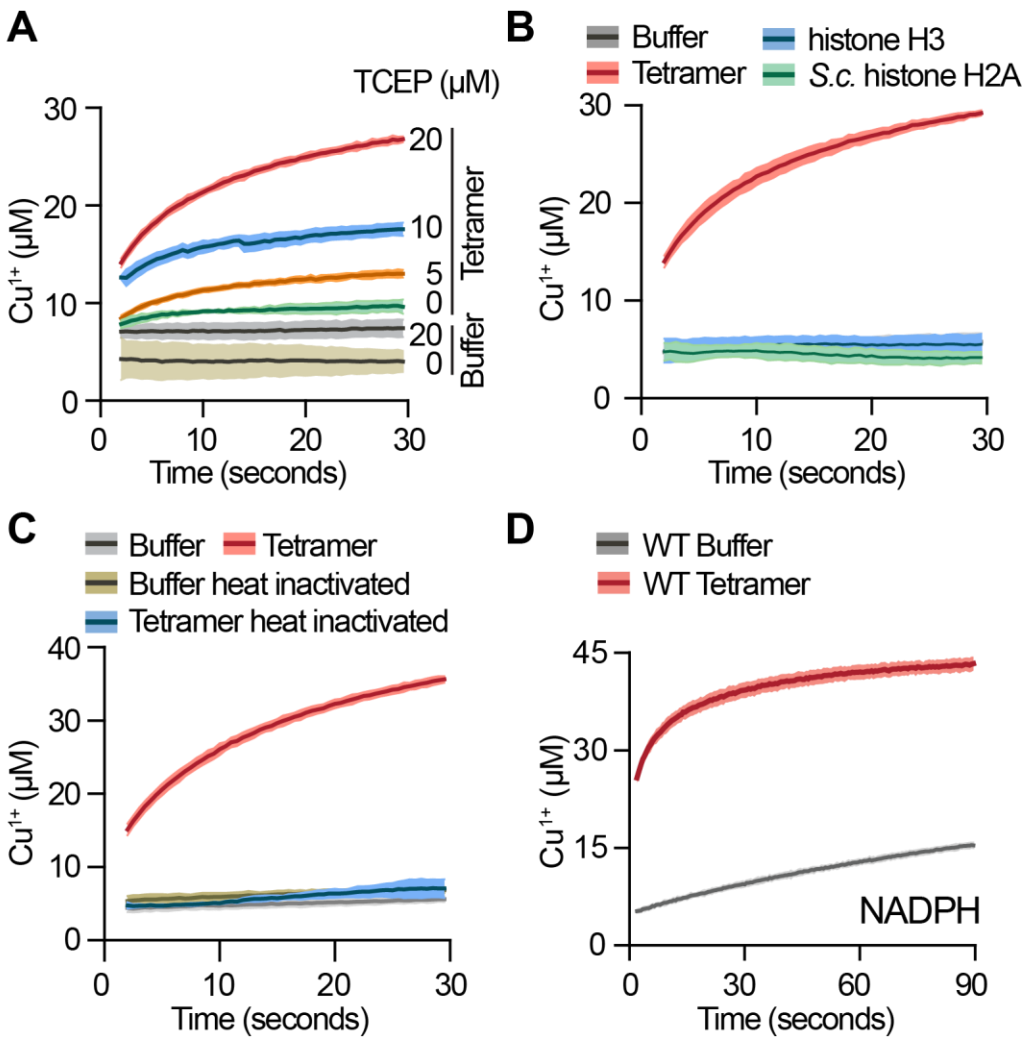


**Figure 4-17: The human H3.2/H4 tetramer is a copper reductase**. **(A)** Reaction profiles of 1 μM H3.2/H4 tetramer or buffer reacted with 1 mM $CuCl_2$ and the indicated TCEP concentrations. Lines and shading represent the mean ± SD of 3-5 assays. **(B)** Same as in (A) including the reaction profiles of 1 μM monomeric histone H3.2 and *S.cerevisiae* histone H2A. **(C)** Same as in (B) except that the H3.2/H4 tetramer and control buffer were incubated at 100°C for 15 minutes. **(D)** Same as in (B) except with 0.5 mM $CuCl_2$ and 30 μM NADPH.

Within the H3-H4 tetramer, the H3C110 residues may get oxidized to form a disulfide bond (Camerini-Otero and Felsenfeld, 1977), in the process causing the reduction of a second reaction component. This raised the possibility that any set of redox active cysteine residues may facilitate reduction of copper in our reaction conditions. To address this possibility, we performed the copper reduction assay either with GSH, present in equimolar amount to the tetramer's cysteine content,

or RNase A, which contains four disulfide bonds (Klink et al., 2000), at the same concentration as the tetramer and detected no significant copper reductase activity above background (Figures 4-18A and 4-18B).

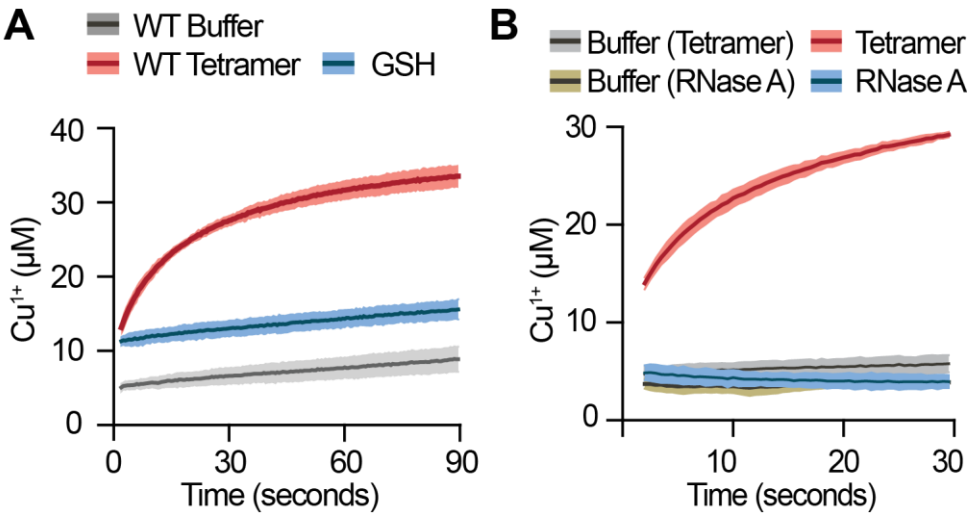


**Figure 4-18: Redox-active thiols do not catalyze copper reduction like the H3.2/H4 tetramer**. **(A)** Reaction profiles of 1 μM H3.2/H4 tetramer, 2 μM GSH, or buffer reacted with 1 mM $CuCl_2$ and 20 μM TCEP. Lines and shading represent the mean ± SD of 3-5 assays. **(A)** Same as in (B) including the reaction profiles for 1 μM FPLC-purified RNase A.

### 4.3.7 Loss of cysteine 110 in the H3-H3' interface affects enzyme activity.

We next examined the role of the pair of cysteine residues in the H3-H3' interface, residues which are common copper-coordinating ligands in other proteins, by examining the effects of the histone *H3C110A* on the *in vitro* enzyme activity of the Xenopus H3-H4 tetramer. The tetramer with histone *H3C110A* mutation assembled similarly to WT tetramer as indicated by their elution profiles from the size exclusion column (Figure 4-19A). However, the *H3C110A* tetramer had substantially decreased copper reductase activity in our assay condition compared to buffer alone (Figure 4-19B), indicating that H3C110 is very important for robust enzymatic activity *in vitro*.

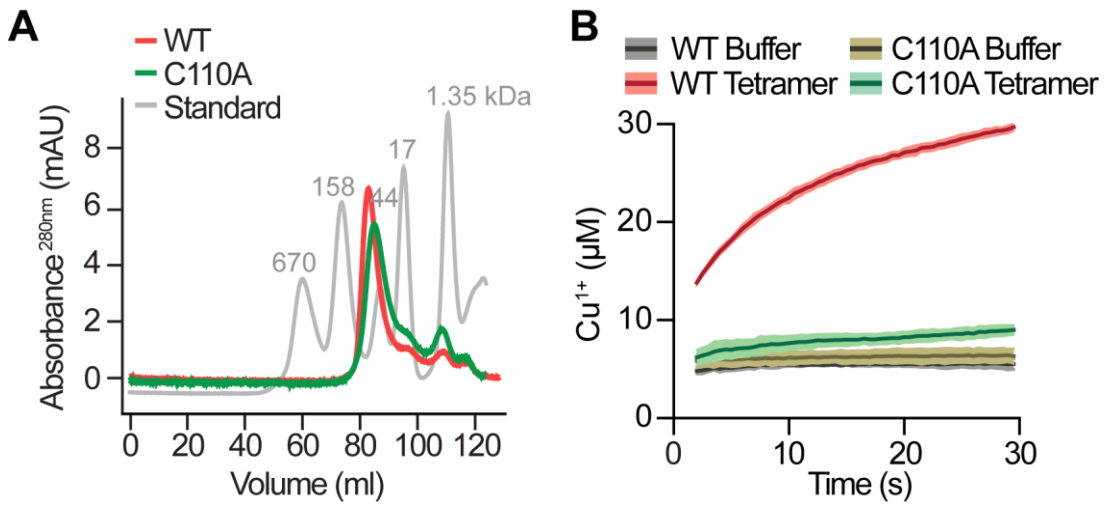


**Figure 4-19: The *H3C110A* mutation in the H3-H3' interface alters the enzyme activity of the tetramer**. **(A)** FPLC elution profiles of the indicated H3.2/H4 tetramers and a protein standard. **(B)** Reaction profiles of 1 μM of the indicated H3.2/H4 tetramers or control buffers, combined with 1 mM $CuCl_2$ in the presence of 20 μM TCEP. Lines and shading represent the mean ± SD of 3-5 assays.

### 4.3.8 Recombinant yeast H3-H4 (yH3-H4) tetramer has copper reductase activity.

We also assembled and tested recombinant yH3-H4 tetramers for copper reductase activity in a reaction condition that was optimized for yeast tetramers (see Methods). The yeast tetramer displayed heat-labile enzymatic activity *in vitro* (Figure 4-20) although the overall activity was much less than the Xenopus tetramer. We then examined the role of the histidine residue in the H3-H3' interface, which like C110, is known to participate in copper-coordinating interactions. We assembled yH3-H4 tetramers containing mutant histones *H3H113N* and *H3H113Y* and tested their effects on *in vitro* copper reduction. Both histidine mutations abrogated copper reductase activity of the tetramer (Figure 4-20C and 4-20D), albeit with a less substantial effect compared to *H3C110A* in the Xenopus tetramer (Figure 4-19B). Altogether, the data indicate that H3C110, in the histones that have it, and H3H113 are important for the enzyme activity of the eukaryotic tetramer.

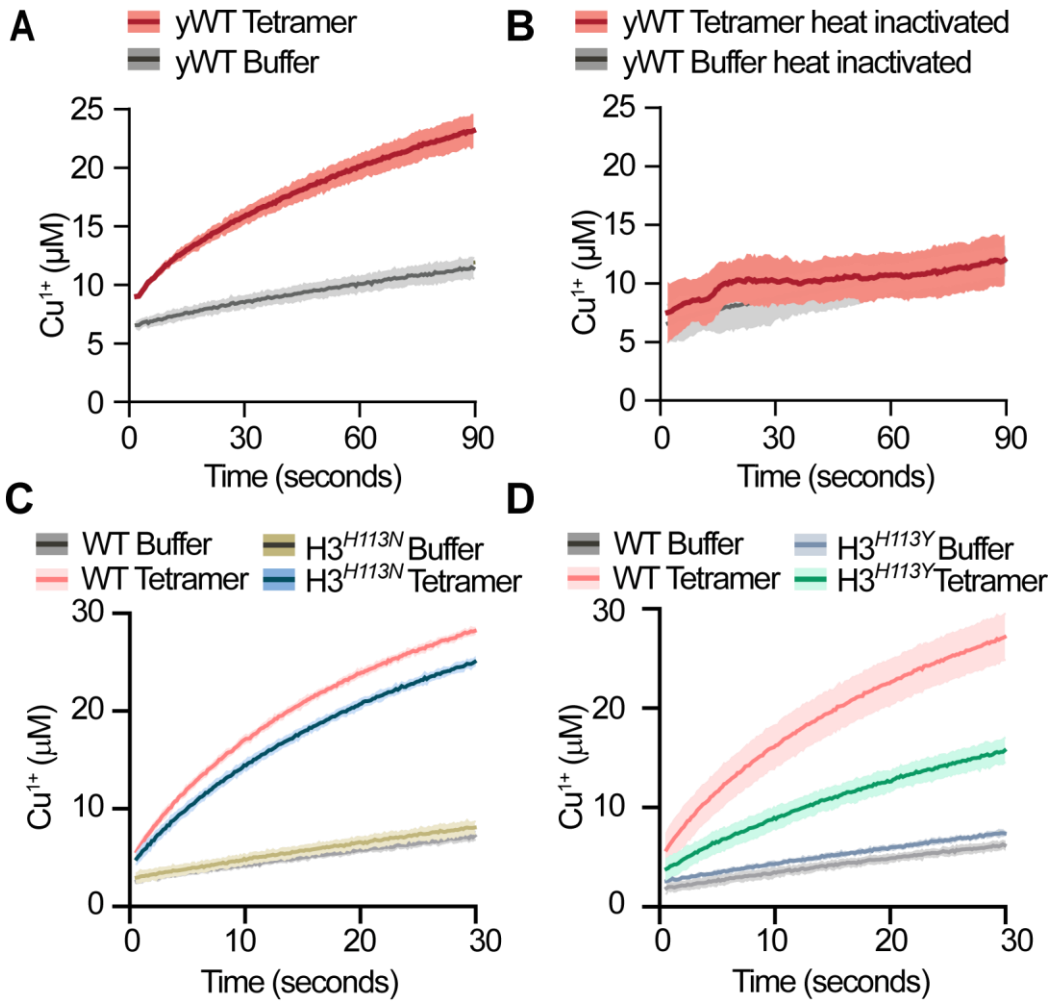


**Figure 4-20: Enzymatic activity of yeast H3-H4 tetramers**. **(A, C, and D)** Reaction profiles of 5 μM of the indicated yeast tetramers or buffer reacted with 0.5 mM $CuCl_2$ and 30 μM TCEP. Lines and shading represent the mean ± SD of 3-5 assays. **(B)** Same as A but tetramers and buffer were heat-inactivated prior to the reaction.

Notably, the yeast histone H3 lacks the C110 residue, instead containing an alanine at this position, reminiscent of the Xenopus *H3C110A* mutant. Despite this and several sequence differences in the C-terminal region of histone H3 between yeast and Xenopus/human, the yH3-H4 tetramer is also a copper reductase (Figure 4-20). We next asked whether substituting the A110 residue of the yeast histone H3 with a cysteine (*H3A110C*) would be sufficient to increase *in vitro* copper reductase activity, since the loss of the equivalent cysteine impaired activity of the Xenopus

tetramer. Indeed, the yeast *H3A110C* tetramer substantially increased copper reductase activity (Figure 4-21). Even diluting the *H3A110C* tetramer 25-fold to 0.2 µM, compared to the 5 µM concentration of the WT tetramer, resulted in a large increase in the rate of copper reduction (Figure 4-21). This observation further indicates that the cysteine at position 110 in the tetramer significantly contributes to copper reduction.

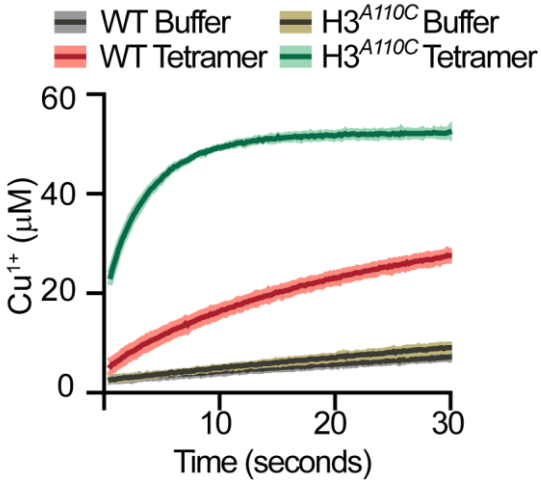


**Figure 4-21: Enhancement of copper reductase activity by the *H3A110C* mutation.** Reaction profiles of 5 µM yeast WT H3/H4 and 0.2 µM H3A110C/H4 tetramers or buffer reacted with 0.5 mM $CuCl_2$ and 30 µM TCEP. Lines and shading represent the mean ± SD of 3-5 assays. Note that the H3A110C tetramer is 1/25 as concentrated as the WT tetramer.

### 4.3.9 The H3A110C mutation enhances copper utilization for respiratory growth.

The substantial enhancement of copper reductase activity of the yeast H3-H4 tetramer when C110 is introduced prompted us to examine whether the *H3A110C* mutation would also enhance copper utilization in cells. We therefore examined the effect of cysteine introduction on the ability to support respiratory growth when copper is limiting. The yeast $H3^{A110C}$ strain did not grow differently than WT cells in YPEG, however, even when extracellular copper is depleted via addition of the copper chelator bathocuproinedisulfonic acid (BCS) to the media (Figure 4-22A). We reasoned that depletion of total copper abundance does not necessarily result in a relative

decrease in the levels of the reduced cuprous ion, thereby precluding any potential advantage of an increased copper reductase function due to the *H3A110C* mutation. We therefore combined the BCS-mediated copper depletion with disruption of cellular reducing power by transcriptionally repressing *GSH1*. Similar to the respiratory growth defect of the *ctr1*Δ*p*$^{(GAL1)}$*-GSH1* strain (Figure 4-8), copper depletion resulted in a growth defect of *p*$^{(GAL1)}$*-GSH1* strain in YPEG (Figure 4-22B). Importantly however, the *H3*$^{A110C}$*p*$^{(GAL1)}$*-GSH1* grew substantially better than the *p*$^{(GAL1)}$*-GSH1* in YPEG, consistent with the *H3A110C* mutation enhancing copper utilization when the reduced cuprous ions are depleted.

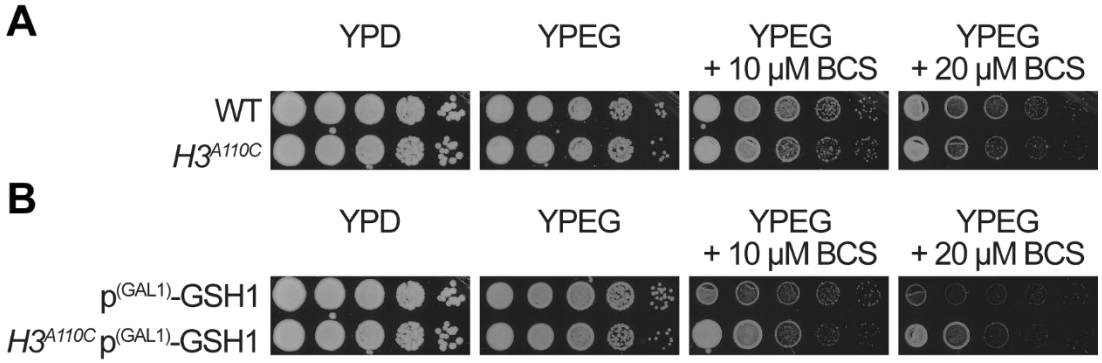


**Figure 4-22: *H3*$^{A110C}$ enhances copper utilization for respiratory growth**. **(A and B)** Spot test assays in the indicated media. Baseline copper concentration in YPD and YPEG medium is ~ 1 µM.

### 4.3.10 Decreasing histone H3 dosage impairs copper homeostasis.

The finding that the H3-H4 tetramer within the nucleosome generates cuprous ions for the cell suggests that decreasing the dosage of histones, and therefore nucleosomes, should decrease availability of cuprous ions and thus the efficiency of copper usage. To test this, we deleted one of the two copies of the histone H3 and H4 genes (*hht1-hhf1*Δ) in WT cells or in the context of *ctr1*Δ. We confirmed that the *hht1-hhf1*Δ strain had less H3 and H4 proteins (Figure 4-23A) and increased susceptibility to chromatin digestion by MNase (Figure 4-23B), consistent with decreased average number of nucleosomes. Deletion of *HHT1* and *HHF1* did not significantly affect growth in YPD

(Figure 4-23C). However, as predicted, combination of *hht1-hhf1*Δ with *ctr1*Δ required more copper for growth on YPEG (Figure 4-23D) and was more sensitive to depletion of copper in lysine deficient medium (Figure 4-23E) compared to *ctr1*Δ alone. These data indicate that the number of nucleosomes, and therefore the number of copper reductase enzymes, affects intracellular copper dependent activities.

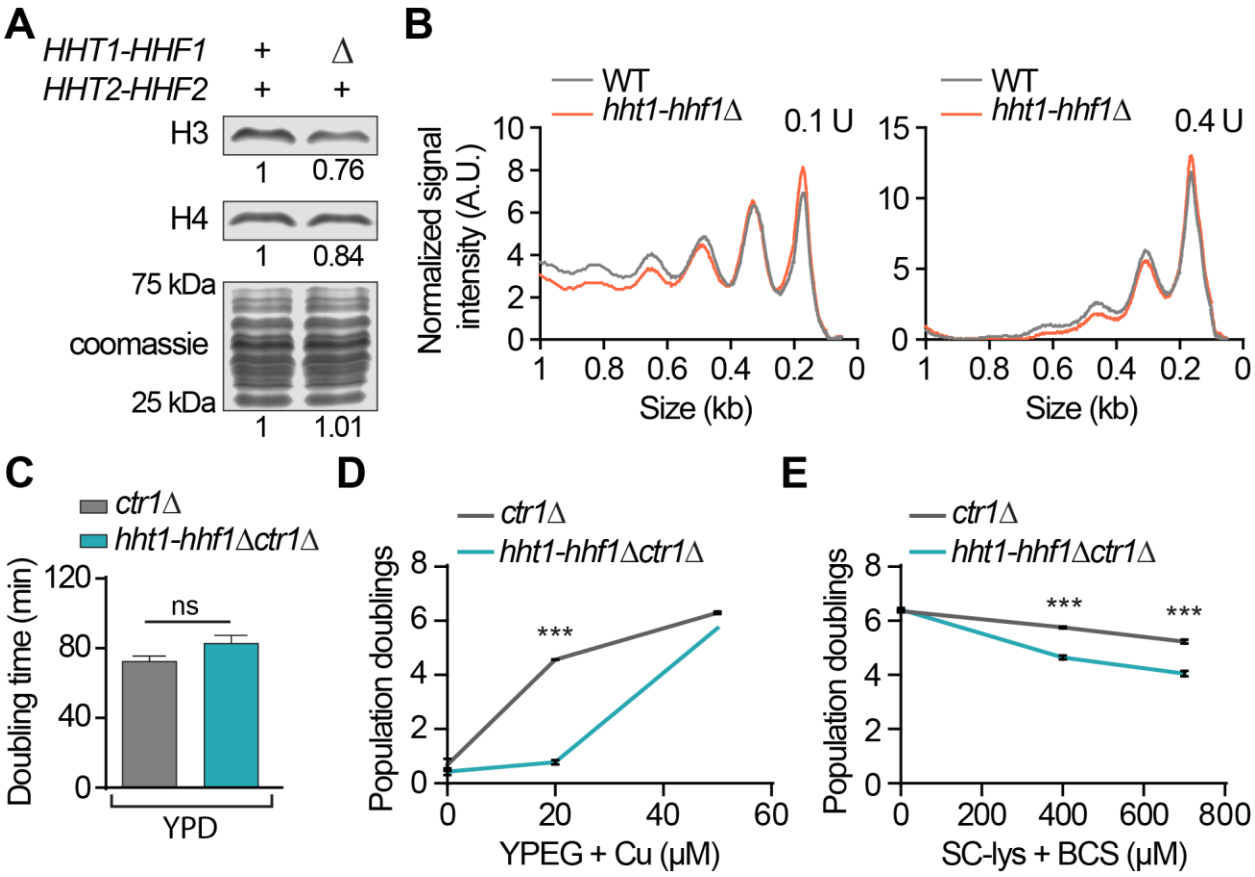


**Figure 4-23: Deletion of one copy of histone H3 and H4 genes renders cells defective in utilizing copper for respiratory growth. (A)** Western blots of histone H3 and H4 and coomassie-stained 15% SDS-PAGE (showing gel segment for 25-75 kDa) including the relative signal intensity for the indicated strains. **(B)** Quantitative representation of the signal intensity profiles from chromatin digested with the indicated amounts of MNase. A.U.: arbitrary units. **(C)** Average doubling times (± SD) from steady-state growth in liquid YPD from three replicate cultures. **(D)** Average population doublings (± SD) for growth in liquid YPEG with increasing amounts of $CuSO_4$ after 36 hrs from three replicate cultures. **(E)** Average population doublings (±SD) for growth in liquid SC-lys with increasing amounts of BCS after 24 hrs from three replicate cultures. ***P≤0.001.

## 4.4 Discussion

Histones were considered initially to only be structural constituents of the eukaryotic genome, serving to package the large amount of DNA into the confines of the nucleus. Pioneering experiments in the 1980s and 90s revealed that histones also function in regulating gene expression and essentially all other processes that contend with DNA through controlling access to certain DNA sequences and post-translational modifications (Felsenfeld, 1992; Grunstein, 1997; Jenuwein and Allis, 2001). We now show that the histone H3-H4 tetramer, a sub-complex of the nucleosome, also catalyzes reduction of $Cu^{2+}$ to $Cu^{1+}$, suggesting that eukaryotic chromatin could be a major nucleocytoplasmic oxidoreductase that provides cuprous ions for cell biology. Considering the importance of copper to processes as diverse as tissue integrity, methylation cycle, iron homeostasis and melanin and neurotransmitter syntheses in mammals (Finney et al., 2014; Nevitt et al., 2012; Winston and Jaiser, 2008), the enzymatic activity of histones could have wide-ranging effects at molecular, cellular, and tissue levels with consequences for organismal physiology and disease.

The enzymatic activity of the H3-H4 tetramer suggests the protein complex has novel features that were previously unsuspected but must be fully discerned through future studies. An important feature is the location of the enzyme active site, which we favor to be at the interface of the two H3 proteins for multiple reasons. First, the H3-H3' interface appears to be under an evolutionary selective pressure beyond what is required for thermodynamic stability of the tetramer (Ramachandran et al., 2011). The active site of an enzyme could constitute such a selective pressure. Second, the positioning of H3H113 at the end of an α-helix is an arrangement that is found commonly in oxidoreductases such as thioredoxin (Hol, 1985). H3H113 may stabilize

the α2 helix dipole near the H3-H3' interface, which may enhance transfer of electrons (Galoppini and Fox, 1996). Third, the potential requirement of H3C110 for the enzymatic activity of histones that contain it, further supports the location of the active site at the H3-H3' interface. The C110 residues from apposing H3s within the tetramer are 6.2Å apart in the crystal structure but *in vivo* can form a disulfide bond, the length of which is 2.05Å (Camerini-Otero and Felsenfeld, 1977). Interestingly, the mechanism of electron transfer by other oxidoreductase enzymes such as thioredoxin reductase (Holmgren, 1995) or ribonucleotide reductase (Kolberg et al., 2004) involves cyclical oxidation and reduction of internal cysteine residues through disulfide bond formation. Yet in others, such as Sod1, the redox reactive cysteine residues play a regulatory role rather than participating in the electron transfer reaction (Furukawa et al., 2004). Whether oxidation/reduction of H3C110 residues is directly involved in electron transfer by the H3-H4 tetramer remains to be determined. Nonetheless, formation of a disulfide linkage requires significant distortion of the conformation of the tetramer, suggesting that the structure of the tetramer, especially around the 4-helix bundle within the nucleosome, is dynamic (Luger et al., 1997). H3C110 is in the center of the bundle and buried within the nucleosome structure but is also readily accessible as evidenced by reactivity with small molecular probes (Garcia-Gimenez et al., 2013). Thus, the potential flexibility of the 4-helix bundle, redox reactivity of H3C110 and accessibility of the H3-H3' interface residues could be important for enzyme activity and/or its regulation. Fourth, the H3-H3' interface coordinates metals such as zinc, cobalt, nickel (Adamczyk et al., 2007) or mercury (Lambert et al., 1999) when incubated with these metals *in vitro*. Finally, the H3-H3' interface assembles *in vivo* only when histones are incorporated into a nucleosome. Therefore, the commencement of enzymatic activity would be inextricably coupled to the protection of DNA as it wraps on the outer surface of the nucleosome. Such a coupling may be a

beneficial adaptation in species that require reduced intracellular copper as a failsafe mechanism to avoid potentially damaging effects of copper.

As a reductase, the H3-H4 tetramer must extract electrons from reducing co-factors, pass them through the protein and transfer them to copper ions at the active site. How the tetramer achieves this is unclear but the position at which electrons are extracted from the reducing co-factor need not be near the active site. In addition, since cellular copper ions are mostly bound by proteins (Rae et al., 1999), copper is likely delivered to and taken away from histones through as-yet-to-be-identified protein or small molecule chaperones. Furthermore, we have assessed the activity of one canonical histone H3, namely, H3.2. However, H3 has several variants with intriguing sequence differences that are functionally characterized based on their modes of incorporation into chromatin, position along the chromosome or expression pattern. Whether the histone H3 variants and/or their location across the genome (e.g., euchromatin vs. heterochromatin) influence the kinetic properties or co-factor requirements of the H3-H4 tetramer enzyme activity remain interesting but open questions. Like copper, iron is also used commonly in its ferrous form and is an important bioessential element for numerous processes including epigenetic gene regulation (Cartularo and Costa, 2014). Although we did not detect any iron reductase activity in our assay condition with H3.2-containing tetramers, we cannot rule out the ability of the tetramer with canonical or variant histones to catalyze reduction of iron in certain conditions or organisms.

Interestingly, *S. cerevisiae* and a number of other fungi possess histone H3 proteins that lack the otherwise highly conserved cysteine residue equivalent to H3C110 in other eukaryotes (data not shown). Other than missing H3C110, the C-terminal region of yeast H3 has additional sequence differences compared to the Xenopus/human H3 (Figure 4-2B, gray highlights). Despite

the lack of H3C110, the yH3-H4 tetramer also reduces copper *in vitro*, albeit with overall less activity compared to the Xenopus/human tetramers. It is conceivable that enzymatic activity of tetramers with histone H3 proteins that lack C110 may proceed through a different reaction mechanism should C110 prove to have a catalytic role. It is also possible that the yH3-H4 tetramer requires additional co-factors or more accurate biochemical reconstitution of cellular conditions for robust activity. These considerations may also explain why the *H3H113N* mutation has a minor effect on the tetramer *in vitro* activity, compared to the effect of *H3C110A*, but displays robust genetic phenotypes in *S. cerevisiae* that are consistent with having a significant impact on copper reductase activity *in vivo*. Our data indicate that the yeast *H3H113N* is a hypomorphic mutation, and may therefore manifest its adverse effects on the enzyme activity in the context of the chromatin polymer in the nuclear milieu. It is possible that a complete loss of enzyme function would be lethal in yeast as several residues in the vicinity of H3-H3' interface are required for viability (Dai et al., 2008).

Eukaryotes evolved from an archaeon that had a small genome but possessed ancestral histones without extended, positively-charged N-terminal tails or abundant posttranslational modifications. This evolutionary timeline questions whether the present-day functions of histones were also the reasons histones evolved to bind DNA and form chromatin in the first place; and if these functions contributed to the successful emergence of early eukaryotes. The appearance of the first eukaryotes coincided with extensive alterations in redox geochemistry with increasing levels of oxygen and decreased biousable forms of transition metals such as iron and copper (Anbar, 2008). This geochemical change presented a daunting challenge to cells for acquisition and intracellular maintenance of bioessential metals, which became rare and toxic in aerobic conditions. The oxidoreductase function of the H3-H4 tetramer, the ancient structural form of

histones, could provide an explanation for why the archaeal ancestor of the eukaryotes possessed histone tetramers.

## 4.5 Materials and Methods

### EXPERIMENTAL MODEL AND SUBJECT DETAILS

### Strains and general growth conditions

Haploid *Saccharomyces cerevisiae* strains used in this study are based on the BY4741 (S288C background, MATa) (Brachmann et al., 1998) strain, and are listed in Table 4-1. All strains were maintained on standard YPD (1% Yeast extract, 2% Peptone, 2% Glucose) plates and were grown at 30°C for varying amounts of time in all experiments as described below. Unless otherwise noted, all yeast experiments were initiated by growing cells overnight to dense cultures in various media conditions. The cells were subsequently diluted in fresh media as described below. Bacteria for histone expression were BL21(DE3)pLysS cells and BL21(DE3) (Agilent). Transformed bacteria were grown on 2xTY media (1.6% Bacto Tryptone, 1% Yeast Extract, 0.5% NaCl) supplemented with 100 μg/mL ampicillin.

**Table 4-1: Yeast strains used in this study**

| Strain name | Mutant short name | Description | Reference |
|---|---|---|---|
| **BY4741** | parental | *MAT*a *his3Δ1 leu2Δ0 met15Δ0 ura3Δ0* | Brachmann et al., 1998 |
| **OCY1131** | WT | *MAT*a *his3Δ1 leu2Δ0 met15Δ0 ura3Δ0, (hht2Δ:: ura3)Δ::HHT2* | This study |
| **OCY1136** | $H3^{H113N}$ | *MAT*a *his3Δ1 leu2Δ0 met15Δ0 ura3Δ0, (hht2Δ:: ura3)Δ::HHT2-H113N HHT1-H113N* | This study |
| **NAY536** | *asf1Δ* | *MAT*a *his3Δ1 leu2Δ0 met15Δ0 ura3Δ0, (hht2::ura3)::HHT2, asf1Δ::hphMX4* | This study |
| **OCY1861** | *ctr1Δ* | *MAT*a *his3Δ1 leu2Δ0 met15Δ0 ura3Δ0, (hht2Δ:: ura3)Δ::HHT2, ctr1Δ:: hphMX4* | This study |
| **OCY1862** | $H3^{H113N}$ *ctr1Δ* | *MAT*a *his3Δ1 leu2Δ0 met15Δ0 ura3Δ0, (hht2Δ:: ura3)Δ::HHT2-H113N HHT1-H113N, ctr1Δ:: hphMX4* | This study |
| **OCY2141** | *asf1Δ ctr1Δ* | *MAT*a *his3Δ1 leu2Δ0 met15Δ0 ura3Δ0, (hht2Δ:: ura3)Δ::HHT2, asf1Δ:: hphMX4, ctr1Δ::His3MX6* | This study |
| **OCY2251** | *mac1Δ* | *MAT*a *his3Δ1 leu2Δ0 met15Δ0 ura3Δ0, (hht2Δ:: ura3)Δ::HHT2, mac1Δ::His3MX6* | This study |

| | | | |
|---|---|---|---|
| **OCY2252** | *H3$^{H113N}$ mac1Δ* | *MAT*a *his3Δ1 leu2Δ0 met15Δ0 ura3Δ0, (hht2Δ:: ura3)Δ::HHT2-H113N HHT1-H113N, mac1Δ::His3MX6* | This study |
| **OCY2621** | *ctr1*Δ | *MAT*a *his3Δ1 leu2Δ0 met15Δ0 ura3Δ0, (hht2Δ:: ura3)Δ::HHT2, ctr1*Δ0 | This study |
| **OCY2622** | *H3$^{H113N}$ ctr1*Δ | *MAT*a *his3Δ1 leu2Δ0 met15Δ0 ura3Δ0, (hht2Δ:: ura3)Δ::HHT2-H113N HHT1-H113N, ctr1Δ0* | This study |
| **NAY…** | *H3$^{H113Y}$* | *MAT*a *his3Δ1 leu2Δ0 met15Δ0 ura3Δ0, HHT2-H113Y HHT1-H113Y* | This study |
| **OCY2623** | *H3$^{H113Y}$ ctr1*Δ | *MAT*a *his3Δ1 leu2Δ0 met15Δ0 ura3Δ0, HHT2-H113Y HHT1-H113Y, ctr1*Δ0 | This study |
| **NAY…** | *H3$^{R116H}$* | *MAT*a *his3Δ1 leu2Δ0 met15Δ0 ura3Δ0, HHT2-R116H HHT1-R116H* | This study |
| **OCY2624** | *H3$^{R116H}$ ctr1*Δ | *MAT*a *his3Δ1 leu2Δ0 met15Δ0 ura3Δ0, HHT2-R116H HHT1-R116H, ctr1*Δ0 | This study |
| **OCY1137** | *H3$^{A111T}$* | *MAT*a *his3Δ1 leu2Δ0 met15Δ0 ura3Δ0, HHT2-A111T HHT1-A111T* | This study |
| **OCY2625** | *H3$^{A111T}$ ctr1*Δ | *MAT*a *his3Δ1 leu2Δ0 met15Δ0 ura3Δ0, HHT2-A111T HHT1-A111T, ctr1*Δ0 | This study |
| **OCY2381** | *p$^{(GAL1)}$-GSH1* | *MAT*a *his3Δ1 leu2Δ0 met15Δ0 ura3Δ0, (hht2Δ:: ura3)Δ::HHT2, kanMX6-PGAL1-GSH1* | This study |
| **OCY2391** | *ctr1*Δ *p$^{(GAL1)}$-GSH1* | *MAT*a *his3Δ1 leu2Δ0 met15Δ0 ura3Δ0, (hht2Δ:: ura3)Δ::HHT2, ctr1Δ:: hphMX4, kanMX6-PGAL1-GSH1* | This study |
| **OCY2131** | *cox17*Δ | *MAT*a *his3Δ1 leu2Δ0 met15Δ0 ura3Δ0, (hht2Δ:: ura3)Δ::HHT2, cox17Δ:: kanMX6* | This study |
| **OCY2132** | *H3$^{H113N}$cox17*Δ | *MAT*a *his3Δ1 leu2Δ0 met15Δ0 ura3Δ0, (hht2Δ:: ura3)Δ::HHT2-H113N HHT1-H113N, cox17Δ:: kanMX6* | This study |
| **OCY1981** | *cup1$^{F8stop}$* | *MAT*a *his3Δ1 leu2Δ0 met15Δ0 ura3Δ0, (hht2Δ:: ura3)Δ::HHT2, cup1-F8stop* | This study |
| **OCY1983** | *cup1$^{F8stop}$H3$^{H113N}$* | *MAT*a *his3Δ1 leu2Δ0 met15Δ0 ura3Δ0, (hht2Δ:: ura3)Δ::HHT2, cup1-F8stop, HHT1-H113N HHT2-H113N* | This study |
| **OCY2181** | *cup1$^{F8stop}$ctr1*Δ | *MAT*a *his3Δ1 leu2Δ0 met15Δ0 ura3Δ0, (hht2Δ:: ura3)Δ::HHT2, cup1-F8stop, ctr1Δ::His3MX6* | This study |
| **OCY2182** | *cup1$^{F8stop}$H3$^{H113N}$ctr1*Δ | *MAT*a *his3Δ1 leu2Δ0 met15Δ0 ura3Δ0, (hht2Δ:: ura3)Δ::HHT2, cup1-F8stop, HHT1-H113N HHT2-H113N, ctr1Δ::His3MX6* | This study |
| **NAY553** | *ccs1*Δ | *MAT*a *his3Δ1 leu2Δ0 met15Δ0 ura3Δ0, (hht2:: ura3)::HHT2, ccs1Δ:: kanMX6* | This study |
| **NAY554** | *H3$^{H113N}$ ccs1*Δ | *MAT*a *his3Δ1 leu2Δ0 met15Δ0 ura3Δ0, (hht2:: ura3)::*HHT2*-H113N HHT1-H113N, ccs1Δ:: kanMX6* | This study |
| **NAY597** | *asf1*Δ *ccs1*Δ | *MAT*a *his3Δ1 leu2Δ0 met15Δ0 ura3Δ0, (hht2Δ:: ura3)Δ::HHT2, asf1Δ:: hphMX4, ccs1Δ::His3MX6* | This study |
| **NAY551** | *sod1*Δ | *MAT*a *his3Δ1 leu2Δ0 met15Δ0 ura3Δ0, (hht2:: ura3)::HHT2, sod1Δ:: hphMX4* | This study |
| **NAY552** | *H3$^{H113N}$ sod1*Δ | *MAT*a *his3Δ1 leu2Δ0 met15Δ0 ura3Δ0, (hht2:: ura3):: HHT2-H113N HHT1-H113N, sod1Δ:: hphMX4* | This study |
| **OCY2211** | *cup1$^{F8stop}$ccs1*Δ | *MAT*a *his3Δ1 leu2Δ0 met15Δ0 ura3Δ0, (hht2Δ:: ura3)Δ::HHT2, cup1-F8stop, ccs1Δ:: kanMX6* | This study |
| **OCY2212** | *cup1$^{F8stop}$H3$^{H113N}$ccs1*Δ | *MAT*a *his3Δ1 leu2Δ0 met15Δ0 ura3Δ0, (hht2Δ:: ura3)Δ::HHT2, cup1-F8stop, HHT1-H113N HHT2-H113N, ccs1Δ:: kanMX6* | This study |
| **OCY1135** | *hht1-hhf1*Δ | *MAT*a *his3Δ1 leu2Δ0 met15Δ0 ura3Δ0, (hht2Δ::URA3)Δ::HHT2, hht1-hhf1Δ::hphMX4* | This study |

| | | | |
|---|---|---|---|
| **OCY2421** | *ctr1*Δ | *MAT*a *his3Δ1 leu2Δ0 met15Δ0 ura3Δ0, (hht2Δ::URA3)Δ::HHT2, ctr1Δ::His3MX6* | This study |
| **NAY564** | *hht1-hhf1Δctr1Δ* | *MAT*a *his3Δ1 leu2Δ0 met15Δ0 ura3Δ0, (hht2Δ::URA3)Δ::HHT2, hht1-hhf1Δ::hphMX4, ctr1Δ::His3MX6* | This study |

**Oligonucleotides, plasmids, and strain generation for yeast experiments**

All yeast strains were generated by the standard lithium acetate-based yeast transformation procedures. DNA fragments used for gene replacement deletions or promoter integrations were generated by PCR from plasmid templates listed in the Key Resources table. DNA fragments used as homology-directed repair templates for CRISPR-Cas9 mutagenesis were generated by primer extension to generate 100-120 bp-long oligonucleotides. Primers used to generate CRISPR repair templates and to amplify selectable markers containing 40-50 bp-long gene-flanking homology regions for gene-specific targeting are listed in Table 4-2.

The histone H3 His113Asn (H3H113N) mutation was generated in both chromosomal loci (*HHT1* and *HHT2*) in a stepwise and marker-less manner. First, using the *delitto perfetto* approach (Storici and Resnick, 2006), H113N was introduced into the *HHT2* locus. The entire *HHT2* coding region was first replaced with a KanMX4-KlURA3 cassette, with selection on Geneticin. Subsequently, the KanMX4-KlURA3 was precisely replaced with either the WT *HHT2* as a control (essentially restoring the BY4741 strain, but distinguished as OCY1131 here to account for its history of temporarily lacking HHT2), or with an *HHT2* variant harboring the H113N mutation (340-CAC-342 becomes 340-AAC-342), with counter-selection on 5-fluroorotic acid. DNA fragments used for the reintroduction of WT *HHT2* or *hht2-H113N* were generated by PCR using plasmids containing the WT *HHT2* (pRM200) (Mann and Grunstein, 1992) or *hht2-H113N* (pYX55) as templates. The pYX55 plasmid was generated by site-directed mutagenesis of the WT

*HHT2* on pRM200 using the Agilent Lightning quick change mutagenesis kit, as directed by the manufacturer, and using primers listed in Table 4-2.

Second, the H113N mutation was introduced in *HHT1* using the CRISPR-Cas9 system optimized for *S. cerevisiae* (Ryan et al., 2014). The pCAS plasmid, containing both the Cas9 gene from *Streptococcus pyogenes* and a single guide RNA, was a gift from Jamie Cate (Ryan et al., 2014). To target Cas9 to the *HHT1* region containing H113, the 20 bp targeting sequence at the 5' end of the sgRNA was changed by PCR. First, pCAS was PCR-amplified with Phusion High-Fidelity DNA Polymerase (NEB) using a 5'-phosphorylated reverse primer immediately upstream of the target sequence, and a forward primer containing the 20 nucleotide *HHT1* region surrounding H113 on its 5' end. The PCR product was treated with DpnI endonuclease (NEB) and re-circularized with T4 DNA ligase (NEB) according to manufacturers' protocols. The H113N mutation (340-CAC-342 becomes 340-AAT-342) was then introduced in yeast by co-transformation with the *HHT1-H113*-targeting pCAS plasmid, and a 100-nt double stranded homology-directed repair template containing the mutation. Successful mutagenesis at both *HHT1* and *HHT2* was confirmed by sequencing of the entire gene coding locus. The histone H3 H113Y, R116H, A111T, and A110C mutations were introduced in a similar manner as described but CRISPR-Cas9 was used for both HHT1 and HHT2.

Subsequent deletions of *ASF1*, *CTR1*, *MAC1*, *COX17*, *CCS1*, *SOD1*, and *HHT1-HHF1* genes, as well as insertion of the GAL1 promoter upstream of *GSH1* and *HHT1* were generated by standard yeast gene replacement and targeted insertion methodology using selectable marker integration (Goldstein and McCusker, 1999; Longtine et al., 1998). Additionally, *CTR1* was deleted in the strains shown in Figure 4-4D and 4-4E using CRISPR-Cas9 targeting system using a homology-directed repair template that skipped the entire gene. This resulted in a marker-less

gene deletion. Successful integrations and deletions were confirmed by PCR. Importantly, combinations of the histone mutants with these gene deletions were generated in the strain already containing the histone mutation in both histone H3 copies.

The only exception is the generation of strains in which Cup1 is disrupted, alone or in combination with H113N. Because of the multi-copy CUP1 gene, and the complexity of the locus with respect to the flanking RSC30 gene, we disrupted the gene by introduction of a stop codon at Phe8 at all CUP1 copies. Introduction of the stop codon was performed using the CRISPR-Cas9 system as described above for generating *hht1-H113N*, and correct mutagenesis was confirmed by sequencing. Lastly, H113N was introduced in both *HHT1* and *HHT2* using the same CRISPR-Cas9 approach for both loci in the strain already containing the *cup1-F8stop* mutation. Primers used to generate the targeting sgRNAs and the repair templates introducing mutations are listed in Table 4-2.

**Table 4-2: Oligonucleotides used in this study**

| Name | Sequence | Description |
|---|---|---|
| **Δhht2-CORE-F** | TTCCAACTGTTCTTCCCCTTTTACTAAAGGATCCAAGCAAA CACTCCACAGAGCTCGTTTTCGACACTGG | Targeted HHT2 deletion using pCORE |
| **Δhht2-CORE-R** | ATGTCCCCCCAGTCTAAATGCATAGAAAAAAAAAAATTCC CGCTTTATATTCCTTACCATTAAGTTGATC | |
| **pRM-HHT2-F** | TGTTTTGTGACTTCCACTTTGG | Targeted HHT2 reintroduction using pRM200 or pYX55 |
| **pRM-HHT2-R** | AAAAGGAGATGTTTGTATGATGTCC | |
| **pCAS-amp-uni-R** | AAAGTCCCATTCGCCACCCG | Universal primer for pCAS sgRNA change |
| **pCAS- HHT1-H113-gRNA-F** | AGTGACACGCTTGGCGTGAAGTTTTAGAGCTAGAAATAGC | HHT1-H113 target sgRNA change on pCAS |
| **pCAS- HHT2-H113-gRNA-F** | TTTGTTTGAAGACACTAATCGTTTTAGAGCTAGAAATAGC | HHT2-H113 target sgRNA change on pCAS |
| **pCAS- CUP1-F8-gRNA-F** | TTAATTAACTTCCAAAATGAGTTTTAGAGCTAGAAATAGC | CUP1-F8 target sgRNA change on pCAS |
| **HHT1-H113N-mutrep-F** | CGAAGCCTACTTAGTCTCTTTATTTGAAGATACCAACTTGG CTGCCATTAATGCCAAGCG | Template for HDR to |

| | | |
|---|---|---|
| **HHT1-H113N-mutrep-R** | TCTTCTAGCCAACTTGATATCCTTCTTTTGGATAGTGACAC GCTTGGCATTAATGGCAGC | introduce HHT1-H113N |
| **HHT2-H113N-mutrep-F** | CTTCTGCTATCGGTGCTTTGCAAGAATCCGTCGAAGCATAC TTAGTCTCTTTGTTTGAAGACACTAATCTTGCTGCTATT | Template for HDR to introduce HHT2-H113N |
| **HHT2-H113N-mutrep-R** | ACCTCTTAGTCTTCTGGCCAATTTGATATCCTTCTTTTGGAT AGTAACACGCTTAGCGTTAATAGCAGCAAGATTAGTGT | |
| **CUP1-F8stop-mutrep-F** | ACAATCAATCAATCAATCATCACATAAAATGTTCAGCGAA TTAATTAACTGACAAAATGA | Template for HDR to introduce CUP1-F8stop |
| **CUP1-F8stop-mutrep-R** | ATTTTTGCAGCTACCACATTGGCATTGGCACTCATGACCTT CATTTTGTCAGTTAATTAA | |
| **Δasf1-Hph-U2** | TAACAGCGTACTCTCCCTACCATCCAATTGAAACATAAGA TATAGAAAAGCCAGCTGAAGCTTCGTACGC | Targeted ASF1 deletion using pAG32 |
| **Δasf1-Hph-D2** | TAAAGTGTACCTCTCTTGCAGGTACCATTAATCTTATAACC CATAAATTCATAGGCCACTAGTGGATCTG | |
| **Δctr1-Hph-U2** | ATAGAAAATAAAAAAAAAGTGTATTATATTTGACATTCAAA CCAGCTGAAGCTTCGTACGC | Targeted CTR1 deletion using pAG32 |
| **Δctr1-Hph-D2** | TGGAAGAAGAAGATATAGGTGGACGAACCTTGTCTAGTTA ATAGGCCACTAGTGGATCTG | |
| **Δctr1-His-F1** | ATAGAAAATAAAAAAAAAGTGTATTATATTTGACATTCAAA CGGATCCCCGGGTTAATTAA | Targeted CTR1 deletion using pFA6a-His3MX6 |
| **Δctr1-His-R1** | TGGAAGAAGAAGATATAGGTGGACGAACCTTGTCTAGTTA GAATTCGAGCTCGTTTAAAC | |
| **Δmac1-His-F1** | CTTGTTTTAAACTTGAAACAGTCTGGTAAGTTCTTCAAGCT CTATCAGAGCGGATCCCCGGGTTAATTAA | Targeted MAC1 deletion using pFA6a-His3MX6 |
| **Δmac1-His-R1** | ATTTTCATTCCTGTTGCCTCAATGTGTTTTCTATCTGTATTT ACGTGATTGAATTCGAGCTCGTTTAAAC | |
| **Kan-PGAL-GSH1-F4** | CTTGTAGAAGCTGAAAATTGAGCAGATTTAGTATAGGGCT GAATTCGAGCTCGTTTAAAC | Targeted $p^{(GAL1)}$-GSH1 insertion using pFA6a-kanMX6-PGAL1 |
| **Kan-PGAL-GSH1-R2** | ACTCAAACCACTGCAAAGGCGTGCCCAAAGCTAAGAGTCC CATTTTGAGATCCGGGTTTT | |
| **Δcox17-Kan-F1** | AGTGTACACAATCAGATAACTACACAATCAATTATACCCA CGGATCCCCGGGTTAATTAA | Targeted COX17 deletion using pFA6a-kanMX6 |
| **Δcox17-Kan-R1** | ATATATACAAGAAATGGTTGTCGGCAGACTGTCAGTAAGA GAATTCGAGCTCGTTTAAAC | |
| **Δccs1-Kan-F1** | ATATCTTTGCAAGGCAGAAACCCATTCGATCAGCACAAAA CGGATCCCCGGGTTAATTAA | Targeted CCS1 deletion using either pFA6a-kanMX6 or pFA6a-His3MX6 |
| **Δccs1-Kan-R1** | TTATATCTGTATTACGCTACGTTGTGCTATCTTGGATGTTG AATTCGAGCTCGTTTAAAC | |
| **Δsod1-Hph-U2** | AACAGGCAAGAAAGCAATCGCGCAAACAAATAAAACATA ATTAATTTATACCAGCTGAAGCTTCGTACGC | Targeted SOD1 deletion using pAG32 |
| **Δsod1-Hph-D2** | CTTACTACTTACTTACATACGGTTTTTATTCAAGTATATTAT CATTAACAATAGGCCACTAGTGGATCTG | |
| **Δhht1-hhf1-Hph-U2** | ATATTTGCTTGTTGTTACCGTTTTCTTAGAATTAGCTAAAA GAATACCCTCCTTGACAGTCTT | Targeted HHT1-HHF1 locus deletion using pAG32 |
| **Δhht1-hhf1-Hph-D2** | TTTTGTTCGTTTTTTACTAAAACTGATGACAATCAACAAAA TACGACTCACTATAGGGAGACCG | |
| **xlH3-A102G-F** | GAGGCTTATCTGGTCGGACTCTTTGAGGACACCA | Mutagenesis primers to generate H3.2 (A102G) |
| **xlH3-A102G-R** | TGGTGTCCTCAAAGAGTCCGACCAGATAAGCCTC | |

**Oligonucleotides, plasmids for histone expression and nucleosome assembly**

Plasmids for expression of *Xenopus laevis* histones are from (Luger et al., 1997). The histone H3 plasmid from this reference contains an H3-G102A mutation, which was corrected to the WT G102 by site directed mutagenesis (QuikChange, Agilent) using primers xlH3-A102G-F and xlH3-A102G-R, resulting in plasmid pH3.2. C110 of histone H3.2 was mutated to alanine using primers xlH3-C110A_F and xlH3-C110A-R to produce pH3.2-C110A. H3H113 was mutated to asparagine using primers xlH3-H113N-F2 and xlH3-H113N-R2, resulting in pH3.2-H113N. A plasmid containing 12 tandem 177 bp repeats of the 601 sequence for nucleosome positioning was kindly provided by Craig L. Peterson (Dorigo et al., 2003). Plasmids used are listed in the Key Resources table, and primers for mutagenesis are listed in Table 4-2.

**METHOD DETAILS**

*Steps were taken to reduce trace metal contamination in glassware. We found these steps to be critical for reliability and reproducibility of all data involving transition metals, especially for the H3-H4 tetramer enzyme activity. Failure to properly remove trace metal contaminants may result in tetramers with no in vitro enzyme activity. In some cases, as described below, Bioultra grade reagents were used to ensure lowest possible trace metal contaminants.*

**Preparation of solutions and glassware**

Buffers and solutions for the *in vitro* enzyme assays were treated with 10% hydrochloric acid for at least 12 hrs (acid-washed glassware) followed by further acid washing for 1 hr in 10% nitric acid. Acid-washed glassware was rinsed thoroughly before solution preparation. Buffers and solutions were prepared from BioUltra quality products and also treated with Chelex 100 (Sigma) to further reduce contaminating transition metals. Powder components were added without the use of metal spatulas to further avoid metal contamination. After components were dissolved, solutions

were filtered through 0.2 μm membranes and stored in acid-washed glass containers or single-use polypropylene containers. Standard RC dialysis tubing for dialysis (Spectrumlabs.com) was washed in 1L of 10 mM EDTA (99.99% trace metal basis – Sigma) for 1h at 80ºC, transferred to fresh 1L of 10 mM EDTA at 80ºC and let cool slowly at room temperature for 16 hours. Clean membranes were dehydrated for 30 min in 95% EtOH and stored at 4ºC in 47% EtOH, 5 mM EDTA. Before usage, the tubing strips were rehydrated in $H_2O$ for several hours at room temperature.

All liquid media for yeast experiments were prepared in glassware that was treated with 10% hydrochloric acid for at least 12 hrs (acid-washed glassware). For yeast media, addition of all components was done without the use of metal spatulas. Media was filtered through 0.2 μm membranes and additional components, BCS and $CuSO_4$, were added from separately filtered stock solutions. Fermentative media was either YPD (1% Yeast Extract, 2% Peptone, 2% glucose), SC (synthetic complete medium with 2% glucose, all amino acids, and uracil and adenine), SC lacking lysine, or minimal medium (with 2% glucose and only the auxotrophic metabolites His, Leu, Met, and uracil). Non-fermentative media was YPEG (1% Yeast Extract, 2% Peptone, 3% ethanol, 3% glycerol).

Agar media was prepared similarly using acid-washed glassware. Additional media components listed in figures such as $FeCl_3$, $ZnSO_4$, and $MnCl_2$, were added after autoclaving and dissolving of agar, and just before pouring of plates. Agar media for hypoxic growth were supplemented with ergosterol and Tween-80. A stock solution of ergosterol at 2 mg/ml was prepared in a solution of 50% ethanol and 50% Tween-80 and added to the media after autoclaving to achieve a final concertation of 20 μg/ml ergosterol, 0.5% Tween-80 and 0.5% ethanol.

**Liquid culture growth curves**

To determine doubling times shown in Fig 4-1 and Fig 4-7, following an overnight growth in SC or YPD media, cells were diluted to $OD_{600}$ = 0.2 in fresh media, and grown at 30°C for up to 10 hrs. Cell density of the culture was measured every 2 hrs and doubling times were calculated from 2-8 hrs of growth, when cells were growing exponentially.

In growth experiments shown in Fig 4-2 and Fig 4-7D, following an overnight growth in YPD media, cells were diluted to $OD_{600}$ = 0.4 in YPEG containing various concentrations of $CuSO_4$, and incubated at 30°C. Growth experiments shown in Fig 4-3 and Fig 4-S3 were done similarly in SC-lys media containing various concentrations of $CuSO_4$. For growth shown in Fig 4-7E, following an overnight growth in SC-lys containing various concentrations of BCS, cells were diluted to $OD_{600}$ = 0.2 in the respective media and incubated at 30°C. At 24 or 36 hrs, culture densities were measured and the total numbers of doublings in that period were calculated.

**Spot tests**

Following an overnight growth, cells were diluted to $OD_{600}$ = 0.3-0.4 in YPD and grown at 30°C for 4-5 hrs to log phase ($OD_{600}$ = 1-2). Cells were subsequently pelleted by centrifugation, washed and resuspended in water to $OD_{600}$ = 5. Cells were then 10-fold serially diluted and 5 µL of cells were spotted on agar plates containing media and additives as indicated in the figures. Cells were incubated at 30°C for up to 7 days and imaged daily using an Epson document scanner. Because of differing growth rates in the various media conditions, images shown in the figures were captured when sufficient growth had occurred and growth differences could be assessed, and this ranged between 2-7 days. The exception is for media conditions that prevented growth (e.g. *ctr1*Δ strains in YPEG), in which images shown were captured at 3 days of incubation. Experiments in hypoxic conditions (Fig 4-S3) were done using a 2.5 L sealable jar and anaerobic gas generating sachets (AnaeroGen) designed to rapidly (i.e. within 30 minutes) generate an

anaerobic environment achieving atmospheric oxygen of <1%. Following growth in liquid media as described above, cells were pelleted by centrifugation, washed and resuspended in water to $OD_{600}$ = 10. Cells were then 5-fold serially diluted and 5 µL of cells were spotted on agar plates with the media indicated in the figure. Media for normoxic and hypoxic conditions was supplemented with 20 µg/ml ergosterol and 0.5% Tween-80 to support growth in low-oxygen conditions. The plates were then placed in the sealed hypoxic jar for 7 days at 30°C before capturing images, while normoxic control plates were incubated as usual.

Images shown are representative examples of at least two replicates performed on different days with the same clones.

**Micrococcal nuclease digestion**

Micrococcal nuclease (MNase) digestion assays were performed to assess chromatin accessibility as an indicator of nucleosome assembly and abundance. MNase digestion was performed similarly to methods described previously (Rando, 2010). Following an overnight growth in SC media, strains indicated in Fig 4-1 and Fig 4-7 were diluted to $OD_{600}$ = 0.25 in 100 mL of fresh SC. Cells were grown at 30°C for ~2 doublings, at which point 37% formaldehyde (Sigma) was added to each culture to a final concentration of 2%. Cells were fixed for 30 min at 30°C. Cells were then transferred to centrifuge bottles and 2.5 M glycine was added to quench formaldehyde reactivity to a final concentration of 125 mM. Cells were pelleted by centrifugation at 3700 rpm, for 10 min, at 4°C and subsequently resuspended in water. A volume corresponding to $2x10^9$ cells was transferred to new 15 mL conical tubes, pelleted and washed with water, and resuspended to $OD_{600}$ = 12.5 in Zymolyase buffer (1 M Sorbitol, 50 mM Tris pH 7.5) on ice. β-mercaptoethanol was added to a concentration of 10 mM. To initiate cell wall digestion, 2 mg of Zymolyase 100-T was added and cells were incubated at 30°C for 35 min. Spheroplasts were

pelleted by centrifuging at 3700 rpm for 10 min at 4°C, and resuspended in 2 mL of MNase digestion buffer (1 M sorbitol, 50 mM NaCl, 10 mM Tris pH 7.5, 5 mM $MgCl_2$, 1 mM $CaCl_2$, 500 μM spermidine, 0.075% Igepal CA-630, 10 mM BME). Resuspended spheroplasts were then equally distributed to 4 tubes, and varying amounts of MNase were added as indicated in the figures. Samples were incubated at 37°C for 20 min, at which point MNase was inactivated by the addition of 5X stop solution (5% SDS, 50 mM EDTA). Proteins were then digested by addition of 160 ug of proteinase K (Sigma), and formaldehyde crosslinks reversed, by incubation at 65°C for ~12 hrs.

DNA was purified by standard phenol-chloroform extraction methods. One volume of phenol:chloroform:isoamyl alcohol (25:24:1) was added to each sample, and the samples were centrifuged at 16,000xg for 5 min to separate the aqueous and phenol phases. The upper aqueous phase was transferred to a new tube, 3 M sodium acetate pH 5.5 was added to 300 mM final concentration, and nucleic acids were precipitated with isopropanol. Nucleic acid pellets were then resuspended in 60 μL Qiagen buffer EB (10 mM Tris, pH 8.5). MNase-digested DNA samples were treated with 10 ug of RNase A (Roche) for 1 hr at 37°C. Lastly, DNA samples were purified using the Wizard SV PCR purification kit (Promega) according to the manufacturer's protocol, and eluted in 30 μL of Qiagen buffer EB. Final DNA concentrations were determined using the Qubit DNA broad range assay (ThermoFisher) according to the manufacturer's protocol. ScreenTape images shown and quantified are representative examples of three replicate MNase digestions from separately grown cultures of the same cell clones.

**MNase accessibility analysis**

MNase-digested DNA samples were normalized by concentration, and visualized using the DNA ScreenTape assay on the TapeStation 2200 instrument (Agilent), according to the

manufacturer's protocol. Using TapeStation Analysis software (Agilent) gel images were exported, without contrast adjustment, and saved in TIFF format. Pixel intensities along a line perpendicular to DNA bands and through the center of each lane were then quantified using FIJI (ImageJ 1.48k).

**Sample preparation for inductively-coupled plasma mass spectrometry (ICP-MS)**

Cells from dense overnight cultures in SC or YPD media were diluted to $OD_{600}$ = 0.2-0.4 and grown at 30°C for ~3 doublings in SC or YPD, or for 18 and 24 hrs in YPEG and SC-lys, respectively. Three replicate cultures were prepared for each sample. Cells (4-12 x $10^8$) were collected by centrifugation, and cell pellets were washed twice in 1 mM EDTA to remove cell surface-associated metals. This was followed by one wash in Nanopure Diamond filtered water to remove residual EDTA. Cell pellets were then stored at -20°C for 1-3 weeks prior to preparation for ICP-MS.

Plastic bottles and cylinders used for preparation of solutions for sample digestion were treated with 7-10% ACS grade nitric acid for 5 days at 50°C. Acid-washed materials were rinsed thoroughly with Nanopure water before use. Frozen cell pellets were thawed at room temperature and packed by centrifugation at 3000xg. Pellets were overlaid slowly (not to disrupt the pellet) with 70% Optima Grade nitric acid and digested at 65°C for 12-16 hrs. Prior to mass spectrometry, the digested samples were diluted with Nanopure water to a final concentration of 2% nitric acid and a final volume of 3-5 mL.

**Inductively-coupled plasma mass spectrometry**

Total Fe and Cu content was measured by inductively coupled plasma mass spectrometry on the Agilent 8800 ICP-QQQ in MS/MS mode. The most abundant isotopes of iron and copper (i.e. $Fe^{56}$ and $Cu^{63}$) were used to determine the total cellular iron and copper levels. Iron was measured both directly, with hydrogen present in the collision/reaction cell, and indirectly, after

mass-shift to FeO with oxygen present in the cell. While both methods produced similar results, the data presented here for iron are from oxygen mass-shift mode. Copper was measured directly in oxygen-mode. The metal content was determined in comparison to an environmental calibration standard (Agilent 5183-4688), which contains 100x higher concentration of Fe compared to Cu, more accurately reflecting biological samples. Every run was calibrated individually, $^{45}Sc$ or $^{89}Y$ were used as internal standards to compare the calibration with the analyzed samples. Average counts of 5 technical replicates were used for each calibration standard and each individual biological sample. The deviation in between technical replicates never exceeded 5%. Standard deviation in figures reflects the standard deviation between biological replicates (n = 3 - 6). Prepared calibration standards ranged from 10 ppt to 500 ppb for $^{63}Cu$ and 1 ppb - 50 ppm for $^{56}Fe$. All Cu and Fe measurements in our study were within the calibrated linear ranges for Cu and Fe and well above the lower limits of detection, which were determined from multiple blank samples. We used ICP MassHunter software for ICP-MS data analysis.

**RNA extraction**

Following an overnight growth, cells were diluted in the various media conditions indicated in the figures. Cells grown in SC were diluted to $OD_{600}$ = 0.05 and grown for 5 doublings at 30°C, at which point they were growing exponentially. Cells grown in YPD and YPEG were diluted to $OD_{600}$ = 0.2 and grown for 3-4 doublings at 30°C, at which point they were growing exponentially. Cells in SC-lys media, with or without extra $CuSO_4$, were diluted to $OD_{600}$ = 0.4 and incubated at 30°C for 24 hrs, at which point they had reached $OD_{600}$ = 0.6–1.6. Approximately $1.5x10^8$ cells were collected by centrifugation and frozen at -20°C until further processing. RNA was extracted using previously published methods (Schmitt et al., 1990) with some modifications. Frozen cell pellets, without significant thawing, were resuspended in 440 µL of AE buffer (50 mM Na acetate

pH 5.2, 10 mM EDTA, 1% SDS), and RNA was extracted by addition of 440 µL of 5:1 phenol:chloroform pH 4.5 (ThermoFisher) and incubation at 65°C for 4 min. Samples were then rapidly frozen in dry ice-ethanol, and centrifuged at 16,000xg to separate the aqueous and phenol phases. The aqueous supernatant (350 µL) was transferred to a new tube, and re-extracted by addition of 300 µL of 25:24:1 phenol:chloroform:isoamyl alcohol, and centrifuged as above to separate phases. 250 µL was transferred to a new tube, 25 µL of 3 M Na acetate pH 5.2 was added, and nucleic acids were ethanol-precipitated. Nucleic acid pellets were then resuspended in 100 µL of nuclease-free water and stored at -20°C until further processing. RNA concentration was measured by Nanodrop 2000 microvolume spectrophotometer. Typical yield from this extraction method was about 30 µg of total RNA. RNA extracted for subsequent RNA-seq analysis are from two replicates of cells grown on different days with different media batches. The exceptions are cells grown in SC (Fig 4-1) which are from three replicates, and cells grown in SC-lys+75 µM $CuSO_4$ (Fig 4-3 and 4-S3) which is from one experiment.

**Sample preparation for poly-A RNA sequencing**

Prior to preparing RNA-seq libraries for Illumina HiSeq sequencing, contaminating DNA was digested, and RNA quality was assessed. Total RNA (10 µg) was treated with Turbo DNase according to the manufacturer's "Routine DNase treatment" procedures, in 50 µL reaction volumes. Samples were incubated at 37°C for 30 min. Following DNAse treatment and reagent inactivation, total RNA concentration was determined using the Qubit RNA broad range assay (ThermoFisher) according to the manufacturer's protocol. RNA quality was then assessed using the RNA ScreenTape assay on the TapeStation 2200 instrument (Agilent), according to the manufacturer's protocol with undiluted RNA samples. Using TapeStation Analysis software (Agilent), RNA Integrity Number equivalent (RINe) scores, which reflects the ratio of abundances

of 28S, 18S, and sub-18S RNAs, were calculated. Only samples with RINe scores greater than 9 (out of 10) were used for sequencing library preparation.

RNA-sequencing libraries were then prepared either manually with the KAPA Stranded mRNA-seq library prep kit (KAPA Biosystems), or with automation, using the Illumina TruSeq Stranded mRNA Library Kit for NeoPrep (Illumina). Both library preparation procedures first isolate polyA$^+$ mRNAs using oligo-dT beads. Isolated polyA$^+$ RNAs are then chemically fragmented, and random primers are used in the first cDNA reverse transcription step. For both approaches, libraries were prepared according to the manufacturer's protocols, with the following important parameters. For libraries constructed using the KAPA kit, 250 ng of DNase-treated total RNA was used as input. Following the mRNA capture step, RNA was fragmented for 8 min at 94°C, which was designed to generate average library insert sizes of 100-200 bp. Illumina HiSeq-compatible adapters were ligated at reaction concentrations of 25 nM and ligation was performed for 15 min at 20°C. Following adapter ligation and post-ligation purification, library fragments were amplified with 15 PCR cycles, using the manufacturer's provided thermal cycling times and temperatures. For libraries constructed using Illumina's Neoprep automated library preparation system, 70 ng of DNase-treated total RNA was used as input. To maximize library product, we disabled the default library normalization step that occurs at the end of the automated library construction and quantification. The number of library amplification cycles was set to 15.

RNA-seq libraries were assessed for correct fragment size and the presence of adapter dimers, using the DNA ScreenTape assay on the TapeStation 2200 instrument (Agilent), according to the manufacturer's protocol. Average library sizes of ~270 bp were observed and deemed correct. Using TapeStation Analysis software (Agilent), library DNA concentrations were estimated. Libraries were then pooled for multiplexed sequencing at equimolar ratios. Because

some libraries contained more than 1% adapter dimers, by concentration, the library pools were further purified using Agencourt RNAClean XP beads. One volume of beads, thoroughly resuspended, was added to the library pool, and allowed to incubate for 15 min at room temperature without perturbation. Beads were then magnetically isolated, and washed twice with 70% ethanol. Beads were air-dried for 5 min, and resuspended, off the magnet, in 30 μL of resuspension buffer provided in TruSeq library preparation kits (Illumina, RSB, part # 15026770). Eluted DNA was transferred to a fresh 1.5 mL microcentrifuge tube. Bead-purified library pool DNA concentration was then measured using the Qubit DNA broad range assay (ThermoFisher) according to the manufacturer's protocol, and total DNA concentration was adjusted to 10 nM for Illumina sequencing.

**mRNA-sequencing and data processing**

High throughput sequencing was performed on Illumina's HiSeq 4000 system, with single-end 50 bp insert reads, and dedicated index reads. Total read count per library ranged from ~1.5-9 million. De-multiplexed reads, in FASTQ file format, were aligned to the R64-1-1 S288C reference genome assembly (sacCer3), downloaded from the UCSC database, using Tophat 2.0.9 (Kim et al., 2013). The "-g 1" parameter was used to limit the number of alignments for each read to one, the top-scoring alignment. In the case of a tie, the read was randomly distributed to one of the tied top-scoring alignments. Percentage of reads aligned once was greater than 90% in all cases.

**Gene expression analysis**

Gene expression values, in reads per kilobase per million mapped reads (RPKMs), for 6692 annotated open reading frames were calculated using SAMMate 2.7.4 (Xu et al., 2011). In calculating RPKM values, only reads that align to annotated exons were considered. Reads aligning to introns or intergenic regions were not counted in normalizing the read counts to the

total number of mapped reads. Many of the 6692 annotated ORFs have no attributed function, localization, mutant phenotypes or interactions and are often labeled as "dubious" or "putative" in the Saccharomyces Genome Database (SGD). Furthermore, these putative ORFs typically have low expression values. We removed 1648 such ORFs from further analysis, and used the remaining 5044 ORFs for comparisons between groups.

**RNA-sequencing gene sets**

Genes that were analyzed as part of functional groups in Fig 4-2 and 4-3 are listed in table 4-3. Each gene set was constructed by downloading and merging gene ontology term gene lists from AmiGO 2 in March 2017. For the "copper homeostasis" and "iron homeostasis" gene sets, we further modified the lists by adding or removing genes based on literature review. The "copper homeostasis" set was generated starting with the following list: GO 0006878 – Cellular copper ion homeostasis. The "iron homeostasis" set was generated by starting with the following list: GO 0055072 – Iron ion homeostasis. The "electron transport and TCA cycle" set was generated by merging the following lists: GO 0022904 – Respiratory electron transport chain, and GO 0006099 – Tricarboxylic acid cycle. The "lysine biosynthesis" set was based on the following list: GO 0006553 – Lysine metabolic process. The "antioxidant" set was based on the following list: GO 0016209 – Antioxidant activity.

**Table 4-3: Gene sets for gene expression analysis**

| Gene set | Genes |
|---|---|
| **Copper homeostasis** | ATX1, CCC2, CCS1, COX11, COX17, COX19, CTR1, CTR2, CTR3, CUP2, FET4, FRE1, FRE2, FRE3, FRE4, FRE5, FRE6, FRE7, MAC1, MRS3, PIC2, SCO1, SCO2, SMF1 |
| **Iron homeostasis** | AFT1, AFT2, ARN1, ARN2, ATX1, CCC2, CTH1, FET3, FET4, FET5, FIT1, FIT2, FIT3, FRE1, FRE2, FRE3, FRE4, FRE5, FRE6, FRE7, FRE8, FTH1, FTR1, HMX1, SIT1, SMF1, SMF3, TIS11 |
| **Electron transport chain and TCA cycle** | ACO1, ACO2, AIF1, CIR2, CIT1, CIT2, CIT3, COR1, COX13, COX4, COX5A, COX5B, COX6, COX7, COX8, COX9, CYC1, CYC7, CYT1, DAL7, DLD2, DLD3, FUM1, ICL1, IDH1, IDH2, IDP1, IDP2, IDP3, KGD1, KGD2, LSC1, LSC2, MAS1, MDH1, MDH2, MDH3, MLS1, MTC3, NDI1, QCR10, QCR2, |

| | |
|---|---|
| | QCR6, QCR7, QCR8, QCR9, RIP1, SDH1, SDH2, SDH3, SDH4, SDH5, SHH3, SHH4, TAZ1, YJL045W, YJL045W, YMR31 |
| **Lysine biosynthesis** | ACO2, ARO8, HOM2, HOM3, HOM6, KGD2, LYS1, LYS12, LYS14, LYS2, LYS20, LYS21, LYS4, LYS5, LYS9 |
| **Antioxidant** | AHP1, CCP1, CCS1, CTA1, CTT1, CUP1-1, CUP1-2, DOT5, ECM4, GLR1, GPX1, GPX2, GRX1, GRX2, GRX6, GRX7, GRX8, GTO1, GTT1, HYR1, MRP1, PRX1, RSM26, SCO1, SCO2, SOD1, SOD2, SRX1, TRR1, TRR2, TRX1, TRX2, TRX3, TSA1, TSA2, URE2 |

**Oxygen consumption assay**

Oxygen consumption rates were measured in whole cells using the Fiber Optic Oxygen Monitor, Model 110 (Instech laboratories Inc., Plymouth Meeting, PA). For experiments shown in Fig 4-2C, cells from dense overnight cultures in YPD medium were diluted in YPEG with the indicated amounts of $CuSO_4$ to $OD_{600}$ = 0.4 and grown at 30°C for 24 hrs. For experiments shown in Fig 4-S2C, cells from dense overnight cultures in YPD media ± 75 μM $CuSO_4$ were diluted in YPEG ± 75 μM $CuSO_4$ and ± 50 μM Antimycin A to $OD_{600}$ = 0.8 and grown at 30°C for 6 hrs. Cells were then collected by centrifugation, and pellets concentrated in fresh media to achieve $OD_{600}$ = 1.5 (Fig 4-2C) or 3 (Fig 4-S2C) in a final volume of 500 μL. The cell suspension was placed in an airtight chamber for oxygen consumption measurement. Oxygen level is sensed by the quenching of fluorescence of an indicator dye. The increase in fluorescence represents a decrease in oxygen levels in the sealed chamber and is a measure of cellular oxygen consumption. Cells were recorded for 5 minutes and the rate of oxygen consumption was determined for a one-minute steady state period during which fluorescence signal increased linearly.

**Sod1 activity assay and disulfide bond measurement**

Sod1p superoxide dismutase activity was assayed by native-PAGE and in-gel staining with nitrotetrazolium blue (NBT), based on previously-reported methodology (Leitch et al., 2009). Following an overnight growth in SC media, strains indicated in Fig 4-3A and Fig 4-S3A were

diluted to $OD_{600}$ = 1 in 100 mL of minimal media with the indicated amounts of $CuSO_4$. Additionally, pilot experiments were performed with the *sod1Δ* strain to determine the location of the Sod1p bands in all assays described (data not shown). Cells were grown at 30°C for 2 hrs, at which point ~2 billion cells were collected by centrifugation, washed with ice-cold water, and resuspended in 133 µL of lysis buffer (600 mM sorbitol, 10 mM HEPES pH 7.5, 5 mM EDTA, and protease inhibitors) on ice. Approximately 300 million cells were also collected from the same cultures for assessment of the Sod1 disulfide bond (Fig 4-S3B; see below). Cells for the Sod1 activity assay were then lysed with acid-washed glass beads (4 rounds of 1 min on, 1 min off vortexing). Lysates were cleared by centrifugation at 16,100 xg for 10 min and supernatants were transferred to new tubes. Total protein content was measured by the BCA protein assay (Thermo Scientific), and aliquots were prepared for both native-PAGE and SDS-PAGE from the same lysates with either native sample buffer (12.5% glycerol, 31.25 mM Tris pH 6.8, 0.005% bromophenol blue, 5 mM EDTA final concentrations) or SDS sample buffer (5% glycerol, 40 mM Tris pH 6.8, 1% SDS, 0.005% bromophenol blue, 50 mM DTT final concentrations), respectively.

For SDS-PAGE and Sod1p western blots, 10 µg of total protein content was run on 10% SDS acrylamide gels. Proteins were transferred to polyvinylidene difluoride (PVDF) membranes and western blots were performed using a primary antibody against Sod1p, which was a gift from Valeria Culotta (JH764). The antibody was diluted 1:5000 in Odyssey blocking buffer (LI-COR biotechnology) and blots were incubated at room temperature for 1.5 hrs. Signal quantifications were obtained using the Odyssey infrared fluorescence imaging system (LI-COR biotechnology) and Image Studio Lite software. Sod1p western blot signal intensities from the initial run were then used to normalize loading for subsequent native-PAGE and the final SDS-PAGE and western blot (shown in the figures). For native-PAGE, ~10 µg (WT and $H3^{H113N}$) or ~100 µg (*ccs1Δ* and

*H3*$^{H113N}$*ccs1Δ*), with loading adjusted for each sample to achieve equivalent Sod1p content, was run on 10% SDS acrylamide gels for 2.5 hrs with 1 mM EDTA in the running buffer. Gels were then sequentially incubated in phosphate buffer (50 mM $K_2HPO_4$ pH 7.8, 1 mM EDTA) for 30 min, 0.48 mM NBT (Sigma) in phosphate buffer for 45 min, and 30 μM riboflavin (Sigma) and 0.02% Tetramethylethylenediamine (TEMED; ThermoFisher) in phosphate buffer for 45 min all at room temperature, in the dark, and with shaking. Finally, gels were exposed to bright light for 20 min and gels scanned using an Epson document scanner, and saved in TIFF format. Signal intensities of the major SOD1 band were then quantified using FIJI (ImageJ 1.48k).

The Sod1p disulfide bond was assayed by iodoacetamide (IAA) labeling of thiols and gel mobility shift based on previously-reported methodology (Leitch et al., 2009). Three hundred million cells grown and collected as described above were resuspended in 80 μL of lysis buffer containing IAA (600 mM sorbitol, 10 mM HEPES pH 7.5, 5 mM EDTA, 100 mM IAA (Sigma-Aldrich), and protease inhibitors). Cells were lysed with acid-washed glass beads (4 rounds of 1 min on, 1 min off vortexing). Lysates were cleared by centrifugation at 16,100 xg for 5 min and supernatants were transferred to new tubes. Total protein content was measured by the BCA protein assay (Thermo Scientific), and non-reducing SDS sample buffer (5% glycerol, 40 mM Tris pH 6.8, 1% SDS, 0.005% bromophenol blue final concentrations) was added. For SDS-PAGE and Sod1p western blots, 10 μg (WT and *H3*$^{H113N}$) or 20 μg (*ccs1Δ* and *H3*$^{H113N}$*ccs1Δ*) of total protein content was run on 18% SDS acrylamide gels. Following electrophoresis, gels were incubated for 45 min with SDS running buffer containing 5% β-mercaptoethanol at room temperature with shaking. Transfer to PVDF membranes, western blotting for Sod1p, and signal quantification were performed as described above, except the primary antibody was diluted 1:2500.

**SDS-PAGE and Western Blotting for histone content**

For assessment of histone protein content shown in Fig 4-7A, whole cell protein extracts were prepared from 500 million cells growing exponentially in YPD medium. Cell pellets were resuspended in 2 mL of 0.2 M NaOH and incubated at room temperature for 15 minutes. The samples were then centrifuged at 12,000 rpm for 5 minutes; pellets were resuspended in 200 µL of SDS-PAGE loading buffer (50 mM Tris-HCl pH 6.8, 2% SDS, 10% glycerol, 1% β-mercaptoethanol) and boiled for 5 minutes. Lysates were cleared by centrifugation at 13,000 rpm for 5 minutes to remove debris. For SDS-PAGE and western blots shown in Fig 4-7, 4 µg of lysate was used. Western blots were performed using the LI-COR Odyssey system. Primary antibodies to histone H3 and H4 were diluted in the recommended Odyssey buffer at 1:5000 and 1:800, respectively, and blots were incubated in diluted antibody at 4°C overnight. Signal quantifications were obtained using Image Studio Lite software.

**Histone purification**

Histone purification was performed essentially as described in (Luger et al., 1999) with some modifications. Histone H3 expression plasmids were transformed into BL21(DE3)pLysS cells (Agilent) and histone H4 expression plasmids into BL21(DE3). The entire transformation reaction was plated onto 2xTY or LB plates containing 100 µg/mL ampicillin. After 16 hrs of growth, the resistant cells were added to 1 L of 2xTY or LB broth containing 100 µg/mL ampicillin and grown to $OD_{600}$ = 0.6. A 100 µL aliquot was taken and analyzed by PAGE as a negative control sample. Expression was then induced with 0.4 µg/mL isopropyl β-D-1-thiogalactopyranoside for 3 hrs. A 50 µL aliquot was analyzed by PAGE to control expression levels. The remaining culture was centrifuged at 5000 rpm for 15 min and the pellet resuspended in 14 mL of Wash Buffer (50 mM Tris pH7.5, 100 mM NaCl, 1 mM EDTA, 1 mM Benzamidine and 5 mM β-mercaptoethanol), flash frozen and stored at -80°C. Frozen cells were thawed at 37°C and sonicated on ice for 3

seconds on, 5 seconds off cycles for a total of 4-6 minutes at intensity setting 6 with a 550 Sonic Dismembrator (Fisher Scientific). The lysate was centrifuged in a Sorvall SS-34 rotor at 4°C at 17000 rpm for 15 min and the supernatant was discarded. The pellet, which contains inclusion bodies, was resuspended in 20 mL ice cold Wash Buffer containing 1% Triton X-100 using a pre-chilled Dounce homogenizer and collected by centrifugation at 17000 rpm. This wash step was repeated once followed by two washes without Triton X-100. The clean inclusion bodies were solubilized at room temperature in 100 μL of DMSO and further resuspended in 15 mL Unfolding Buffer (7 M Guanidinium-HCl, 20 mM Tris-HCl pH 7.5, 10 mM DTT). Histones were extracted for 2 hrs. Debris was removed by centrifugation at 17000 rpm for 20 minutes and the supernatant, containing extracted histones, was dialyzed at 4°C two times into 1 L of SAU200 Buffer (7 M Urea, 20 mM NaOAc pH 5.2, 200 mM NaCl, 1 mM EDTA, 5 mM β-Mercaptoethanol) for 1 hr, followed by one overnight dialysis. Histones in SAU200 Buffer were centrifuged in a Sorvall SS-34 at 10000 rpm for 10 min at 4$^{o}$C to eliminate possible debris. The histones were then pre-cleared by running the preparation over a Hi-Trap Q-Sepharose column (GE healthcare), after which they were loaded onto a Hi-Trap SP-Sepharose column (GE healthcare) and eluted by a salt gradient from SAU200 Buffer (buffer A) to SAU600 Buffer (same as SAU200, but 600 mM NaCl) (buffer B). Aliquots of 1 mL were collected and 3 μL of each was analyzed by PAGE on a 15% gel. Fractions containing pure histones were pooled and dialyzed 3 times against 4 L of 2 mM β-mercaptoethanol in water. Histones were then divided into aliquots, flash frozen and lyophilized.

**Tetramer assembly**

*Please see above for critical notes on preparation of acid-washed glassware and buffers with low trace metal contaminants.*

H3/H4 tetramer assembly was performed as described in (Luger et al., 1999) with some adjustments. Equimolar amounts of H3 and H4 were dissolved in Unfolding Buffer (see above) at a concentration of 2 mg/mL total protein content and incubated for 1 hr with rotation at room temperature. Refolding was achieved by 2X 1 hr dialysis at 4°C against 1 L of Low Salt Refolding Buffer (500 mM NaCl, 10 mM Tris-HCl pH 7.5, 1 mM EDTA, 5 mM β-mercaptoethanol), followed by one dialysis >16 hrs Tetramers used in figures 4-4E, 4-4H and 4-S6 A-D were dialized for 1 hr at 4ºC against 1 L High Salt Refolding Buffer, 1 hr in 1 L Medium Salt Refolding Buffer (1 M NaCl, 10 mM Tris-HCl pH 7.5, 1 mM EDTA, 5 mM β-mercaptoethanol), followed by 16 hrs in Low Salt Refolding Buffer. The refolded tetramer was centrifuged for 1 min at full speed at 4°C to eliminate any insoluble particles and purified by size exclusion chromatography on a HiLoad 16/600 Superdex 200 column (GE healthcare) at 1 ml/min in Low Salt SE-Buffer (500mM NaCl, 10 mM Tris-HCl pH7.5). Fractions containing the tetramer were concentrated using Amicon Ultra–15/Ultracel-10K centrifugal filters (Millipore). The flow-through buffer was used as negative control ("buffer") in the copper reductase assay, described below.

***In vitro* copper reductase assay**

The H3/H4 tetramer, or the same volume of control buffer, was resuspended to a final concentration of 1 μM in 100 mM NaCl, 1 mM Neocuproine (Sigma) and 20 μM BioUltra tris(2-carboxyethyl)phosphine (TCEP, Sigma), unless otherwise stated. The reaction was started by adding a mix of $CuCl_2$ and Tricine-HCl, pH 7.5, at final concentrations of 1 mM and 5 mM, respectively. The reaction was monitored by measuring absorbance at 448 nm every 0.5 seconds using a Hewlett-Packard HP8453 diode-array UV/Visible spectrophotometer. Nicotinamide Adenine Dinucleotide (NADH), Nicotinamide Adenine Dinucleotide Phosphate (NADPH), Dithiobutylamine (DTBA), Tris(hydroxypropyl)phosphine (THP) and glutathione (GSH) were

also used as reducing co-factors, but showed high spontaneous reduction of copper under these conditions (data not shown). Hence, TCEP was the reducing co-factor of choice during these studies, unless otherwise stated. $CuCl_2$ reduction using NADPH as electron donor was performed using a final concentration of H3/H4 tetramer of 7.5 µM in 116.6 mM Na-acetate, 1 mM Neocuproine, 30 µM NADPH and started by the addition of 0.5 mM $CuCl_2$ / 3.5 mM Tricine-HCl, pH 7.5. Yeast tetramers were used at a final concentration of 5 µM in 33.3 mM NaCl, 15 mM Urea, 1 mM Neocuproine, 30 µM TCEP and the reaction was started by the addition of 0.5 mM $CuCl_2$ / 0.5 mM Tricine-HCl, pH7.5.

**QUANTIFICATION AND STATISTICAL ANALYSIS**

The number of experimental replicates (n), and the observed significance levels are indicated in figure legends. All statistical analyses were performed using Graphpad Prism 5 or 7, unless otherwise stated. Significance values for pair-wise comparisons of doubling times (Fig 4-3C and 4-22C) were calculated using the Mann-Whitney test. Significance values for comparisons of the number of population doublings in Fig 4-5A, 4-22D and 4-22E and oxygen consumption rates in Fig 4-5A and 4-5C were calculated using the Holm-Sidak method for multiple t-tests, with alpha = 0.05. Significance values for comparisons of the number of population doublings in Fig 4-11A and 4-14B were calculated using a mixed model Two-Way ANOVA with Bonferroni post-hoc test for pair-wise comparisons. For inductively coupled mass spectrometry, 3-9 replicates were measured for each sample (n) from 1-3 separate experiments. Statistical testing for iron and copper measurements was done using unpaired Student's t- tests. For gene expression data, we averaged RPKM values from replicates and used mean values for calculation of global gene expression correlations (e.g. Fig 4-3E) and for analyzing gene sets (e.g. Fig 4-7C). For global correlations, Spearman's rank correlation coefficients were calculated. Significance values for pair-wise

comparisons of gene expression levels of gene sets (e.g. Fig 4-7B) were calculated using the Mann-Whitney test. We also assessed differential gene expression, using the SAMMate RPKM values, for each gene and between WT and $H3^{H113N}$ strains grown in SC media. Student's t-test was used to calculate p values with the Benjamini-Hochberg procedure to control the false discovery rate at 0.1. This analysis was performed using Microsoft Excel 2016. No genes were found to be significantly differentially expressed by this procedure. For MNase digestion profiles (Fig 4-3D), signal intensities measured using FIJI were scaled to DNA length using a gel migration distance-to-DNA fragment size calibration curve. Signal intensities were also normalized by dividing by the total lane intensity and multiplying by 1000. Curve fitting for enzymatic kinetic analysis was performed online using "mycurvefit" tool (https://mycurvefit.com), taking zero as starting value. Predicted values for 0.3 seconds were within 20% of the maximum values detected and used to calculate the initial velocities. These initial velocities were then transferred to Graphpad Prism version 5.01 and fitted with the Michaelis-Menten non-linear regression function to determine enzymatic parameters. The "area under curve" non-linear regression function of the same software was used to determine the value of the area under progress curves for p value measurement by the t-test.

**Table 4-4: Key resources**

| REAGENT or RESOURCE | SOURCE | IDENTIFIER |
|---|---|---|
| Antibodies | | |
| Rabbit polyclonal anti histone H3 (C-terminal) | Active motif | Cat# 39163 |
| Rabbit polyclonal anti histone H4 | Abcam | Cat# 10158 |
| Rabbit polyclonal anti Sod1 | (Jensen and Culotta, 2005) | JH764 |
| IRDye® 800CW Goat anti-Rabbit IgG (H + L), 0.1 mg | LI-COR | Cat# 925-32211 |
| IRDye® 680RD Goat anti-Rabbit IgG (H + L), 0.1 mg | LI-COR | Cat# 925-68071 |
| Bacterial and Virus Strains | | |
| BL(DE3) | Agilent Technologies | Cat# 200131 |
| BL(DE3)pLysS | Agilent Technologies | Cat# 200132 |
| Chemicals, Peptides, and Recombinant Proteins | | |

| | | |
|---|---|---|
| BD Bacto™ Dehydrated Culture Media Additive: Tryptone | Fisher Scientific | Cat# 211705 |
| BD Bacto™ Dehydrated Culture Media Additive: Yeast Extract | Fisher Scientific | Cat# 212750 |
| BD BBL™/Difco™ Bacto™ Media Additives/Ingredients/Reagents: Peptone | Fisher Scientific | Cat# 211677 |
| BD™ Difco™ Yeast Nitrogen Base without Amino Acids and Ammonium Sulfate | Fisher Scientific | Cat# 233520 |
| BD Bacto™ Dehydrated Agar | Fisher Scientific | Cat# 214010 |
| SC Powder, 30 grams | Sunrise Science Products | Cat# 1300-30 |
| SC-lys Powder, 30 grams | Sunrise Science Products | Cat# 13007-30 |
| Ampicillin Sodium Salt | Sigma-Aldrich | Cat# A9518 |
| Isopropyl β-D-thiogalactopyranoside | Goldbio.com | Cat# 12481C25 |
| Ergosterol ≥95.0% (HPLC) | Sigma-Aldrich | Cat# 45480 |
| Geneticin | Gibco | Cat# 11811-031 |
| Bathocuproinedisulfonic acid disodium salt hydrate | Sigma-Aldrich | Cat# 146625 |
| Copper(II) chloride | Sigma-Aldrich | Cat# C1654 |
| Copper(II) sulfate pentahydrate | Sigma-Aldrich | Cat# C6283 |
| Manganese Chloride Tetrahydrate (Crystalline/Certified ACS) | Fisher Scientific | Cat# M87-100 |
| Iron(III) chloride hexahydrate | Sigma-Aldrich | Cat# 236489 |
| Zinc sulfate heptahydrate | Sigma-Aldrich | Cat# 221376 |
| Nitric Acid 67-69%, Optima™, for Ultra Trace Elemental Analysis | Fisher Scientific | Cat# A467 |
| Nitric Acid (Certified ACS Plus) | Fisher Scientific | Cat# A200-212 |
| Hydrochloric acid | Fisher Scientific | Cat# A144SI-212 |
| Hydrochloric acid (ACS grade) | Sigma-Aldrich | Cat# 320331 |
| ICP-MS Multi-element calibration standard | Agilent Technologies | Cat# 5183-4688 |
| 1000 ppm (µg/mL) Sulfur for ICP | Inorganic Ventures | Cat# CGS1 |
| 1000 ppm (µg/mL) Phosphorus for ICP | Inorganic Ventures | Cat# CGP1 |
| 1000 ppm (µg/mL) Scandium for ICP | Inorganic Ventures | Cat# CGSC1 |
| 100 ppm (µg/mL) Yttrium for ICP-MS | Inorganic Ventures | Cat# MSY-100PPM |
| Agencourt RNAClean XP beads | Beckman Coulter | Cat# A63987 |
| Zymolyase® 100-T | Nacalai USA | Cat# 07665-55 |
| Nuclease micrococcal from Staphylococcus aureus | Sigma-Aldrich | Cat# N5386 |
| RNase A from bovine pancreas (RNASEA-RO ROCHE) | Sigma-Aldrich | Cat# 10109142001 |
| Proteinase K from Tritirachium album | Sigma-Aldrich | Cat# P6556 |
| Trizma Base (BioUltra) | Sigma-Aldrich | Cat# 93362 |
| Sodium Chloride (BioUltra) | Sigma-Aldrich | Cat# 71376 |
| Tris(2-carboxyethyl)phosphine hydrochloride (BioUltra) | Sigma-Aldrich | Cat# 75259 |
| β-Mercaptoethanol (Pharmagrade) | Sigma-Aldrich | Cat# 07604 |
| Tris(hydroxymethyl)phosphine | Sigma-Aldrich | Cat# 177881 |
| Dihydrolipoic acid | Sigma-Aldrich | Cat# T8260 |
| DL-Dithiothreitol | Goldbio.com | Cat# DTT25 |
| (S)-2-Aminobutane-1,4-dithiol hydrochloride | Sigma-Aldrich | Cat# 774405 |

| | | |
|---|---|---|
| β-Nicotinamide adenine dinucleotide 2-phosphate reduced sodium salt | Sigma-Aldrich | Cat# N9660-15VL |
| β-Nicotinamide adenine dinucleotide reduced disodium salt hydrate | Sigma-Aldrich | Cat# N8129 |
| L-Glutathione reduced | Sigma-Aldrich | Cat# G4251 |
| Neocuproine | Sigma-Aldrich | Cat# N1501 |
| Chelex 100 (Mol. Biol. Grade Resin) | Biorad | Cat# 142-1253 |
| Ethylenediaminetetraacetic acid (99.99% trace metal basis) | Sigma-Aldrich | Cat# 431788 |
| Poly(ethyleneglycol) 3500 | Sigma-Aldrich | Cat# 202444 |
| Poly(ethyleneglycol) 6000 (BioUltra) | Sigma-Aldrich | Cat# 81255 |
| Sodium hydroxide (semiconductor grade) | Sigma-Aldrich | Cat# 306575 |
| Sodium Acetate Trihydrate | Fisher Scientific | Cat# S209-500 |
| Urea | Affimetrix/USB | Cat# 23036 |
| Guanidine hydrochloride | Sigma-Aldrich | Cat# G3272 |
| Nitrotetrazolium Blue chloride, ~98% (TLC) | Sigma-Aldrich | Cat# N6876 |
| (−)-Riboflavin | Sigma-Aldrich | Cat# R9504 |
| Iodoacetamide, BioUltra | Sigma-Aldrich | Cat# I1194 |
| **Critical Commercial Assays** | | |
| Stranded mRNA-Seq Kit, with KAPA mRNA Capture Beads | KAPA Biosystems | Cat# KK8420 |
| TruSeq Stranded mRNA Library Prep Kit for NeoPrep | Illumina | Cat# NP-202-1001 |
| D1000 ScreenTape | Agilent Technologies | Cat# 5067-5582 |
| D1000 Sample Buffer | Agilent Technologies | Cat# 5067-5602 |
| RNA ScreenTape | Agilent Technologies | Cat# 5067-5576 |
| RNA ScreenTape Sample Buffer | Agilent Technologies | Cat# 5067-5577 |
| Qubit dsDNA BR Assay Kit | ThermoFisher Scientific | Cat# Q32850 |
| TURBO DNA-free Kit | ThermoFisher Scientific | Cat# AM1907 |
| Quickchange II sitedirected mutagenesis kit | Agilent Technologies | Cat# 200523 |
| **Deposited Data** | | |
| Raw and analyzed data | This study | GEO: GSE100034 |
| **Experimental Models: Organisms/Strains** | | |
| See Table S1 | | |
| **Oligonucleotides** | | |
| See Table S2 | | |
| **Recombinant DNA** | | |
| pCORE (KanMX4-KlURA3) | (Storici and Resnick, 2006) | Addgene plasmid #72231 |
| pRM200 (HHT2-HHF2, TRP1) | (Mann and Grunstein, 1992) | N/A |
| pYX55 (*HHT2-H113N*-HHF2, TRP1) | This study | N/A |
| pCAS (LYP1 sgRNA, kanMX) | (Ryan et al., 2014) | Addgene plasmid #60847 |
| pCASk-HHT1-H113 (HHT1-H113 sgRNA, kanMX) | This study | N/A |

| | | |
|---|---|---|
| pCASk-HHT2-H113 (HHT2-H113 sgRNA, kanMX) | This study | N/A |
| pCASk-CUP1-F8 (CUP1-F8 sgRNA, kanMX) | This study | N/A |
| pET3a-H3 | (Luger et al., 1997) | N/A |
| pET3a-H4 | (Luger et al., 1997) | N/A |
| pET3a-H2A | (Luger et al., 1997) | N/A |
| pET3a-H2B | (Luger et al., 1997) | N/A |
| pH3.2 | This study | N/A |
| pH3.2-C110A | This study | N/A |
| pH3.2-H113N | This study | N/A |
| p601-12-177 | (Dorigo et al., 2003) | N/A |
| Software and Algorithms | | |
| SAMMate 2.7.4 | (Xu et al., 2011) | http://sammate.sourceforge.net/ |
| Tophat 2.0.9 | (Kim et al., 2013) | https://ccb.jhu.edu/software/tophat/index.shtml |
| Agilent 2200 Tapestation Software A.02.01 | Agilent Technologies | http://www.genomics.agilent.com/article.jsp?pageId=9100002 |
| MassHunter | Agilent Technologies | http://www.agilent.com/en-us/products/software-informatics/masshunter-suite/masshunter/masshunter-software |
| Prism | GraphPad Software | https://www.graphpad.com/scientific-software/prism/ |
| Image Studio Lite | LI-COR | https://www.licor.com/bio/products/software/image_studio_lite/index.html |
| My Curve Fit (beta) | My Assays Ltd. | https://mycurvefit.com/ |
| FIJI | (Schindelin et al., 2012) | https://imagej.net/Fiji/Downloads |
| Other | | |
| AnaeroGen sachet | Thermo Scientific | Cat# AN0025 |
| Falcon™ 15mL Conical Centrifuge Tubes | Corning Inc. | Cat# 352097 |
| Spectra/Por standard RC dialysis tubing (50mm Nominal Flat Width) | Spectumlabs.com | Cat# 132665 |

| | | |
|---|---|---|
| Spectra/Por standard RC dialysis tubing (23mm Nominal Flat Width) | Spectumlabs.com | Cat# 132650 |
| Hi-Trap Q-HP column | GE Healthcare | Cat# 17-1154-01 |
| Hi-Trap SP-HP column | GE Healthcare | Cat# 17-1152-01 |
| HiLoad 16/600 Superdex 200 column | GE Healthcare | Cat# 28989335 |
| Amicon Ultra–15/Ultracel-10K centrifugal filters | Millipore | Cat# UFC901024 |

## 4.6 References


Adamczyk, M., Poznanski, J., Kopera, E., and Bal, W. (2007). A zinc-finger like metal binding site in the nucleosome. FEBS Lett. *581*, 1409-1416.

Adkins, M.W., Howar, S.R., and Tyler, J.K. (2004). Chromatin disassembly mediated by the histone chaperone Asf1 is essential for transcriptional activation of the yeast PH05 and PH08 genes. Mol. Cell *14*, 657-666.

Agez, M., Chen, J., Guerois, R., van Heijenoort, C., Thuret, J.Y., Mann, C., and Ochsenbein, F. (2007). Structure of the histone chaperone ASF1 bound to the histone H3 C-terminal helix and functional insights. Structure *15*, 191-199.

Anbar, A.D. (2008). Oceans. Elements and evolution. Science *322*, 1481-1483.

Bar-Even, A., Noor, E., Savir, Y., Liebermeister, W., Davidi, D., Tawfik, D.S., and Milo, R. (2011). The moderately efficient enzyme: Evolutionary and physicochemical trends shaping enzyme parameters. Biochemistry *50*, 4402-4410.

Bleackley, M.R., and Macgillivray, R.T. (2011). Transition metal homeostasis: from yeast to human disease. Biometals *24*, 785-809.

Brachmann, C.B., Davies, A., Cost, G.J., Caputo, E., Li, J.C., Hieter, P., and Boeke, J.D. (1998). Designer deletion strains derived from Saccharomyces cerevisiae S288C: a useful set of strains and plasmids for PCR-mediated gene disruption and other applications. Yeast *14*, 115-132.

Brochier-Armanet, C., Forterre, P., and Gribaldo, S. (2011). Phylogeny and evolution of the Archaea: one hundred genomes later. Cur. Opin. Microbiol. *14*, 274-281.

Burkhead, J.L., Ralle, M., Wilmarth, P., David, L., and Lutsenko, S. (2011). Elevated Copper Remodels Hepatic RNA Processing Machinery in the Mouse Model of Wilson's Disease. J. Mol. Biol. *406*, 44-58.

Camerini-Otero, R.D., and Felsenfeld, G. (1977). Histone H3 disulfide dimers and nucleosome structure. Proc. Natl. Acad. Sci. USA *74*, 5519-5523.

Cartularo, L., and Costa, M. (2014). Role of iron in epigenetic regulation of gene expression. In Nutrition and Epigenetics, E. Ho, and F. Domann, eds. (CRC Press), pp. 253-272.

Corson, L.B., Strain, J.J., Culotta, V.C., and Cleveland, D.W. (1998). Chaperone-facilitated copper binding is a property common to several classes of familial amyotrophic lateral sclerosis-linked superoxide dismutase mutants. Proc. Natl. Acad. Sci. USA *95*, 6361-6366.

Culotta, V.C., Klomp, L.W.J., Strain, J., Casareno, R.L.B., Krems, B., and Gitlin, J.D. (1997). The copper chaperone for superoxide dismutase. J. Biol. Chem. *272*, 23469-23472.

Dai, J., Hyland, E.M., Yuan, D.S., Huang, H.L., Bader, J.S., and Boeke, J.D. (2008). Probing nucleosome function: A highly versatile library of synthetic histone H3 and H4 mutants. Cell *134*, 1066-1078.

Dancis, A., Yuan, D.S., Haile, D., Askwith, C., Eide, D., Moehle, C., Kaplan, J., and Klausner, R.D. (1994). Molecular characterization of a copper transport protein in Saccharomyces cerevisiae: an unexpected role for copper in iron transport. Cell *76*, 393-402.

Davey, C.A., Sargent, D.F., Luger, K., Maeder, A.W., and Richmond, T.J. (2002). Solvent mediated interactions in the structure of the nucleosome core particle at 1.9 angstrom resolution. J. Mol. Biol. *319*, 1097-1113.

Dorigo, B., Schalch, T., Bystricky, K., and Richmond, T.J. (2003). Chromatin fiber folding: Requirement for the histone H4 N-terminal tail. J. Mol. Biol. *327*, 85-96.

Felsenfeld, G. (1992). Chromatin as an essential part of the transcriptional mechanism. Nature *355*, 219-224.

Finney, J., Moon, H.J., Ronnebaum, T., Lantz, M., and Mure, M. (2014). Human copper-dependent amine oxidases. Arch. Biochem. Biophys. *546*, 19-32.

Forbes, A.J., Patrie, S.M., Taylor, G.K., Kim, Y.B., Jiang, L., and Kelleher, N.L. (2004). Targeted analysis and discovery of posttranslational modifications in proteins from methanogenic archaea by top-down MS. Proc. Natl. Acad. Sci. USA *101*, 2678-2683.

Forbes, S.A., Beare, D., Gunasekaran, P., Leung, K., Bindal, N., Boutselakis, H., Ding, M.J., Bamford, S., Cole, C., Ward, S., et al. (2015). COSMIC: exploring the world's knowledge of somatic mutations in human cancer. Nucleic Acids Res. *43*, D805-D811.

Furukawa, Y., Torres, A.S., and O'Halloran, T.V. (2004). Oxygen-induced maturation of SOD1: a key role for disulfide formation by the copper chaperone CCS. EMBO J. *23*, 2872-2881.

Galoppini, E., and Fox, M.A. (1996). Effect of the electric field generated by the helix dipole on photoinduced intramolecular electron transfer in dichromophoric alpha-helical peptides. J. Am. Chem. Soc. *118*, 2299-2300.

Garcia-Gimenez, J.L., Olaso, G., Hake, S.B., Bonisch, C., Wiedemann, S.M., Markovic, J., Dasi, F., Gimeno, A., Perez-Quilis, C., Palacios, O., et al. (2013). Histone h3 glutathionylation in proliferating mammalian cells destabilizes nucleosomal structure. Antioxid. Redox Signal. *19*, 1305-1320.

Glerum, D.M., Shtanko, A., and Tzagoloff, A. (1996). Characterization of COX17, a yeast gene involved in copper metabolism and assembly of cytochrome oxidase. J. Biol. Chem. *271*, 14504-14509.

Goldstein, A.L., and McCusker, J.H. (1999). Three new dominant drug resistance cassettes for gene disruption in Saccharomyces cerevisiae. Yeast *15*, 1541-1553.

Graden, J.A., and Winge, D.R. (1997). Copper-mediated repression of the activation domain in the yeast Mac1p transcription factor. Proc. Natl. Acad. Sci. USA *94*, 5550-5555.

Grunstein, M. (1997). Histone acetylation in chromatin structure and transcription. Nature *389*, 349-352.

Hassett, R., Dix, D.R., Eide, D.J., and Kosman, D.J. (2000). The Fe(II) permease Fet4p functions as a low affinity copper transporter and supports normal copper trafficking in Saccharomyces cerevisiae. Biochem. J. *351*, 477-484.

Hol, W.G. (1985). The role of the alpha-helix dipole in protein function and structure. Prog. Biophys. Mol. Biol. *45*, 149-195.

Holmgren, A. (1995). Thioredoxin structure and mechanism: conformational changes on oxidation of the active site sulfhydryls to a disulfide. Structure *3*, 239-243.

Huang, H.L., Maertens, A.M., Hyland, E.M., Dai, J.B.A., Norris, A., Boeke, J.D., and Bader, J.S. (2009). HistoneHits: A database for histone mutations and their phenotypes. Genome Res. *19*, 674-681.

Huster, D., Finegold, M.J., Morgan, C.T., Burkhead, J.L., Nixon, R., Vanderwerf, S.M., Gilliam, C.T., and Lutsenko, S. (2006). Consequences of copper accumulation in the livers of the Atp7b(-/-) (Wilson disease gene) knockout mice. Am. J. Pathol. *168*, 423-434.

Jensen, L.T., and Culotta, V.C. (2005). Activation of CuZn superoxide dismutases from Caenorhabditis elegans does not require the copper chaperone CCS. J. Biol. Chem. *280*, 41373-41379.

Jensen, L.T., Howard, W.R., Strain, J.J., Winge, D.R., and Culotta, V.C. (1996). Enhanced effectiveness of copper ion buffering by CUP1 metallothionein compared with CRS5 metallothionein in Saccharomyces cerevisiae. J. Biol. Chem. *271*, 18514-18519.

Jenuwein, T., and Allis, C.D. (2001). Translating the histone code. Science *293*, 1074-1080.

Karin, M., Najarian, R., Haslinger, A., Valenzuela, P., Welch, J., and Fogel, S. (1984). Primary structure and transcription of an amplified genetic locus: the Cup1 locus of yeast. Proc. Natl. Acad. Sci. USA *81*, 337-341.

Kim, H., Esser, L., Hossain, M.B., Xia, D., Yu, C.A., Riso, J., van der Helm, D., and Deisenhofer, J. (1999). Structure of antimycin A1, a specific electron transfer inhibitor of ubiquinol-cytochrome c oxidoreductase. J Am Chem Soc *121*, 4902-4903.

Kim, D., Pertea, G., Trapnell, C., Pimentel, H., Kelley, R., and Salzberg, S.L. (2013). TopHat2: accurate alignment of transcriptomes in the presence of insertions, deletions and gene fusions. Genome Biol. *14*, R36.

Klink, T.A., Woycechowsky, K.J., Taylor, K.M., and Raines, R.T. (2000). Contribution of disulfide bonds to the conformational stability and catalytic activity of ribonuclease A. Eur. J. Biochem. *267*, 566-572.

Kolberg, M., Strand, K.R., Graff, P., and Andersson, K.K. (2004). Structure, function, and mechanism of ribonucleotide reductases. Biochim. Biophys. Acta *1699*, 1-34.

Koonin, E.V. (2015). Origin of eukaryotes from within archaea, archaeal eukaryome and bursts of gene gain: eukaryogenesis just made easier? Philos. Trans. R. Soc. Lond. B. Biol. Sci. *370*, 20140333.

Krishnamoorthy, L., Cotruvo, J.A., Jr., Chan, J., Kaluarachchi, H., Muchenditsi, A., Pendyala, V.S., Jia, S., Aron, A.T., Ackerman, C.M., Wal, M.N., et al. (2016). Copper regulates cyclic-AMP-dependent lipolysis. Nat. Chem. Biol. *12*, 586-592.

Lambert, S.J., Nicholson, J.M., Chantalat, L., Reid, A.J., Donovan, M.J., and Baldwin, J.P. (1999). Purification of histone core octamers and 2.15 A X-ray analysis of crystals in KCl/phosphate. Acta Crystallogr. D. Biol. Crystallogr. *55*, 1048-1051.

Leitch, J.M., Jensen, L.T., Bouldin, S.D., Outten, C.E., Hart, P.J., and Culotta, V.C. (2009). Activation of Cu,Zn-Superoxide Dismutase in the Absence of Oxygen and the Copper Chaperone CCS. J Biol Chem *284*, 21863-21871.

Lek, M., Karczewski, K.J., Minikel, E.V., Samocha, K.E., Banks, E., Fennell, T., O'Donnell-Luria, A.H., Ware, J.S., Hill, A.J., Cummings, B.B., et al. (2016). Analysis of protein-coding genetic variation in 60,706 humans. Nature *536*, 285-291.

Li, W.T., Grayling, R.A., Sandman, K., Edmondson, S., Shriver, J.W., and Reeve, J.N. (1998). Thermodynamic stability of archaeal histones. Biochemistry *37*, 10563-10572.

Lin, S.J., and Culotta, V.C. (1996). Suppression of oxidative damage by Saccharomyces cerevisiae ATX2, which encodes a manganese-trafficking protein that localizes to Golgi-like vesicles. Mol. Cell. Biol. *16*, 6303-6312.

Longtine, M.S., McKenzie, A., Demarini, D.J., Shah, N.G., Wach, A., Brachat, A., Philippsen, P., and Pringle, J.R. (1998). Additional modules for versatile and economical PCR-based gene deletion and modification in Saccharomyces cerevisiae. Yeast *14*, 953-961.

Luger, K., Mader, A.W., Richmond, R.K., Sargent, D.F., and Richmond, T.J. (1997). Crystal structure of the nucleosome core particle at 2.8 A resolution. Nature *389*, 251-260.

Luger, K., Rechsteiner, T.J., and Richmond, T.J. (1999). Preparation of nucleosome core particle from recombinant histones. Methods Enzymol. *304*, 3-19.

Macomber, L., and Imlay, J.A. (2009). The iron-sulfur clusters of dehydratases are primary intracellular targets of copper toxicity. Proc. Natl. Acad. Sci. USA *106*, 8344-8349.

Mann, R.K., and Grunstein, M. (1992). Histone H3 N-terminal mutations allow hyperactivation of the yeast Gal1 gene in vivo. EMBO J. *11*, 3297-3306.

Mattiroli, F., Bhattacharyya, S., Dyer, P.N., White, A.E., Sandman, K., Burkhart, B.W., Byrne, K.R., Lee, T., Ahn, N.G., Santangelo, T.J.*, et al.* (2017). Structure of histone-based chromatin in Archaea. Science *357*, 609-611.

McRae, R., Lai, B., and Fahrni, C.J. (2013). Subcellular redistribution and mitotic inheritance of transition metals in proliferating mouse fibroblast cells. Metallomics *5*, 52-61.

Nevitt, T., Ohrvik, H., and Thiele, D.J. (2012). Charting the travels of copper in eukaryotes from yeast to mammals. Biochim. Biophys. Acta *1823*, 1580-1593.

Pereira, S.L., Grayling, R.A., Lurz, R., and Reeve, J.N. (1997). Archaeal nucleosomes. Proc. Natl. Acad. Sci. USA *94*, 12633-12637.

Peterson, C.L. (2008). Salt gradient dialysis reconstitution of nucleosomes. CSH Protoc. *2008*, pdb.prot5113.

Pufahl, R.A., Singer, C.P., Peariso, K.L., Lin, S.J., Schmidt, P.J., Fahrni, C.J., Culotta, V.C., PennerHahn, J.E., and OHalloran, T.V. (1997). Metal ion chaperone function of the soluble Cu(I) receptor Atx1. Science *278*, 853-856.

Rae, T.D., Schmidt, P.J., Pufahl, R.A., Culotta, V.C., and O'Halloran, T.V. (1999). Undetectable intracellular free copper: The requirement of a copper chaperone for superoxide dismutase. Science *284*, 805-808.

Ramachandran, S., Vogel, L., Strahl, B.D., and Dokholyan, N.V. (2011). Thermodynamic stability of histone H3 is a necessary but not sufficient driving force for its evolutionary conservation. PLoS Comput. Biol. *7*, e1001042.

Rando, O.J. (2010). Genome-wide mapping of nucleosomes in yeast. Methods Enzymol. *470*, 105-118.

Ryan, O.W., Skerker, J.M., Maurer, M.J., Li, X., Tsai, J.C., Poddar, S., Lee, M.E., DeLoache, W., Dueber, J.E., Arkin, A.P., et al. (2014). Selection of chromosomal DNA libraries using a multiplex CRISPR system. Elife *3*, e03703.

Saavedra, R.A. (1986). Histones and metal-binding domains. Science *234*, 1589-1589.

Saito, M.A., Sigman, D.M., and Morel, F.M.M. (2003). The bioinorganic chemistry of the ancient ocean: the co-evolution of cyanobacterial metal requirements and biogeochemical cycles at the Archean-Proterozoic boundary? Inorg. Chim. Acta *356*, 308-318.

Sandman, K., Krzycki, J.A., Dobrinski, B., Lurz, R., and Reeve, J.N. (1990). HMf, a DNA-binding protein isolated from the hyperthermophilic archaeon Methanothermus fervidus, is most closely related to histones. Proc. Natl. Acad. Sci. USA *87*, 5788-5791.

Sandman, K., and Reeve, J.N. (1998). Origin of the eukaryotic nucleus. Science *280*, 501-503.

Schindelin, J., Arganda-Carreras, I., Frise, E., Kaynig, V., Longair, M., Pietzsch, T., Preibisch, S., Rueden, C., Saalfeld, S., Schmid, B., et al. (2012). Fiji: an open-source platform for biological-image analysis. Nat. Methods *9*, 676-682.

Schmitt, M.E., Brown, T.A., and Trumpower, B.L. (1990). A rapid and simple method for preparation of RNA from Saccharomyces cerevisiae. Nucleic Acids Res. *18*, 3091-3092.

Soares, D., Dahlke, I., Li, W.T., Sandman, K., Hethke, C., Thomm, M., and Reeve, J.N. (1998). Archaeal histone stability, DNA binding, and transcription inhibition above 90 degrees C. Extremophiles *2*, 75-81.

Storici, F., and Resnick, M.A. (2006). The delitto perfetto approach to in vivo site-directed mutagenesis and chromosome rearrangements with synthetic oligonucleotides in yeast. Methods Enzymol. *409*, 329-345.

Turski, M.L., and Thiele, D.J. (2009). New roles for copper metabolism in cell proliferation, signaling, and disease. J. Biol. Chem. *284*, 717-721.

Winston, G.P., and Jaiser, S.R. (2008). Copper deficiency myelopathy and subacute combined degeneration of the cord - why is the phenotype so similar? Med. Hypotheses *71*, 229-236.

Xu, G., Deng, N., Zhao, Z., Judeh, T., Flemington, E., and Zhu, D. (2011). SAMMate: a GUI tool for processing short read alignments in SAM/BAM format. Source Code Biol. Med. *6*, 2.

Yang, L.C., McRae, R., Henary, M.M., Patel, R., Lai, B., Vogt, S., and Fahrni, C.J. (2005). Imaging of the intracellular topography of copper with a fluorescent sensor and by synchrotron x-ray fluorescence microscopy. Proc. Natl. Acad. Sci. USA *102*, 11179-11184.

# Chapter 5

## The histone cupric reductase regulates iron homeostasis via Cu-Zn superoxide dismutase

## 5.1 Summary

The link between copper and iron metabolism has been described in many organisms, mainly through the role of copper in uptake and acquisition of iron. Here we describe the impact of histone H3-mediated copper regulation on cellular iron homeostasis. Using *Saccharomyces cerevisiae*, we provide evidence that disruption of the histone H3-H3' dimerization interface, which we have previously shown to impair the novel copper reductase activity of histones, makes cells sensitive to iron deficiency in a copper-dependent manner. This is not due to disruption of the known copper-dependent iron uptake machinery. Instead, the function of Cu-Zn superoxide dismutase is important in supporting growth under iron-deficient conditions and depends on provision of biousable copper by the nucleosome.

## 5.2 Introduction

Iron, one of the most abundant elements on Earth, is an essential metal for all biological systems. The use of iron as a co-factor in cellular functions is wide-ranging, and includes DNA replication and repair, ribosome biogenesis, metabolic catalysis, and oxygen transport (Lieu et al., 2001; Zhang, 2014). Iron may exist in several oxidation states, with +2 (ferrous) and +3 (ferric) being the most common and biologically relevant. The redox property of iron makes it suitable for a variety of cellular electron transfer processes (Aisen et al., 2001). Iron cofactors in proteins exist in various forms, either as mono- or di-iron clusters or as part of the prosthetic groups iron-sulfur clusters or heme. The biousability of iron ions as cofactors in proteins depends on several factors, including its oxidation state (Dlouhy and Outten, 2013). Oxidized iron ($Fe^{3+}$) is the prominent form found in the aerobic environment since the Great Oxygenation Event. The ferric form of iron is poorly soluble in water and forms precipitates with inorganic molecules such as phosphate (Hong Enriquez and Do, 2012). Organisms have devised mechanisms for

enhancing the bioavailability and acquisition of $Fe^{3+}$. These include cell-surface reduction of iron to soluble $Fe^{2+}$, acidification of the extracellular environment to solubilize ferric iron, and the use of ferric-binding siderophores (Dlouhy and Outten, 2013; Schroder et al., 2003).

Assimilatory iron reduction—the process of enzymatic $Fe^{3+}$ reduction for uptake and intracellular utilization—has been found in nearly all organisms. Most ferric reductases in eukaryotes are associated with cellular membranes that make $Fe^{2+}$ available for iron transport systems (Schroder et al., 2003). Intriguingly, a major iron transport pathway involves re-oxidation of ferrous to ferric iron in the process, and this system involves multicopper oxidases that produce $Fe^{3+}$ ions for ferric transporters (Taylor et al., 2005). This copper-dependent mechanism of iron acquisition partly accounts for the interdependency observed between copper and iron homeostasis in both eukaryotes and prokaryotes. This system has been well-defined in *Saccharomyces cerevisiae* and includes the multicopper ferroxidase, Fet3, coupled to the ferric transporter Ftr1. Fet3 contains four copper ions and depends on the redox property of copper for its iron oxidase activity (Kosman, 2003; Taylor et al., 2005). In yeast, the Fet3-Ftr1 system constitutes the high affinity iron ion uptake machinery and is induced in response to iron depletion. A second homologous ferroxidase, Fet5, is involved in mobilization of iron from the vacuole, a major organelle for metal storage (Urbanowski and Piper, 1999). The analogous multicopper ferroxidases in mammals, hephaestin and ceruloplasmin, are also involved in iron uptake and mobilization between organs (Hellman and Gitlin, 2002). Given the requirement of copper for iron mobilization via this system, disruption of copper homeostasis would be expected to indirectly impact iron metabolism. The significance of this molecular-level connection is highlighted by the fact that iron disorders result from copper deficiency or genetic lesions in ceruloplasmin (Frieden, 1971).

Copper is an essential transition metal and its homeostasis is tightly regulated to ensure efficient utilization while simultaneously preventing toxicity. Copper, much like iron, is a redox-active transition metal, shifting between its cupric ($Cu^{2+}$) and cuprous ($Cu^{1+}$) forms when utilized as a co-factor in proteins for electron transfer reactions. The oxidation state of copper is also important for its proper intracellular trafficking, which is mediated by chaperones that carry the cuprous form of copper (Palumaa, 2013). Thus, reduced copper is the more biousable form of copper for cell biology.

It is presumed that the reducing environment of the eukaryotic cell is responsible for non-specifically maintaining the reduced state of copper ions. Although a reasonable assumption based on the ease with which glutathione can interact with copper ions *in vitro*, it is not yet proven to be the case in the complex milieu of the cell cytoplasm. In the case of copper, the recently described function of the yeast and human histones as a cupric reductase provides evidence for an active mechanism that ensures copper is reduced for use by the cell and mitochondria (see Chapter 4). The enzymatic function of the eukaryotic nucleosome was shown to be important for two copper-dependent processes, mitochondrial respiration and superoxide dismutase activity. Here, we asked whether the nucleosome copper reductase also provides biousable copper for the regulation of iron homeostasis.

We provide evidence that mutation of H3H113 to asparagine in the H3-H3' dimerization interface of the nucleosome, the likely active site for the cupric reductase activity, leads to poor survival in iron-limiting conditions in *S. cerevisiae.* This defect cannot be accounted for by diminished iron uptake capacity, suggesting that the copper-dependent iron transport systems is unaffected by the H3H113N mutation. Interestingly, we found that Cu-Zn superoxide dismutase 1 (Sod1) contributes to the ability of cells to survive iron limitation. Our data reveal the

previously unappreciated role of Sod1 in iron deficiency, and the novel process in which Sod1 activity is dependent on the provision of reduced copper ions by the nucleosome.

The link between Sod1 function and the integrity of iron metabolism described here has important implications for understanding the pathogenic mechanisms underlying many diseases. Sod1 is implicated in certain human pathologies, most notably amyotrophic lateral sclerosis, as well as Parkinson's disease and cancer (Papa et al., 2014; Saccon et al., 2013). The occurrence of iron deficiency is widespread and has implication for diseases ranging from anemias to neurodegeneration and numerous chronic diseases (Kotze et al., 2009). The role of histones in providing copper for Sod1 functions, including its role in iron homeostasis, can provide new insights into such diseases and a novel perspective for understanding the role of copper in iron metabolism.

## 5.3 Results

### 5.3.1 Residues in the histone H3 dimerization region are required for copper-dependent growth in iron-limiting conditions.

Histidine residue 113 in histone H3 lies at the interface between the two H3 molecules at the core of the nucleosome. We previously showed that the mutation of this histidine to asparagine (H113N) disrupts copper-dependent processes in *S. cerevisiae* because of defects in the copper reductase activity of the nucleosome. Given the copper dependency of the high affinity iron uptake system based on the multicopper ferroxidase Fet3 in *S. cerevisiae*, we asked whether the H113N mutation results in diminished iron uptake abilities and survival in iron-limiting conditions.

We examined the ability of $H3^{H113N}$ mutant to grow in iron-deplete media using the iron chelator, bathophenanthrolinedisulfonic acid (BPS), which limits iron availability for cellular

uptake. Although *H3*$^{H113N}$ has a slower growth rate than the strains with wild-type histones (WT) in rich media, it does not show enhanced sensitivity to iron depletion, even at BPS concentrations that significantly reduce growth (Figure 5-1A). Upon iron depletion, a cellular response is mediated by the iron-responsive transcription factor Aft1, that induces the expression of multiple iron uptake systems and downregulates non-essential iron consuming processes (Kaplan and Kaplan, 2009; Rutherford and Bird, 2004). We reasoned that the function of Fet3 may still be dependent on nucleosome copper reduction but a defect may be difficult to detect given the robust presence of other iron uptake systems. To examine the ability to deliver copper for Fet3 function more directly, we deleted the copper-transporting P-type ATPase Ccc2, which transports $Cu^{1+}$ into the endomembrane system for constitution of enzymatically active Fet3 in the secretory pathway (Yuan et al., 1995). As expected *ccc2Δ* strains are more sensitive to iron depletion when compared with the wildtype counterpart. The combination of H3H113N with *ccc2Δ* exacerbates the growth defect in iron-limiting conditions (Figure 5-1B). This defect is rescued by addition of excess copper to the media suggesting a copper-related deficiency in *H3*$^{H113N}$*ccc2Δ* compared to *ccc2Δ* alone in iron-limiting conditions. Deletion of *AFT1* to disable the overall transcriptional response to iron depletion significantly reduces growth in iron-limited media. Intriguingly, the defect of *aft1Δ* strain in iron limitation is recovered by addition of exogenous copper; however, more copper is needed to achieve a similar rescue in *H3*$^{H113N}$*aft1Δ* (Figure 5-1C). These results highlight the copper-dependent defect in strains harboring H3H113N.

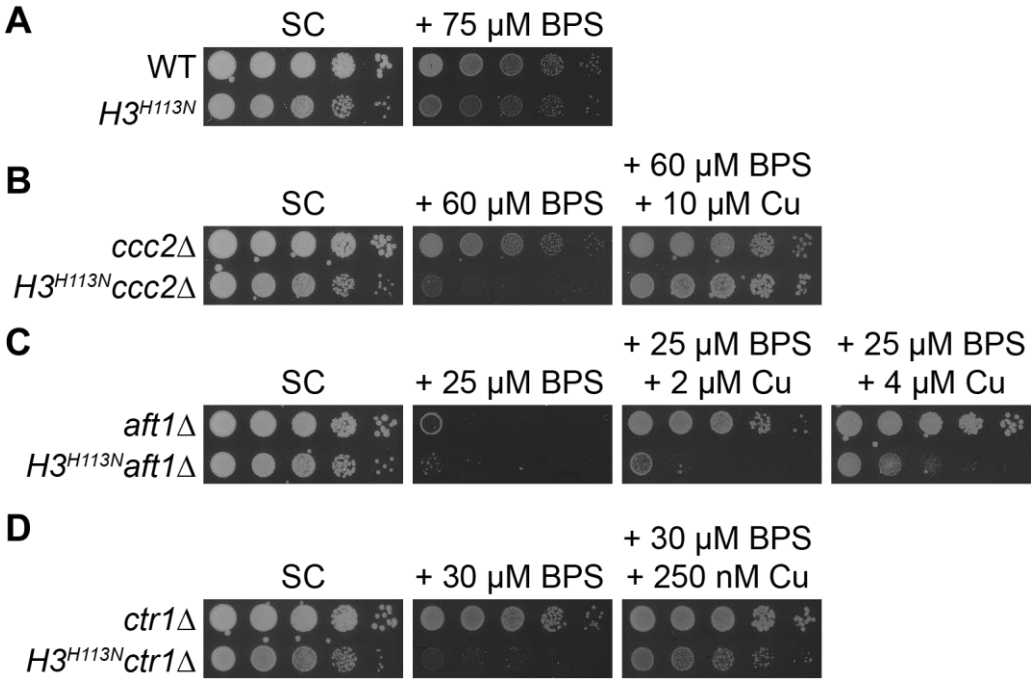


**Figure 5-1: *H3*$^{H113N}$ diminishes copper utilization for iron homeostasis. (A-D)** Spot test assays with the indicated strains in rich glucose-containing media (SC) with the indicated amounts of $CuSO_4$. Baseline copper concentration in SC media is ~ 0.16 μM.

Deletion of *CTR1*, a primary copper transporter renders cells sensitive to iron depletion, confirming the known requirement of copper for Fet3 activity and iron uptake (Yuan et al., 1995) (Figure 5-1D). Similar to *ccc2Δ* and *aft1Δ*, combination with the H3H113N mutation significantly reduces growth in iron depletion when combined with *ctr1Δ* alone. The greater defect of *H3*$^{H113N}$*ctr1Δ* compared with *ctr1Δ* is recovered by addition of excess exogenous copper (Figure 5-1D). In our previous work, it was observed that other residues in the vicinity of histidine 113 in the nucleosome structure contributed to the function of the nucleosome in copper provision. We first confirmed that another histidine 113 substitution, H3H113Y, also abrogated copper utilization of *ctr1Δ* in iron-limited media. The observation that *H3*$^{H113Y}$*ctr1Δ*, like *H3*$^{H113Y}$*ctr1Δ*, had greater sensitivity to BPS than *ctr1Δ* alone confirms the loss of function of the histidine residue and its role in utilizing copper for iron homeostasis (Figure 5-2A). Furthermore,

mutation of alanine 111 to threonine in histone H3 similarly negatively affected the ability to grow in iron-limited conditions. The growth defect of *H3*$^{A111T}$*ctr1Δ* in the presence of BPS was rescued by extra exogenous copper further supporting the role of histone H3, and the nucleosome copper reductase, in facilitating the use of copper for iron homeostasis. Mutation of arginine 116 to asparagine, which indirectly disrupts the positioning of histidine 113 in the nucleosome structure (Muthurajan et al., 2004), resulted in a severe growth defect even in rich media, as we had observed previously (see Chapter 4). This general growth defect confounds the interpretation of a specific defect in iron-limiting conditions, but considering that with the re-addition of copper in the presence of 45 µM BPS, the *H3*$^{R116H}$*ctr1Δ* grows to about the same extent as *H3*$^{H113N}$*ctr1Δ*, this suggests that the impact of the H3R116H mutation on copper utilization is much less significant than the effect of the H3H113N mutation.

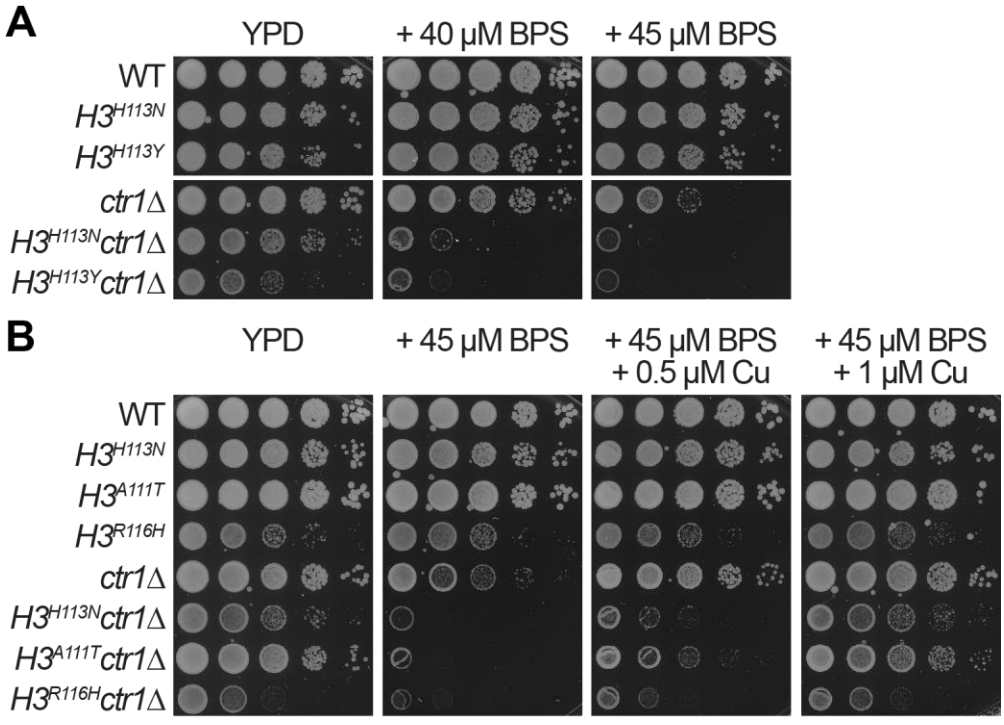

**Figure 5-2: Histone H3 mutants disrupt copper utilization of *ctr1Δ* for iron homeostasis. (A, B)** Spot test assays with the indicated strains in rich glucose-containing media (YPD) with the indicated amounts of $CuSO_4$. Baseline copper concentration in YPD media is ~ 1 μM.

The reduced survival of strains with H3H113N in iron-depleted media was not due to differences in gene expression, since strains harboring H3H113N mutation have similar global gene expression patterns as the WT counterpart (Figure 5-3A). The expression of genes involved in iron homeostasis and the induction of the iron-deficiency response mediated by Aft1 is similar between strains with WT and H113N histone H3 (Figure 5-3B). Altogether our data suggest that H3H113 contributes to growth or survival in iron-limiting conditions, likely through the nucleosome copper reductase activity and provision of biousable copper.

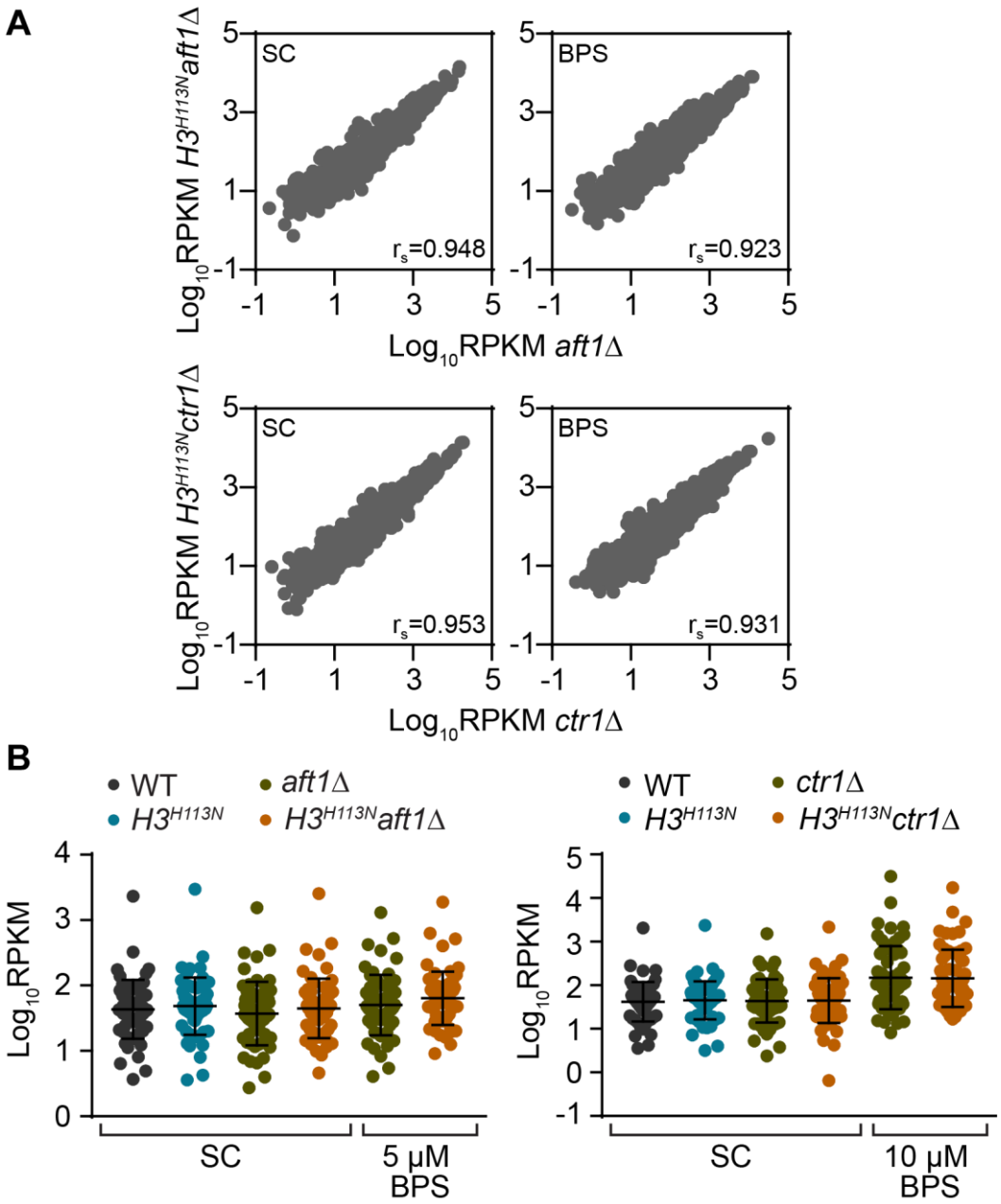


**Figure 5-3: The H3H113N mutation does not affect expression of genes involved in iron homeostasis. (A)** Scatterplots of average global gene expression values from exponentially growing cells in SC and SC containing BPS, with Spearman's rank correlation coefficient ($r_s$) as indicated. **(B)** Average mRNA expression levels for genes involved in iron homeostasis in iron replete and deplete growth conditions from two independent experiments.

### 5.3.2 Diminished survival of H3H113N mutant strains in iron limitation is not due to differences in total cellular iron content or iron uptake capacity.

We hypothesized that defective iron uptake due to decreased copper provision for Fet3 is

the reason the H3 mutants sensitize cells to iron limitation. To determine whether this is the case, we first measured intracellular iron content using inductively-coupled mass spectrometry (ICP-MS). Deletion of *AFT1* or *CTR1* results in an expected reduction in steady-state levels of intracellular iron in rich media (Figure 5-4). When grown in BPS-containing media, a further reduction in iron levels is detected (Figure 5-4). However, strains harboring H3H113N have similar levels of intracellular iron as the WT counterpart both in iron-replete and iron-deplete conditions. Surprisingly, addition of exogenous copper in BPS-containing media, which we show to enhance growth of *AFT1* and *CTR1* deletion strains, does not lead to a detectable increase in intracellular iron levels (Figure 5-4). These findings suggest that a copper-dependent process other than Fet3-mediated iron uptake is responsible for enhancing iron homeostasis in iron-limited conditions. Likewise, they challenged our hypothesis that the defect in H3H113N strains is due to defective copper delivery for Fet3 function.

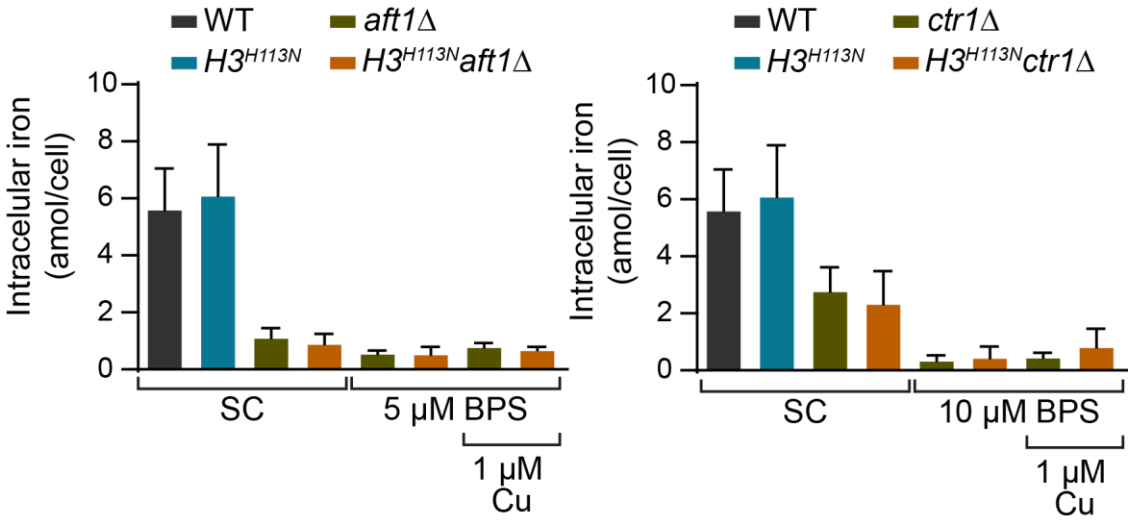


**Figure 5-4: Histone H3 H113 residue does not regulate iron accumulation in iron-limiting conditions.** Intracellular iron content of cells grown in the indicated media for 3-4 doublings. Bar graphs represent mean ± SD from 3-6 replicate cultures.

Steady-state iron contents in *aft1Δ* and *ctr1Δ* backgrounds, especially in low iron conditions, are significantly lower than the WT. The measurements are close to or below the

lower limit of the linear range in our ICP-MS experiments. This poses a technical problem for the accurate detection of differences between strains. We therefore decided to assess the high affinity iron uptake machinery in a different manner, by testing the ability of strains with WT or H3H113N to functionally induce iron uptake in response to a period of iron depletion. To do so, strains were grown in high concentration of BPS to significantly deplete intracellular iron content, leading to induction of the iron deficiency response and upregulation of iron uptake mechanisms. After a period of growth in the presence of BPS, cells were transferred to iron-replete media and intracellular iron was measured after one hour and one population doubling of recovery. Total cellular iron content during the depletion phase is reduced equally in both WT and $H3^{H113N}$ (Figure 2B). Following removal of BPS, a large increase in intracellular iron is observed as a result of the activation of the iron deficiency response during the depletion phase. However, WT and $H3^{H113N}$ increase intracellular iron to the same level (Figure 5-5A). Similarly, iron uptake after a period of depletion in the c*tr1Δ* or *ccc2Δ* strains is identical between strains harboring WT and H113N histone H3 (Figure 5-5B). Note that the iron uptake response is substantially attenuated in both c*tr1Δ* and *ccc2Δ* strains compared to WT, confirming the requirement of copper delivery to Fet3 for iron uptake. To further limit copper availability for Fet3 activation, copper chelator Bathocuproinedisulfonic acid (BCS) was used during iron addback for experiments done with *ccc2Δ* strains. However, even in such copper-limiting media no iron uptake defect was observed in $H3^{H113N}$*ccc2Δ* compared with *ccc2Δ* (Figure 5-5B). These findings are in agreement with steady-state measurements that also revealed wildtype levels of iron in the context of H3H113N. Despite diminished survival conferred by H3H113N mutation in iron-limiting conditions, we have not detected a defect in iron uptake capacity and iron accumulation in this context. This suggests that the copper-related defect of $H3^{H113N}$ strains in

coping with iron depletion is not primarily due to limited provision of copper for Fet3 activity.

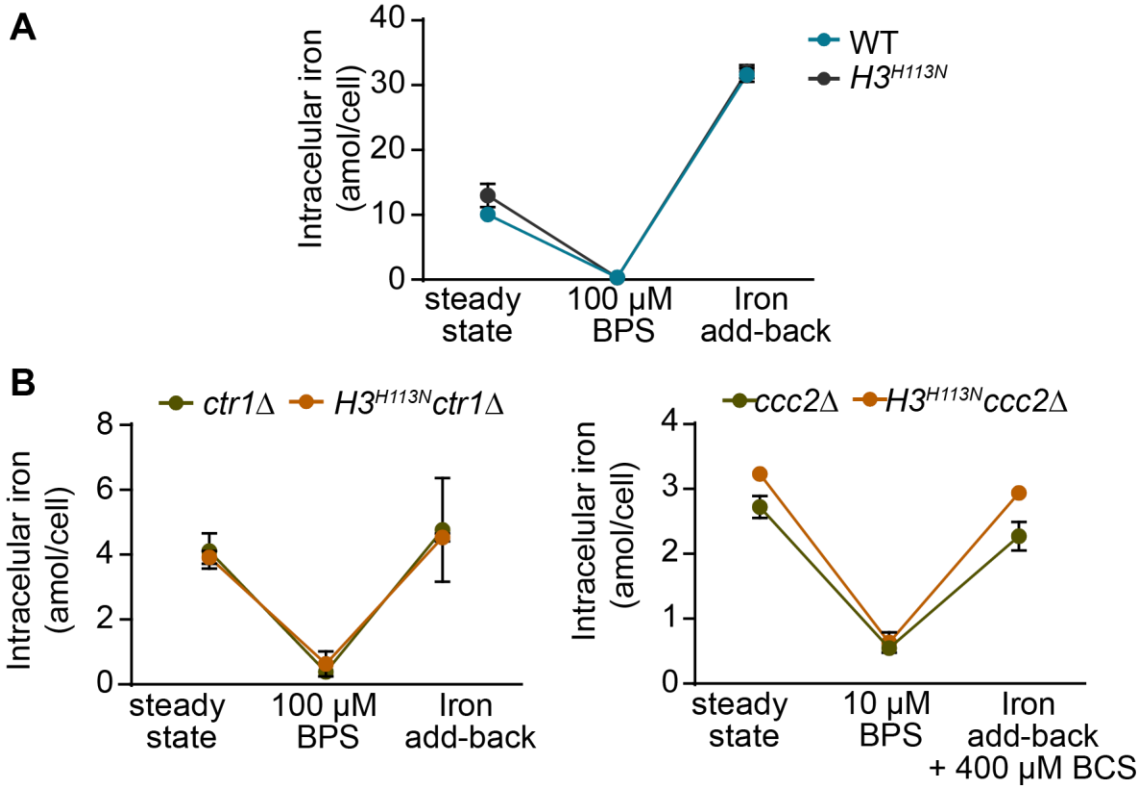


**Figure 5-5: The H3H113N mutation does not inhibit the iron uptake response. (A)** and **(B)** Assay for iron uptake capacity showing intracellular iron content from exponentially growing cells in SC and cells grown in SC containing BPS for 2-3 doublings followed by incubation in SC for 1 population doubling **(B)** or 1 hour **(C)**. Note: the copper chelator Bathocuproinedisulfonic acid (BCS) is used to deplete copper during iron addback for experiments done with *ccc2Δ* strains to further limit copper availability for Fet3 activation.

### 5.3.3 The defect of H3H113N in iron limitation is due to Sod1 function.

Since the functionality of Fet3 is intact in *H3*$^{H113N}$, we wondered whether other components of iron metabolism are dependent on utilization of copper. The Fet3-related multicopper ferroxidase, Fet5, and the ferric transporter Fth1 form a complex analogous to Fet3-Ftr1 on the vacuolar membrane. Fet5 uses the same copper-dependent redox mechanism as Fet3 for transport of iron across the vacuolar membrane into the cytoplasm (Spizzo et al., 1997). This intracellular iron transport system is induced by iron limitation in an Aft1-dependent manner and can contribute to iron metabolism by allowing the utilization of stored vacuolar iron

(Urbanowski and Piper, 1999). We deleted *FET3* alone and in combination with *FET5* in the context of WT or H113N histone H3. Deletion of *FET3* renders cells defective in low iron conditions, while deletion of *FET5* has a minor effect alone and does not enhance the growth defect of *fet3Δ* strains (Figure 5-6). Interestingly, the growth defect in low iron associated with H3H113N is still observed in the absence of Fet3 and Fet5 (Figure 5-6). Furthermore, exogenous copper can still rescue the growth defect of *fet3Δ* and *fet5Δ* strains, albeit at a higher copper concentration (Figure 5-6), despite the lack of a multicopper ferroxidase to utilize the copper for the iron uptake response. These genetic data further suggest the contribution of histones to a Fet3-independent, copper-dependent process in supporting iron homeostasis.

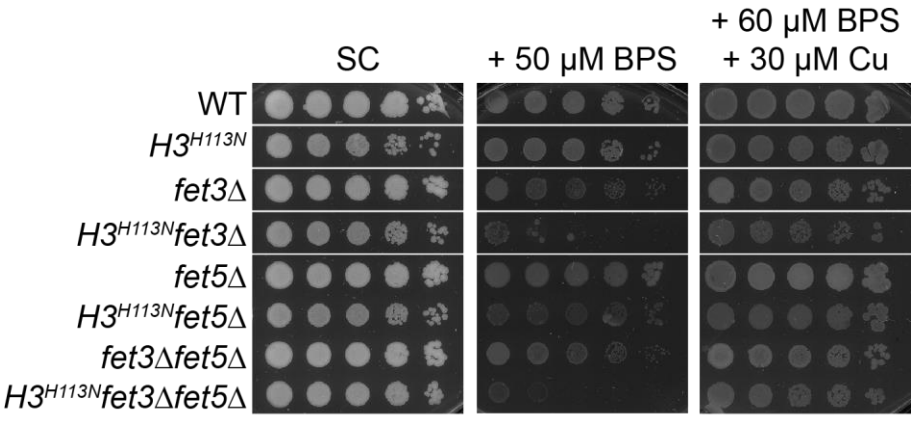


**Figure 5-6: Loss of multicopper ferroxidase function cannot account for the defect of *H3$^{H113N}$* strains in iron-limited media.** Spot test assays with the indicated strains in rich glucose-containing media (SC) with the indicated amounts of BPS and $CuSO_4$. Baseline copper concentration in SC media is ~ 0.16 μM.

Iron metabolism and utilization depends not only on the intracellular concentration but also proper trafficking, storage and speciation of iron (Dlouhy and Outten, 2013). An essential species of iron used ubiquitously as a co-factor in all forms of life are the iron-sulfur (Fe-S) cluster prosthetic groups (Lill, 2009). The properties of Fe-S clusters, such as oxidation states and the local protein environment, are important for the function of these co-factors in diverse biological reactions (Rouault and Tong, 2005). The activity of these co-factors is therefore

sensitive to oxidation. The Cu-Zn superoxide dismutase, as one of the major cytosolic antioxidant defense systems, is important for protecting Fe-S clusters (Popovic-Bijelic et al., 2016; Rouault and Tong, 2005; Wallace et al., 2004). For instance, Sod1 is probably required for maintaining the activity of Fe-S cluster containing enzymes in certain amino acid biosynthetic pathways, explaining the auxotrophy of *sod1Δ* for those amino acids (Wallace et al., 2004). Indeed, in our previous work (see Chapter 4), we observed that the H3H113N mutation resulted in decreased Sod1 activity which in turn explained a copper-dependent lysine auxotrophy.

The integrity of Fe-S clusters and the potential protective role of Sod1 may be even more imperative when iron is limiting. Since the nucleosome copper reductase activity has been shown to be required for optimal Sod1 function, we questioned whether in iron limitation suboptimal Sod1 function underlies the poor survival of strains harboring H3H113N. Deletion of SOD1 in the context of WT or H113N histone H3 results in a growth defect in iron limitation suggesting a requirement of this enzyme for iron metabolism (Figure 5-7A). In contrast to what we observed in strain backgrounds null for components of the iron regulon, $H3^{H113N}$*sod1Δ* does not show any additional defect in iron-deplete conditions compared to *sod1Δ* alone (Figure 5-7A). This suggests that the defect in coping with iron depletion due to H3H113N may be attributed to Sod1 function. In support of these results, combination of *aft1Δ* and *sod1Δ* results in a substantial and synergistic growth defect in the presence of BPS, further illustrating the role of Sod1 in iron homeostasis (Figure 5-7B). Importantly, the iron homeostasis defect of the *aft1Δ sod1Δ* mutant is comparable in magnitude to the $H3^{H113N}$*aft1Δ* mutant, and likewise the H3H113N mutation does not result in further growth defect compared to the *aft1Δ sod1Δ* mutant (Figure 5-7B). Thus, the growth defect of H3H113N strains in iron-limited media can be accounted for by a copper-dependent defect in Sod1 function.

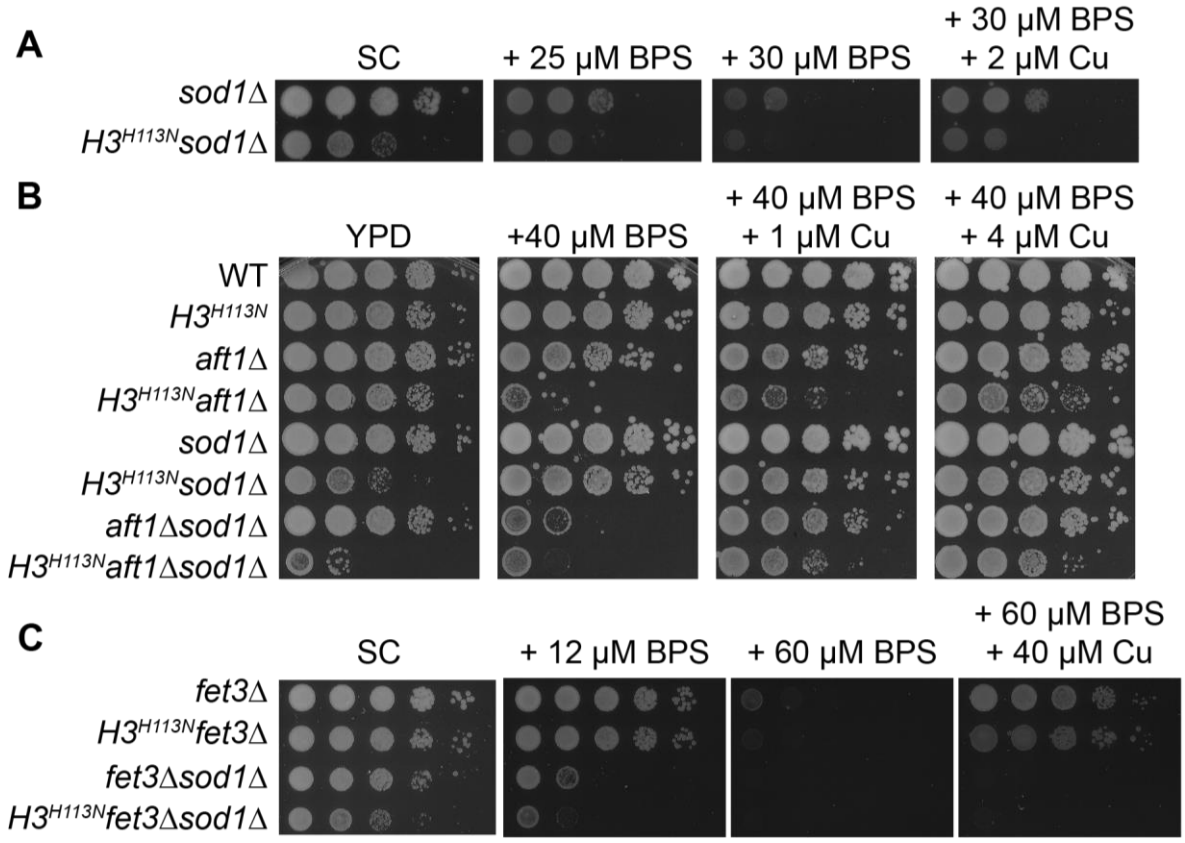


**Figure 5-7: Loss of Sod1 results in sensitivity to iron deficiency and explains the defect of *H3$^{H113N}$* strains. (A-C)** Spot test assays with the indicated strains in rich glucose-containing media (SC or YPD) with the indicated amounts of BPS and $CuSO_4$. Baseline copper concentration in SC media is ~ 0.16 μM and is ~ 1 μM in YPD.

Addition of exogenous copper rescues the growth defect of *sod1Δ, H3$^{H113N}$sod1Δ, aft1Δsod1Δ,* and *H3$^{H113N}$aft1Δsod1Δ* similarly, probably via the activation Fet3-mediated iron uptake system in both strains (Figure 5-7B). Combination of FET3 and SOD1 deletion leads to an even greater growth defect in low iron than the deletion of either gene alone (Figure 5-7C). Importantly, the double deletion abrogates the copper-mediated rescue in low iron media regardless of histone H3 (Figure 5-7C). This finding strongly indicates that the exogenous copper is utilized by these two independent pathways to support growth in iron limitation. While both high-affinity iron uptake system and Sod1-mediated antioxidant defense are required for supporting growth under iron limitation, the enzymatic activity of the nucleosome only impacts

the latter.

Lastly, the functions of Sod1 and the multicopper oxidases Fet3 and Fet5 are only relevant in the presence of oxygen. Together with our findings that histone H3, and the nucleosome copper reductase function, supports Sod1 function in iron homeostasis, this leads to the prediction that disruption of histone H3 would not result in iron homeostasis defects in hypoxic conditions where Sod1 function is not required. Indeed, both *sod1Δ* and *fet3Δ* strains, regardless of the histone H3 allele did not have a noticeable growth defect in the presence of BPS in hypoxic conditions relative to WT (Figure 5-8). Interestingly, *aft1Δ* strains were slightly more sensitive to iron limitation in hypoxia than in normoxia, but importantly, hypoxia rescued the additional growth defect of the H3H113N mutation (Figure 5-8). This is consistent with oxygen-mediated damage contributing to the growth defect in iron-limiting media and to the non-essentiality of providing copper for Sod1 function in the absence of oxygen and superoxide. Together, these data indicate that the enzymatic activity of the nucleosome can have far-reaching effects on numerous biological processes through supporting Sod1 activity and the iron metabolome.

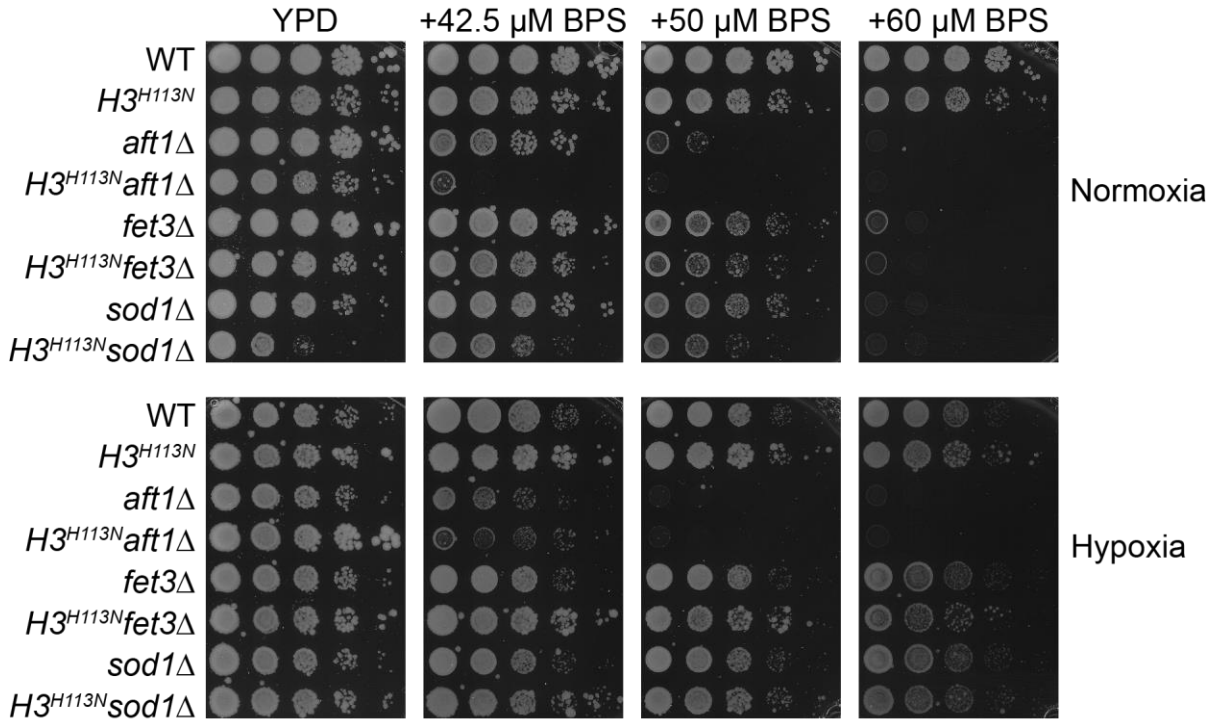


**Figure 5-8: *H3$^{H113N}$* strains do not have a specific iron homeostasis defect in hypoxia.** Spot test assays with the indicated strains in rich glucose-containing media (YPD) with the indicated amounts of BPS and in either normoxia or hypoxia. Media also contain 0.5% Tween-80, 0.5% ethanol, and 20 μg/uL ergosterol to support growth in the absence of oxygen. Baseline copper concentration in YPD media is ~ 1 μM.

## 5.4 Discussion

The link between iron and copper metabolism has been well established for decades. The notion that copper can interfere with iron metabolism by competition for metal uptake or by displacement of protein-bound iron is certainly a consideration when copper is in excess or improperly handled (Arredondo et al., 2006; Foster et al., 2014). Conversely, iron homeostasis depends on copper utilization, and the discovery of multicopper ferroxidases involved in iron mobilization has provided a molecular explanation for this connection (Lang et al., 2012; Vashchenko and MacGillivray, 2013).

More recently, sparse evidence suggesting a connection between iron homeostasis and oxidative damage of iron cofactors—as opposed to iron-mediated oxidative damage—have been

put forth. Deficiencies in iron homeostasis achieved by limiting iron abundance, either via deletion of components of the iron regulon in yeast (e.g. Fet3) or by use of iron chelators, have been shown to render cells sensitive to oxidants (Castells-Roca et al., 2011). Conversely, oxidative stress partially induces the iron deficiency response and plays a role in activating Aft1 in yeast (Castells-Roca et al., 2011; Pujol-Carrion et al., 2006). Although multiple interpretations can be offered, these findings can suggest a vulnerability to oxidative damage during iron deprivation due to a further depletion of biousable iron. Alternatively, under conditions of oxidative stress, cells may require greater iron utilization for antioxidant defense. Although more work is required to understand the underlying mechanisms, these findings suggest a regulatory link between iron metabolism and cellular redox states.

Superoxide dismutase 1, a major contributor to redox homeostasis, has been shown to affect iron homeostasis as its deletion results in upregulation of genes involved in iron uptake (De Freitas et al., 2000). Vulnerability of iron-sulfur clusters to oxidation in the absence of Sod1 anti-oxidant activity is suggested to account for these observations. It is well established that disruptions in Fe-S cluster homeostasis, as may be the case in absence of Sod1, lead to the activation Aft1 and the iron regulon (Outten and Albetel, 2013; Rutherford et al., 2005). Reactive oxygen species can oxidize Fe-S clusters and bring about conformational changes leading to disassembly, inactivation or interconversion between different Fe-S cluster forms (Rouault and Tong, 2005). In all cases, the activity of these essential iron co-factors can be diminished or altered by oxidative stress and thus may be dependent on the function of Sod1. We now provide evidence for the requirement of the highly conserved eukaryotic Cu-Zn Sod1 for surviving iron limitation in the model organism *S. cerevisiae*. We further reveal a novel role of the copper reductase activity of the nucleosome in iron metabolism through supporting Sod1 function,

rather than supporting the high affinity iron uptake system.

The newly discovered function of histones in copper homeostasis may open a window into other possible links between biousability of copper and iron metabolism. A direct crosstalk between the nucleosome and the iron metabolome can be hypothesized involving the regulation of copper reductase activity in response to cellular iron status. Low levels of bioavailable iron, through activating the iron-deficiency response, may increase the nucleosome copper reductase activity to meet the demand for cuprous ions by Sod1 in protecting the remaining Fe-S clusters from oxidative damage.

Our data indicate that provision of $Cu^{1+}$ by nucleosomes for intracellular copper-dependent processes may be specific, although the determinants of this specificity remain to be determined. Copper-dependent processes in the mitochondrial and cytoplasmic compartments, respiration (see Chapter 4) and Sod1 function, respectively, but not the endomembrane compartment (i.e. Fet3 activation) are dependent on the copper reductase activity of the nucleosome. This could mean that there is a functional separation between potentially distinct intracellular pools of biousable copper. It will be informative to investigate whether such functional separation stems from compartmentalization or other mechanisms. Of course, it is important to note that the lack of a measurable defect in iron uptake in our system may not completely rule out the dependency of this copper-dependent process on the nucleosome copper reductase activity. The H113N mutation investigated in this study may represent a mild disruption of the copper reductase activity of the nucleosome, whereby it still maintains sufficient cuprous ion generation for utilization by Fet3. Further investigation of the nucleosome enzymatic activity is required to address this possibility.

An important remaining question involves determining which iron cofactor(s) are the

most susceptible to oxidative damage, and thus are the most dependent on the nucleosome copper reductase function. An intriguing possibility is that mitochondrial Fe-S cluster proteins are the most dependent on the histones. By supplying copper for respiration and Sod1 function, histones seem to support a network of mitochondrial processes, such as the electron transport chain. By supporting mitochondrial respiration via copper provision for cytochrome c oxidase, iron-sulfur cluster assembly is indirectly supported also, which in turn supports mitochondrial respiration since Fe-S cofactors are used in the electron transport chain (Lill, 2009). Yet, oxygen consumption by the mitochondria can inadvertently produce reactive oxygen species which imposes pressure for protection of Fe-S clusters (Turrens, 2003). The integrity of Fe-S clusters is therefore a critical parameter for mitochondrial function itself and likely for general cellular fitness when mitochondrial respiration is elevated. In any case, our knowledge of the nucleosome copper reductase activity in modern eukaryotes is limited. More investigation is warranted to better understand the impact of this novel function of histones on metal homeostasis. Given the essential nature of iron for diverse cellular processes, the enzymatic activity of the nucleosome in supporting iron metabolism can have far-reaching effects for eukaryotic biology, human physiology and disease.

## 5.5 Materials and Methods

### Strains and general growth conditions

Haploid *Saccharomyces cerevisiae* strains used in this study are based on the BY4741 (S288C background, MATa) (Brachmann et al., 1998) strain. All strains were maintained on standard YPD (1% Yeast extract, 2% Peptone, 2% Glucose) plates and were grown at 30°C for varying amounts of time in all experiments as described below. Unless otherwise noted, all yeast

experiments were initiated by growing cells overnight to dense cultures in various media conditions. The cells were subsequently diluted in fresh media as described below.

**Oligonucleotides, plasmids, and strain generation for yeast experiments**

All yeast strains were generated by the standard lithium acetate-based yeast transformation procedures. DNA fragments used for gene replacement deletions or promoter integrations were generated by PCR from plasmid templates. DNA fragments used as homology-directed repair templates for CRISPR-Cas9 mutagenesis were generated by primer extension to generate 100-120 bp-long oligonucleotides.

The histone H3 His113Asn (H3H113N) mutation was generated in both chromosomal loci (*HHT1* and *HHT2*) in a stepwise and marker-less manner. First, using the *delitto perfetto* approach (Storici and Resnick, 2006), H113N was introduced into the *HHT2* locus. The entire *HHT2* coding region was first replaced with a KanMX4-KlURA3 cassette, with selection on Geneticin. Subsequently, the KanMX4-KlURA3 was precisely replaced with either the WT *HHT2* as a control (essentially restoring the BY4741 strain, but distinguished as OCY1131 here to account for its history of temporarily lacking HHT2), or with an *HHT2* variant harboring the H113N mutation (340-CAC-342 becomes 340-AAC-342), with counter-selection on 5-fluroorotic acid. DNA fragments used for the reintroduction of WT *HHT2* or *hht2-H113N* were generated by PCR using plasmids containing the WT *HHT2* (pRM200) (Mann and Grunstein, 1992) or *hht2-H113N* (pYX55) as templates. The pYX55 plasmid was generated by site-directed mutagenesis of the WT *HHT2* on pRM200 using the Agilent Lightning quick change mutagenesis kit, as directed by the manufacturer.

Second, the H113N mutation was introduced in *HHT1* using the CRISPR-Cas9 system optimized for *S. cerevisiae* (Ryan et al., 2014). The pCAS plasmid, containing both the Cas9

gene from *Streptococcus pyogenes* and a single guide RNA, was a gift from Jamie Cate (Ryan et al., 2014). To target Cas9 to the *HHT1* region containing H113, the 20 bp targeting sequence at the 5' end of the sgRNA was changed by PCR. First, pCAS was PCR-amplified with Phusion High-Fidelity DNA Polymerase (NEB) using a 5'-phosphorylated reverse primer immediately upstream of the target sequence, and a forward primer containing the 20 nucleotide *HHT1* region surrounding H113 on its 5' end. The PCR product was treated with DpnI endonuclease (NEB) and re-circularized with T4 DNA ligase (NEB) according to manufacturers' protocols. The H113N mutation (340-CAC-342 becomes 340-AAT-342) was then introduced in yeast by co-transformation with the *HHT1-H113*-targeting pCAS plasmid, and a 100-nt double stranded homology-directed repair template containing the mutation. Successful mutagenesis at both *HHT1* and *HHT2* was confirmed by sequencing of the entire gene coding locus. The histone H3 H113Y, R116H, and A111T mutations were introduced in a similar manner as described but CRISPR-Cas9 was used for both HHT1 and HHT2.

Subsequent deletions of *CTR1*, *CCC2*, *AFT1*, *FET3*, *FET5*, and *SOD1* were generated by standard yeast gene replacement and targeted insertion methodology using selectable marker integration (Goldstein and McCusker, 1999; Longtine et al., 1998). Successful integrations and deletions were confirmed by PCR. Importantly, combinations of the histone mutants with these gene deletions were generated in the strain already containing the histone mutation in both histone H3 copies.

**Spot tests**

Following an overnight growth, cells were diluted to OD600 = 0.3-0.4 in YPD and grown at 30°C for 4-5 hrs to log phase (OD600 = 1-2). Cells were subsequently pelleted by centrifugation, washed and resuspended in water to OD600 = 5. Cells were then 10-fold serially

diluted and 5 µL of cells were spotted on agar plates containing media and additives as indicated in the figures. Cells were incubated at 30°C for up to 7 days and imaged daily using an Epson document scanner. Because of differing growth rates in the various media conditions, images shown in the figures were captured when sufficient growth had occurred and growth differences could be assessed, and this ranged between 2-7 days. Media for normoxic and hypoxic conditions was supplemented with 20 µg/ml ergosterol, 0.5% Tween-80 and 0.5% ethanol to support growth in low-oxygen conditions. The plates were then placed in a sealed hypoxic jar for 5 days at 30°C before capturing images, while normoxic control plates were incubated as usual.

**RNA extraction**

Following an overnight growth, cells were diluted in the various media conditions indicated in the figures. Cells grown in SC were diluted to OD600 = 0.05 and grown for 5 doublings at 30°C, at which point they were growing exponentially. Approximately 1.5x108 cells were collected by centrifugation and frozen at -20°C until further processing. RNA was extracted using previously published methods (Schmitt et al., 1990) with some modifications. Frozen cell pellets, without significant thawing, were resuspended in 440 µL of AE buffer (50 mM Na acetate pH 5.2, 10 mM EDTA, 1% SDS), and RNA was extracted by addition of 440 µL of 5:1 phenol:chloroform pH 4.5 (ThermoFisher) and incubation at 65°C for 4 min. Samples were then rapidly frozen in dry ice-ethanol, and centrifuged at 16,000xg to separate the aqueous and phenol phases. The aqueous supernatant (350 µL) was transferred to a new tube, and re extracted by addition of 300 µL of 25:24:1 phenol:chloroform:isoamyl alcohol, and centrifuged as above to separate phases. 250 µL was transferred to a new tube, 25 µL of 3 M Na acetate pH 5.2 was added, and nucleic acids were ethanol-precipitated. Nucleic acid pellets were then resuspended in 100 µL of nuclease-free water and stored at -20°C until further processing. RNA

concentration was measured by Nanodrop 2000 microvolume spectrophotometer. Typical yield from this extraction method was about 30 μg of total RNA. RNA extracted for subsequent RNA-seq analysis are from two replicates of cells grown on different days with different media batches.

**Sample preparation for poly-A RNA sequencing**

Prior to preparing RNA-seq libraries for Illumina HiSeq sequencing, contaminating DNA was digested, and RNA quality was assessed. Total RNA (10 μg) was treated with Turbo DNase according to the manufacturer's "Routine DNase treatment" procedures. RNA-sequencing libraries were then prepared either manually with the KAPA Stranded mRNA-seq library prep kit (KAPA Biosystems), or with automation, using the Illumina TruSeq Stranded mRNA Library Kit for NeoPrep (Illumina). Both library preparation procedures first isolate polyA+ mRNAs using oligo-dT beads. Isolated polyA+ RNAs are then chemically fragmented, and random primers are used in the first cDNA reverse transcription step. For both approaches, libraries were prepared according to the manufacturer's protocols.

**mRNA-sequencing and data processing**

High throughput sequencing was performed on Illumina's HiSeq 4000 system, with singleend 50 bp insert reads, and dedicated index reads. Total read count per library ranged from ~1.5-9 million. De-multiplexed reads, in FASTQ file format, were aligned to the R64-1-1 S288C reference genome assembly (sacCer3), downloaded from the UCSC database, using Tophat 2.0.9 (Kim et al., 2013). The "-g 1" parameter was used to limit the number of alignments for each read to one, the top-scoring alignment. In the case of a tie, the read was randomly distributed to one of the tied top-scoring alignments. Percentage of reads aligned once was greater than 90% in all cases.

**Gene expression analysis**

Gene expression values, in reads per kilobase per million mapped reads (RPKMs), for 6692 annotated open reading frames were calculated using SAMMate 2.7.4 (Xu et al., 2011). In calculating RPKM values, only reads that align to annotated exons were considered. Reads aligning to introns or intergenic regions were not counted in normalizing the read counts to the total number of mapped reads. Many of the 6692 annotated ORFs have no attributed function, localization, mutant phenotypes or interactions and are often labeled as "dubious" or "putative" in the Saccharomyces Genome Database (SGD). Furthermore, these putative ORFs typically have low expression values. We removed 1648 such ORFs from further analysis, and used the remaining 5044 ORFs for comparisons between groups.

**Sample preparation for inductively-coupled plasma mass spectrometry (ICP-MS)**

Cells from dense overnight cultures in SC media were diluted to OD600 = 0.2-0.4 and grown at 30°C for ~3 doublings in SC or SC containing the iron chelator, bathophenanthrolinedisulfonic acid (BPS). Three replicate cultures were prepared for each sample. Cells (4-12 x 108) were collected by centrifugation, and cell pellets were washed twice in 1 mM EDTA to remove cell surface-associated metals. This was followed by one wash in Nanopure Diamond filtered water to remove residual EDTA. Cell pellets were then stored at -20°C for 1-3 weeks prior to preparation for ICP-MS. Plastic bottles and cylinders used for preparation of solutions for sample digestion were treated with 7-10% ACS grade nitric acid for 5 days at 50°C. Acid-washed materials were rinsed thoroughly with Nanopure water before use. Frozen cell pellets were thawed at room temperature and packed by centrifugation at 3000xg. Pellets were overlaid slowly (not to disrupt the pellet) with 70% Optima Grade nitric acid and digested at 65°C for 12-16 hrs. Prior to mass spectrometry, the digested samples were diluted

with Nanopure water to a final concentration of 2% nitric acid and a final volume of 3-5 mL.

**Inductively-coupled plasma mass spectrometry**

Total Fe content was measured by inductively coupled plasma mass spectrometry on the Agilent 8800 ICP-QQQ in MS/MS mode. The most abundant isotopes of iron (i.e. Fe56) was used to determine the total cellular iron and copper levels. Iron was measured both directly, with hydrogen present in the collision/reaction cell, and indirectly, after mass-shift to FeO with oxygen present in the cell. While both methods produced similar results, the data presented here for iron are from oxygen mass-shift mode. The metal content was determined in comparison to an environmental calibration standard (Agilent 5183-4688) reflecting biological samples. Every run was calibrated individually, 45Sc or 89Y were used as internal standards to compare the calibration with the analyzed samples. Average counts of 5 technical replicates were used for each calibration standard and each individual biological sample. The deviation in between technical replicates never exceeded 5%. Standard deviation in figures reflects the standard deviation between biological replicates (n = 3 - 6). Prepared calibration standards ranged from 1 ppb - 50 ppm for 56Fe. All Fe measurements in our study were well above the lower limits of detection, which was determined from multiple blank samples. We used ICP MassHunter software for ICP-MS data analysis.

**Liquid cultures for iron uptake assays**

To assess iron uptake capacity, following an overnight growth in SC media, cells were diluted to OD600 = 0.2 in fresh media with or without the iron chelator, bathophenanthrolinedisulfonic acid (BPS), and grown at 30°C for 2-3 doublings. Cell density of the culture was measured after this period and cells were collected from growth in SC media for preparation for ICP-MS. Cells grown in presence of BPS were washed with Nanopure Diamond

filtered water and diluted to OD600 = 0.5 in fresh SC media. Cells were grown at 30°C for 1 hour or 1 doubling after which point they were collected for ICP-MS.

## 5.6 References


Aisen, P., Enns, C., and Wessling-Resnick, M. (2001). Chemistry and biology of eukaryotic iron metabolism. Int J Biochem Cell Biol *33*, 940-959.

Arredondo, M., Martinez, R., Nunez, M.T., Ruz, M., and Olivares, M. (2006). Inhibition of iron and copper uptake by iron, copper and zinc. Biol Res *39*, 95-102.

Brachmann, C.B., Davies, A., Cost, G.J., Caputo, E., Li, J.C., Hieter, P., and Boeke, J.D. (1998). Designer deletion strains derived from Saccharomyces cerevisiae S288C: a useful set of strains and plasmids for PCR-mediated gene disruption and other applications. Yeast *14*, 115-132.

Castells-Roca, L., Muhlenhoff, U., Lill, R., Herrero, E., and Belli, G. (2011). The oxidative stress response in yeast cells involves changes in the stability of Aft1 regulon mRNAs. Molecular microbiology *81*, 232-248.

De Freitas, J.M., Liba, A., Meneghini, R., Valentine, J.S., and Gralla, E.B. (2000). Yeast lacking Cu-Zn superoxide dismutase show altered iron homeostasis - Role of oxidative stress in iron metabolism. J Biol Chem *275*, 11645-11649.

Dlouhy, A.C., and Outten, C.E. (2013). The iron metallome in eukaryotic organisms. Met Ions Life Sci *12*, 241-278.

Foster, A.W., Osman, D., and Robinson, N.J. (2014). Metal preferences and metallation. J Biol Chem *289*, 28095-28103.

Frieden, E. (1971). Ceruloplasmin, a Link between Copper and Iron Metabolism. Adv Chem Ser, 292-+.

Goldstein, A.L., and McCusker, J.H. (1999). Three new dominant drug resistance cassettes for gene disruption in Saccharomyces cerevisiae. Yeast *15*, 1541-1553.

Hellman, N.E., and Gitlin, J.D. (2002). Ceruloplasmin metabolism and function. Annu Rev Nutr *22*, 439-458.

Hong Enriquez, R.P., and Do, T.N. (2012). Bioavailability of metal ions and evolutionary adaptation. Life *2*, 274-285.

Kaplan, C.D., and Kaplan, J. (2009). Iron acquisition and transcriptional regulation. Chem Rev *109*, 4536-4552.

Kosman, D.J. (2003). Molecular mechanisms of iron uptake in fungi. Molecular microbiology *47*, 1185-1197.

Kotze, M.J., van Velden, D.P., van Rensburg, S.J., and Erasmus, R. (2009). Pathogenic Mechanisms Underlying Iron Deficiency and Iron Overload: New Insights for Clinical Application. EJIFCC *20*, 108-123.

Lang, M.L., Braun, C.L., Kanost, M.R., and Gorman, M.J. (2012). Multicopper oxidase-1 is a ferroxidase essential for iron homeostasis in Drosophila melanogaster. P Natl Acad Sci USA *109*, 13337-13342.

Lieu, P.T., Heiskala, M., Peterson, P.A., and Yang, Y. (2001). The roles of iron in health and disease. Mol Aspects Med *22*, 1-87.

Lill, R. (2009). Function and biogenesis of iron-sulphur proteins. Nature *460*, 831-838.

Longtine, M.S., McKenzie, A., Demarini, D.J., Shah, N.G., Wach, A., Brachat, A., Philippsen, P., and Pringle, J.R. (1998). Additional modules for versatile and economical PCR-based gene deletion and modification in Saccharomyces cerevisiae. Yeast *14*, 953-961.

Mann, R.K., and Grunstein, M. (1992). Histone H3 N-Terminal Mutations Allow Hyperactivation of the Yeast Gal1 Gene Invivo. Embo J *11*, 3297-3306.

Muthurajan, U.M., Bao, Y., Forsberg, L.J., Edayathumangalam, R.S., Dyer, P.N., White, C.L., and Luger, K. (2004). Crystal structures of histone Sin mutant nucleosomes reveal altered protein-DNA interactions. Embo J *23*, 260-271.

Outten, C.E., and Albetel, A.N. (2013). Iron sensing and regulation in Saccharomyces cerevisiae: Ironing out the mechanistic details. Current opinion in microbiology *16*, 662-668.

Palumaa, P. (2013). Copper chaperones. The concept of conformational control in the metabolism of copper. Febs Lett *587*, 1902-1910.

Papa, L., Hahn, M., Marsh, E.L., Evans, B.S., and Germain, D. (2014). SOD2 to SOD1 switch in breast cancer. J Biol Chem *289*, 5412-5416.

Popovic-Bijelic, A., Mojovic, M., Stamenkovic, S., Jovanovic, M., Selakovic, V., Andjus, P., and Bacic, G. (2016). Iron-sulfur cluster damage by the superoxide radical in neural tissues of the SOD1(G93A) ALS rat model. Free Radic Biol Med *96*, 313-322.

Pujol-Carrion, N., Belli, G., Herrero, E., Nogues, A., and de la Torre-Ruiz, M.A. (2006). Glutaredoxins Grx3 and Grx4 regulate nuclear localisation of Aft1 and the oxidative stress response in Saccharomyces cerevisiae. J Cell Sci *119*, 4554-4564.

Rouault, T.A., and Tong, W.H. (2005). Iron-sulphur cluster biogenesis and mitochondrial iron homeostasis. Nat Rev Mol Cell Bio *6*, 345-351.

Rutherford, J.C., and Bird, A.J. (2004). Metal-responsive transcription factors that regulate iron, zinc, and copper homeostasis in eukaryotic cells. Eukaryot Cell *3*, 1-13.

Rutherford, J.C., Ojeda, L., Balk, J., Muhlenhoff, U., Lill, R., and Winge, D.R. (2005). Activation of the iron regulon by the yeast Aft1/Aft2 transcription factors depends on mitochondrial but not cytosolic iron-sulfur protein biogenesis. J Biol Chem *280*, 10135-10140.

Ryan, O.W., Skerker, J.M., Maurer, M.J., Li, X., Tsai, J.C., Poddar, S., Lee, M.E., DeLoache, W., Dueber, J.E., Arkin, A.P., *et al.* (2014). Selection of chromosomal DNA libraries using a multiplex CRISPR system. Elife *3*.

Saccon, R.A., Bunton-Stasyshyn, R.K.A., Fisher, E.M.C., and Fratta, P. (2013). Is SOD1 loss of function involved in amyotrophic lateral sclerosis? Brain *136*, 2342-2358.

Schroder, I., Johnson, E., and de Vries, S. (2003). Microbial ferric iron reductases. FEMS Microbiol Rev *27*, 427-447.

Spizzo, T., Byersdorfer, C., Duesterhoeft, S., and Eide, D. (1997). The yeast FET5 gene encodes a FET3-related multicopper oxidase implicated in iron transport. Mol Gen Genet *256*, 547-556.

Storici, F., and Resnick, M.A. (2006). The delitto perfetto approach to in vivo site-directed mutagenesis and chromosome rearrangements with synthetic oligonucleotides in yeast. Method Enzymol *409*, 329-+.

Taylor, A.B., Stoj, C.S., Ziegler, L., Kosman, D.J., and Hart, P.J. (2005). The copper-iron connection in biology: structure of the metallo-oxidase Fet3p. Proceedings of the National Academy of Sciences of the United States of America *102*, 15459-15464.

Turrens, J.F. (2003). Mitochondrial formation of reactive oxygen species. J Physiol *552*, 335-344.

Urbanowski, J.L., and Piper, R.C. (1999). The iron transporter Fth1p forms a complex with the Fet5 iron oxidase and resides on the vacuolar membrane. J Biol Chem *274*, 38061-38070.

Vashchenko, G., and MacGillivray, R.T.A. (2013). Multi-Copper Oxidases and Human Iron Metabolism. Nutrients *5*, 2289-2313.

Wallace, M.A., Liou, L.L., Martins, J., Clement, M.H., Bailey, S., Longo, V.D., Valentine, J.S., and Gralla, E.B. (2004). Superoxide inhibits 4Fe-4S cluster enzymes involved in amino acid biosynthesis. Cross-compartment protection by CuZn-superoxide dismutase. J Biol Chem *279*, 32055-32062.

Yuan, D.S., Stearman, R., Dancis, A., Dunn, T., Beeler, T., and Klausner, R.D. (1995). The Menkes/Wilson disease gene homologue in yeast provides copper to a ceruloplasmin-like oxidase required for iron uptake. Proceedings of the National Academy of Sciences of the United States of America *92*, 2632-2636.

Zhang, C. (2014). Essential functions of iron-requiring proteins in DNA replication, repair and cell cycle control. Protein Cell *5*, 750-760.